STRUCTURAL EVOLUTION, PETROPHYSICS, AND LARGE-SCALE

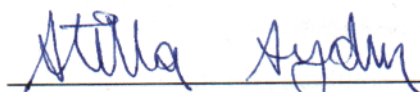PERMEABILITY OF FAULTS IN SANDSTONE, VALLEY OF FIRE, NEVADA

A DISSERTATION

SUBMITTED TO THE DEPARTMENT OF GEOLOGICAL AND

ENVIRONMENTAL SCIENCES

AND THE COMMITTEE ON GRADUATE STUDIES

OF STANFORD UNIVERSITY

IN PARTIAL FULFILLMENT OF THE REQUIREMENTS

FOR THE DEGREE OF

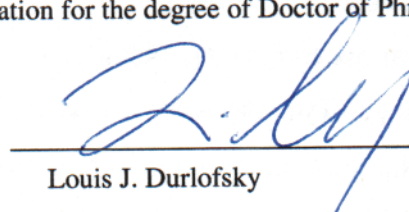DOCTOR OF PHILOSOPHY

Eric Anders Flodin

January 2003

I certify that I have read this dissertation and that in my opinion it is fully adequate, in scope and quality, as a dissertation for the degree of Doctor of Philosophy.

_____

Atilla Aydin, Principal Advisor

I certify that I have read this dissertation and that in my opinion it is fully adequate, in scope and quality, as a dissertation for the degree of Doctor of Philosophy.

_____

Louis J. Durlofsky

I certify that I have read this dissertation and that in my opinion it is fully adequate, in scope and quality, as a dissertation for the degree of Doctor of Philosophy.

_____

David D. Pollard

Approved for the University Committee on Graduate Studies:

_____

Abstract

Faults in porous sandstone act to both impede and enhance the flow of fluids in subsurface aquifers and reservoirs. Surface analogs of exhumed faulted sandstones can provide valuable information concerning fault geometry and flow characteristics. This study focuses on the geometric evolution and flow characteristics of faults in the Aztec sandstone, Valley of Fire State Park, southern Nevada.

Previous studies have identified two distinct faulting mechanisms that localize deformation in sandstone: (1) deformation band-style faulting, which involves pore collapse and grain-scale fracturing, and (2) sheared joint-style faulting, which involves the progressive formation and subsequent shearing of splay fractures. The faults in this study formed via the later mechanism, shearing along joint zones.

In the Valley of Fire, the Aztec sandstone is deformed by a network of two predominately strike-slip fault sets with opposite slip sense. An outcrop- to kilometers-scale conceptual model for the evolution of the strike-slip fault network is presented whereby the network forms by linking of first generation faults via Mode I splay fracturing. These splay fractures are subsequently sheared to form a second generation of faults that have slip sense opposite to the prior generation. At the outcrop-scale at least five hierarchical generations of structures are identified. It is proposed that shearing of Mode I splay fractures is facilitated by material rotation near and between slipping faults and/or local stress rotation due to fault interaction. The final geometry of the fault network is dictated by the characteristic splay fracture kink angle.

Cross-fault flow characteristics are quantified by way of detailed petrophysical analysis. Petrophysical data indicate that fault rock permeability is significantly lower than host rock permeability, and that the faults will act as lateral barriers with respect to reservoir production time-scales. The petrophysical data also show that fault rocks are capable of sealing small to moderate hydrocarbon columns with respect to geologic time-scales, assuming adequate continuity of the fault rock over large areas of the fault.

Large-scale permeability characteristics of the faults are quantified by way of numerical flow simulation techniques that utilize idealizations of detailed field maps. Faults with slips

iv

of magnitude 6 m, 14 m and 150 m are considered. The computed fault zone permeabilities are strongly anisotropic in all cases. Permeability enhancement of nearly an order of magnitude (relative to the host rock) is observed for the fault-parallel component in some regions. Computed fault-normal permeability, by contrast, may be two orders of magnitude less than the host rock permeability. The fault-normal permeability is a minimum for the fault with the highest slip.

The numerical flow models of sheared joint faults in sandstone are shown to be highly sensitive to the chosen boundary conditions. Pressure - no-flow and mirror-periodic boundary conditions capture the global flow characteristics of upscaled fault regions. Periodic boundary conditions tend to break connectivity between both high and low permeability features, which tends to result in erroneous upscaled permeabilities in regions with through-going features. Due to the small dimensions and high permeability of some through-going structural features (e.g., slip surfaces), globally upscaled models are inadequate for the modeling of transport. In these cases, transport predictions are improved by a step-wise method of removing the through-going high-permeability features from the fine model, upscaling to a coarse grid, and then reintroducing the high-permeability features in the coarsened model.

Acknowledgements

I am indebted to the following faculty and research staff who guided various parts of this research: Atilla Aydin, Lou Durlofsky, Peter Eichhubl, Peter Kitanidis, Keith Loague, Dave Pollard, and Manika Prasad. Atilla, my principal advisor, had a particularly large impact on this research. I thank him for instilling in me a sense of scientific rigor and focus. Lou's guidance was indispensable for the completion of the flow modeling aspects of this work. I also enjoyed research collaborations with Martha Gerdes, Xian-Huan Wen, and Dave Wiggins, all with ChevronTexaco Petroleum Technology Company. Lastly, I thank the faculty (particularly, Andy Barth) and staff of the Indiana/Purdue University at Indianapolis (IUPUI) Geology Department, for first introducing me to the wonderful world of geologic research.

Thanks to my friends who accompanied me in the field: Fabrizio Agosta, Billy Belt, Stephan Bergbauer, Jeff Chapin, Nick Davatzes, Hervé Jourde, Frantz Maerten, and Frank Schneider. Some of the best times during my graduate student tenure were had in the field. I also thank my fellow graduate students in the Rock Fracture Project research group for providing a friendly, fun, open, and honest working environment. I cannot imagine a better place to spend one's workday. Lastly, thanks to Scott Young and Brita Graham for being great officemates.

Deep gratitude goes to my parents, Anders and Barbara. My father instilled in me the concept of commitment that enabled me to complete this thesis. My mother instilled in me the concept of compassion that enabled me to embrace things outside of my academic endeavors, particularly my family. I also thank my best friend and wife, Laura, who supported me throughout this project and allowed me time to work, albeit sometimes begrudgingly, late into the night. This thesis is dedicated to her.

EAF, December 4th, 2002

Table of Contents

List of Tables

List of Illustrations

Introduction

Faults in porous sandstone act to both impede and enhance the flow of fluids in subsurface aquifers and reservoirs. Information on the geometry of faults in the subsurface and their flow properties are therefore important prerequisites to making accurate aquifer/reservoir performance predictions. However, these data are not readily available from typical 3-D seismic data, 1-D borehole data, and well-production data. Recognizing these limitations, this study focuses on outcrop exposures of deformed aeolian Aztec sandstone in the Valley of Fire State Park, southern Nevada, which can be considered an exhumed analog to a subsurface aquifer/reservoir.

The material covered in this thesis integrates techniques from the fields of structural geology, rock petrophysics, and reservoir engineering to describe the structural evolution and fluid flow properties of sheared joint-style faults in porous sandstone. Each section of this thesis focuses primarily on one of these sub-disciplines and is meant as a stand-alone manuscript ready for peer-reviewed journal submission. As such, some material is repeated between chapters, particularly the introductory material. The thesis is divided into five chapters and two appendices, all of which are individually discussed below. In an attempt to give the reader a general introduction to the study locality, a summary of the geologic setting of the Aztec sandstone in the vicinity of the Valley of Fire, southern Nevada is presented following this introduction.

Chapter 1 describes the formation and evolution of the strike-slip fault network in the Aztec sandstone using outcrop- to kilometer-scale field observations. This chapter was submitted to the *Geological Society of America Bulletin* in October 2002 for publication under the title "Evolution of a strike-slip fault network, Valley of Fire, southern Nevada," and includes Atilla Aydin as co-author.

Chapter 2 focuses on the petrophysical properties of undeformed Aztec sandstone as they relate to various deformation styles found within the Aztec sandstone. Laboratory data for this study was collected by me in the Stanford Rock Physics Lab under the close supervision and tutelage of Manika Prasad. This chapter was accepted for publication in *Pure and Applied Geophysics* under the title "Petrophysical constraints on deformation styles in Aztec sandstone, southern Nevada, USA," and is co-authored by Prasad and Aydin.

Chapter 3 analyzes the petrophysical properties of fault rocks obtained from fault zones in Aztec sandstone. Martha Gerdes and Dave Wiggins, affiliated with ChevronTexaco Exploration and Production Technology Company (EPTC), were outside mentors for this project. Porosity, permeability, particle-size, X-ray diffraction, and capillary pressure data were collected by Core Laboratories, USA, while petrographic and SEM data were collected by me. Additionally, data collected in Chapter 2 is used as a supplement to data presented in this chapter. A manuscript, based on this chapter, entitled "Petrophysical properties and sealing capacity of fault rock from sheared-joint based faults in sandstone" was submitted September 2002 for publication in a special *American Association of Petroleum Geologists Memoir* dedicated to fault seal and flow problems. The manuscript is co-authored by Gerdes, Aydin and Wiggins. ChevronTexaco provided the funding for the collection of the analytical data.

Chapter 4 describes the bulk fluid flow characteristics of the faults in the Aztec sandstone. This study utilized highly detailed fault maps provided by Rod Myers (1999) and a numerical flow modeling code developed by Xian-Huan Wen at EPTC. The first draft and initial research for this paper was performed by Hervé Jourde during a postdoctoral study under the tutelage of Atilla Aydin. Following the departure of Jourde, I completed the project by simulating new numerical upscaling results of fault zone permeability, which formed the basis of the material presented in Chapter 4. I also drafted the figures, and along with Aydin and Lou Durlofsky, revised and updated the text of the first draft. The revised version of this paper, along with my cover photograph submission, was accepted for publication and appears in the July 2002 edition of the *American Association of Petroleum Geologists Bulletin* under the title "Computing permeability of fault zones in eolian sandstone from outcrop measurements." The author list for this paper appears in the following order: Jourde, Flodin, Aydin, Durlofsky, and Wen.

Chapter 5 investigates the effects of boundary conditions on upscaling fault zone permeability, and provides a modeling framework for explicitly representing through-going, high-permeability fault elements in coarsened fault permeability models. Xian-Huan Wen

(EPTC) and Mohammad Karmini-Fard (Stanford University) developed the numerical codes utilized in this chapter. At present, submission of this chapter to a peer-reviewed journal remains under consideration.

Appendix A is a short contribution that details the formation of asymmetric damage zones about sheared-joint faults. This chapter was submitted to the *Journal of Structural Geology* in July 2002 for publication under the title "*Brevia*: Faults with asymmetric damage zones in sandstone, Valley of Fire State Park, southern Nevada," and includes Atilla Aydin as co-author.

Appendix B applies the upscaled fault permeability values obtained in Chapter 4 to reservoir-scale (kilometer-scale) multiphase flow problems. Burak Yeten guided me in the use of ECLIPSE, a commercially available multiphase numerical flow simulator. This paper appeared as Paper #71617 in the 2001 *Society of Petroleum Engineers Annual Technical Conference and Exhibition Proceedings* under the title "Representation of fault zone permeability in reservoir flow models," and is co-authored by Aydin, Durlofsky, and Yeten.

Geologic setting of the Aztec sandstone, Valley of Fire, Nevada

This study focuses on strike-slip faults found within the aeolian Jurassic Aztec sandstone (AZS) exposed in the Valley of Fire State Park (Valley-of-Fire) in the Northern Muddy Mountains of southern Nevada (see Figure 1.1). The AZS in the Valley-of-Fire is a fine to medium grained sub-arkose characterized by large-scale tabular-planar and wedge-planar cross-strata (Marzolf, 1983; Marzolf, 1990). Host rock sandstone porosities range from 15-25%, while permeabilities range from 100-2500 md. Within the Valley-of-Fire, the AZS has a stratigraphic thickness of approximately 800 m (Longwell, 1949) and is divided into three sub-units based on gross outcrop color (Taylor, 1999). From the stratigraphically low-est position, the sub-units are lower red unit, middle buff unit, and upper orange unit. The lower red unit is well cemented and has a low average porosity; the middle buff unit is poorly cemented and has a high average porosity; the upper orange unit is moderately ce-mented an has a high average porosity (Flodin et al., in press).

The AZS was deposited in early Jurassic time in a back-arc basin setting (Marzolf, 1983) and was part of a more continuous aeolian erg system that included the Navajo sand-stone of the Colorado Plateau (Poole, 1964; Blakey, 1989). The Aztec and Navajo sand-stones are the upper most members of the Glen Canyon group (Pipiringos and O'Sullivan, 1978). In the study area, the lower members of the Glen Canyon Group are present as undif-ferentiated Jurassic Moenave and Kayenta Formations (Wilson and Stewart, 1967). These two units are fluvial to marginal marine in origin and are found intertonguing with the base of the AZS (Bohannon, 1983a).

The middle to late Jurassic San Rafael Group and Morrison Formation (Pipiringos and O'Sullivan, 1978), found on the nearby Colorado Plateau unconformably overlying the Na-vajo (Aztec) sandstone, is absent in southern Nevada (Marzolf, 1990). These younger units were either non-depositional in southern Nevada or were removed prior to deposition of the overlying Cretaceous units (discussed below). However, it is unlikely that the AZS was not buried to depths great enough for diagenesis to occur as the AZS appears to have been cemented prior to the onset of Sevier deformation (discussed below) (Flodin et al, in press). Some evidence does exist that these younger units were at least in part present in southern Nevada. Bohannon (1983a) tentatively identified a thin slice of Jurassic Carmel Formation

4

overlying the AZS in the Buffington Pockets area, about 15 km to the southwest of the study area. This would be the only known exposure of middle to late Jurassic sedimentary unit lithostratigraphically equivalent to Colorado Plateau units in southern Nevada (Marzolf, 1990).

Unconformably underlying the Glen Canyon Group are the continental deposits of the upper Triassic Chinle Formation (Stewart et al., 1972a) and the coastal-plain to marginal marine deposits of the lower Triassic Moenkopi Formation (Stewart et al., 1972b). These Triassic units in turn unconformably overlie the thick Paleozoic passive continental margin deposits that comprise the Cordilleran miogeocline (Stewart, 1980).

Post-Aztec sandstone depositional history

<u>Mesozoic contractional deformation and sedimentation</u>

Since deposition, the AZS has experienced a long and varied deformation history (Figure I.1). The earliest stage of deformation is attributable to regionally extensive, thin-skinned east-directed thrusting associated with the Sevier orogeny (Armstrong, 1968). Following deposition and likely burial, the AZS was once again exhumed to the surface in late Jurassic
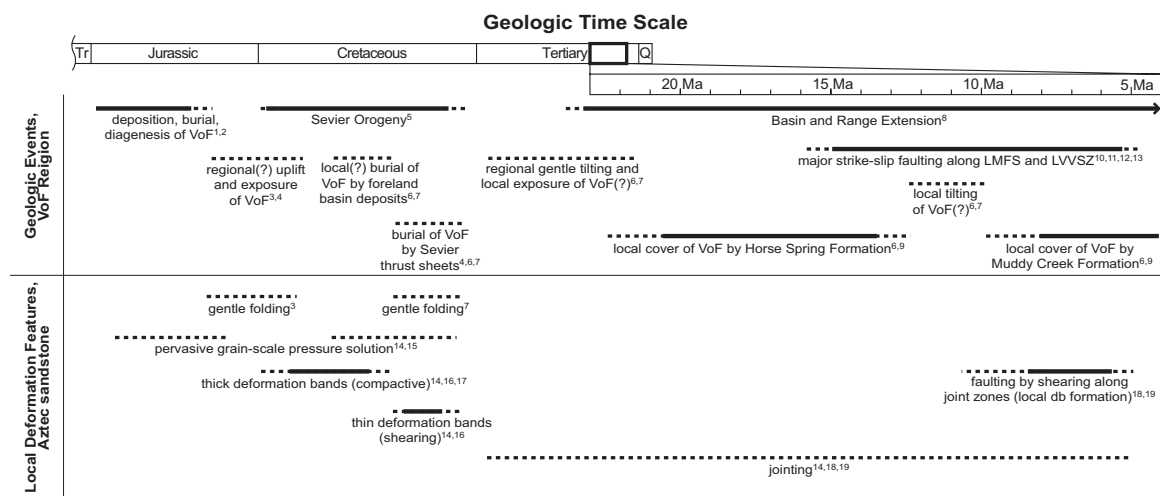
Figure I.1. Summary of geologic and tectonics events for the Aztec sandstone in the vicinity of the Valley of Fire, southern Nevada. References are as follows: [1]Poole (1964); [2]Marzolf (1983); [3]Fleck (1970); [4]Brock and Engelder (1977); [5]Armstrong (1968); [6]Bohannon (1983a); [7]Carpenter and Carpenter (1994); [8]Zoback et al. (1981); [9]Bohannon (1984); [10]Beard (1996); [11]Campagna and Aydin (1994); [12]references in Duebendorfer et al. (1998); [13]Langenheim et al. (2001) and referenced therein; [14]Taylor (1999); [15]Flodin et al. (in press); [16]Hill (1989); [17]Sternlof (2001); [18]Myers (1999); and, [19]this study.

5

to early Cretaceous time. Fleck (1970) attributes the local exposure of the AZS to regional uplift, possibly accompanied by gentle folding, associated with the earliest stages of the Sevier Orogeny.

In the Valley-of-Fire region, the upper stratigraphic contact of the AZS is a slight angular unconformity with the overlying synorogenic Cretaceous Willow Tank Formation and Baseline Formation sandstone (Bohannon, 1983a; Carpenter and Carpenter, 1994). These units were deposited in a foreland basin associated with the advancing Sevier thrust front (Armstrong, 1968). The basal conglomerate unit of the Willow Tank Formation was deposited on regionally exposed erosional surface of AZS and consists of both locally derived and far traveled lithic clasts (Bohannon, 1983a). Quartz arenite beds in the lower White Member of the Baseline Formation appear to be derived and reworked from highlands of AZS to the west (Longwell, 1949; Carpenter and Carpenter, 1994). In contrast, the upper red member of the Baseline Formation is less mature than that of the lower White Member and appears to be locally derived from exposures of AZS (Carpenter and Carpenter, 1994).

At least two large thrust faults were emplaced over the AZS in the vicinity of the Valley-of-Fire in middle Cretaceous time (Bohannon, 1983a; Carpenter and Carpenter, 1994). The earlier Summit-Willow Tank thrust places stratigraphically lower red AZS over upper orange AZS, as well as the overlying synorogenic Cretaceous Willow Tank Formation and the white member of the Baseline sandstone (Bohannon, 1983a). Longwell (1949) estimated slip along a portion of this fault to be on the order of a few kilometers. The Summit-Willow Tank thrust was in turn over-ridden by the regionally extensive and far traveled Muddy Mountain thrust (Longwell, 1949; Bohannon, 1983a). In the Valley-of-Fire, erosion has either removed the upper plate of the Muddy Mountain thrust sheet or the Muddy Mountain thrust sheet was never emplaced over the Valley-of-Fire, as speculated by Bohannon (Plate 1, 1984) and Taylor (1999). However, the AZS in the Valley-of-Fire was buried by at least 1.6 km (approximate thickness of the over lying Cretaceous formations and the Summit-Willow Tank thrust sheet, Bohannon, 1983a). A few kilometers south of the study area in the Muddy Mountains, the Muddy Mountain thrust places Cambrian Bonanza King Formation over the AZS (Bohannon, 1983b). In the Buffington Window of the Muddy Mountains, Brock and Engelder (1979) estimated the thickness of the Muddy Mountain thrust sheet to be 2-5 km.

6

Cenozoic extensional and strike-slip deformation and sedimentation

Cenozoic Basin and Range extensional and strike-slip deformation followed the Sevier orogeny. The Valley-of-Fire region was apparently unaffected by deformation associated with the late Cretaceous - early Tertiary Laramide orogeny (Bohannon, 1983a). The first recorded Cenozoic event to occur in the vicinity of the Valley-of-Fire was the unconformable deposition of non-marine Tertiary sediments atop the Cretaceous Baseline sandstone (Bohannon, 1983a). At this time, much of the southern Nevada region was structurally characterized by a broad, gently north plunging arch, of which the Valley-of-Fire was on the gently north-northeasterly dipping side (Bohannon, Plate 1, 1984). Stratigraphic dips between the Cretaceous units and the overlying basal Tertiary units differ by only 5-10º.

The Tertiary sediments in the Valley-of-Fire region include the Rainbow Gardens and Thumb Members of the Horse Spring Formation [26 Ma - 13.5 Ma (Bohannon, 1984; Beard, 1996)], and the Muddy Creek Formation [10 Ma - 4 Ma (Bohannon et al., 1993)] (Bohannon, 1983a). Intervening upper members of the Horse Spring Formation and the red sandstone unit of Bohannon (1984) are notably missing in the Valley-of-Fire. Tilting of the Valley-of-Fire of up to 25º in a northeasterly direction occurred prior to deposition of the Muddy Creek Formation. Present day bedding dips in the Horse Spring Formation are approximately 30º to the northwest, while in the overlying Muddy Creek Formation they are approximately 5º to the northeast (Carpenter, Plate 1.3, 1989).

Three major structural features related to Miocene Basin and Range deformation define the landscape in the vicinity of the Valley-of-Fire (Figure I.1; also see Figure 1.1). These are: (1) The left-lateral Lake Mead Fault System (LMFS) (Anderson, 1973; Bohannon, 1979), which consists of several strands that show cumulative left-lateral offset of approximately 65 km (Bohannon, 1984). Activity along the LMFS occurred between 16 and 5 Ma (references in Duebendorfer, 1998). (2) The right-lateral Las Vegas Valley Shear Zone (LVVSZ) (Longwell, 1960), which consists of several right stepping segments that form the Las Vegas Valley pull-apart basin (Campagna and Aydin, 1994; Langenheim et al., 2001). Slip along the LVVSZ is estimated to be from 40 to 65 km (Bohannon, 1984), and occurred between 14 and 7.5 Ma (references in Duebendorfer, 1998). Both the LMFS and the LVVSZ

were active contemporaneously based on mutual crosscutting relationships at their intersection in the Gale Hills (Çakir et al., 1998). As mapped by Anderson et al. (1994), the LVVSZ abuts against the more extensive LMFS. (3) The Virgin River depression (VRd), an anomalously deep and complex extensional basin atypical of other basins in the Basin and Range province (Bohannon et al., 1993). Subsidence of the VRd began slowly around 24 Ma, with rapid subsidence occurring between 13-10 Ma (Bohannon et al., 1993). Subsidence is ongoing as evidenced by offset Quaternary deposits in the eastern reaches of the VRd (e.g., Billingsley and Bohannon, 1995). The VRd is divided in the two right-stepping, and north-south elongated sub-basins that are divided by a buried basement ridge. The Mesquite basin to the northeast reaches depths approaching 10 km, while the Mormon basin to the southwest approaches depths of 5km (Langenheim et al., 2000).

Based on stratigraphic offsets, activity along the predominantly strike-slip faults in the Valley-of-Fire (see Figures 1.3 and 1.5) was contemporaneous with the three crustal-scale structures discussed in the previous paragraph. Presently, the faults in the Valley-of-Fire appear to be inactive as evidenced by a lack of recent surface deformation and seismicity in the immediate vicinity (Rogers and Lee, 1976). However, sparse earthquakes near the western lobe of Lake Mead indicate right-lateral slip on north-trending faults. These right-lateral faults share orientation with large-offset left-lateral faults in the Valley-of-Fire (see Chapter 1) and must indicate either local stress reorientations between the two areas, or a change in remote stress orientation following the formation of the Valley-of-Fire fault system.

Chapter 1

Evolution of a strike-slip fault network, Valley of Fire, southern Nevada

Abstract

In the Valley of Fire State Park of southern Nevada, the Jurassic Aztec sandstone is deformed by two predominately strike-slip fault sets with opposite slip sense. One fault set is NNE-oriented and shows maximum left-lateral offsets that range between centimeters and 2.4 km. The other fault set is NW-oriented and shows maximum apparent right-lateral offsets that range between centimeters and 290 m. At a regional scale, most of the right-lateral faults terminate against the larger-offset left-lateral faults and are found localized between en echelon and parallel left-lateral faults, and at the ends of the larger left-lateral faults. At a local scale, right- and left-lateral faults of smaller size show mutually abutting relationships. Also, Mode I splay fractures related to fault slip are observed sharing the same orientation and abutting relationships as members of the left- and right-lateral fault sets. A conceptual model for the evolution of the strike-slip fault network in the Valley-of-Fire is presented whereby the fault network forms via shearing of earlier formed joint zones, followed by progressive Mode I splay fracturing and subsequent shearing of the splay fractures. At the outcrop scale at least five hierarchical generations of structures are identified. It is proposed that shearing of Mode I splay fractures is facilitated by material rotation near and between slipping faults and/or local stress rotation due to fault interaction.

Introduction

Knowledge of subsurface fault geometries is important to both economic and societal needs: Faults have been shown to localize mineral deposits (Sibson, 1987; Curewitz and Karson, 1997), entrap hydrocarbon accumulations (Smith, 1980), and influence the thermal convection of groundwater in sedimentary basins (Smith et al., 1990). In some cases, potentially hazardous seismogenic faults are not well expressed in the surface geology (Nicholson et al., 1986; Nur et al., 1993). Conceptual models of how these structures form and evolve are therefore important to earthquake hazard studies that require *a priori* knowledge of subsurface fault geometries.

This study focuses on the evolution of a strike-slip fault network that developed within the Cenozoic Basin and Range orogen of the western United States. A field-based approach is employed to study an ancient fault network developed in Aztec sandstone now exposed at the surface in the Valley of Fire State Park in the Northern Muddy Mountains of southern Nevada (Valley-of-Fire) (Figure 1.1). The purpose of this paper is to extend conceptual models of faults formed along preexisting weaknesses (e.g., Martel et al., 1988; Myers, 1999; Pachell and Evans, 2002) to explain the evolution of the strike-slip fault network that occurs in the Aztec sandstone.

In this paper, we first review terminology and examine concepts relevant to nucleation and growth of the faults formed by shearing of preexisting weaknesses, with a focus primarily on models developed by Myers (1999) for faults formed by shearing along joint zones in sandstone. Then, we introduce the geologic setting and deformation history of the study area. In the main body of the manuscript, we present field data on the geometric and kinematic properties of faults at a variety of scales in the Valley-of-Fire. These data form the bases of a conceptual model for the evolution of strike-slip fault network in the Aztec sandstone, which invokes, in addition to an earlier set of joint zones, multiple and progressively formed generations of genetically related sheared joints and joints. We conclude with a comparison of our conceptual model to extant models, such as models for strike-slip fault development in other lithologies and models based on Coulomb failure theory, and a brief discussion of regional implications.

Terminology

A *joint* (or Mode I crack) is a mechanical discontinuity that exhibits dominantly opening displacements. Two adjacent material particles in the undeformed state are perpendicularly displaced with respect to the material discontinuity in the deformed state (Engelder, 1987; Pollard and Aydin, 1988). A *sheared joint* is a structure that originated as a joint and was later subjected to shearing due to either stress or material rotation. Related to sheared joints are *splay fractures*. These features are joints that form in response to tensile stress concentration near the ends of, and possibly along, sheared joints (Nemat-Nasser and Horii, 1982; Segall and Pollard, 1983; Engelder, 1989; Cooke, 1997; Martel and Boger, 1998).

10
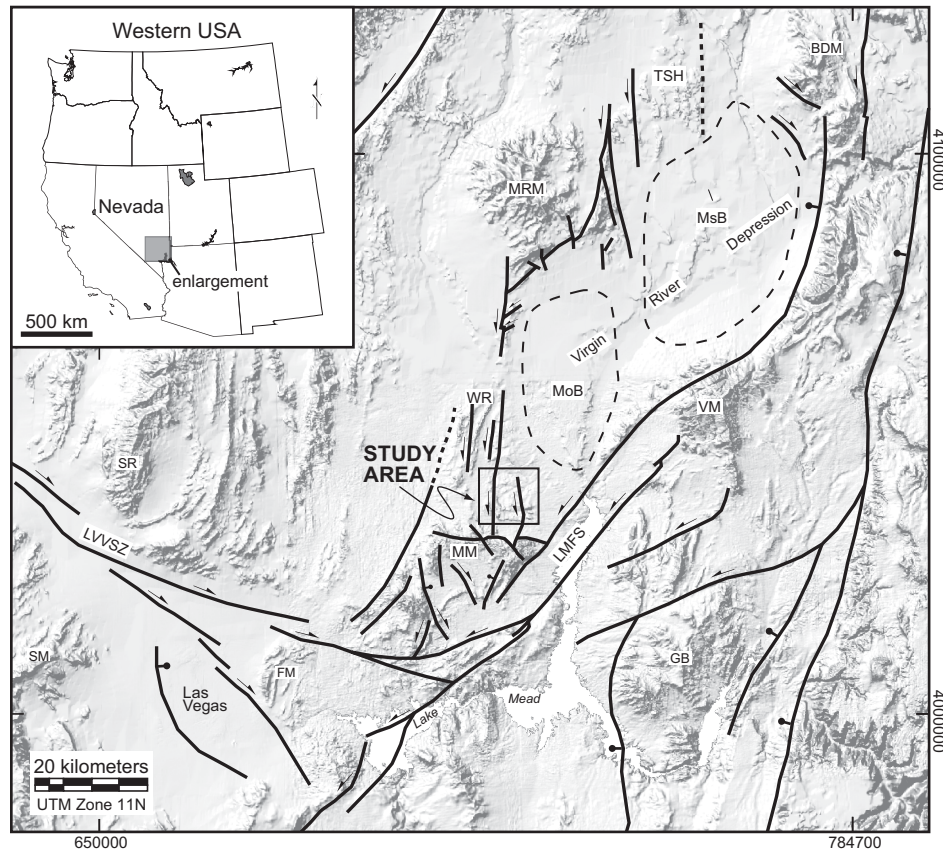
Figure 1.1. Generalized map of Cenozoic faults in the Lake Mead region of southern Nevada. In general, the north to northeast trending faults are predominantly left-lateral strike-slip and the northwest trending faults are predominantly right-lateral strike-slip. Heavy lines are faults; dashed where inferred. Arrows indicate faults with primarily lateral slip sense. Ball and tick symbols indicate faults with primarily normal slip sense. Approximate basin boundaries of the Virgin River depression are indicated by a thin-dashed line. *Inset:* Map of the western United States. LMFS = Lake Mead Fault System, LVVSZ = Las Vegas Valley Shear Zone, BDM = Beaver Dam Mountains, FM = Frenchman Mountain, GB = Gold Butte, MoB = Mormon sub-basin, MsB = Mesquite sub-basin, MM = Muddy Mountains, MRM = Mormon Mountains, SM = Spring Mountains, SR = Sheep Range, TSH = Tule Spring Hills, VM = Virgin Mountains, WR = Weiser Ridge. Base-image is a mosaic of 1:250,000 USGS DEMs. Faults from Stewart and Carlson (1978), Bohannon (1983b), Bohannon (1992), Anderson and Barnhard (1993), Axen (1993), Campagna and Aydin (1994), and Beard (1996).

Splay fractures have also been termed horse tails (Granier, 1985), pinnate joints (Engelder, 1989), secondary fractures (Segall and Pollard, 1980), splay cracks (Martel et al., 1988), tail fractures (Cruikshank and Aydin, 1995), tip cracks (Kim et al., 2001), and wing cracks (Willemse and Pollard, 1998). Splay fractures form at an acute angle (called the *kink angle*)

11

with respect to the parent sheared joint in a clockwise sense for right-lateral shear and in a counterclockwise sense for left-lateral shear. Field observations of kink angles vary over a wide range of values, and have been reported between 3º and 40º in granite (Engelder, 1989), between 35º and 50º in massive sandstone (Cruikshank et al., 1991), and between 20º and 70º in layered clastic rocks (Kim et al., 2001). *Deformation bands* are narrow, tabular zones of continuous shear displacement accompanied by pore volume loss and grain crushing (Engelder, 1974; Aydin, 1978; Jamison and Stearns, 1982). Offset across individual deformation bands is generally on the order of millimeters, but can be as great as a few centimeters.

Sandstone faulting mechanisms

Two mechanisms of fault formation are known to operate in porous sandstone (Myers, 1999): (1) *Deformation band-based faulting* is a progressive process that begins with the localization and amalgamation of individual deformation bands to form a zone of deformation bands. Short, discontinuous slip surfaces that accommodate discrete offsets also begin to nucleate during this stage (Shipton and Cowie, 2001). With progressive strain localization, zones of deformations bands and discontinuous slip surfaces coalesce to form a throughgoing deformation band style fault (Aydin and Johnson, 1978; Antonellini and Aydin, 1995; Shipton and Cowie, 2001). (2) *Sheared joint-based faulting* is a hierarchical and progressive process that involves shearing along preexisting joints and joint zones, and results in the subsequent formation of secondary and higher order joints, fragmented rock, and fault rock (Myers, 1999). This paper focuses on the latter faulting mechanism, that is, faults formed by shearing of joints in aeolian sandstone.

Sheared joint-based faulting

A solid basis exists for understanding the initiation and evolution of faults formed along preexisting weaknesses (e.g., joints, veins, bedding surfaces) in rock. Much of the early work concerning the formation of this class of faults was focused in crystalline rock (McGarr et al., 1979; Segall and Pollard, 1983; Granier, 1985; Martel et al., 1988; Martel 1990; Pachell and Evans, 2002). Other workers extended these concepts of fault formation to sedimentary lithologies including carbonate (Willemse et al., 1997; Kelly et al., 1998;

Mollema and Antonellini, 1999; Peacock, 2001; Graham et al., in press), shale (Engelder et al., 2001), siliceous shale (Dholakia et al., 1998), sandstone (Cruikshank et al., 1991; Zhao and Johnson, 1992; Myers, 1999; Davatzes and Aydin, in press), and competent members of layered clastic sequences (Kim et al., 2001; Wilkins et al., 2001).

Joint-based faulting as a prominent deformation mechanism in sandstone was first described by Myers (1999). Earlier studies recognized the concept of sheared joints with centimeter-scale slip magnitudes (Barton, 1983; Dyer, 1983; Cruikshank et al., 1991; Zhao and Johnson, 1992), while Myers (1999) was able to document that a similar process of faulting along joint zones can operate over a wide range of slip magnitudes, from centimeters to hundreds of meters. Using a series of outcrop-scale maps of faults with different initial joint zone configurations and slip magnitudes, Myers developed a conceptual model that describes a hierarchical process of fault evolution beginning with shearing along earlier formed joint zones. Shearing of joints in turn creates splay fractures at joint tiplines, stepovers, and intersections, which leads to the formation of fragmentation zones (or brecciated zones). This process is repeated as localized shear strain accumulates. Fragmentation zones are further crushed to form isolated pockets of fault rock (or gouge) along small faults. Eventually, a through going slip surface develops, and the once discontinuous pockets of fault rock coalesce to form a continuous zone.

Myers (1999) further recognized that these faults evolved with different geometries depending on the original joint configuration. He developed a classification scheme to illustrate the idealized evolution of three end-member joint configurations (Figure 1.2): (1) en echelon joint zones that have step-sense opposite to shear-sense (e.g., right-stepping and left-lateral shearing); (2) en echelon joint zones that have step-sense similar to shear-sense (e.g., right-stepping and right-lateral shearing); and, (3) subparallel joint zones characterized by a large joint-length to joint-spacing ratio. For en echelon joint zones that have step-sense opposite to slip-sense the overlapping region between stepping joints is subject to a localized contractional strain (Segall and Pollard, 1980; Lin and Logan, 1991), which results in the frictional breakdown of host rock material. Damage in the form of joints and sheared joints is outwardly developed (Myers, 1999). In contrast, en echelon joint zones that have the same step- and slip-sense are subject to a localized dilational strain that results

13

initial joints   early stage   late stage

Contractional step

En echelon joint zone

Dilational step

Sub-parallel joint zone

Asymmetric breakdon fringe
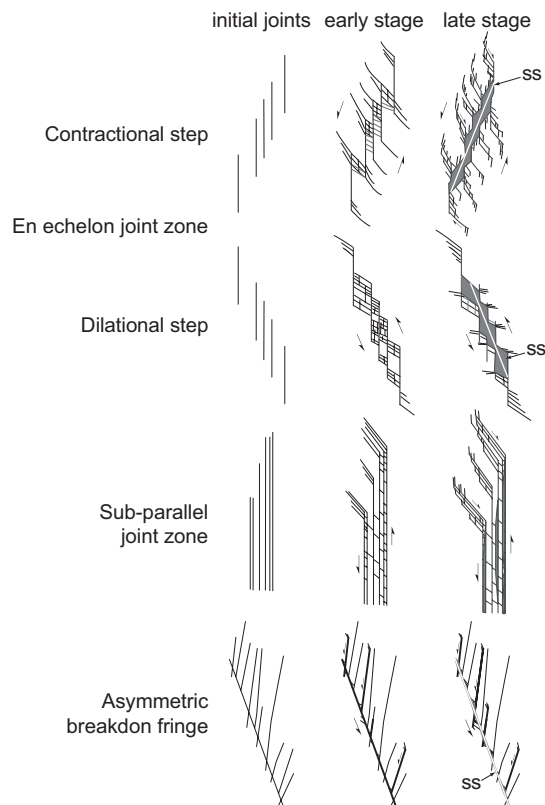
Figure 1.2. Conceptual model for faults formed by shearing of joint zones in sandstone. Top three models after Myers (1999); bottom model from appendix A.

in the fragmentation of rock that spans the overlapping en echelon joints by inwardly directed splay fractures. For subparallel joint zones, strain is accommodated by the formation splay fractures that span the distance between the overlapping joint segments. Accumulated shear strain is preferentially localized along the closely spaced subparallel sheared-joints. Flodin (2002) recently proposed a fourth end-member case whereby damage is localized primarily along one side of the fault due to the inherited geometry of a parent joint with an asymmetrically distributed peripheral joint breakdown fringe (Figure 1.2).

Geologic setting

This study focuses on strike-slip faults in aeolian Jurassic Aztec sandstone exposed in the Valley-of-Fire (Figure 1.1). The Aztec sandstone was deposited in early Jurassic time in a back-arc basin setting (Marzolf, 1983) and was part of a larger aeolian system that included the Navajo sandstone of the Colorado Plateau (Blakey, 1989). The Aztec sandstone is a fine to medium grained sub-arkose to quartz arenite that is characterized by large-scale tabular-planar and wedge-planar cross-strata (Marzolf, 1983; Marzolf, 1990). Within the Valley-of-Fire, the Aztec sandstone has a stratigraphic thickness of approximately 800 m (Longwell,

14

1949) and is divided into three sub-units based on rock color and diagenesis (Figure 1.3) (Carpenter and Carpenter, 1994; Taylor, 1999). From the stratigraphically lowest position, the sub-units are lower red unit, middle buff unit, and upper orange unit. The petrophysical properties of these units were recently described by Flodin et al. (in press).

Aztec sandstone deformation history

Deformation bands are the oldest deformational structures in Aztec sandstone (Hill, 1989; Taylor, 1999), and are thought to be related to Cretaceous-aged thrusting during Sevier Orogeny (Bohannon, 1983a; Hill, 1989). Two deformation band phases are recognized: (1) Phase I deformation bands that show little to no shear offset; and, (2) Phase II deformation bands that show shear offsets on the order of centimeters to decimeters. Phase I deformation bands group within three general orientations (north-northeast, north-northwest, and north-west) (Hill, 1989) and occur as individual bands or small clusters. Phase II deformation bands crosscut and offset the earlier formed set and are found in both low- and high-angle orientations with respect to bedding. Low-angle Phase II deformation bands are short and discontinuous, show offsets of 1-3 cm, and are generally found localized along stratigraphic bedding planes (Hill, 1989). In contrast, high-angle Phase II deformation bands are continuous for hundreds of meters, and are found as zones of deformation bands with cumulative offsets on the order of decimeters.

Based on crosscutting relationships, jointing of the Aztec sandstone followed deformation banding and preceded the latest sheared-joint fault stage (Myers, 1999; Taylor et al., 1999). In outcrop, many joints are found both localized along and abutted against deformation bands, indicating that joint propagation was influenced by the presence of the earlier formed deformation bands. Although many of the pre-faulting joint geometries have been obscured by subsequent shearing, Taylor (1999) was able to identify three joint orientations unassociated with faults: a north-south joint set with both vertical, and east- and west-dipping orientations, and two en echelon joint sets trending about 30º east and west of north. Both Myers (1999) and Taylor et al. (1999) speculate that the joints formed during the earliest stages of Miocene extension. It is also possible that an earlier jointing event occurred during unroofing and possible gentle folding (Fleck, 1970) of the Aztec sandstone prior to reburial by synorogenic Cretaceous sediments and Sevier thrust sheets.

15
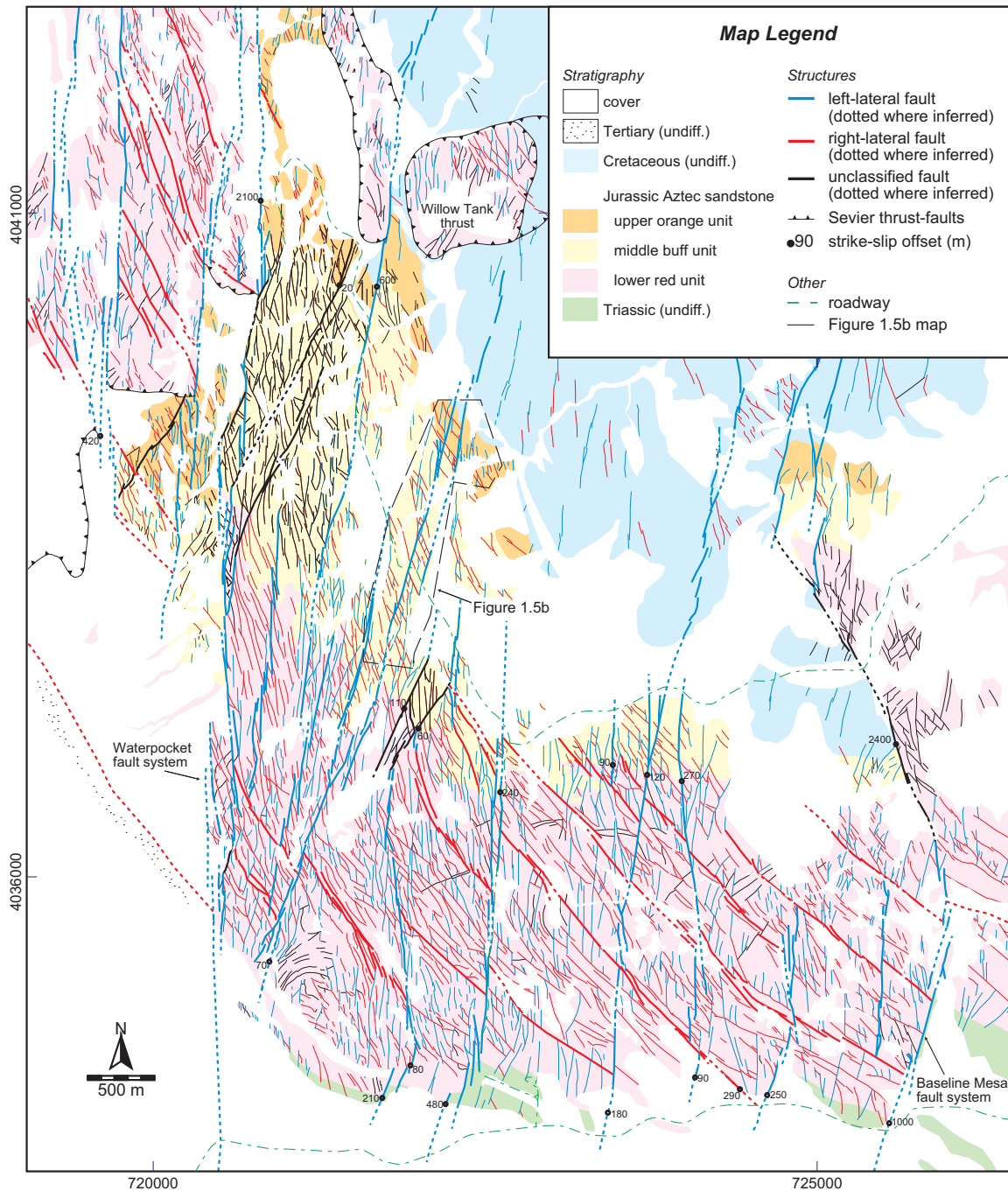
Figure 1.3. Aerial photograph structural interpretation and geology of the Valley of Fire State Park, southern Nevada. Heavy lines are faults that show more than 20 m of offset. Many of these larger faults have been field-checked for accuracy. Thin lines are photo-lineament interpretations, except where noted in the area shown in Figure 1.5b. Apparent strike-slip offsets of unit and structural contacts are shown for many of the larger faults. Locations of Mesozoic thrust faults adapted from Bohannon (1983b), and Carpenter and Carpenter (1994).

16

Strike-slip faults with some normal-slip component that formed by shearing along pre-existing joints and joint zones are the last recorded deformation features in the Aztec sand-stone (Myers, 1999; Taylor, 1999). Crosscutting relationships illustrating the relative age differences between Phase I and Phase II deformation bands, joints and sheared-joint faults are shown in Figure 1.4. At the initiation of faulting the Aztec sandstone was buried by at least 1.6 km of Cretaceous and Tertiary sediments (based on stratigraphic thicknesses provided by Bohannon, 1983a). The youngest rocks that these faults deform are the stratigraphically lowest members of the Muddy Creek Formation (as mapped by Carpenter, Plate 1.3, 1989), which was deposited between 10 and 4 Ma (Bohannon et al., 1993).

Mapping methods

Mapping for this research was carried out at scales ranging from 1:5 to 1:30,000. Outcrop scale maps were made using base photographs taken from a pole-mounted camera at heights between 2-3 m and a balloon-mounted camera at heights between 10-20 m. Meso-scale maps (1:200 and 1:825) were made using basemap enlargements of low-altitude aerial photographs taken at scales of 1:1,600 and 1:6,600. The low-altitude aerial photo-basemaps were georeferenced in the field by locating map control points using differentially-corrected GPS. The smallest-scale mapping (1:30,000) was carried out using digitally orthorectified aerial-photo quads (DOQ). Using GIS software, the georeferenced basemaps made it possible to merge data collected on different basemaps and at different scales into a single, scaled project.

Offset markers used in this study include primary dune boundary surfaces, lithologic and diagenetic contacts, and preexisting structures (mostly Phase I and II deformation bands). Sometimes due to the lack of adequate offset markers, fault offsets were estimated based on the fault architecture. Our estimates are calibrated to both the unambiguous examples that we located and the fault maps provided by Myers (1999). Lastly, we note that all structural orientation data presented in this paper uses the right-hand-rule convention (Marshak and Mitra, 1988).
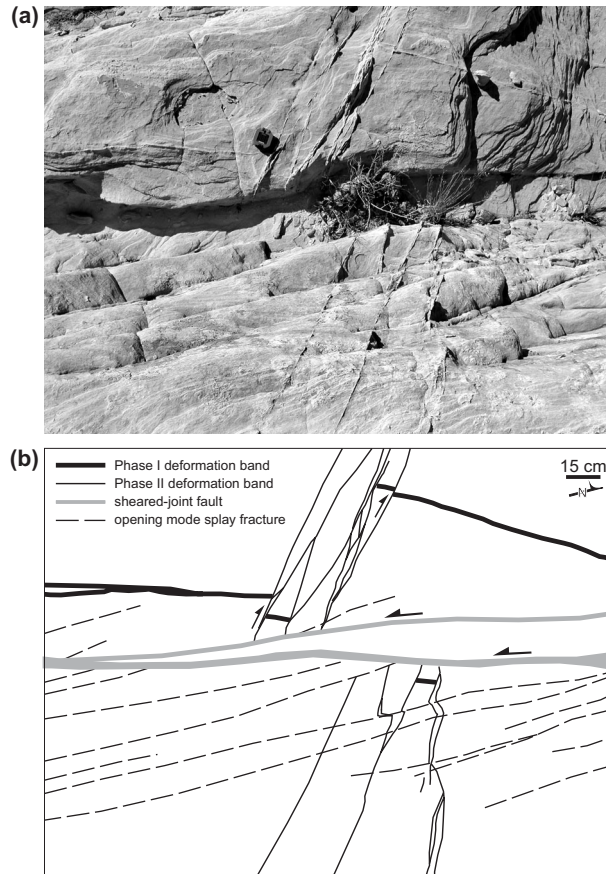
Figure 1.4. (a) Field photo of structural features in Aztec sandstone showing crosscutting relationships between elements of different generations. **(b)** Schematic drawing of *part (a)*. Based on crosscutting relationships, the structures from earliest to latest are: (1) Phase I deformation bands that show little or no shear offset; (2) Zones of Phase II deformation bands that show cumulative shear offsets on the order of decimeters; (3) joints; and, (4) sheared joints with associated splay fractures.

Strike-slip fault network: Field description

A strike-slip fault system comprising primarily two sets occurs in the Aztec sandstone of the Valley-of-Fire (Figure 1.3): A NNE-trending fault set showing predominantly left-lateral slip with a normal component (blue lines, Figure 1.3), and a NW-trending fault set showing predominantly right-lateral slip with a normal component (red lines, Figure 1.3). Bounding this network of faults within the Valley-of-Fire is the Waterpocket fault system to the west, and the Baseline Mesa fault system to the east (Figure 1.3). Both the Waterpocket and Baseline Mesa fault systems show nearly 2.5 km of apparent left-lateral slip, and appear to be part of a larger family of approximately north-trending left-lateral faults that occur to the northeast along Weiser Ridge (Bohannon, 1992) and to the north in the southern and

eastern Mormon Mountains (Anderson and Barnhard, 1993) and the Tule Spring Hills (Axen, 1993) (Figure 1.1). In the following sections, we document the geometric, kinematic, and timing relationships of the left- and right-lateral faults that occur between the Waterpocket and Baseline Mesa faults, the two large-offset faults that bound the Valley-of-Fire.

Large-offset left-lateral faults

Three principal faults oriented NNE are identified in the map shown in Figure 1.5 (see Figure 1.3 for location). The central, through-going fault is the Lonewolf fault (LWf) (Myers, personal communication, 1998), and the faults to the west and east are the Wall fault and the Classic fault, respectively (Figure 1.5a). In the northern half of the area shown in Figure 1.5b, the next major fault comparable to these faults to the west is about 700 m distant, while the next comparable fault to the east is at least 1 km distant. This is contrasted by the southern portion of Figure 1.5b, where the next major fault west of the Wall fault is 150 m away, and the next major fault east of the LWf is 200-300 m away (cf. Figure 1.2). An aerial photograph of most of the northern part of the mapped area in Figures 1.5a and 1.5b is shown in Figure 1.6. The location of the most detailed map in Figure 1.5c is outlined in the photograph.

The LWf has an overall exposed length of about 2 km and consists of eight sub-parallel, linked segments that have individual lengths ranging from 200 to 550 m. Mean strikes for the segments range from 193º to 201º, while mean dips range from 59º to 70º (Figure 1.7). These main fault segments are sometimes further segmented into an overlapping en echelon array of slip surfaces within the fault core (Myers, 1999). However, given the scale of mapping shown in Figure 1.5, these finer scale fault segmentations all occur within the line-widths that represent the faults. This limit of resolution holds also for the other faults discussed below.

Most of the segments that comprise the LWf are relatively in-line with each other and are characterized by short overlap width and length on the order of meters. However, three large right steps or jogs, characterized by overlap widths and lengths of tens of meters, are recognized that effectively divide the LWf into four principal segments: north, north-central, south-central, and south (Figure 1.5a). Region 1 (Figure 1.5a) highlights the location of

19
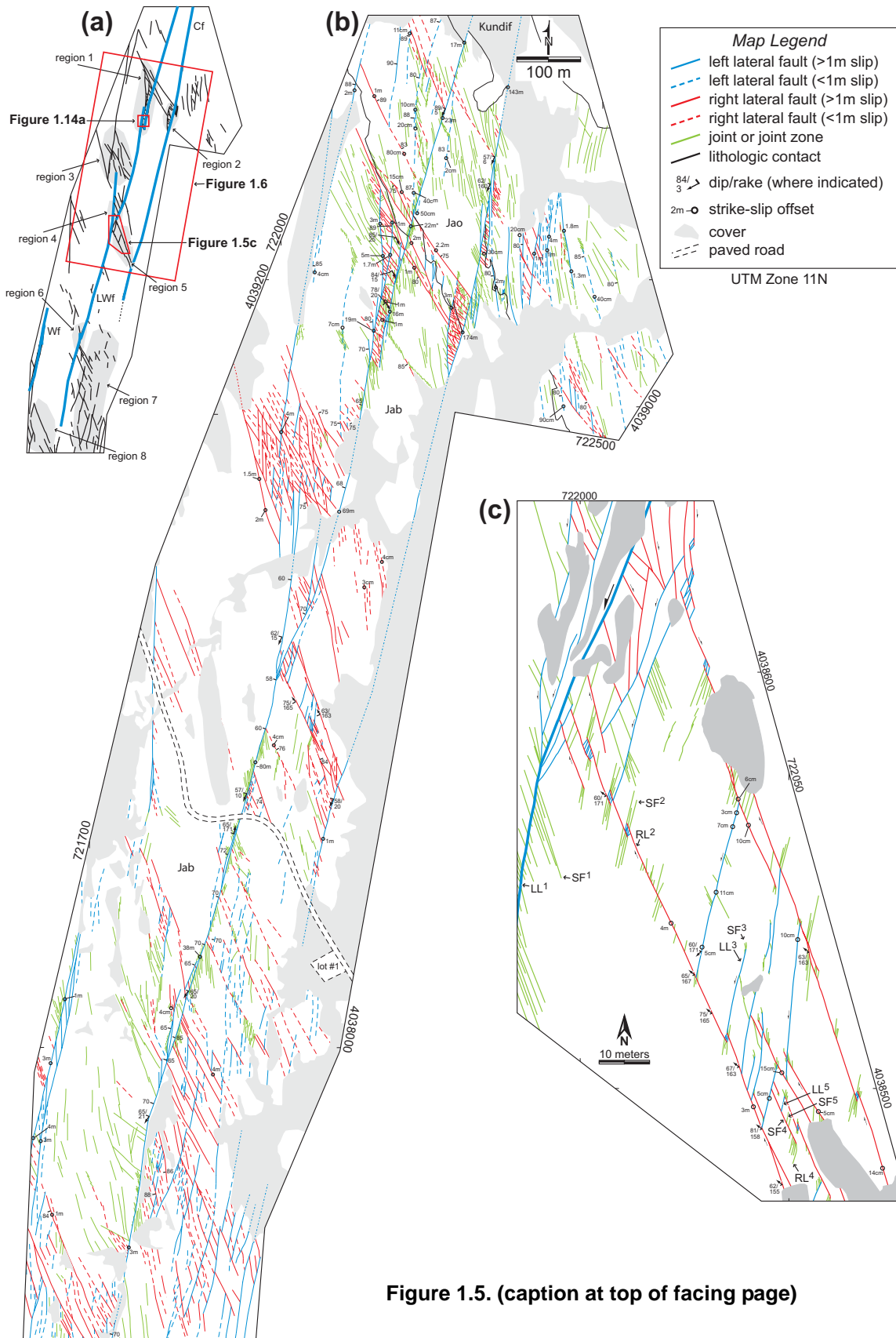
Figure 1.5. (caption at top of facing page)

Figure 1.5. (a) Index map for *part (b)*. Highlighted regions are referenced in the text. Also note the location of the detail map shown in *part (c)*, the aerial photograph shown in Figure 1.6, and the map shown in Figure 1.14a. Fault names are as follows: Cf = Classic fault, LWf = Lonewolf fault, Wf = Wall fault. **(b)** Structure map of a portion of the Valley-of-Fire originally mapped at a scale of 1:825. See Figure 1.2 to locate this map within the context of the Valley-of-Fire. Jab = beige subunit of Jurassic Aztec sandstone; Jao = orange subunit of Jurassic Aztec sandstone; Kundif = undifferentiated Cretaceous sediments. **(c)** Detail structure map of a portion of the Lonewolf fault originally mapped at a scale of 1:200 [see *part (a)* for map location]. Note the shared orientation between splay fractures and right-lateral faults originating from the LWf, as well as the shared orientation between splay fractures and left-lateral faults originating from the secondary right-lateral faults. At least five generations of splay fracturing and shearing of splay fractures are identified on this map. Examples of each generation are as indicated: SC = splay fracture; LL = left-lateral fault; RL = right-lateral fault; numbers indicate generation (e.g., SC[1] = first generation splay fracture). Note that given the scale of mapping, not all fractures are shown.

a right-step that separates the north and north-central segments of the LWf. These two segments are not connected by a through-going left-lateral fault. Rather, they are linked by a dense network of right-lateral faults (discussed later). In contrast, the right-jogs that separate the north-central, south-central, and southern segments are linked by through-going left-lateral faults (regions 4 and 6, respectively, Figure 1.5a).

Evidence for predominantly strike-slip motion along the LWf is abundant. In the northern part of the fault, a three-plane solution between the fault plane, the shallow dipping contact between the middle and upper units of the Aztec sandstone, and a steeply dipping deformation band zone (Phase II) at high-angle to the fault indicates a slip rake of 14º, as projected onto the west-dipping fault plane. Where identified, slickenlines and groove marks on primary slip surfaces along the LWf yielded rakes between 2º and 21º, with a trend for progressively steeper rakes from north to south. An example of shallow plunging slip indicators on a primary plane of the LWf is shown in Figure 1.8. Meter-wavelength fault groove marks have rakes that plunge 2º to 4º to the south. Smaller, centimeter-wavelength groove marks with rakes plunging from 4º to 14º overprint the larger grooves. Similar to the LWf, the two faults described below also have offset markers and kinematic features indicating predominantly left-lateral, strike-slip slip sense.
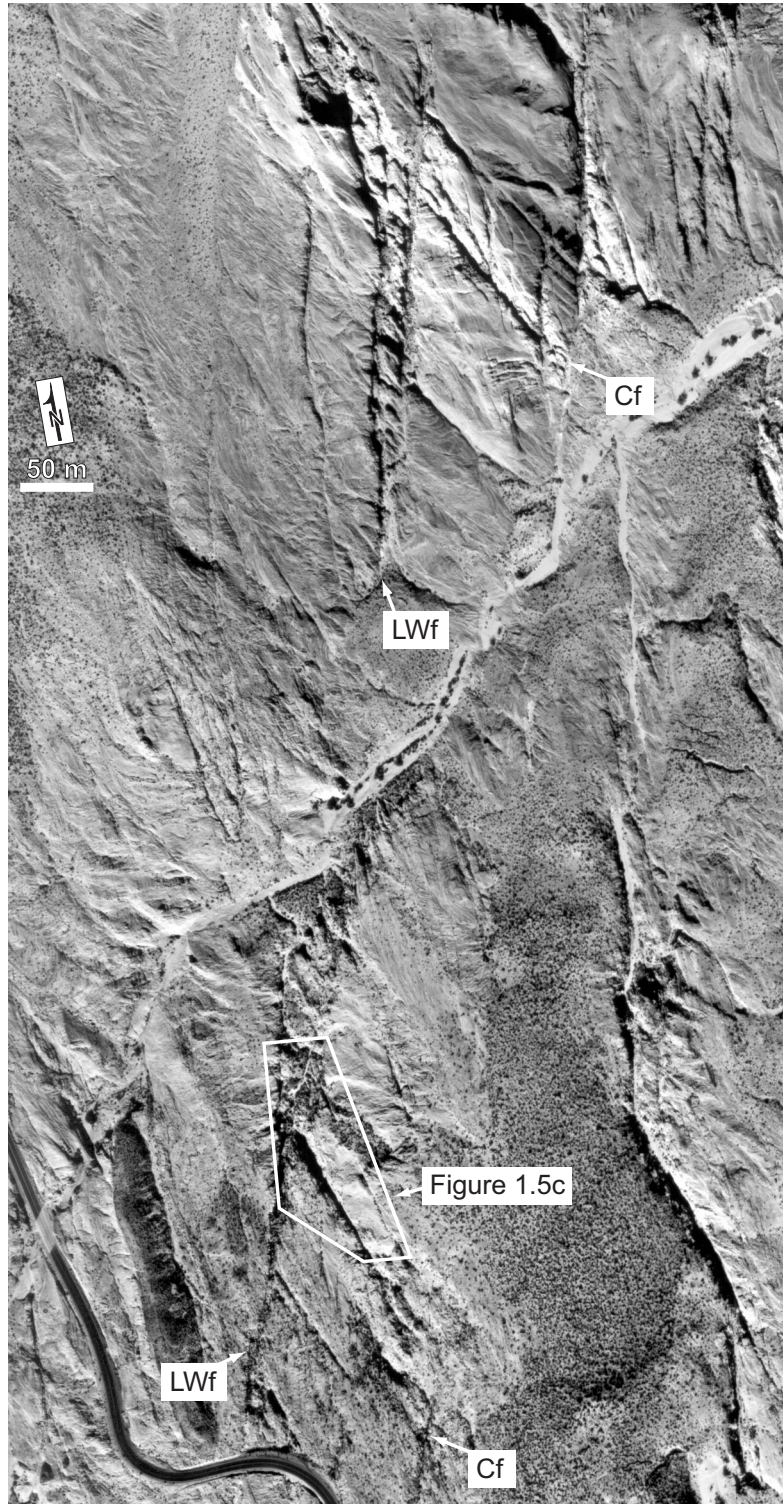
Figure 1.6. Low-altitude aerial photograph (1:4,400 scale) of a portion of the mapped area shown in Figure 1.5 (see Figure 1.5a for location). Note two sets of lineaments with systematic trends: one slightly east of north including lineaments that correspond to the LWf and Cf, and another west of north, which are bounded by the first set. LWf = Lonewolf fault; Cf = Classic fault.

22
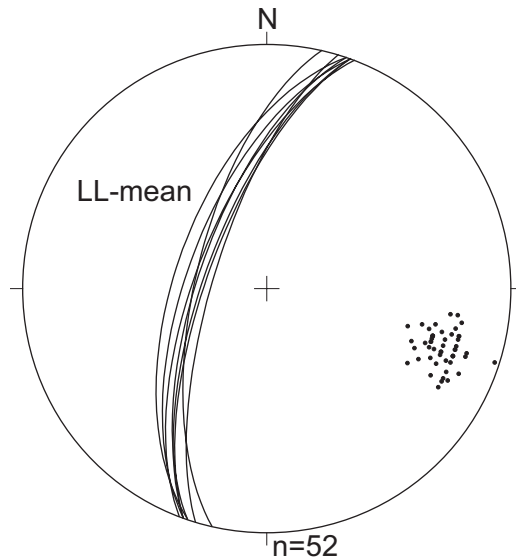
Figure 1.7. Equal-area stereographic projection of slip surface data collected along the LWf. Mean orientations of the eight segments that comprise the LWf are shown as great circles. Individual data points used to calculate the mean planes are shown as poles.

The Classic fault to the east of the LWf (Figure 1.5b) consists of subtly right-stepping, subparallel segments that are linked by through-going left-lateral faults. Region 2 (Figure 1.5a) highlights a particularly large left-lateral segment that merges with the Classic fault. Similar to region 1 along the LWf, a dense network of right-lateral faults occurs between the left-lateral segments. South of where these two segments merge, cover conceals much of the Classic fault. To the south of this area, the next major exposure is the apparent tip region of the Classic fault. Slip near the fault end is accommodated along at least two subparallel segments. To the north, the last documented evidence of the Classic fault is the offset (143 m) of overlying Cretaceous sediments.

The Wall fault is to the west of the LWf (Figure 1.5b). Much of this fault disappears beneath the cover to the north and must end prior to reaching the overlying Cretaceous sediments as the basal conglomerate member is not noticeably offset where the Wall fault projects (cf. Figure 1.2). However, the Wall fault does continue to the south for more than a kilometer. As shown in the detailed map (Figure 1.5b), the Wall fault consists of many sub-parallel fault strands (also noted by Myers, 1999).

Slip profiles for all three faults are presented in Figure 1.9. Offset markers in the northern part of Figure 1.5b are abundant and consist of unit boundaries and nearly vertical Phase II deformation bands that strike at high angle to the faults. Offset markers in the central and southern portions of the mapped area were sparse, making it difficult to divide
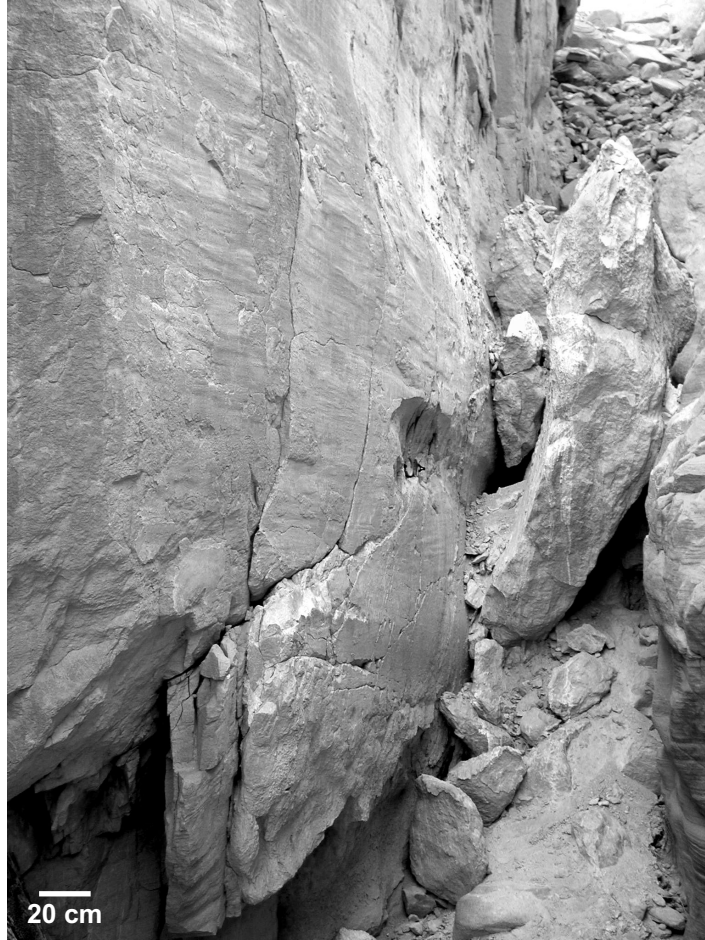
Figure 1.8. Fault grooves with ~1 m wavelength overprinted by smaller grooves with centimeter-wavelength on a primary slip plane of the LWf. Rake of the large grooves is 2-4º, while the smaller grooves rakes range from 4-14º, both indicating predominantly left-lateral with a small normal slip component. The average dip of the fault plane is 88º to the west. Location is near the north end of the LWf. View is to the south.

slip between the southern segments of the LWf. Because of this, these three segments are lumped together in the slip distribution. Offset markers in the southern part of the mapped area consist solely of primary and secondary dune boundaries. Of the three faults, the Classic fault has the largest maximum offset of 173 m, while the LWf shows a maximum offset of about 80 m. The largest offset measured along the Wall fault is 7 m. A cumulative slip profile across Figure 1.5b shows a maximum of about 200 m near the northern end of the map (Figure 1.9).
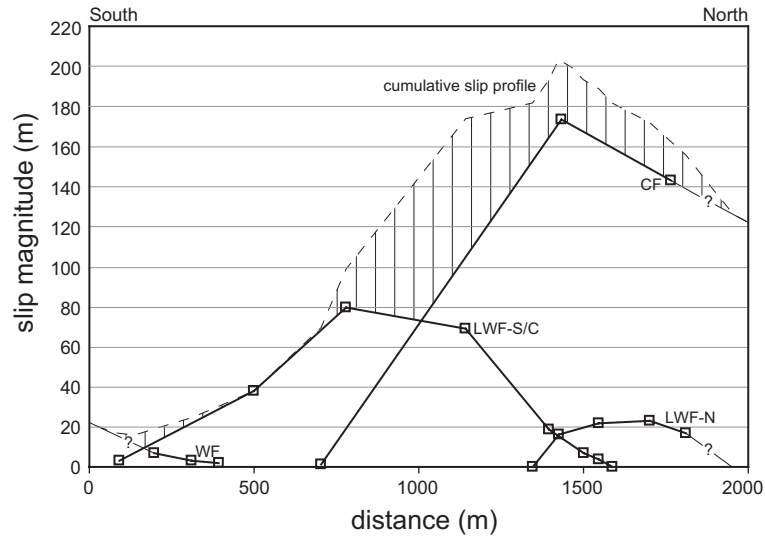
Figure 1.9. Fault slip profiles for the three large left-lateral faults shown in Figure 1.5. LWf-N = Lonewolf fault – north branch; LWf-S/C = Lonewolf fault – north-central, south-central, and south branches; Cf = Classic fault; Wf = Wall fault.

Smaller-offset, discontinuous faults and fractures

In contrast to the few through-going, large-offset faults shown in Figure 1.5b, numerous structures exist that are discontinuous and shorter, and are generally bound in extent by the larger faults. In this class of shorter structures, two general sets with different orientations are recognized: (1) a set comprising NW-oriented splay fractures and right-lateral faults, both emanating from left-lateral faults; and, (2) a set comprising NNE-oriented splay fractures and left-lateral faults, both emanating from right-lateral faults. Some field relations deviate from these generalizations, which will be discussed later.

The density and distribution of these structures are not random, but are systematically localized near the ends of the larger NNE-trending left-lateral fault segments. Regions 1-8 highlighted in Figure 1.5a are selected examples of such structures, two scales of which are observed on the map (Figure 1.5b). Regions 1, 2, 4, and 6 show a high concentration of right-lateral faults that occur between closely spaced steps along the large-offset, left-lateral faults. In these areas, the right-lateral faults are found in multiple orientations and are almost always bound in extent by the larger left-lateral faults. Regions 3, 5, 7, and 8 highlight larger-scale domains of left- and right-lateral faults that are bound between neighboring large-offset, left-lateral faults. In region 3, discontinuous right-lateral faults dominate the

25

left-step between the LWf and the end of the left-lateral fault to the west. In this region, similar to the other regions, multiple orientations of right-lateral faults occur. However, unlike the other areas mapped in Figure 1.5b, many of the right-lateral faults in region 3 have nearly north-south strikes. Most of these north-south striking right-lateral faults appear to have formed along preexisting Phase I deformation bands. Regions 5, 7, and 8 have nearly equal proportions of mutually abutting right- and left-lateral faults. Structures in region 7 are localized between the end of the LWf and the next large left-lateral fault east of the mapped area, while structures in region 8 are localized between the Wall fault and the end of the fault that is inline and south of the LWf (Figures 1.3 and 1.5). Region 5 is similar in style to regions 7 and 8, but is smaller in scale. This region is located between the end of the Classic fault and the juncture of the south and central segments of the LWf (Figures 1.5b and 1.5c), and is the subject of more detailed analysis in the following paragraph.

Mutual abutting relationships between different sets of left- and right-lateral faults, and splay fractures imply a hierarchical sequence of formation (Figure 1.5c). The largest structure shown in Figure 1.5c is the left-lateral LWf (labeled LL^1). We consider the LWf primary in nature because it bounds all other structures. Emanating from the LWf are splay fractures and right-lateral faults that share the same orientation (e.g., SF^2 and RL^2, respectively in Figure 1.5c). These structures are considered to be second generation because they appear to have formed in response to activity along the primary LWf. All secondary structures have at least one end that abuts against a primary left-lateral fault. Two of the second-generation right-lateral faults extend through the map area to the southwest where they join with the end of the Classic fault to the southwest and outside of the mapped area (see Figure 1.5b and photograph in Figure 1.6 for location). Emanating from, and localized between, these two right-lateral faults are splay fractures and left-lateral faults (e.g., SF^3 and LL^3, respectively), both of which have the same intersection angle (Figure 1.5c). These structures are considered to be third generation because they appear to be genetically related to activity along the second-generation structures. All third generation structures are bound on at least one end by a second generation right-lateral fault. Further branching occurs from the third generation left-lateral faults in the form of fourth generation splay fractures (e.g., SF^4), the subsequent shearing of which produced a fourth generation of right-lateral faults

26

(e.g., RL[4]). The highest order structure identified in this area is a fifth generation left-lateral fault and related splay fractures (e.g., SF[5] and LL[5]).

So far, we have broken down structures into smaller and smaller components. To reverse this trend, we now focus on the large map in Figure 1.3 that covers the area between the Waterpocket and Baseline Mesa faults, two regional, left-lateral faults with kilometer-scale slip. Here, we see elongated domains of discontinuous right- and left-lateral faults (thin-red and blue lines, respectively) localized between large-offset, N- to NNE-oriented left-lateral faults (heavy-blue lines). These domains include second-generation right-lateral faults, and third generation left-lateral faults, and are arranged in a fault pattern that is reminiscent of the pattern previously described in detail in Figure 1.5c. A few areas have structures that occur at odd orientations (black lines) with respect to the overall pattern of left- and right-lateral faults (Figure 1.3). For example, the NE-oriented structures resulting from the shearing of preexisting joints (heavy-black lines, northwest portion of Figure 1.3) have apparent splay fracture configurations that might be related to an earlier episode of right-lateral slip along the Waterpocket fault. However, present-day offsets along both sets of structures are left-lateral. Finally, we note that there is a higher concentration of structures within the lower-red unit of the Aztec sandstone compared to the upper two units (Figure 1.3). This variability in structural occurrence has been interpreted to be related to diagenetical differences between the sandstone units, and is discussed elsewhere by Taylor (1999) and Flodin et al. (in press).

Structural orientations

The orientation of faults and splay fractures within mapped area fall into two subsets (Figure 1.10): (1) NW-oriented structures, which consist of right-lateral faults that strike between 130º and 181º, and splay fractures that emanate from left-lateral faults that strike between 135º and 197º; and, (2) NNE-oriented structures, which consist of left-lateral faults that strike between 165º and 207º, and splay fractures that emanate from right-lateral faults that strike between 167º and 209º. In the data shown in Figure 1.10, both structural elements (i.e., faults of one set and splay fractures of faults from the other set) show nearly complete overlap within their own orientation subset. Between the two subsets, similar orientations
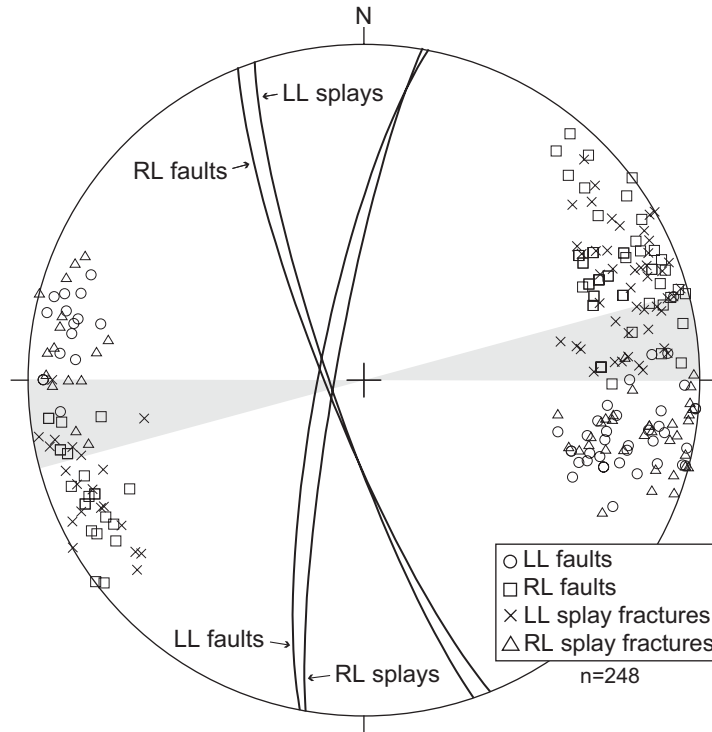
Figure 1.10. Equal-area stereographic projection of structural orientation data collected within the mapped area shown in Figure 1.5b. In general, the data show two clear trends defined by left-lateral faults and splay fractures of right-lateral faults, and right-lateral faults and splay fractures of left-lateral faults. However, the two groups overlap by as much as 13⁰ (gray-shaded region). Mean planes for each group of data are shown as great circles. LL = left-lateral fault; RL = right-lateral fault.

occur over a range of approximately 13° (shaded area, Figure 1.10). Splay fractures that have this intermediate orientation are usually localized between left- and right-lateral fault junctures on the side of the juncture that has an obtuse angle of intersection (Figure 1.11), and in general, only occur within meters of the originating fault zone (cf. Myers, 1999, p. 37). Splay fractures that extend outside of the fault damage zone generally have higher kink angles (cf. Myers, 1999, p. 38). Overall, splay fracture kink angles show a large variation ranging from 12° to 70°. Mean planes for fault and splay fracture sets are shown as great circles in Figure 1.10. The average kink angle between mean planes of the left-lateral faults and the splay fractures of right-lateral faults is 30°, while for right-lateral faults and splay fractures of left-lateral faults the angle is 32°.
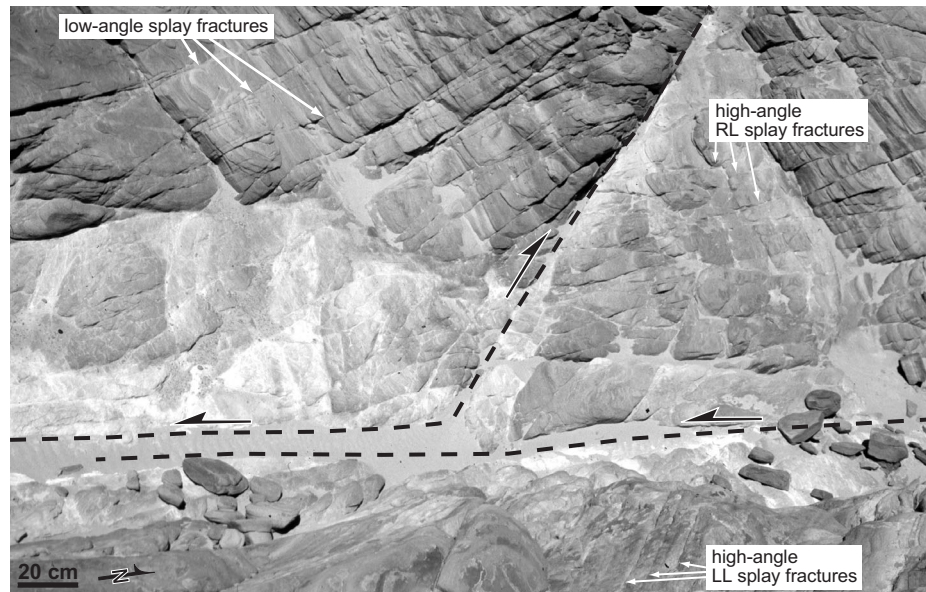
Figure 1.11. Map-view photograph of an intersection between left- and right-lateral faults. Note the orientation the low- and high-angle splay fractures. The low-angle splay fractures are localized between the two faults and are younger based on the abutting relationships.

The data on the intersection angles between the structural elements in Figure 1.5b are plotted in a different way as a basis for appreciation of the consistency and variability of the field data (Figure 1.12). The mean intersection angle between right-lateral faults that abut against left-lateral faults is 37º, and is 31º for the opposite abutting relationship (Figure 1.12a). Mean angles between intersecting left-lateral faults and intersection right-lateral faults are 13º and 24º, respectively (Figure 1.12b). Mean splay fracture kink angles from left- and right-lateral faults center on 32º and differ by 1º, and range between 13º and 72º (Figure 1.12c). Note that the lower angle splay fractures mentioned in the previous paragraph are not represented at the scale of mapping shown in Figure 1.5b. Intersection angles between faults with opposite sense of slip show the widest spread in orientation ranging between 12º and 85º (Figure 1.12a). In particular, angles between right-lateral faults that abut against left-lateral faults are skewed towards greater intersection angles. Angles between faults that have the same slip-sense range between 4º and 43º and are markedly lower than those for opposite slip sense (Figure 1.12b). Splay fracture kink angles are more similarly oriented to the faults with opposite slip-sense, with the greatest spread occurring in the splay fracture set that emanates from left-lateral faults (Figure 1.12c).

29
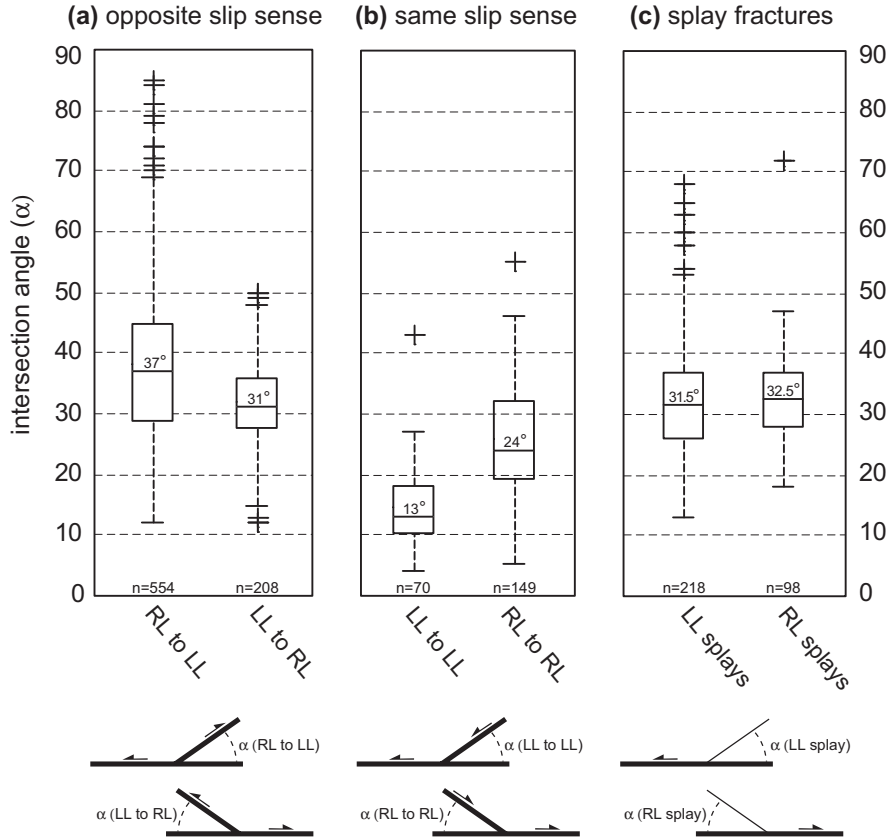
Figure 1.12. Boxplot statistics for apparent intersection angles between structural elements as measured from the map shown in Figure 1.5b. **(a)** Angles between intersecting faults that have opposite slip sense. **(b)** Angles between intersecting faults that have the same slip sense. **(c)** Splay fracture kink angles. The line and number at the center of the box is the sample median; box bottom and top are respectively the first and third quartiles; dashed lines indicate 1.5 times the interquartile range; a cross explicitly indicates outliers.

Material rotation

The orientations and intersection angles presented in the previous section reflect the present day values and might be different than those of the original values when the structures formed. In fact, Myers (1999) noted material rotations of host rock fragments of up to 40° in the central core of fault zones. Because of the importance of the notion of material rotation in our conceptual model of faulting, we offer field examples of material rotation within the area mapped in Figure 1.5b. Earlier studies proposed that material between subparallel faults is expected to rotate counterclockwise for right-lateral bounding faults, and clockwise for left-lateral bounding faults (Freund, 1974; Nur et al., 1986). We present examples of both scenarios below.

30

The first example is from a left-stepover between right-lateral bounding faults that show cumulative offsets on the order of a few meters (Figure 1.13). Traversing the stepover area are a set of left-lateral faults and two preexisting, subparallel Phase I deformation bands (labeled db[1] and db[2], Figure 1.13a) that enter the fault zone from the northeast. Outside of the fault zone (lower left, Figure 1.13), both deformation bands continue with a straight trace for many meters towards the northwest. Within the fault zone the deformation bands are broken and offset by left-lateral faults that are bound between two sets of overlapping right-lateral faults. Between the left-lateral faults, the deformation band segments approximately retain their straight trace. The deformation band segments are progressively rotated in a clockwise sense with increasing distance to the lower right-lateral fault (Figure 1.13b). At the last documented juncture between the deformation bands and the right-lateral fault, the bands are rotated by as much as 60°. Both deformation bands are rotated about axes that plunge approximately 70°.

The second example is larger in scale and opposite in rotation sense (Figure 1.14). In this case, the bounding faults are left-lateral and the internal faults are right-lateral. The bounding faults are the right-stepping northern and central segments of the LWf (region 1, Figure 1.5a). The internal right-lateral faults intersect their bounding faults at angles ranging from 27° to 60°. Oriented perpendicular to, and offset by, the two segments of the left-lateral LWf is a zone of earlier formed Phase II deformation bands (Figure 1.14a). The zone of deformation bands itself consists of bounding deformation bands that show right-lateral offset and internal deformation bands that show left-lateral offset and are similar in geometry to zones of deformation bands described by Davis et al. (2000). The mean angle of intersection between the two deformation band sets is approximately 26° both inside and outside of the bounding segments of the LWf. However, the mean orientations of the two sets that occur between the fault segments are rotated approximately 15° in a counterclockwise sense with respect to the zones of deformation bands found outside of these segments (Figure 1.14b). Some of the internal right-lateral faults appear rotated, as well.

Evidence for material rotations might also be reflected in the data shown in Figure 1.12. The median intersection angle between the left-lateral faults and the right-lateral faults that emanate from them is slightly higher (5°) than the median intersection angle between left-lateral

31
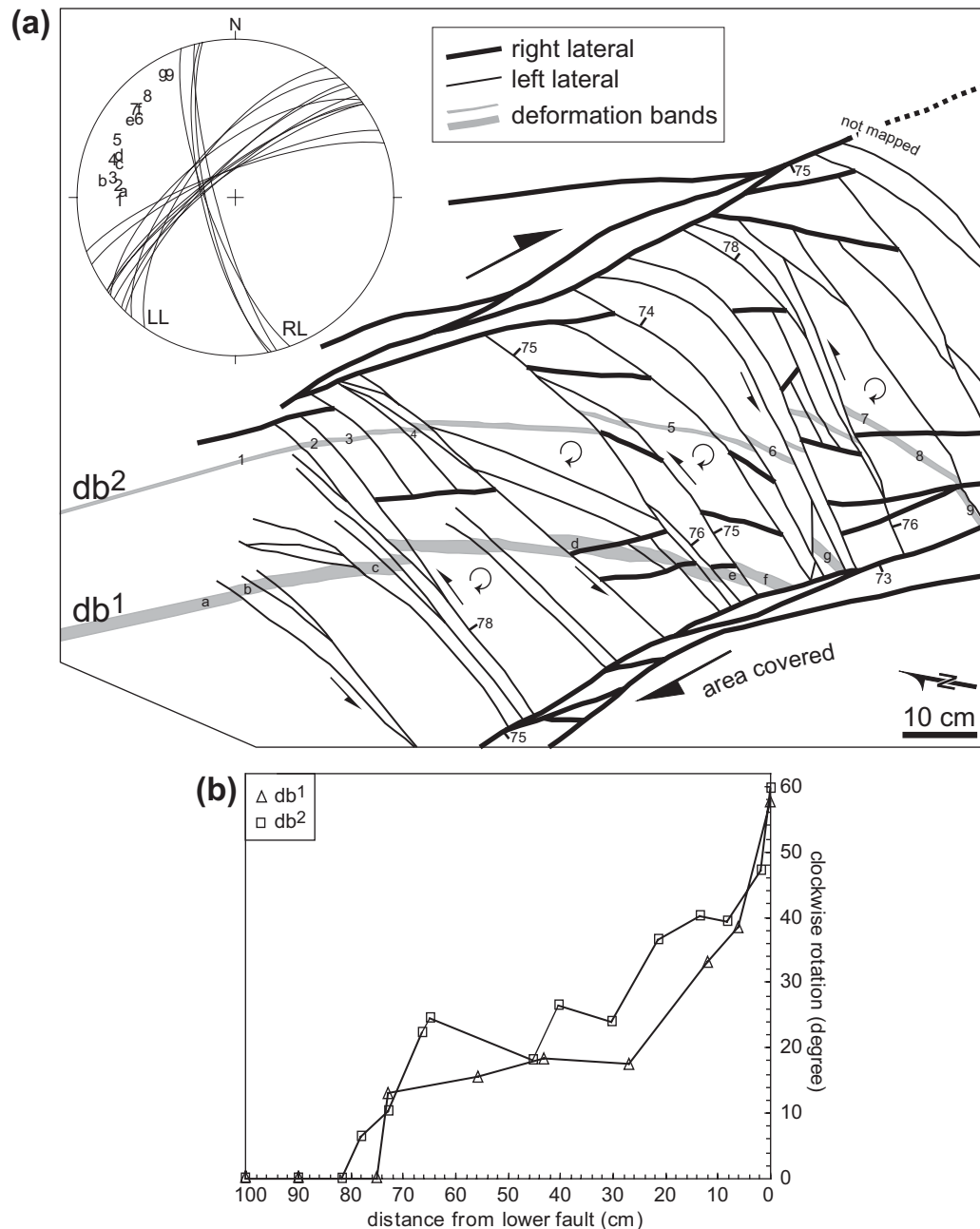
Figure 1.13. Field example of counterclockwise material rotation between overlapping right-lateral fault segments. **(a)** Field map showing left-stepping, right-lateral faults bounding a series of left-lateral faults. Two subparallel, earlier formed Phase I deformation bands with straight traces outside of the overlap area enter the fault zone from the lower-left and are progressively rotated in a clockwise sense. Note that the curved trace of the left-lateral faults in the upper-right portion of this figure is due to topographic effects. *inset*: Equal-area stereographic projection of fault planes and Phase I deformation band orientations. Numbers and letters correspond to the orientations of deformation band located in the map. LL = left-lateral; RL = right-lateral. **(b)** Plot showing progressive rotations of the deformation bands db[1] and db[2] in the map.

faults and the splay fractures that emanate from them. Also, the intersection angle between right-lateral faults abutting against left-lateral faults is skewed towards higher intersection angles than the angles between left-lateral faults and related splay fractures. If the right-lateral faults formed by shearing of the earlier formed splay fractures as we propose in the
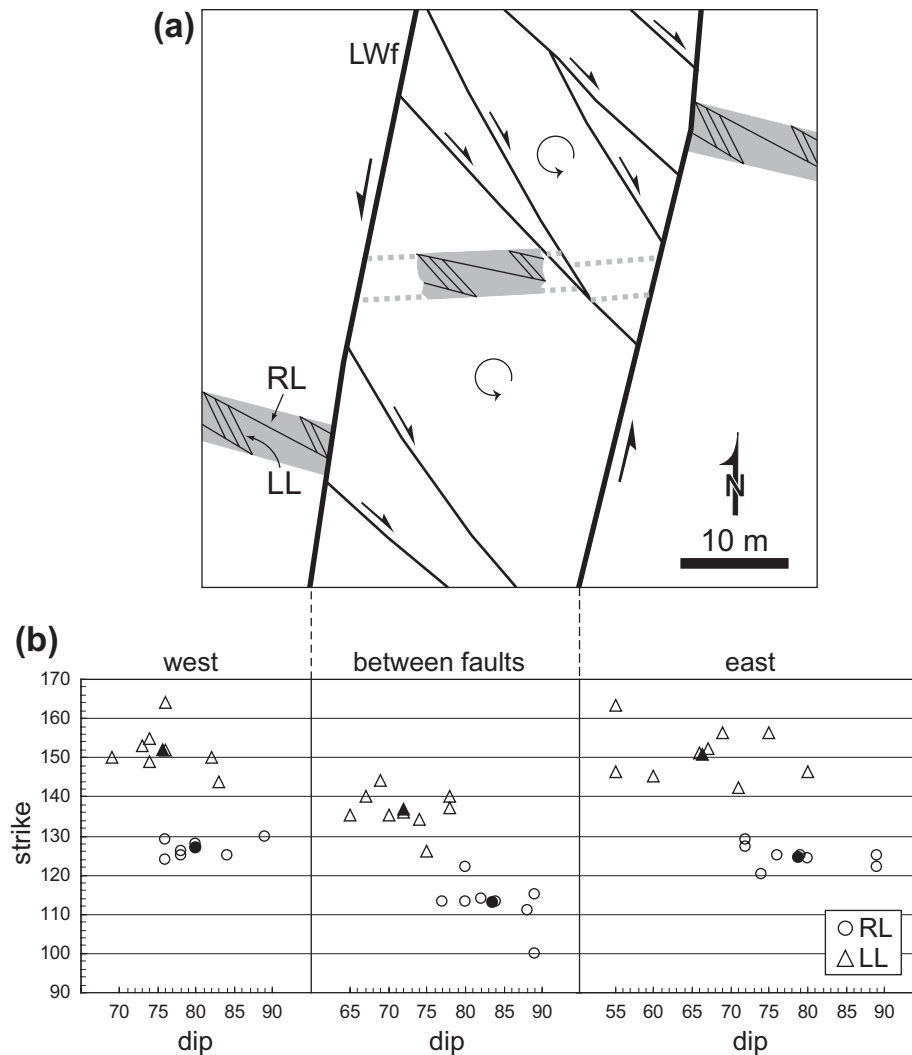
Figure 1.14. Field example of clockwise material rotation between the overlapping northern and central segments of the left-lateral LWf (Figure 1.5a). **(a)** Sketch of the through-going left-lateral LWf (heavy lines) and internal right-lateral faults. A zone of Phase II deformation bands (gray-shaded line) is offset in a left-lateral sense across segments of the LWf, and in a right-lateral sense across internal faults. The zone of Phase II deformation bands itself consists of a mutual crosscutting set of left- and right-lateral deformation band faults. Zone of deformation bands shown as dashed outline where inferred. **(b)** Strike and dip of the Phase II deformation bands both inside and outside of the LWf. Filled symbols are mean orientations for the respective groups. LL = left-lateral; RL = right-lateral.

following section, this discrepency in intersection angle between left-lateral faults and their splay fractures, and left-lateral faults and abutting right-lateral faults, might reflect counter-clockwise rotation of the slab between the right-lateral faults.

Conceptual model for fault network evolution

We propose that the fault network in the Valley-of-Fire evolved through a hierarchical and progressive process of shearing of joints, splay fracturing, and subsequent shearing of the splay fractures as presented in Figure 1.15. The fault network evolution model begins with a set of discontinuous joints, which are individually zonal in character (Myers, 1999). These joints either formed during an earlier tectonic event (i.e., preexisting joints) (e.g., Segall and Pollard, 1983) or they are the first structures formed during a progressive process that eventually led to the formation of the faults (i.e., precursor joints) (e.g., McGarr et al., 1979) (Figure 1.15a). Regardless of their relative timing, these joints and joint zones are the initial discontinuities on which the first generation of faults nucleated (Myers, 1999).

In the conceptual model shown in Figure 1.15b, the first generation of faults with a left-lateral sense of shearing produces opening mode splay fractures that are primarily localized at or near the end, and in the immediate vicinity, of the first generation structures. However, due to mechanical interaction between adjacent first generation faults (Martel, 1990) and in response to increasing slip, some splay fractures propagate across the distance of undeformed rock that spans these neighboring structures (Figure 1.15b). Due to local stress rotations between overlapping faults (e.g., Segall and Pollard, 1980; Ohlmacher and Aydin, 1997; Kattenhorn et al., 2000) and/or material rotations (e.g., Nicholson et al., 1986; Swanson, 1988), shear stress is imposed across the first generation splay fractures to form a second generation of faults (right-lateral) with their associated splay fractures (Figure 1.15c). This second generation of splay fractures, like the first generation splay fractures, forms locally between fault stepovers and outwardly from fault ends. The second generation faults almost always have a slip sense opposite to that of the first generation faults formed earlier (Figure 1.15c). An exception to the rule is illustrated where an earlier formed splay fracture emanating from a primary left-lateral fault is more optimally oriented for the imposition of left-lateral shear (upper right, Figure 1.15d), and thus forms a left-lateral fault in a rather

34

uncommon orientation. Splay fractures formed from right sense of slip across the second-generation faults are oriented subparallel to the first generation left-lateral faults. This process is repeated to form successively younger generations of faults and splay fractures as slip accumulates along, and transfers between, the first generation faults (Figure 1.15e). The final fault network geometry is defined by the characteristic splay fracture kink angle. Deviations that occur for intersection angles between faults and splay fractures (Figure 1.12) might stem from the presence of complex preexisting joint geometries, the formation of splay fractures at lower angles between left- and right-lateral faults (Figure 1.11), and/or material rotations.

The progressive formation of faults and associated splay fractures leads to characteristic fault slip magnitude and structural spacing for each of the higher order structural generations. Slip between each successively higher generation of faults is approximately an order of magnitude less than the previous generation of faults. In accord with the pattern of slip distribution, each progressively higher order fault generation has a roughly factor two smaller spacing than the previous generation. However, the spacing of higher order structures is also affected by the spacing of the bounding faults (e.g., compare regions 2 and 7, Figure 1.5b), and the magnitude of slip transferred between them. The smaller slip on the higher
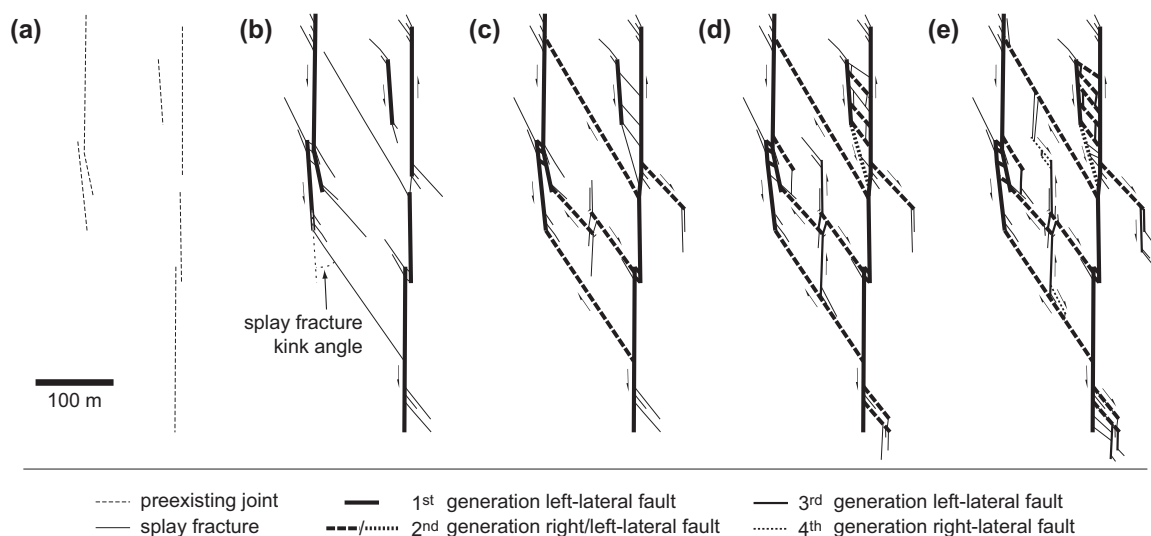
Figure 1.15. Conceptual model for the evolution of the strike-slip fault network in the Valley-of-Fire. **(a)** Preexisting joints prior to, or at the earliest phase of, faulting. **(b)-(e)** Progressive stages of splay fracturing and sequential shearing of splay fractures that evolve into sets of left- and right-lateral faults.

order structures accommodates shear strain across a greater number of closely spaced faults. However, comparing shear strains between different generations of faults indicates that the majority of the shear strain is accommodated by the through-going, first generation faults. Representative shear strains for each generation were approximated by dividing the average fault slip by the average fault spacing. Calculated shear strains for the first through the fourth generation structures are 0.71, 0.23, 0.21, and 0.06, respectively.

Discussion

Comparison with other fault network models

The geometry of the faults in the Valley-of-Fire bears resemblance to structural networks described elsewhere in granite (McGarr et al., 1979; Segall and Pollard, 1983; Martel et al., 1988; Martel, 1990; Pachell and Evans, 2002), clastic rocks (Kelly et al., 1998; Myers, 1999), and carbonates (Willemse et al., 1997; Kim et al., 2001; Graham et al., in press). However, some important differences exist. Martel (1990) documented no more than three structural generations for compound fault zones in granite, compared to the five generations of structures that occur in the Valley-of-Fire. Martel et al. (1988) found that the splay fractures that cross between the first generation left-lateral faults were more likely to be sheared in a left-lateral sense than a right-lateral sense. This contrasts with observation in the Valley-of-Fire where the first generation splay fractures are almost always sheared in a right-lateral sense. Based on observations of predominantly left-lateral slip on these internal crossing faults and in light of kinematic models (Freund, 1974), Martel et al. also argued that material between the bounding left-lateral faults rotated in a clockwise sense and was under contraction. These rotations are opposite to those observed between the left-lateral faults in the Valley-of-Fire, and in corollary, we suggest that the material between the overlapping faults experienced extension.

Kim et al. (2001) document the formation of faults along earlier formed splay fractures. However, direct comparison with the faults in the Valley-of-Fire is difficult, as the faults they studied appear to have undergone two deformation events where earlier formed right-lateral faults were reactivated to slip in a left-lateral sense. They find splay fractures formed at the ends of right-lateral faults to be reactive in left-lateral shear. However, the left-lateral

36

shear appears to be resolved not only along the earlier formed splay fracture, but also along the end of the earlier right-lateral fault. In their conceptual model of fault evolution, Kelly et al. (1998) describe the formation of isolated conjugate faults that later link to form a fault network. This contrasts with our observation of faults in the Valley-of-Fire where we see a causative relationship between each progressively higher order generation of faults with opposite (or conjugate) slip sense. That is, each generation appears to have formed in response to deformation accommodated by earlier generations, in contrast to the faults that Kelly et al. (1998) describe where the faults appear to develop independent of each other.

The evolutionary aspects of our fault network model most resemble that of models developed by Willemse et al. (1997) and Graham et al. (in press) for faults in limestone, and, not surprisingly, by Myers (1999) for faults in sandstone–albeit all of these studies focused on the internal geometry of the faults at the outcrop scale in comparison to the larger-scale observations used in this study. The fault development model described by Willemse et al. (1997) and Graham et al. (in press) relies primarily on the progressive formation and subsequent shearing of pressure solution seams; splay fracturing via vein formation plays a somewhat less important role. They describe up to five successive generations of structures, each with opposing slip sense, in the formation of mature fault zones. Although mass transfer via the formation of solution seams is not identified to operate in a localized manner in the Valley-of-Fire, analogies between the two models can still be drawn. Similar, but opposite in opening sense to Mode I fractures, solution seams can be idealized as "interpenetrating" anti-Mode I fractures that form in the compressional quadrant of a sliding fracture (Fletcher and Pollard, 1981). In the case of the limestones described by Willemse et al. (1997), the higher order structures are generally in the form of solution seams that localize in the compressional quadrant of the sheared parent fracture, whereas in the Valley-of-Fire, the higher order structures are in the form of joints that localize in the extensional quadrant (Myers, 1999).

The strike-slip faults in the Valley-of-Fire are not well explained by Riedel shear zone models (Riedel, 1929) as interpreted in terms of the Coulomb failure criterion (e.g., Tchalenko, 1970; Logan et al., 1979) (Figure 1.16a). In Riedel models for simple shear, the

first expected structures to form are synthetic slipping R shear fractures oriented 45°–ϕ/2, and antithetic R' shear fractures oriented 45°+ϕ/2, where ϕ is the angle of internal friction. With increasing slip magnitude, synthetic P shear fractures form at an angle of –45°+ϕ/2. For fault zones with large offset magnitudes, Y shear fractures are expected to form parallel to the shear direction (Tchalenko, 1970; Logan et al., 1979) (Figure 1.16a). In some fault zones, T fractures, or joints, form at an angle of 45° from the trend of the zone, which is parallel to the direction of maximum compression, σ_1 (positive compression; $\sigma_1 > \sigma_2 > \sigma_3$) (Tchalenko and Ambraseys, 1970).

Considering the faults that comprise the network in the Valley-of-Fire, the formation sequence of the faults and splay fractures does not fit the Riedel model. Using Riedel terminology for the Valley-of-Fire structures, the Y structures (through-going, first generation left-lateral faults) would be the first to form, followed by T and then R' structures (splay fractures and second generation right-lateral faults, respectively). R and P structures are notably absent. It can similarly be shown that the angular relationships in the Valley-of-Fire do not fit the Riedel model. Choosing an angle of internal friction of 35° for the Aztec sandstone, R' shears (second generation faults) should be oriented 62.5° away from the
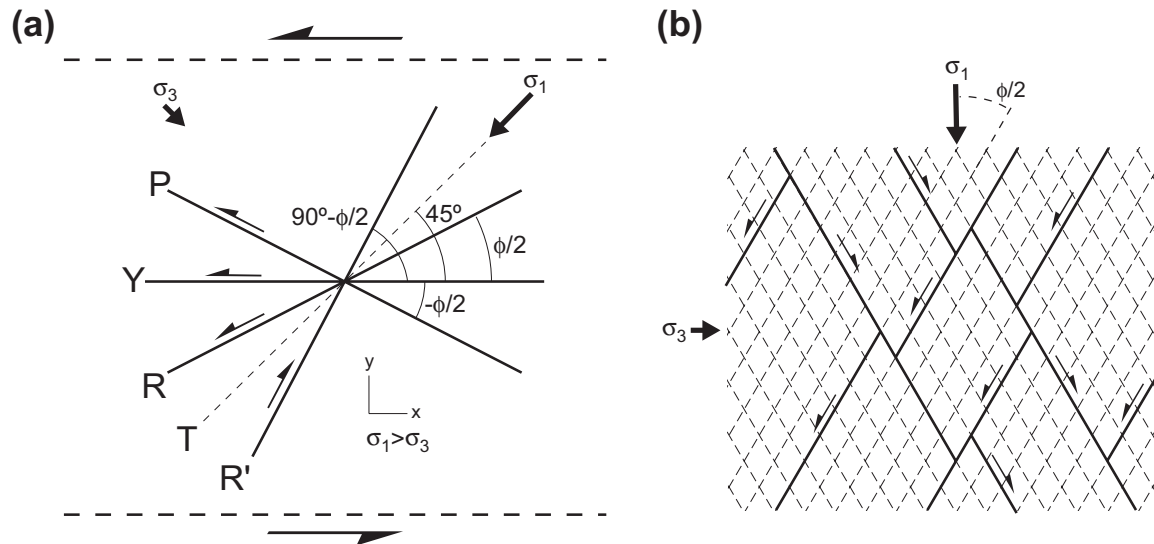
Figure 1.16. (a) Schematic illustration of a Riedel shear zone (adapted from Tchalenko, 1970; Swanson, 1988). **(b)** Possible geometry of a conjugate strike-slip fault network predicted by Anderson's (1951) faulting theory for horizontally oriented maximum and minimum principal stress, σ_1 and σ_3, and a vertically oriented intermediate stress (not shown), σ_2.

38

main fault trend, and T fractures (splay fractures) should be oriented 45º. We find them oriented closer to 30º, which better corresponds to the splay fracture kink angle (Cruikshank et al., 1991; Cooke, 1997; Willemse and Pollard, 1998).

The left- and right-lateral strike-slip faults in the Valley-of-Fire might also be considered a manifestation of conjugate R and R' Riedel shears where σ_1 bisects the angle between the two shears (Figure 1.16a). This would be equivalent to conjugate strike-slip faults in Anderson's (1951) faulting theory when σ_1 and σ_3 are oriented in the horizontal plane, and σ_2 is vertical (Figure 1.16b). However, neither model satisfactorily explains the development of the fault network in the Valley-of-Fire. The R and R' shear fractures form in Riedel models at small fault offsets. With increasing offset, P and Y shears are expected to form (Tchalenko, 1970). In the Valley-of-Fire, where the faults have offsets ranging between millimeters and kilometers, the two major fault orientations might correspond to the R and R' shear orientations, but the P and Y shears are absent. In Anderson's (1951) model, the angle between the greatest compression, σ_1, and the conjugate faults is, according to Coulomb failure criterion, 45º±ϕ/2. Assuming σ_1 bisects the orientation of the faults in the Valley-of-Fire, this angle would be approximately ±16º, which corresponds to an internal friction angle of 58º. However, we note that such large internal friction angles generally correspond to fine to very fine grain crystalline rocks (Brace, 1964), and that values reported for sandstone are closer to 32º (Jaeger and Hoskins, 1966).

Perhaps the most significant difference between our model and the Riedel (1929) and Anderson (1951) models is the inability of the later models to predict spatial distributions of structures. In particular, the Riedel and Anderson models do not describe intersection relationships and formation hierarchies between faults with different slip sense. Any plane that shares orientation with potential conjugate failure planes has equal likelihood of becoming a fault. Faults formed under these conditions are generally shown to have mutual crosscutting relationships (e.g., Figure 1.16b). However, in our model, faults rarely offset each other. Rather, higher order faults nucleate from the ends of, and are bound between, older faults.

Role in Basin and Range tectonics

It is important to place the strike-slip fault network in the Valley-of-Fire within a more regional context as much debate has centered on the role strike-slip faults play in Basin and Range tectonics. Activity along the sheared-joint faults that deform the Aztec sandstone appears to be contemporaneous with the formation of three crustal-scale structures found in the vicinity of the Valley-of-Fire based on stratigraphic offsets: the Lake Mead fault system (LMFS), Las Vegas Valley shear zone (LVVSZ), and the Virgin River depression (Figure 1.1). The left-lateral LMFS (Anderson, 1973; Bohannon, 1979) consists of several strands that show cumulative left-lateral offset of approximately 65 km (Bohannon, 1984). The right-lateral LVVSZ (Longwell, 1960) consists of several right stepping segments that form the Las Vegas Valley pull-apart basin (Campagna and Aydin, 1994; Langenheim et al., 2001). Slip along the LVVSZ is estimated to be from 40 to 65 km (Bohannon, 1984; Wernicke et al., 1988). The LMFS and the LVVSZ have mutual abutting relationships at their intersection in the Lovell Wash, north of the LVVSZ (Çakir et al., 1998). The Virgin River depression (VRD) consists of two north-trending and right-stepping sub-basins that are divided by a buried basement ridge and are fault bounded (Bohannon et al., 1993). However, the nature of these faults are not well constrained. The northeastern Mesquite sub-basin is as deep as 8-10 km, while the southeastern Mormon sub-basin is up to 5 km deep (Langenheim et al., 2000).

There have been heated debates on the role of strike-slip faults in the Basin and Range and the nature of rotation (e.g., Ron et al., 1986; Anderson and Barnhard, 1993; Çakir et al., 1998). It has been suggested that the strike-slip faults are the result of a more local process of transform faulting between differently extended terrenes (e.g., Wernicke et al., 1988; Duebendorfer and Black, 1992). While we do not wish to reopen a discussion on such a contentious issue, we should bring up the implications of the new data presented in this study for the issues expressed earlier. The strike-slip fault system in the Valley-of-Fire occurs over a broad area (~9 km in width) and appears to accommodate both NNW–SSE directed shortening and ENE–WSW directed extension. We suggest that the these faults, as well as the larger system of strike-slip faults to the north in Mormon Mountains and Tule Spring Hills [Anderson and Barnhard (1993), and Axen (1993), respectively], are pervasive

40

and have no obvious kinematic link to a transform fault-like system. The estimated net extension direction in this region of the Basin and Range province is oriented approximately WNW–ESE (Wernicke et al., 1988). The large-offset, left-lateral faults in the Valley-of-Fire are oriented approximately orthogonal to this direction, in contrast to transform faults oriented parallel to the extension direction (Wilson, 1965; Freund, 1974). We ascribe the shortening direction to approximately bisect the acute angle made by the left- and right-lateral fault pairs. The extension direction is orthogonal to the shortening and is facilitated by both the conjugate sense of slip and perhaps material rotation. Anderson and Barnhard (1993) similarly conclude approximately N–S shortening and E–W directed extension in their more regional study of strike-slip faults including the Lake Mead fault system. The same notion was also promoted by Wernicke et al. (1988).

Conclusions

This paper documented how two sets of strike-slip faults with opposing slip sense with an apparent conjugate pattern can form by sequential opening mode fracturing and shearing. A conceptual model was presented for the growth and evolution of the strike-slip fault network in Aztec sandstone that involves multiple generations of Mode I splay fracturing and their subsequent shearing. Most of the structures are localized at fault segment ends and stepovers. Shear is imposed across earlier formed opening mode splay fractures due primarily to material rotations between adjacent faults. This process results in the formation of two consistently oriented fault sets that have an opposing slip sense and consist of multiple hierarchical orders of structures with abutting, but no crosscutting relationships

The fault network in the Aztec sandstone of the Valley-of-Fire has the following salient characteristics:

1. Mean angles between structural generations range from 30° to 32° and are related to the Mode I splay fracture kink angle. However, considerable variability exists with intersection angles ranging between 12° and 85°. Deviations from the mean values are caused by local stress perturbations and material rotations. It is also possible that the presence of preexisting structures at odd orientations is responsible for some of the variability.

2. Material rotation occurs in blocks confined between faults and around large faults about a near-vertical axis. In the Valley-of-Fire, the largest scale rotation is counterclockwise and occurs between the secondary higher order right-lateral faults that are bound by the primary left-lateral faults. Clockwise rotations occur between higher order left-lateral faults that are bound by right-lateral faults.

3. Fault offset magnitudes are characteristic for each of the progressively higher order hierarchical structural elements. The largest offset faults (100s to 1000s of meters) are first generation structures. Higher order fault generations are generally younger and show approximately an order of magnitude less slip than the generation preceding it.

4. Spacing of structures depends on their hierarchy. Higher order structures tend to have closer spacing. Spacing of higher order structures also appears to be controlled by the spacing of the lower order bounding faults.

In this paper we have presented a conceptual model, based on field observations and the principals of fracture mechanics, for analysis of strike-slip fault network development. This model can also be used as a predictive tool in other regions providing that the faulting mechanism is the same or similar to the one elucidated in the Valley-of-Fire.

Chapter 2

Petrophysical constraints on deformation styles in Aztec sandstone, southern Nevada, USA

Abstract

Adjacent stratigraphic units that have undergone an identical deformation history often show variability with regard to deformation style. We present one such example and attribute the variability in deformation to variations in host rock properties. The Aztec sandstone of southern Nevada has two distinct zones of deformation style, the Lower and Upper structural domains. The Lower domain has deformed predominantly by opening mode fractures, whereas the Upper domain has deformed predominantly by deformation band faulting. Within a Transitional domain, deformation band abundance increases toward the Upper domain. We use petrophysical data (ultrasonic velocity, elastic moduli, grain and bulk density, helium porosity, and gas permeability) to distinguish among the host rocks of the differently deformed domains. The laboratory results of 29 samples of Upper, Transitional, and Lower domain Aztec sandstone impart the following petrophysical distinctions among the structural domains: (1) the Lower and Transitional domains show similarly high V_P and V_S and are both well cemented; (2) the Transitional and Upper domains show similarly high porosity and permeability; and, (3) the Upper domain is poorly cemented. We demonstrate that: (1) the nature of intergranular cement controls V_P and V_S; and, (2) based on the petrophysical properties we have examined, deformation style is controlled by porosity.

Introduction

Knowledge of the petrophysical characteristics of porous rock bodies is of great importance to understanding the amount of fluids and their movement in the subsurface. In addition, knowledge of the distribution and nature of deformational features within a given porous body are necessary for proper subsurface characterization as these features have been shown to produce wide ranging effects on fluid flow (Knipe et al., 1998; Aydin, 2000). In this

paper, we integrate laboratory rock physics and field structural geology to characterize a surface analogue of a subsurface sandstone reservoir/aquifer. In particular, we relate varying petrophysical characteristics to different strain-partitioned domains within an essentially homogeneous eolian sandstone.

The Aztec sandstone, located in the Valley of Fire State Park, southern Nevada (Figure 2.1), has excellent outcrop exposure well preserved by an arid climate. Within the Valley of Fire, the Aztec sandstone is characterized as having two distinct domains of deformation style:

> *Lower domain:* dominated by opening mode fractures

> *Upper domain:* dominated by deformation band faults

There is a third *Transitional domain* that lies stratigraphically between the Lower and Upper domains. As the name suggests, this domain is transitional in character between the Lower and Upper domains and shows a trend for greater deformation band abundance toward the Transitional – Upper contact.

In this paper, we first introduce the geologic setting of the study area and provide a brief review of the deformation features identified within the structural domains. We then discuss how these structures are distributed within the Aztec sandstone of the Valley of Fire State Park, southern Nevada. Our experimental procedures are presented, followed by a discussion of the experimental results. We conclude with a discussion of our primary findings and discuss possible implications for subsurface characterization of sandstone reservoirs.

Geologic setting

The Jurassic Aztec sandstone is an eolian sandstone correlated to the more widespread Navajo sandstone of the Colorado Plateau (Blakey, 1989). Compositionally, the Aztec sandstone is a feldspathic quartz arenite composed mostly of rounded to well-rounded quartz (> 95% detrital quartz). Grain size ranges from 100 to 1000 μm. The most dominant sedimentary structures are large-scale tabular-planar and wedge-planar cross-strata (Marzolf, 1983).

44
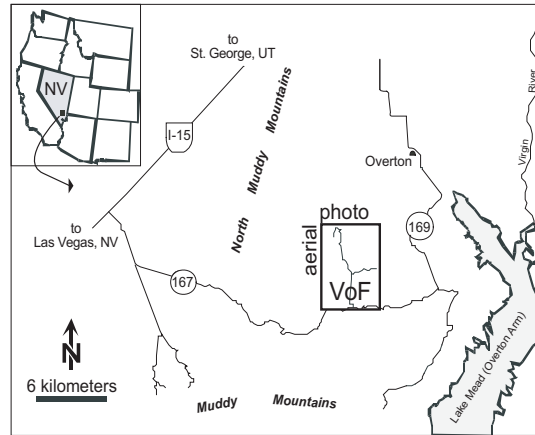
Figure 2.1. Study area location map. Samples of Aztec sandstone for this study were collected in, and within the vicinity of, the Valley of Fire State Park, southern Nevada. The box right-of-center shows the approximate boundaries of the aerial photograph shown in Figure 2.2a. VoF = Valley of Fire State Park. *inset*: Map of the western United States.

Within the Valley of Fire State Park (Figure 2.1), we divide the Aztec sandstone into various subunits based on stratigraphy, gross outcrop color, cementation, and deformation style (Table 2.1). According to gross outcrop color, the Aztec sandstone can be divided into three subunits: lower red, middle buff, and upper orange. This gross outcrop color is a manifestation of the type and abundance (or lack) of grain lining cement found within in each subunit. The lower, middle, and upper subunit designations coincide with stratigraphic position. The lower subunit is red in color and well cemented. The middle subunit is generally buff in color with lesser zones of orange, purple, and gray and is poorly cemented. The upper subunit is orange in color and is moderately to poorly cemented. According to field observations of deformation styles (discussed later), we place the stratigraphic upper and

Table 2.1. Nomenclature used to describe the Aztec sandstone, Valley of Fire State Park, southern Nevada.

Stratigraphic	Outcrop Color	Cementation	*Structural*
upper	orange	poor-moderate	*Upper*
middle	buff (minor orange, purple, gray)	poor	*Upper*
			Transitional
lower	red	well	*Lower*

45

(a)

legend
○ sample locality
- - - domain boundary
— roadway

1 kilometer

71

60 58

35 33

74
73
72

61a

57

56

54/55

Upper
Domain
Aztec SS

70

A'

Cretaceous Units

B'

69

23

66 68

A

Lower
Domain
Aztec SS

65

Transitional

64

B

63

20

36

Triassic Units

(b)

A   A'

1000 ft

500 ft   JaU

JaT

JaL   K

0

-500 ft   Tr
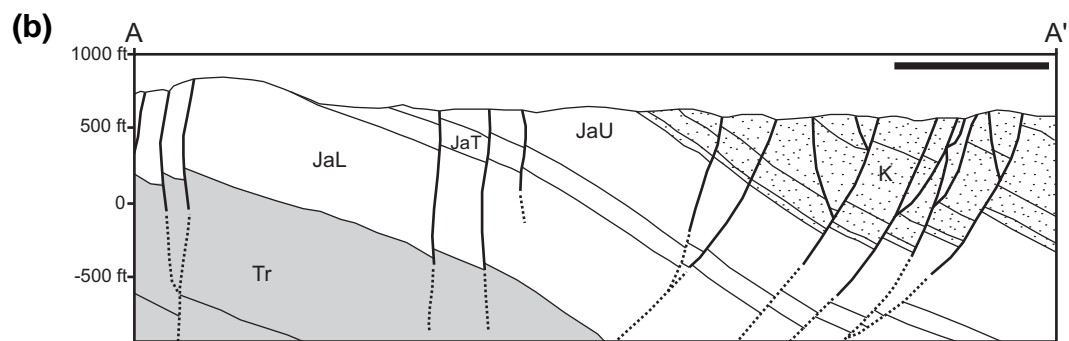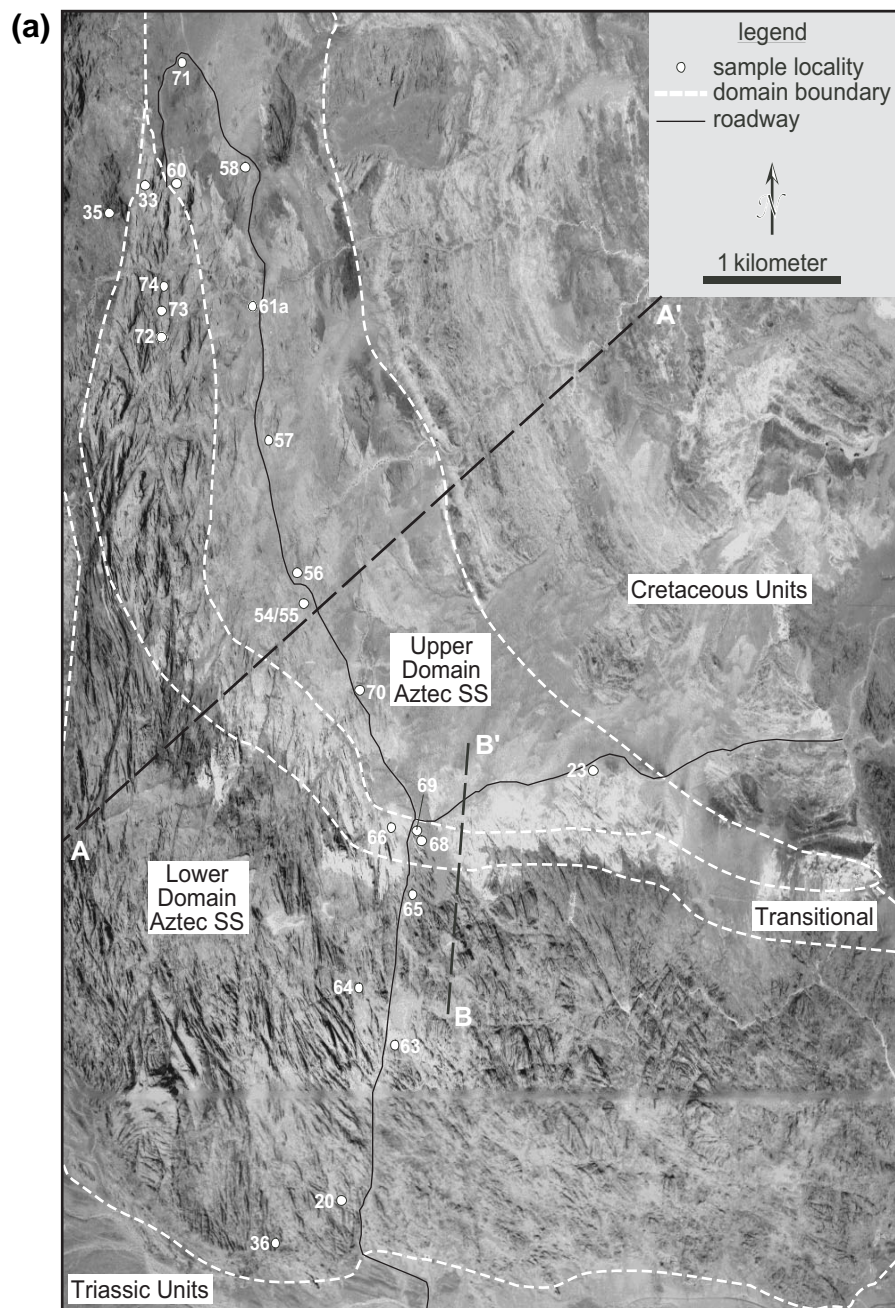
Figure 2.2 (caption at top of facing page)

46

Figure 2.2. (a) Aerial photograph of the Valley of Fire region showing the approximate boundaries of the defined deformation domains. The Lower domain is dominated by opening mode fractures; the Upper domain is dominated by deformation band faults. The Transitional domain shows no dominant deformation style, though, does show a trend for greater deformation band abundance toward the Transitional – Upper contact. Dashed line A-A' shows the trace of the cross-section shown in Figure 2.2b. Dashed line B-B' shows the data collection trace shown in Figure 2.3. Sample collection localities are shown for most samples listed in Table 2.2. The horizontal linear blur in the lower portion of the image is a photomosaic artifact. **(b)** Cross-section A-A'. Tr = Triassic units. Ja = Jurassic Aztec sandstone; suffixes L, T, and U respectively refer to the Lower, Transitional and Upper structural domains. K = Cretaceous units. Thin lines demarcate unit boundaries; thick lines are faults (dashed where inferred).

middle subunits of the Aztec sandstone within the Upper structural domain; the Lower structural domain consists entirely of lower subunit Aztec sandstone; the Transitional structural domain lies along the contact between the Lower and Upper structural domains (Figures 2.2a and 2.2b).

The observed color differences (i.e., upper, middle, and lower) discussed above occurred sometime after deposition and during diagenesis as the contacts between the subunits do not always coincide with sedimentary bedding (Taylor, 1999). We consider these bulk diagenetical provinces to have been established prior to initial deformation based on crosscutting relationships between the Cretaceous Muddy Mountain thrust (discussed below) and the Aztec sandstone.

Following stable, sub-aerial deposition in Jurassic time, the Aztec sandstone in the Valley of Fire region was subjected to at least two major deformational events. (1) *Shortening*: According to Bohannon (1983), during the Cretaceous and early-Tertiary(?) Sevier orogeny, the Aztec sandstone was over-ridden by the Muddy Mountain thrust sheet; a thrust sheet consisting primarily of Paleozoic carbonate rocks derived from the North American Cordilleran miogeocline to the west. Two generations of compressional shortening are assigned to this period: first generation east-directed vergence and second-generation east-northeast-directed vergence (Bohannon, 1983; Carpenter and Carpenter, 1994). Within the Valley of Fire region, these compressional deformation events are manifest by small-scale

47

deformation band faults (Hill, 1989). (2) *Extension and strike-slip faulting*: The next major deformation event occurred in Miocene time with the onset of Basin and Range extension. During this period, the most prominent style of deformation in the Valley of Fire region was sheared joint based strike-slip faulting with a lesser amount of oblique-normal slip (Myers, 1999). Jointing of the Aztec sandstone is considered to have occurred sometime after the formation of the deformation bands and before the formation of the strike-slip faults (Myers, 1999).

Structural domains

This paper focuses on contrasting the relative abundance of two distinct deformation mechanisms known to operate in porous sandstone, deformation band faulting and opening mode jointing. Deformation band faults result from shear strain localization along narrow tabular zones that are 1 mm - 1 cm wide and up to 100 m long. Deformation associated with this mechanism can include pore volume loss or gain, grain translation and rotation, cataclasis, grain indentation and clay smearing (Aydin, 1978; Jamison and Stearns, 1982; Antonellini et al., 1994; Ogilvie and Glover, 2001a). The deformation bands in the Valley of Fire exhibit pore volume loss, cataclasis, and grain indentation. These features can reduce host rock permeability by up to 5 orders of magnitude, providing a substantial barrier to fluid flow (Antonellini and Aydin, 1994, Taylor and Pollard, 2000; Ogilvie and Glover, 2001b).

The second deformation mechanism, the opening mode joint (mode I) (Pollard and Aydin, 1988), begins in response to localized tensile stress around a microscopic imperfection (e.g. pore space or irregular grain contact). Opening displacement perpendicular to the fracture walls accommodates deformation. Further growth of the discontinuity continues as long as the localized tensile stress at the joint tip exceeds the tensile strength of the rock. In contrast to deformation bands, these features are estimated to increase host rock permeability by as much as five orders of magnitude (Taylor et al., 1999).

Taylor (1999) made short scan-lines that record the relative abundance of joints and deformation bands with respect to the various alteration units found in the Aztec sandstone.

48
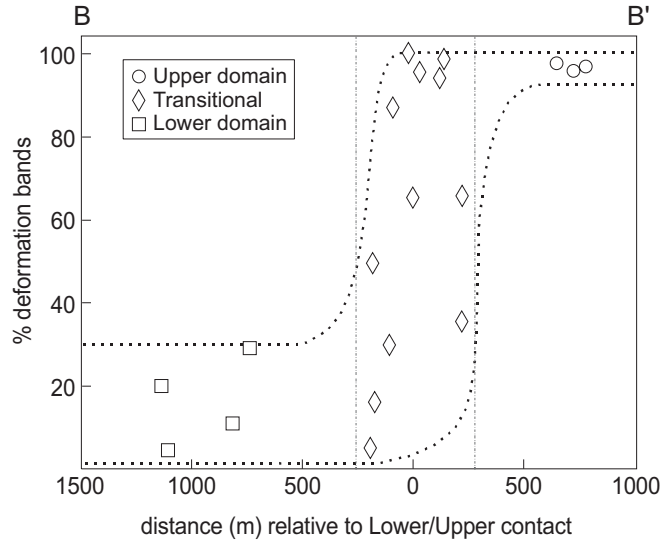
Figure 2.3. Plot showing the percentage of deformation bands relative to opening mode joints present at a given outcrop. Data collected along short individual scanlines at selected outcrops within the three structural domains. The approximate transect line is shown in Figure 2.2a, dashed line B-B'. Data from Taylor (1999).

Results of his study (Figure 2.3) show that deformation bands are more abundant in the Upper domain of the Aztec sandstone, while joints are more abundant within the Lower domain. A Transitional zone, coincident with the contact between the red and buff alteration units, shows a trend toward greater deformation band abundance nearer to the Transitional – Upper domain contact. Note that all domains are pervasively deformed with moderate to large offset (1 – 100 m) strike-slip faults. As these faults are considered to have formed subsequent to the formation of the joints and deformation bands (Myers, 1999), this study focuses on the distribution of structures in the Aztec sandstone prior to the onset of strike-slip faulting.

Experimental methodology

Twenty-nine host rock samples of Aztec sandstone were collected within the Valley of Fire State Park (see Figure 2.2 for sample collection localities). Care was taken in choosing samples from fresh, unweathered outcrop away from deformation features (i.e. joints, deformation bands, and major faults). Samples were chosen from Lower domain (red), Upper

49

domain (buff), and the Transition zone between the two (Figure 2.2b). Additionally, two well-cemented concretions were sampled. The concretions, which are considered to be a sub-set of the Lower domain, have very low porosity ($< 3\%$) and are densely fractured. The concretions are only found within 300 meters of the stratigraphic base of the Aztec sandstone.

Cylindrical plug samples with 25 mm diameter and 20-30 mm length were prepared with their faces ground parallel to within 100 mm. We present data from sample plugs cut perpendicular to bedding. A preliminary analysis comparing data from bedding parallel and perpendicular plugs showed negligible ($< 5\%$) anisotropy. Thus, the data presented in this study can be considered representative of the Aztec sandstone. A Helium porosimeter was used to measure bulk and grain densities and porosity at ambient conditions, after drying the samples overnight at 50°C. The microstructure of the samples was examined under an optical microscope and by scanning electron microscopy (SEM). Permeability was measured using a steady-state gas probe permeameter (or minipermeameter) (Goggin et al. 1988). Acoustic wave velocity data was collected using the pulse transmission technique (described below).

Ultrasonic experimental setup

The pulse transmission technique was used for P- and S-wave velocity measurements (V_P, V_S, respectively). The experimental setup (Figure 2.4) consists of a digital oscilloscope (Tektronix Model TDS 420A) and a pulse generator (Velonex Model 345). The sample was jacketed with rubber tubing to isolate it from the confining pressure medium. PZT-crystals mounted on steel endplates were used to generate P- and S-waves. The principal frequency was about 1 MHz for P- and 700 MHz for S-waves. A high viscosity bonding medium (Panametrics SWC) was used to bond the endplates to the sample. A pore fluid inlet in each endplate allowed passage of pore fluids through the sample. A full description of the experimental setup can be found in Prasad et al. (1999) and Prasad (2001). In this report, results of V_P and V_S from room dry measurements are presented.

50
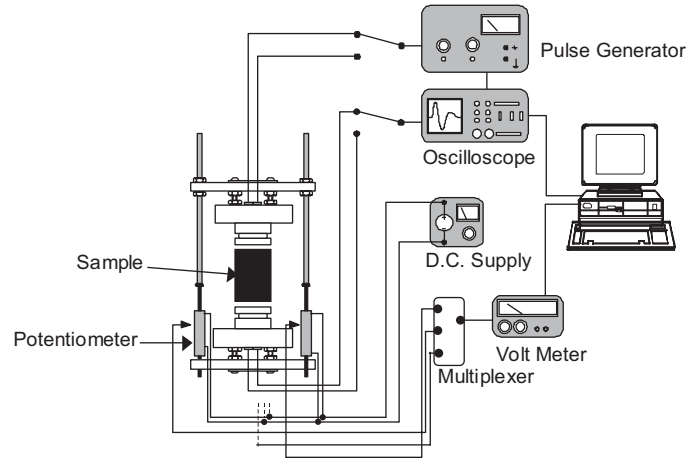
Figure 2.4. Schematic illustration of experimental setup. Not shown in this drawing is the hydrostatic pressure vessel in which the sample holding apparatus (shown on the left) resides.

The experimental configuration allowed simultaneous measurements of P- and S-waves at various pressures up to 60 MPa. The pressure limits were defined by an estimated maximum depth of burial for the samples (no more than 4 kilometers; Bohannon, 1983). Length change in the sample as a function of pressure was monitored using three linear potentiometers. Porosity changes were estimated from these changes in length at each pressure step. Traveltime was measured after digitizing each trace with 1024 points at a time sweep of 5 ms, thus allowing a time resolution of about 5 ns or about 0.2% error in velocity. Actual error in velocity measurement is estimated to be around 1% due to operator error in picking first arrival. The system delay time was measured by taking head-to-head time at 2 MPa and confirmed by measuring an aluminum cylinder at different pressures.

Experimental results

The petrophysical data collected in this study reveals distinct trends with respect to the Upper and Lower structural domains. The Transitional domain in some instances is found to be more similar in petrophysical characteristics to the Upper domain, while in other instances it is more similar to the Lower domain. Implications of this finding are discussed in detail in the Discussion section.

Table 2.2. Compiled petrophysical data gathered in this study for 29 samples of Aztec sandstone (see Fig. 2.2a for sample localities). Porosity was determined with a helium porosimeter. Permeability data were collected with a probe permeameter; values shown are the average (+/- 5%) of five clustered measurements made perpendicular to sedimentary bedding. Velocity data were collected using the pulse transmission technique. c = concretion; l = Lower domain; t = Transitional domain; u = Upper domain.

					Confining Pressure									
					5 MPa		10 MPa		20 MPa		40 MPa		60 MPa	
ID	domain	porosity	permeability (mD)	bulk density (g/cm3)	Vp (km/s)	Vs (km/s)	Vp (km/s)	Vs (km/s)	Vp (km/s)	Vs (km/s)	Vp (km/s)	Vs (km/s)	Vp (km/s)	Vs (km/s)
26	c	0.025	31.2	2.56	3.388	2.239	3.625	2.361	3.998	2.559	4.384	2.849	4.585	2.994
35	c	0.029	9.3	2.54	4.114	2.592	4.224	2.657	4.331	2.732	4.534	2.828	4.628	2.910
15	l	0.200	579.3	2.12	2.881	1.379	3.201	1.794	3.486	2.009	3.802	2.260	3.973	2.402
20	l	0.169	89.0	2.18	3.001	1.870	3.277	2.019	3.591	2.171	3.906	2.381	4.038	2.512
30	l	0.105	51.3	2.36	2.581	1.477	2.919	1.656	3.318	1.876	3.708	2.170	3.988	2.359
36	l	0.078	47.0	2.45	2.989	1.724	3.303	1.926	3.700	2.181	4.096	2.496	4.436	2.701
61b	l	0.240	567.3	2.02	2.902	1.889	3.228	2.023	3.400	2.170	3.677	2.322	3.810	2.396
62	l	0.219	1932.5	2.09	-	-	3.249	1.993	3.739	2.240	3.840	2.443	4.046	2.542
63	l	0.159	70.6	2.19	2.656	1.762	2.995	1.862	3.402	2.085	3.817	2.326	3.978	2.478
64	l	0.206	-	2.10	2.635	1.745	2.907	1.862	3.264	2.058	3.565	2.267	3.783	2.384
65	l	0.204	262.0	2.11	2.927	1.748	3.071	1.911	3.386	2.108	3.699	2.308	3.826	2.425
68	t	0.232	2128.4	2.04	-	-	-	1.763	3.776	2.211	3.810	2.403	3.924	2.502
69	t	0.233	3062.7	2.03	-	-	3.659	2.198	3.660	2.291	3.802	2.471	3.967	2.551
72	t	0.245	1713.4	1.99	-	-	2.856	1.830	3.193	2.022	3.611	2.200	3.742	2.307
73	t	0.185	80.6	2.15	3.217	1.936	3.399	2.090	3.668	2.235	3.865	2.378	3.914	2.460
74	t	0.243	2225.4	2.01	2.943	1.895	3.300	2.092	3.519	2.247	3.808	2.397	3.934	2.486
75	t	0.205	355.0	2.10	-	-	-	1.768	3.410	2.003	3.710	2.224	3.777	2.337
23	u	0.229	-	2.05	3.088	1.920	3.228	2.013	3.377	2.146	3.604	2.278	3.692	2.351
33	u	0.222	1568.8	2.08	-	1.696	3.090	1.865	3.332	2.034	3.594	2.207	3.730	2.306
54	u	0.238	696.5	2.03	2.844	1.732	3.106	1.876	3.261	2.042	3.623	2.191	3.734	2.276
55	u	0.212	319.4	2.09	2.891	1.904	3.080	2.032	3.285	2.156	3.481	2.266	3.627	2.329
56	u	0.234	510.8	2.03	2.628	1.597	2.957	1.817	3.176	2.021	3.489	2.228	3.746	2.350
57	u	0.301	3734.8	1.86	-	-	2.440	1.735	3.182	1.943	3.369	2.121	3.697	2.209
58	u	0.143	301.9	2.24	2.976	1.585	3.108	1.785	-	1.965	3.599	2.151	3.705	2.262
60	u	0.244	626.7	2.01	-	-	-	-	3.285	1.953	3.633	2.222	3.769	2.338
61a	u	0.255	1821.5	1.98	2.465	1.614	2.659	1.745	2.889	1.888	3.168	2.030	3.324	2.113
66	u	0.215	-	2.09	2.682	-	2.955	1.903	3.239	2.134	3.564	2.312	3.721	2.429
70	u	0.257	1106.3	1.97	-	-	-	1.919	3.287	2.059	3.380	2.181	3.693	2.251
71	u	0.224	361.7	2.07	2.932	1.758	3.221	1.894	3.368	2.064	3.624	2.209	3.763	2.297
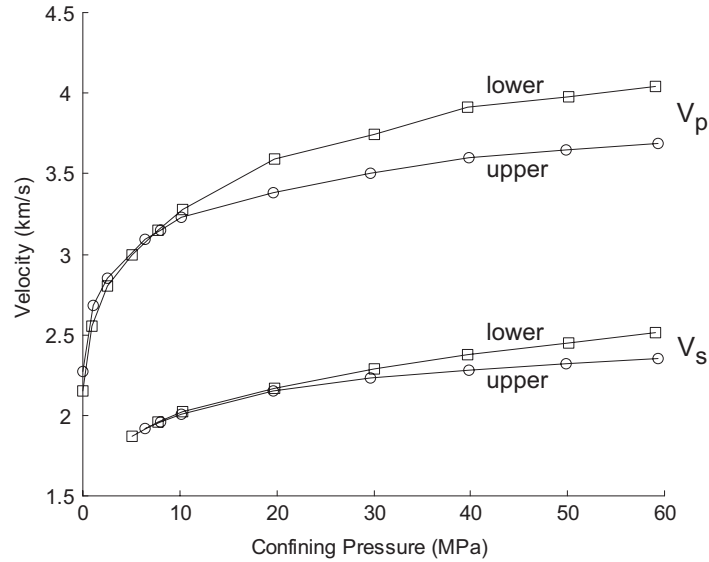
Figure 2.5. Typical data collection run for pulse-transmission velocity (compressional and shear) versus confining pressure for both Lower and Upper domain samples. Note the similarity between the samples below 10 MPa confining pressure. Above 10 MPa, the Upper domain samples show smaller velocity increases with increasing confining pressure when compared to the Lower domain samples.

All petrophysical data collected in this study are summarized in Table 2.2. Figure 2.5 shows an example data collection run of V_P and V_S from both the Upper and Lower domains. Below 10 MPa confining pressure, both sample suites show similar trends (note, below 5 MPa confining pressure the V_S signal was too attenuated and not interpretable). Above 10 MPa confining pressure, the Lower domain sample suite shows a consistently higher velocity with increasing pressure with respect to the Upper domain suite. In addition, the terminal slope of the velocity-pressure trend for the Lower domain suite tends to be greater than that of the Upper domain suite, indicating that a further increase in confining pressure would lead to yet further velocity differences between the sample suites.

The velocity – pressure relation for all samples is summarized in Figure 2.6a for V_P and Figure 2.6b for V_S. The data, classified according to their structural domains, confirm the general trend of Figure 2.5:

· The Lower domain suite consistently reaches higher terminal V_P than the Upper domain.
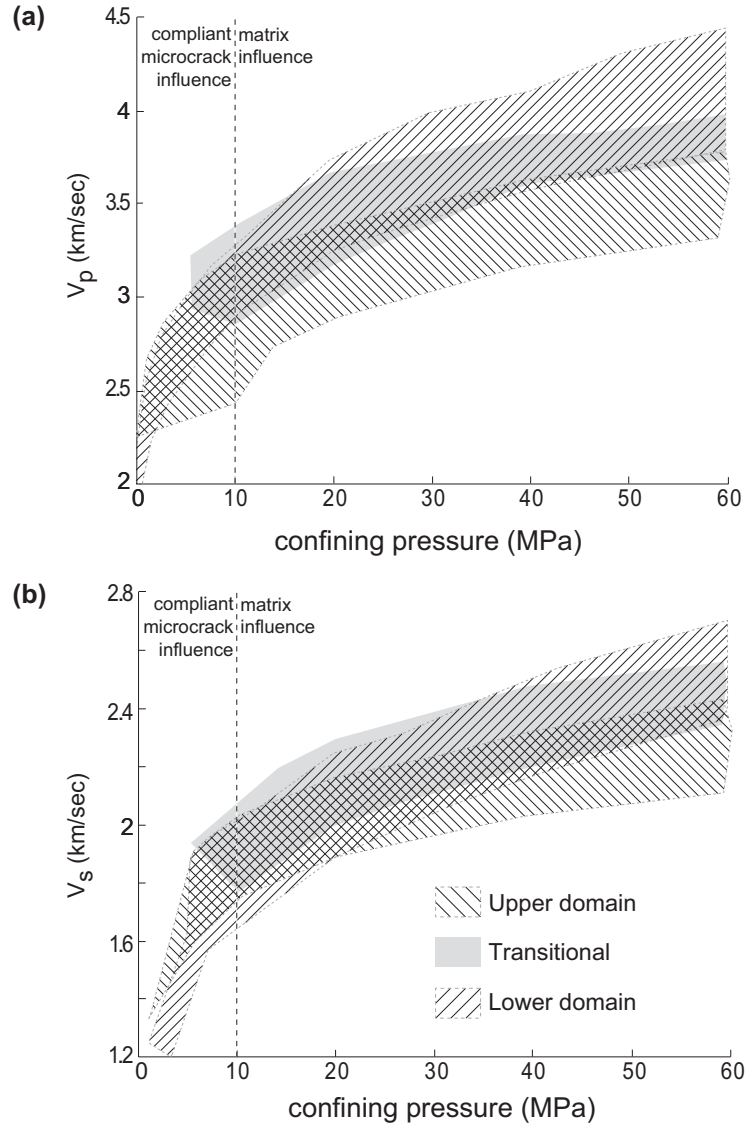
Figure 2.6. Area-scatter plots showing all pulse-transmission velocity data collected in this study. Each region is demarcated by the greatest and least measured sample quantity for each respective structural domain (i.e., Lower, Transitional and Upper). **(a)** Compressional wave velocity (V_P) versus confining pressure. **(b)** Shear wave velocity (V_S) versus confining pressure.

· V_S is also higher in the Lower domain suite. However, there is more overlap in velocity values at all confining pressures.

· V_P and V_S in the Transitional domain suite shows greater affinity to the Lower domain suite.

54
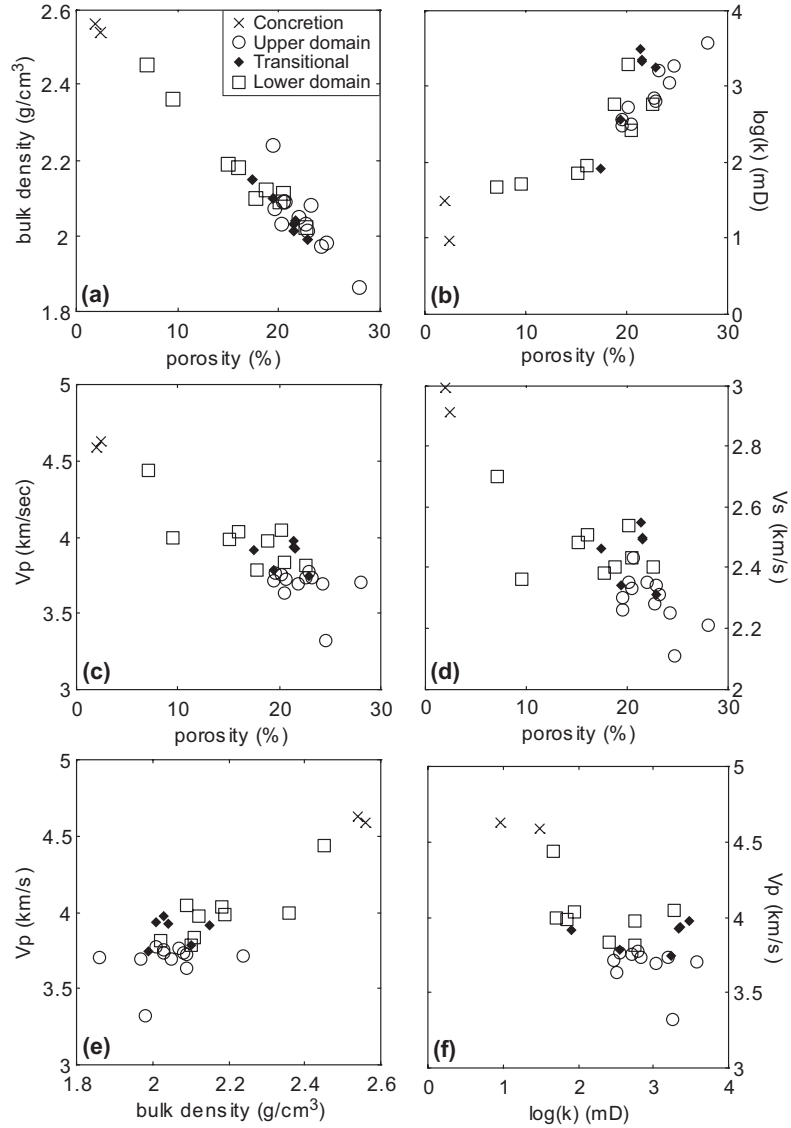
Figure 2.7. Cross-plot relationships between some petrophysical quantities. **(a)** Bulk density versus porosity. Note, the outlier Upper domain sample contains iron oxide banding and thus has anomalously high bulk density. **(b)** Log permeability versus porosity. **(c)** V_P (at 60 MPa confining pressure) versus porosity. **(d)** V_S (at 60 MPa confining pressure) versus porosity. **(e)** V_P (at 60 MPa confining pressure) versus bulk density. **(f)** V_P (at 60 MPa confining pressure) versus Log permeability.

In order to understand the velocity differences between the three domains, we examine cross-plot relationships between some petrophysical properties shown in Figures 2.7a through 2.7f. Both bulk density and permeability (Figures 2.7a and 2.7b, respectively) show good correlation with porosity. The domains can be separated by absolute porosity values; Lower

domain samples generally have lower porosity than Transitional and Upper domain samples. Furthermore, at the same porosity the Lower domain suite shows higher bulk density than the Upper domain due to the presence of higher density cement. The velocity – porosity plots (Figure 2.7c for V_P, Figure 2.7d for V_S, both at 60 MPa confining pressure) show that velocity correlates well with porosity. Generally, the Lower domain is separated from the Upper domain by lower porosity and higher velocity values. The higher bulk density in the Transitional domain suite serves to also increase velocity (Figure 2.7e). Thus, where porosity values overlap, the Lower and Transitional domains samples have higher velocity values than the Upper domain suite. The concretion samples with about 3% porosity show highest velocity values, approaching that of pure quartz (6.05 km/s) (Mavko et al., 1998). A negative correlation is found between increasing P-wave velocity and increasing permeability (Figure 2.7f). This correlation is related to the negative correlation found between increasing velocity and porosity.

Microstructural variations are also known to influence bulk seismic properties (Prasad, 2001). Three typical SEM images of Lower, Transitional, and Upper domain samples are respectively shown in Figures 2.8a through 2.8c. The light gray grains are detrital feldspar, while the somewhat darker gray grains are detrital quartz. Black is pore space. Intergranular microcracks are common within all examined samples with the lesser abundant feldspar grains showing the highest microcrack densities. Lower domain samples (Figure 2.8a) are well cemented by both grain coating and pore filling cement that give them lower porosity and higher strength. Notice that in some cases, pore spaces are completely filled. Upper domain samples (Figure 2.8c) generally have very little cement, both in terms of grain coating and pore filling cement. These samples also have higher porosity and lower strength. Transitional domain samples (Figure 2.8b) have a similar abundance of grain coating cements when compared to the Lower domain samples, but generally lack the pore filling cements. Thus, although the Transitional domain samples have higher velocities due to the strong grain lining cement, they also have higher porosity due to the lack of pore filling cement.

(a) Lower domain   **(b)** Transitional   **(c)** Upper domain
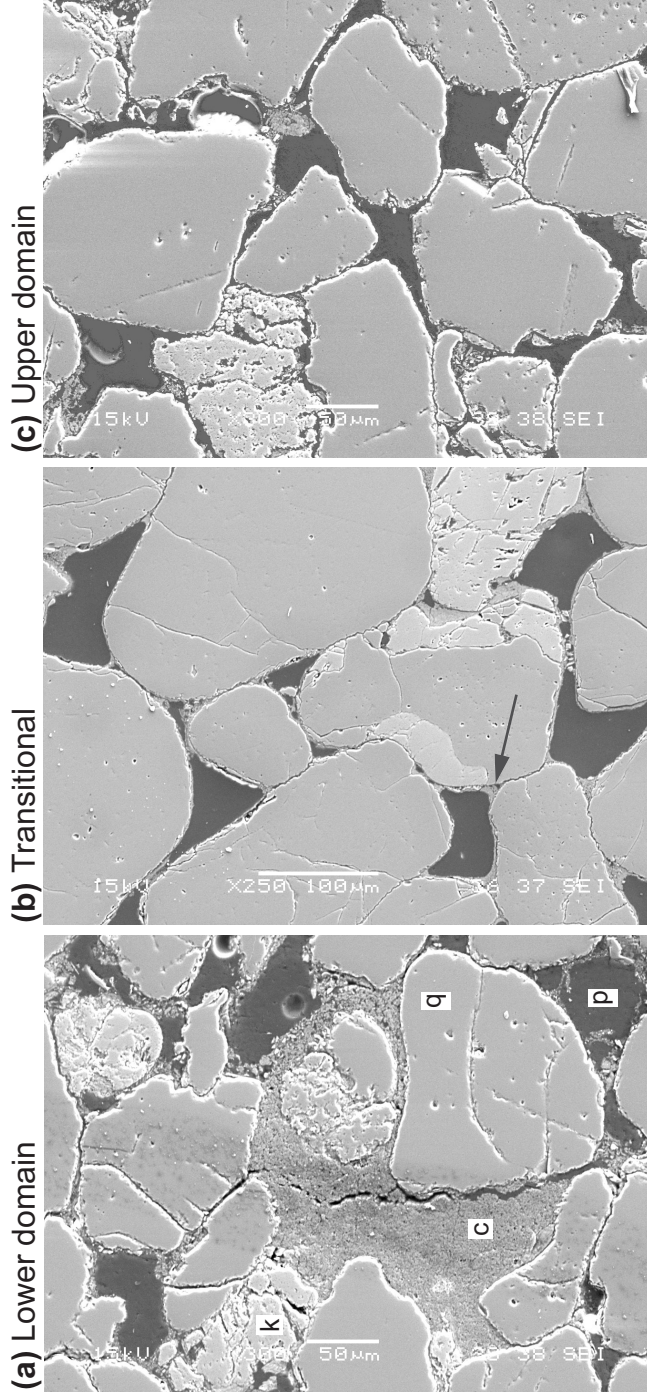
Figure 2.8. SEM images showing the general differences in the type and quantity of cement between the structural domains. Microcracks were found within all samples. **(a)** Lower domain (sample 65). Note the relative abundance of grain-to-grain contact cements, as well as pore-filling cements. The pore-filling cements generally do not completely fill pores and therefore do not add much elastic rigidity to the rock by their presence. **(b)** Transitional domain (sample 68). The grain-to-grain contact cement (arrow indicates cement) found in this sample domain is similar in nature to that of the Lower domain. In general, this domain lacks the abundant pore filling cement. **(c)** Upper domain (sample 54). This sample domain is characterized as having very little grain-to-grain contact cement. Light gray grains are feldspar (k); medium gray grains are quartz (q); black is pore space (p); intergranular material is cement (c).

57
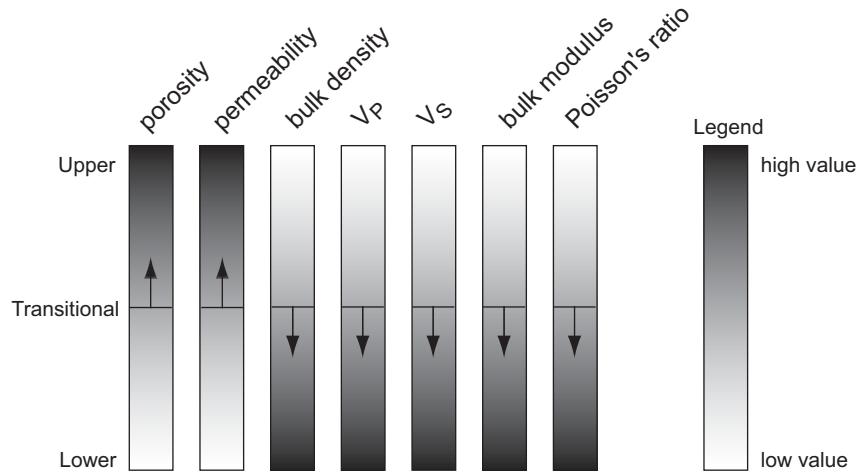
Figure 2.9. Generalized comparison of petrophysical properties between the different structural domains of the Aztec sandstone. The arrows indicate to which domain the Transitional domain has more affinity. Black indicates high values, while white indicates low values.

Petrophysical generalizations drawn from the collected data are shown in Figure 2.9. In the cases of porosity and permeability, the Transitional domain is more similar to the Upper structural domain. In the cases of V_P, V_S, Poisson's ratio, bulk modulus, and bulk density, the Transitional domain is more similar to the Lower structural domain. These observations of differences and similarities between the Lower and Upper domains and the Transitional domain in between form the basis for our discussion below.

Discussion

The petrophysical data presented in this study differ enough so that one can distinguish between the domains based on petrophysical characterization, alone. These differences are also manifest in the varying abundance of structures among the structural domains caused by different deformation mechanisms, that of opening mode jointing and deformation band faulting. In this discussion, we first offer some explanations for the differing velocities between the structural domains and then discuss how these different petrophysical quantities might contribute to the formation of one preferred deformation style over another.

Petrophysical controls on velocity

The velocity signatures of the Aztec sandstone are best understood by separately consider-ing low confining pressure response and high confining pressure response. At low confin-ing pressures (< 10 MPa), velocity data (V_P and V_S) are found to be nondistinctive. In the 0 – 10 MPa confining stress range, all samples show relatively low velocities, as well as steep increases in velocity with increasing confining pressure (compared to the more shal-low slopes found at higher confining pressures). We consider the velocity similarities be-tween the suites to be caused by the ubiquitous presence of compliant microcracks within the Aztec sandstone. All examined samples show a similar occurrence of microcracks within the framework grains (cf. Figures 2.8a to 2.8c), as well as in contact cements, where present (cf. Figure 2.8a).

At low confining pressures, microcracks have been shown to reduce elastic wave veloc-ity (Nur and Simmons, 1969). The similar distribution of microcracks between structural domains causes the similar velocity signature found at low confining pressures. Increasing the confining stress above atmospheric pressure closes compliant microcracks, and as a result velocity increases. The abrupt closure of compliant microcracks with relatively small confining pressure increases explains the similarly steep slopes found for all samples in the 0 – 10 MPa pressure range (cf. Figure 2.6) (Lo et al., 1986; Wepfer and Christensen, 1990; Prasad et al, 1994).

In the 10 – 60 MPa pressure range, velocity (V_P and V_S) differences between the struc-tural domains become distinct as the compliant microcrack effect becomes negligible and the effects due to the nature of the framework grain contacts dominate. The presence of grain binding cements has been shown to greatly enhance elastic wave velocities in granular rocks by increasing the overall framework rigidity of the system (Dvorkin and Nur, 1996; Prasad and Manghnani, 1997). Furthermore, the presence of less-compliant cement between a more-compliant framework has been shown to increase the overall effective contact area between grains with increasing confining pressure, thereby increasing overall elastic wave velocity (Christensen and Wang, 1985; Prasad, 2001).
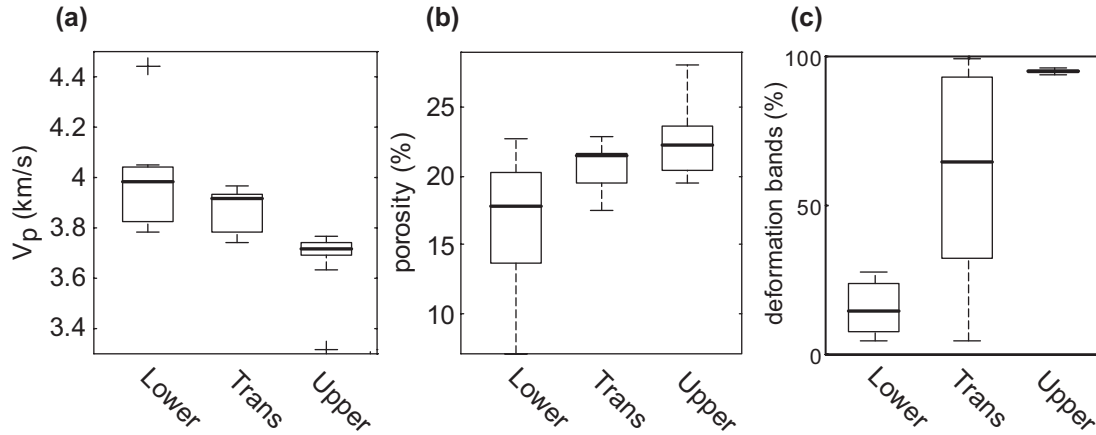
Figure 2.10. Boxplot statistics for all three structural domains. **(a)** Compression wave velocity collected at 60 MPa confining pressure. **(b)** Porosity. **(c)** Relative percent deformation bands at a given locality. Line in the center of a box is the mean; box bottom and top are respectively the first and third quartiles; dashed lines indicate 1.5 times the interquartile range; outliers are explicitly indicated by a cross.

The microstructural differences explain the variations in petrophysical properties observed in Figure 2.8. Thus, the presence of grain coating cements in the Lower and Transitional domain samples increases frame stiffness and seismic velocity. The Upper domain samples with less cement have lower frame stiffness and lower velocity. On the other hand, "non-contact" pore filling cements do not affect velocity but further decrease porosity in the Lower domain sample suite (Dvorkin and Brevik, 1999; Gal et al., 1999). The Transitional and Upper domain suites that did not experience a pore-filling event show higher porosity.

Petrophysical controls on deformation

We now compare petrophysical quantities with the deformation styles in Aztec sandstone (Figure 2.10). We use V_P as a proxy for all other petrophysical properties (V_S, elastic moduli, density, permeability, and type and quantity of cement) except porosity. V_P (Figure 2.10a), porosity (Figure 2.10b), and percent of deformation bands at a given outcrop (Figure 2.10c) plotted for the three suites show that velocity in the Lower and Transitional domains are similar and higher than the Upper domain samples. However, deformation band abundance and porosity are similar in the Upper and Transitional domains and higher than the Lower

domain. These observations imply that, given the set of parameters measured, porosity is the major controlling parameter in terms of deformation style. Porosity is the only property that sets the more similarly deformed Transitional and Upper domains apart from the Lower domain.

From field studies of porous sandstones found within Arches National Park, USA, Antonellini et al. (1994) concluded porosity was one of four parameters controlling deformation style. Additionally, they identified clay content, confining pressure, and bulk strain as controlling parameters. In the case of the Aztec sandstone, we do not consider clay content as a contributing factor as its abundance is negligible. Confining pressure and bulk strain are likely contributing factors, though they likely only contribute to the relative timing between the formation of the different deformation styles. The structural domains are subunits within the same stratigraphic formation and have therefore been subjected to nearly identical loading conditions. Antonellini et al. (1994) found that high porosities promoted the formation of compaction bands with cataclasis, and that low porosities promoted the formation of dilatant bands without cataclasis. In the case of the Valley of Fire, it could be that conditions during deformation only favored the formation of deformation bands within the high porosity Upper domain, and later a different set of conditions dictated the formation of joints within the lower porosity Lower domain.

The field observations of Antonellini et al. (1994) are corroborated by the experimental work of Dunn et al. (1973), Scott and Nielson (1991), and Wong et al. (1997). Dunn et al. (1973) performed biaxial compression tests on sandstones with a variety of porosities. Given similar conditions, they found that samples with low porosity exhibited extensive jointing at the grain-scale level, while in the higher porosity samples deformation bands formed. They additionally found no trend with regard to variability in diagenetic cementation. In brittle-ductile transition studies by Scott and Nielson (1991) and Wong et al. (1997), porosity is cited as the dominant inherent sample property (i.e. not an environmental variable such as pore pressure) that controls the style of deformation given a set of confining conditions.

Variations in cementation might play a role in the differences in deformation style according to experimental work by Bernabe et al. (1992) and Yin and Dvorkin (1994). In triaxial tests of synthetically cemented granular media, Bernabe et al. (1992) concluded that cements have a tendency to prevent grain sliding and rotation. Yin and Dvorkin (1994) performed isotropic compaction tests on cemented and uncemented packed glass beads. For the same confining conditions, they found intense grain crushing to occur in the uncemented bead pack, while for the cemented packs, failure was less intense and localized within the cements. These observations do not necessarily explain the distribution of deformation features in the Aztec sandstone as the Lower and Transitional domains have similar grain binding cements, though the Transitional and Upper domains have a more similar deformation style. It could be that the presence of the pore filling cements in the Lower domain samples greatly inhibits the formation of deformation bands.

Implications for subsurface characterization

Our observation that pore filling and contact cement governs petrophysical variability (e.g., porosity), which in turn influences seismic properties and deformation style, has important implications for subsurface characterization. Judging by host rock properties alone, the Upper domain might be considered a better target for development based on higher detected permeability and porosity (cf. Table 2.2). However, the Upper domain has greater a concentration of permeability reducing deformation bands (up to 5 orders of magnitude *below* matrix permeability; Antonellini and Aydin, 1994; Taylor and Pollard, 2000; Ogilvie and Glover, 2001b), while the Lower domain has greater a concentration of permeability enhancing opening mode joints (up to 5 orders of magnitude *above* matrix permeability; Taylor et al., 1999). A reservoir development plan would need to take these structural effects into account in order accurately represent the flow system.

Conclusions

1. The Aztec sandstone within the Valley of Fire State Park has two distinct domains with respect to deformation style. The Lower domain is dominated by opening mode joints; the Upper domain is dominated by deformation band faults. A third Transitional domain shows a trend for greater deformation band density towards the Transitional – Upper domain contact.

2. The structural domains differ with respect to petrophysical characteristics:

   i. Lower domain: higher V_P and V_S at high confining pressure ($> 10\,\text{MPa}$); lower porosity and permeability; well cemented.

   ii. Transitional domain: V_P and V_S similar to Lower domain; porosity and permeability similar to Upper domain; well cemented.

   iii. Upper domain: lowest V_P and V_S at high confining pressure ($> 10\,\text{MPa}$); higher porosity and permeability; poorly cemented.

3. At low confining pressures ($< 10\,\text{MPa}$), the structural domains are similarly low in velocity due to the attenuating nature of the microcracks found in both the framework grains and the grain binding cements. The observed steep increase in velocity for all samples is due to the closure of these microcracks. Above 10 MPa confining pressure the nature of the grain contacts and cement dominates the velocity signature. The well-cemented Lower and Transitional domains show the highest velocities.

4. Given the set of petrophysical parameters examined in this study, porosity appears to be the controlling parameter with respect to deformation style, with possible secondary effects caused by cement variability. Likenesses are found between the Lower and Transitional domains except for porosity and deformation band abundance.

Acknowledgments

Chapter 3

Petrophysical properties and sealing capacity of fault rock from sheared-joint based faults in sandstone

Abstract

The incorporation of shale into fault zones is widely recognized to increase the sealing capacity of a fault on both exploration and production time-scales. In contrast, the hydrodynamic behavior of sand-dominated fault zones is less well-understood and therefore not routinely considered as part of fault seal and flow prediction. In order to refine flow models for sand-dominated fault rock, we present petrophysical data of host and fault rock samples from aeolian Aztec sandstone, Valley of Fire State Park, Nevada, that has been deformed by strike-slip faults formed by progressive shearing along joint zones. The data include bulk mineralogy, porosity, permeability, grain-size distribution, and mercury-injection capillary pressure measurements of forty host, fragmented, and fault rock samples. To investigate the impact of shear strain on fault zone properties, three sample localities with average shear strains of 28, 63, and 80 were investigated (25 to 160 m slip). No bulk mineralogical changes due to fault zone cementation or recrystallization were detected when comparing host and fault rock. Fault rock permeability is significantly lower than calculated median host rock permeability, showing a one to three order of magnitude reduction in fault rock permeability. Porosity reductions are less pronounced and show considerable overlap in values between the sample suites. Some fault rock samples appear to have dilated with respect to median host rock porosity. Median grain sizes for fault rock samples range between 3 and 51 μm, which is up to two orders of magnitude reduction from host rock median grain size. There appears to be a lower limit of median grain size of 3 μm for fault rock samples irrespective of average fault shear strain. Fault rock breakthrough pressures range from one to almost two orders of magnitude higher than host rock equivalent. For standard fluid properties, calculated maximum sealable hydrocarbon column heights range between 10-69 m of gas, and 17-120 m of oil. These petrophysical data show that faults formed by shearing of joints in high permeability sand-prone systems will act as significant barriers to

fluid flow during reservoir production and might be capable of sealing small to moderate hydrocarbon columns on an exploration time-scale as well, assuming adequate continuity of the fault rock over large areas of the fault.

Introduction

The petrophysical characteristics of fault rocks are input required for predicting flow in faulted reservoirs. Specifically, fault rock petrophysical properties are used in calculations of fault transmissibility (Walsh et al., 1998; Manzocchi et al., 1999) and fault permeability upscaling models (Myers, 1999; Flodin et al., 2001; Jourde et al., 2002) to constrain reservoir simulation predictions for transient flow problems. Fault rock capillary properties have recently been introduced to hydrocarbon migration and flow models (Childs et al., 2002, and Manzocchi et al., 2002, respectively), and are more generally used in exploration to predict fault seal capillary strength (e.g., Smith, 1966; Watts, 1987; Gibson, 1994; Knipe et al., 1997). Subsurface fault seal applications benefit from calibration to fault rock petrophysical data in order to obtain accurate and predictive results, but such data are rarely available from subsurface studies. In this regard, outcrop studies of well-exposed fault zones have improved the understanding of the variety of classes of faults and their detailed damage architectures. Geometric and petrophysical characterizations from such studies will aid in reducing exploration risk and predicting faulted reservoir performance. In practice, most focus has been given to shale dominated fault zones, which are recognized to increase fault sealing capacity on both exploration and production time-scales. In contrast, the hydrodynamic behavior of sand-dominated fault zones is less well-understood and therefore not routinely considered as part of fault seal and flow prediction.

Two types of faulting mechanisms are recognized to operate in sandstone: deformation band faulting (Aydin and Johnson, 1978; Jamison and Stearns, 1982) and sheared-joint based faulting (Myers, 1999; Myers and Aydin, in review). In this paper, we focus on fault rock collected from faults formed by shearing across joint zones through splay fracturing and subsequent shearing of splay fractures. This process and the resultant fault architecture are distinct from faults formed by deformation band style faulting. The petrophysical and flow properties of fault rock related to deformation band style faults have received much

66

attention in the literature (e.g., Engelder, 1974; Pittman, 1981; Antonellini and Aydin, 1994; Fowles and Burley, 1994; Fisher and Knipe, 1998; Gibson, 1998; Main et al., 2000; Taylor and Pollard, 2000; Ogilvie and Glover, 2001; Shipton et al., 2002). In contrast, fault rocks associated with sheared-joint style faults have only been investigated by Myers (1999).

Myers (1999), using image analysis techniques (Ehrlich et al., 1984), studied the porosity and grain size characteristics of host and fault rock samples from the Aztec sandstone at the Valley of Fire State Park, Nevada. His estimates of fault rock porosity from image analyses ranged between 0.5 to 7%, while mean fault rock grain size estimates ranged between approximately 20 and 40 μm. Based on these data, Myers estimated fault rock permeability using a modified Kozeny-Carmen relationship (Bear, 1972). His calculated permeability estimates ranged between 0.002 and 7 md. Myers (1999) also analyzed several samples using a conventional permeameter and found order of magnitude agreement between measured and estimated permeabilities.

In this paper, we present new petrophysical data from forty host and fault rock samples of Aztec sandstone collected from three outcrop localities that have different average shear strains, corresponding to throws between 25 and 160 m. We proceed by describing the structural elements that comprise sheared-joint based faults focusing on two elements, fragmented rock and fault rock. Fault maps of the three sample localities are shown to document the fault zone architecture and our sampling strategy. We then present mineralogical and petrophysical data, which include porosity and permeability, grain size distribution, and capillary pressure curves from the fault zone elements and the host rock. We conclude with a discussion of our findings in relation to fault rock petrophysical evolution, and the significance of sand-prone fault zones as barriers to hydrocarbon flow for production and exploration (i.e., reservoir simulation and fault seal analysis, respectively).

Geologic setting

This study focuses on predominantly-strike-slip faults that occur within aeolian Jurassic Aztec sandstone exposed in the Valley of Fire State Park of southern Nevada (Figure 3.1). The Aztec sandstone was deposited in early Jurassic time in a back-arc basin setting and was part of a broad aeolian erg system that included the Navajo sandstone of the Colorado

Plateau (Blakey, 1989). The Aztec sandstone is a fine to medium grained sub-arkose to quartz arenite characterized by large-scale tabular-planar and wedge-planar cross-strata (Marzolf, 1983). Aztec sandstone porosities range from 15-25%, while permeabilities range from 100-5900 md (Myers, 1999; Flodin et al., in press). Within the Valley of Fire, the Aztec sandstone has a stratigraphic thickness of approximately 800 m (Longwell, 1949).

Structures in the Aztec sandstone record two phases of deformation: early thrust faulting related to the Cretaceous Sevier Orogeny (Armstrong, 1968), and later strike-slip and minor normal faulting related to Miocene Basin and Range tectonics (Bohannon, 1983). The strike-slip faults we study formed during the later deformation event (Myers, 1999; Taylor, 1999) and were active between 12 and 4 Ma (Carpenter and Carpenter, 1994; Flodin and Aydin, in review-a). At the initiation of strike-slip faulting, the Aztec sandstone in the vicinity of the Valley of Fire was buried by at least 1.6 km of sediments (based on
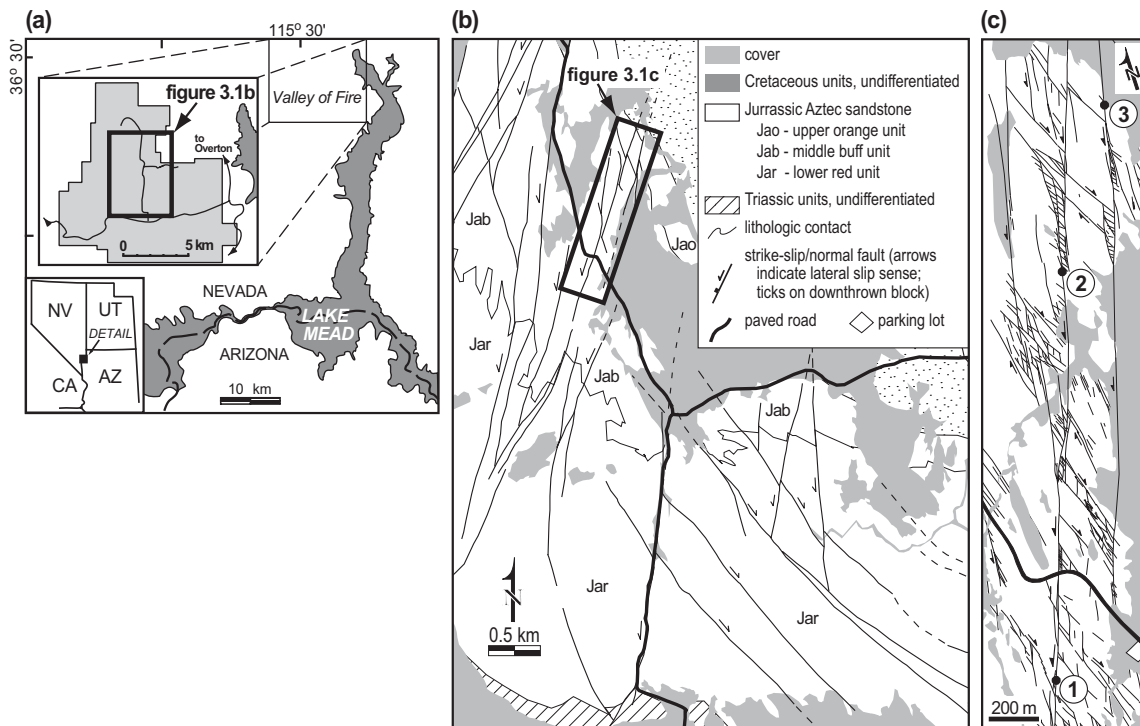
Figure 3.1. (a) Map showing the location of the study area in the Valley of Fire State Park, southern Nevada (after Myers, 1999). **(b)** Geologic map of the greater study area (after Myers, 1999; Taylor, 1999). **(c)** Detail map showing the localities for sample stations 1, 2, and 3 (circled numbers). Northeast oriented structures are left-lateral strike-slip faults, whereas northwest oriented structures are right-lateral strike-slip faults. Some faults are labeled with arrows indicating slip sense.

68

stratigraphic thicknesses provided by Bohannon, 1983), and possibly by an additional 1-4 km of overlying Sevier related thrust sheets (Brock and Engelder, 1977).

Fault zone elements

Strike-slip faults with a minor normal component in Aztec sandstone in the Valley of Fire were formed by a hierarchical process of shearing along preexisting joint zones. For sheared-joint based faults, the initial shearing of planar joints is followed by the creation zones of fragmented rock at joint stopovers and bends and newly formed splays near the ends of preexisting joints (Myers, 1999; Davatzes and Aydin, in review; Flodin and Aydin, in review-b). With increasing shear strain, this process is repeated in a progressive manner as fragmented rock is further crushed to form isolated pockets of fault rock. Eventually, a through going slip surface develops and the discontinuous fault rock pockets coalesce to form a continuous seam along the fault.

Damage associated with shear-joint faults can be divided into an inner fault core and an outer fault damage zone (Caine et al., 1996; Aydin, 2000) (Figure 3.2). Fault zone elements in the fault core consist of sheared joints, deformation bands, fragmented rock, fault rock, and slip surfaces, while damage outside of the core is in the form of splay fractures and sheared splay fractures (Myers and Aydin, in review). Because this study focuses on the flow properties at the scale of 2.5 cm diameter core plugs, the individual hydrodynamic behavior of structural elements that are smaller than our measurement scale (i.e., joints,
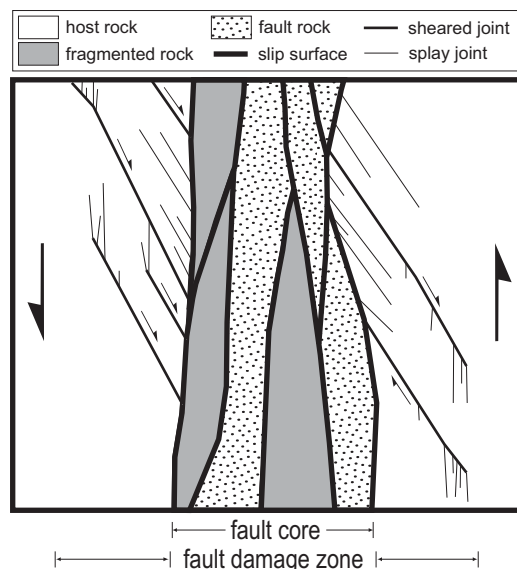
Figure 3.2. (a) Schematic drawing of a sheared-joint based fault zone in sandstone. Arrows indicate slip sense along sheared structures. Map view.

69

sheared joints, deformation bands, and slip surfaces) are not considered here. The characteristics of these discrete structural elements in relation to joint-based faults in sandstone are described by Myers (1999), Taylor (1999), and Aydin (2000). We focus on the two elements that volumetrically comprise most of the fault core, fragmented rock and fault rock, as well as the host rock from which these elements were derived. Our results are therefore relevant to lateral fault sealing and flow as opposed to along fault fluid transport.

In the field, the fault core is defined as a zone of fault rock and intensely fragmented pockets of host rock that is both divided up and bound by slip surfaces along which the majority of the slip has occurred (Figure 3.3). Fault core widths range from centimeters to meters, while damage zone widths range from meters to tens of meters (Myers, 1999). At the scale of fault slip magnitudes at our sample localities (25 to 160 m), the damage zone is more or less symmetrically distributed with respect to the centrally located fault core. Fragmented rock is host rock divided by a network of fractures (joints and small faults) into blocks or clasts of various size. These pieces of host rock are typified by the preservation of recognizable sedimentary cross-bedding. In some cases, fragmented rock is adjacent to but separated from the main body of host rock by sheared joints and slip surfaces, while in other cases the fragmented rock is completely isolated from the main host rock body by fault rock (Figure 3.3). Fragmented rock bodies range in size from centimeters to meters, and are almost always internally deformed by joints, sheared joints, and deformation bands. Brecciated rock is a kind of fragmented rock with strongly angular clasts that are generally detached from the host rock. In contrast to fragmented and brecciated rock, fault rock visually lacks recognizable sedimentary features. In outcrop, fault zone rock is very fine grained (as determined with a hand lens) and is often colored differently than the host rock (usually lighter or white). Slip surfaces bound and sometimes cut across individual bodies of fault rock. The slip surfaces are planar in map view and are commonly identifiable by millimeter-wide seams of what appears to be red alteration staining. Slip surface faces are usually smooth to the touch, and in many instances, display preserved kinematic indicators (i.e., slickensides and grooves).

Differences between fragmented and fault rock samples representing various strain levels are apparent at the microscopic scale of observation (Figure 3.4). The sample shown in

70
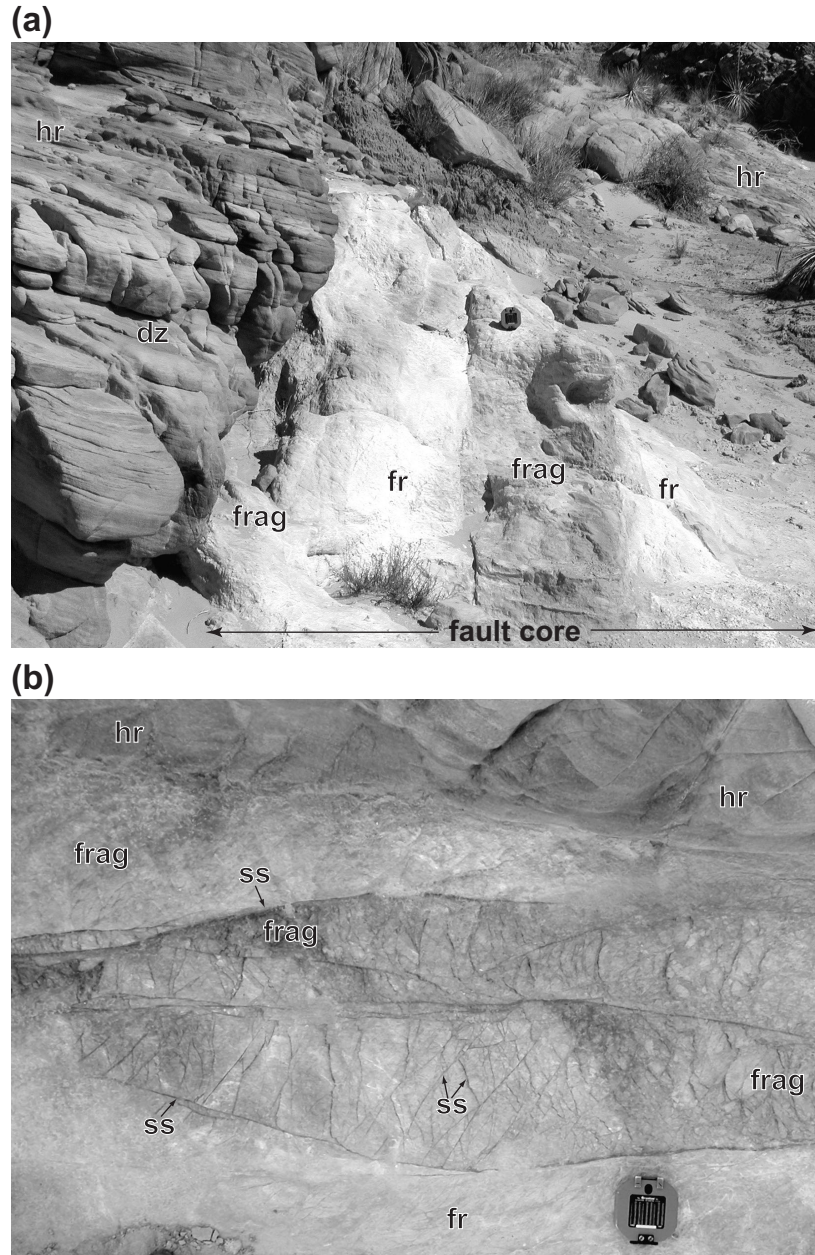
Figure 3.3. (a) Oblique cross-sectional view of a sheared-joint based fault in Aztec sandstone. 25 m of left-lateral slip has occurred across the width of the fault zone. View north. **(b)** Detail map view of a fault core. dz = damage zone; fr = fault rock; frag = fragmented rock; hr = host rock; ss = slip surfaces. Brunton compass for scale in both photographs.

Figure 3.4a was collected from a fairly large and intact body of fragmented rock sandwiched between two bodies of fault rock. Many of the grains in this sample are fractured. However, they preserve their original shape and nearly all of the primary porosity remains open. Elsewhere in this sample, we observed regions of nearly undeformed host rock, as well as zones of localized deformation. Host rock samples collected in the vicinity of a slip surface (Figure 3.4b) typically show grain fracturing similar to the previous sample. However, in places the primary porosity is filled with secondary pore filling cement. An example of a higher level of strain in fragmented rock is shown in Figure 3.4c. Here, many of the grains are almost completely fragmented and much of the primary porosity has collapsed or is filled by smaller angular clasts; only a few grains remain undamaged.

Fault rocks are the most strained samples we examined (Figure 3.4d); these samples show a severe reduction in grain size and primary porosity. Thin sections of fault rocks exhibit areas that possess varying degrees of grain size reduction and porosity loss, which we interpret as evidence for varying strains. Based on the greatest reduction in grain size, the region to the left of the slip surfaces (Figure 3.4d) appears to have accommodated the most strain. Here, pore space (black) is nearly absent, and the broken grains are generally equant in shape and lack a preferred orientation. To the right of the slip surfaces larger pores are evident, and individual grains are slightly more elongate in shape and show weak alignment. Most of the grains shown in Figures 3.4a to 3.4c do not appear to have undergone significant grain rotation and/or translation, because original grain roundness and outlines of relic grain coating cements (viewed elsewhere in these samples) are preserved. In contrast, the grains in the fault rock sample (Figure 3.4d) are angular, and show evidence for translation in the form of dislocated cleavage in feldspars, and spalling of edges on quartz grains. Grain rotation within the fault rocks must surely occur (e.g., Engelder, 1974), but evidence for it was not detected due to the fragmentation of the original grains and the lack of appropriate offset markers.

Sample stations with different average shear strain

Twelve host rock, eight fragmented rock, and twenty fault rock samples of Aztec sandstone in the Valley of Fire were collected in the vicinity of three different sample localities along
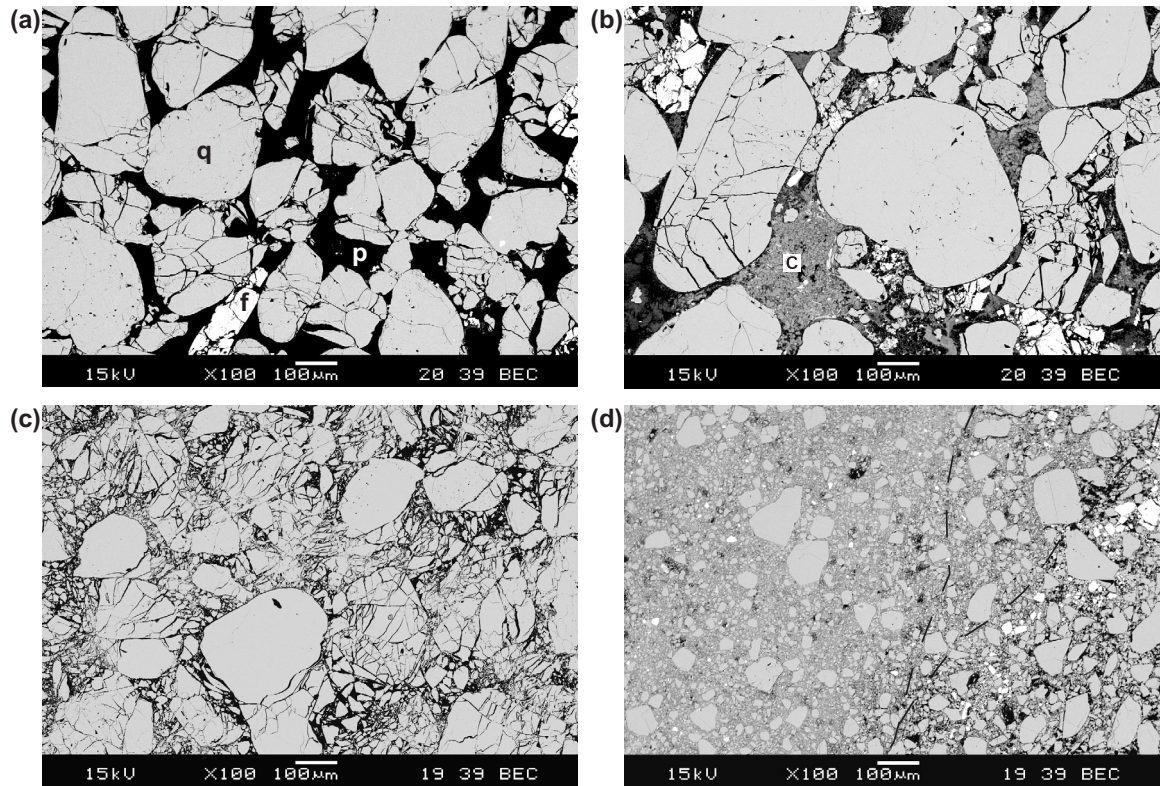
Figure 3.4. Compositional backscattered electron (BEC) images of variously deformed Aztec sandstone. White minerals are potassium-feldspar, light-gray minerals are quartz, dark-gray minerals are clays, and black is pore space. **(a)** Host rock fragment showing earliest signs of grain-scale fragmentation (sample 30). Nearly every grain shows varying degrees of fracturing, however the primary pore space is preserved. f = potassium-feldspar; p = pore space; q = quartz. **(b)** Host rock collected adjacent to the fault core (sample 36). Note that many of the grains are fractured and that much of the pore space is occupied by clay minerals. c = clay. **(c)** Host rock collected adjacent to the fault core showing signs of severe grain-scale fragmentation, collapse of pores, and loss of primary porosity (sample 22). **(d)** Well-developed fault rock characterized by severe grain size reduction and a complete loss of primary porosity (sample 49). Dashed lines are approximate locations of slip surfaces. Note the variability with respect to pore space (black) between the left and right sides of the image.

seismic-scale faults (Figure 3.1c). Sample stations 1 and 2 are at two different locations along the same fault, while station 3 is located on the next major fault to the east (Figure 3.1). Total fault slip was estimated to be 25 m for both locations 1 and 2, and 160 m for location 3. Fault core thicknesses for stations 1, 2, and 3 range between 40-70 cm, 160-175 cm, and 210-240 cm, respectively (Figure 3.5). Cumulative fault rock thicknesses

[(fault core thickness) – (fragmented rock thickness)] across these same zones ranged between 30-50 cm, 80-100 cm, and 185-215, respectively. We calculated the average shear strain (γ) accommodated across the fault core by dividing the estimated fault slip magnitude by the average fault rock thickness. Using this relationship, we obtained average shear strains of 63, 28, and 80 for stations 1, 2, and 3, respectively.

Sample collection methods

Samples of seismic-scale faults are rarely recovered from subsurface drill core. Therefore, exhumed large-offset faults now exposed in surface outcrops provide an opportunity to study petrophysical and geometrical characteristics of fault zones. We have chosen a field area with an arid desert climate and a general lack of vegetation to minimize effects due to surficial weathering processes. A series of samples was collected from three sites, with efforts made to transect systematically from undeformed host rock through the damage zone and fault core. Host rock samples were collected at different distances from the main fault in an attempt to detect fault-related damage of host rock away from the fault. Distances listed for the host rock in Table 3.1 (labeled *Type*) are made with reference to the nearest fault core and associated bounding slip surface. A few host rock samples were collected immediately adjacent to the fault core. Care was taken in choosing samples that were least affected by very-near surface weathering processes. Approximately 10 cm of surface material was removed from each sample area prior to collection (e.g., Dinwiddie et al., 1999). In most cases, hand samples were carefully chiseled from the outcrop. However, due to the difficulty of collecting small samples of sometimes nearly cohesionless fault rock, some samples as large as 6000 cm^3 were collected. Core plugs approximately 2.5 cm in diameter and 5 cm in length were extracted from the central parts of the samples in a laboratory under dry conditions. For host and fragmented rock samples, plugs were cut both perpendicular and parallel to bedding. For fault rock samples, two orientations were considered. Eleven plugs were oriented perpendicular to the primary slip surface, while nine plugs were oriented parallel to both the fault slip vector and the primary slip surface.

74
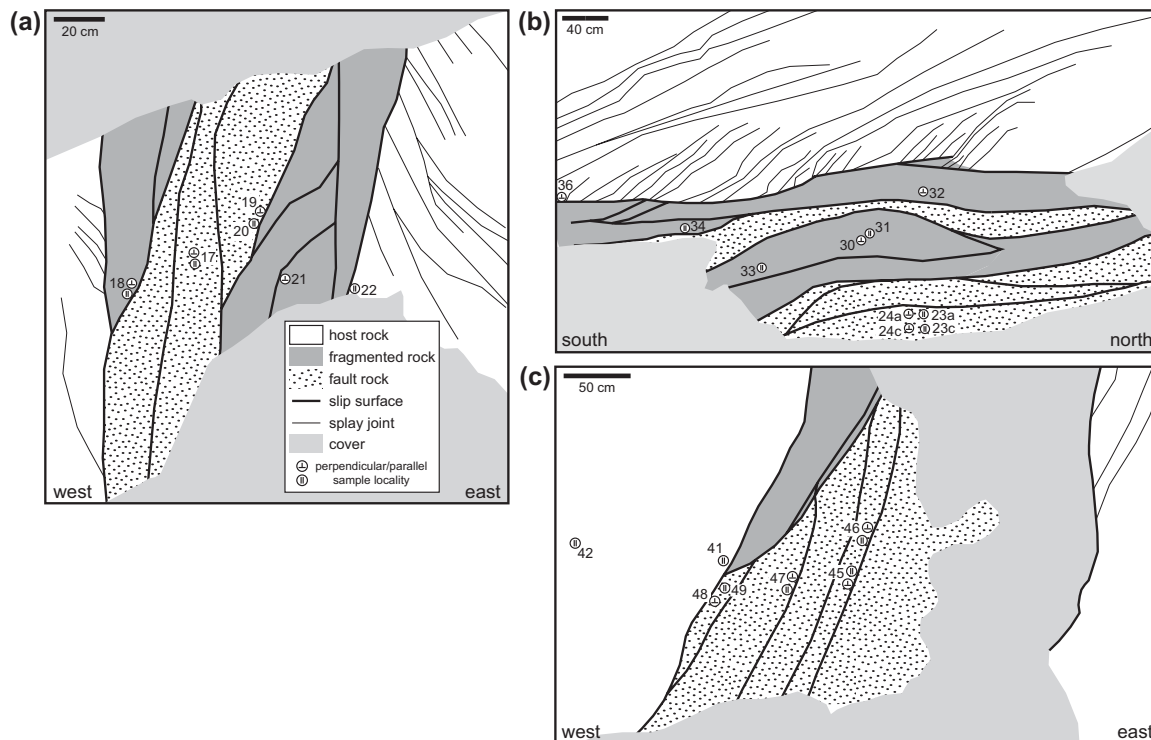
Figure 3.5. Fault zone maps for each sample station locality. Note that some samples were collected outside of the areas shown in the maps. **(a)** Station 1 (cross-section view north). **(b)** Station 2 (oblique map view west). **(c)** Station 3 (cross-section view north).

Mineralogy

Bulk mineralogy of host and fault rock samples was identified using an X-ray diffractometer (XRD) (Table 3.1). Thirteen samples were chosen from stations 1 and 3 in order to assess bulk mineralogical changes between undeformed and deformed rock. Station 3 shows slightly larger quartz abundance than station 1 samples, and consistently more clay in the host rock than in the fault rock. These differences are negligible relative to overall host rock variability and likely indicate no bulk mineralogical change during the transformation of host rock to fault rock (Figure 3.6). However, some samples suggest a trend for slightly elevated clay abundance in the host rock with approaching distance to the fault core (discussed below).

The bulk mineralogy of both host and fault rock samples consists of an average of 94% quartz, with a small range of distribution from 88 to 97%. The next most abundant mineral phase is potassium-feldspar, which comprises about 3% of both host and fault rock. Authigenic clays also make up about 3% of both host and fault rock. Trace amounts of dolomite (< 1%), ferroan dolomite or ankerite were detected in nearly all samples.

Table 3.1. Summary of petrophysical data. hr = host rock (distance collected from fault core); hr-a = host rock adjacent to the fault core; frag = fragmented and damaged host rock; fr = fault rock; fr-s = fault rock with slip surface.

Sample ID	Direction	Station	Type	Air-Permeability (md)	Porosity (%)	Hg-air Threshold Pressure (psia) 7.5%	Hg-air Threshold Pressure (psia) 10%	Grain Size Median (μm)	Grain Size Sorting (Folk)	XRD Quartz	XRD Dolomite	XRD K-spar	XRD Total Clay
12	para	1	hr (1m)	166.	19.2								
13	para	1	hr (1m)	2099.	17.4								
14	para	1	hr (10m)	1173.	16.7								
55	perp	1	hr (25m)	123.	22.7								
56	perp	1	hr (50m)	2620.	22.0	11	11						
62	perp	1	hr (50m)	5991.	23.5	7	7	332.	1.66	92.6%	-	1.2%	6.1%
22	para	1	hr-a	82.1	24.4			139.	1.85	91.9%	0.5%	4.5%	3.0%
18	para	1	frag	23.6	22.4					96.5%	0.4%	2.7%	-
18	para	1	frag	90.7	22.2	36	41			96.8%	0.3%	1.4%	1.5%
19	perp	1	fr-s	0.353	13.3	496	544			91.6%	0.4%	2.6%	5.4%
20	para	1	fr-s	921.	14.3								
78	perp	1	fr	3.07	16.4	77	89	3.5	1.76	92.9%	0.3%	1.4%	5.5%
21	perp	1	fr	4.17	15.7					96.1%	-	1.4%	2.5%
17	para	1	fr	36.1	19.4					95.8%	-	1.2%	3.0%
39	perp	2	hr (4m)	166.	19.7			170.	1.61				
36	perp	2	hr-a	1.19	18.4			48.	2.98				
30	perp	2	frag	1406.	24.5			135.	2.13				
31	para	2	frag	194.	25.8								
33	para	2	frag	792.	27.5								
32	perp	2	frag	133.	23.3								
34	para	2	frag	93.7	23.1								
79	perp	2	frag	273.	22.5								
80	perp	2	fr	21.5	21.0			4.0	1.73				
23a	para	2	fr	38.6	22.7			50.	2.81				
23c	para	2	fr	12.0	22.7			51.	2.95				
24a	perp	2	fr	2.88	21.4								
24c	perp	2	fr	21.1	21.7								
42	para	3	hr (1m)	135.	18.0			160.	2.46	91.5%	0.7%	4.7%	3.1%
44	para	3	hr (10m)	264.	20.1			168.	2.38				
41	para	3	hr-a	29.4	16.6			127.	2.59				
48	perp	3	fr-s	4.21	17.5	13	17	3.6	1.74	87.6%	-	5.3%	7.1%
49	para	3	fr-s	2.31	17.5								
81	perp	3	fr	0.293	16.2	392	466			94.2%	0.8%	5.1%	1.7%
45	para	3	fr	8.73	19.7								
45	perp	3	fr	5.28	17.5			6.0	1.81	92.6%	0.7%	5.0%	-
46	para	3	fr	4.66	18.8			3.6	1.77				
46	perp	3	fr	3.32	19.4			3.1	1.78				
47	para	3	fr	0.284	15.7	97	113		1.65				
47	perp	3	fr	0.501	17.5	275	327	3.5	1.72	92.7%	0.7%	4.9%	1.6%

Individual mineral grains were identified using a scanning electron microscopy (SEM) equipped with an energy dispersive spectrometer (EDS). Detrital grains in the host rock consist almost entirely of quartz with minor amounts of potassium-feldspar and trace occurrences of igneous accessory minerals, such as zircon, apatite, and monazite. In host and fault rock, nearly all potassium-feldspar grains show signs of replacement by authigenic kaolinite, and minor illite. Host rock cements, where present, include both iron-oxide and clay minerals that generally occur at grain-grain contacts and as grain coatings. These cements volumetrically comprise less the 1% of the total rock volume. Based on rock color and lack of magnetic properties in hand sample, the most abundant iron-oxide cement appears to be hematite with lesser amounts of goethite and limonite (Taylor, 1999). The majority of the clay cements appear to be kaolinite. Kaolinite is sometimes found also as a pore filling phase not associated with potassium-feldspar. For host rock away from fault zones, the occurrence of pore filling kaolinite is generally limited to the stratigraphically lowest parts of the Aztec sandstone (Flodin et al., in press). However, elevated levels of pore filling kaolinite occur in a few host rock samples that were collected adjacent to the fault core and the bounding slip surface (samples 36, 41, and 44) (Figure 3.4b). The majority of the fault
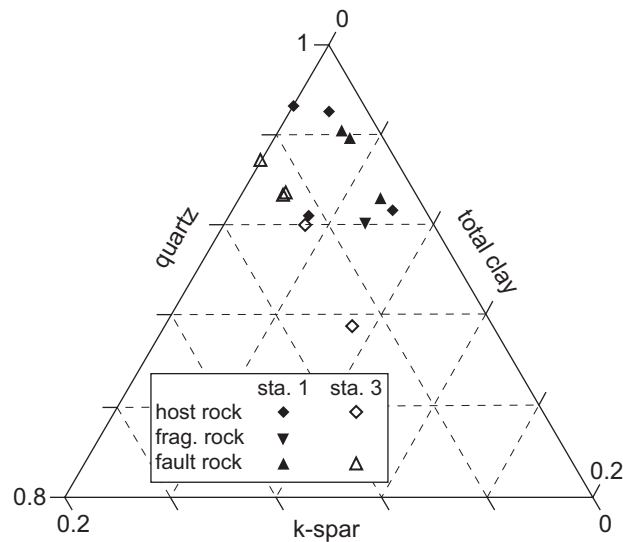
Figure 3.6. Quartz – total-clay – potassium-feldspar ternary plot of whole-rock x-ray diffraction (XRD) data collected from select samples of host rock, fragmented rock, and fault rock. Note that the ternary diagram displays a limited scale range of 20% for each phase.

rock samples are nearly uncemented. Exceptions to this observation include the occurrence of iron-oxide and clays minerals localized within a reddish seam along individual slip surfaces, and minor occurrences of silica-cemented zones within the fault core (Myers, 1999). We note that the clay and iron-oxide cements localized along slip surfaces are volumetrically minor and were difficult to detect with the SEM-EDS due to the overwhelming signal from detrital quartz.

Petrophysical characteristics

Porosity and permeability

Porosity was measured with a helium porosimeter. Permeability was measured in a steady-state Hassler-sleeve air permeameter under a confining pressure of 2.8 MPa, and is presented uncorrected for Klinkenberg gas slippage effects. Gas slippage effects become relevant at low flow velocities (low permeability) and tend to produce over-estimated sample permeabilities (Goggin et al., 1988). This effect is most pronounced for samples with less than 1 md permeability, though the overestimation is generally less than a factor of two.

Porosity and permeability data organized by sample genesis are presented in Figure 3.7 and Table 3.1. In each sample suite, excluding those collected immediately adjacent to the fault core, samples were oriented both perpendicular and parallel to either host rock bedding or the fault rock slip direction.

Measured host rock porosity values range between 16.6 and 24.4%. Three host rock samples (41, 42, and 44) collected along the same sedimentary bed at distances of 10 m, 1 m, and 1 cm from the fault core show a trend for decreasing porosity with proximity to the fault. Porosity values for the fragmented rock samples were the highest detected in this study, ranging from 22.2 to 27.5%. Fault rock porosity values were the lowest measured, ranging between 13.3 and 22.7%. Although fault rock porosities include the lowest values measured, there is considerable overlap in fault rock and host rock values (Figure 3.7).

Permeability data for pristine host rock samples range over two orders of magnitude, from 123 to 5991 md. Given the relatively small number (11) of host rock samples the true range could be even greater. Host rock permeability variations ranging over five orders of

78
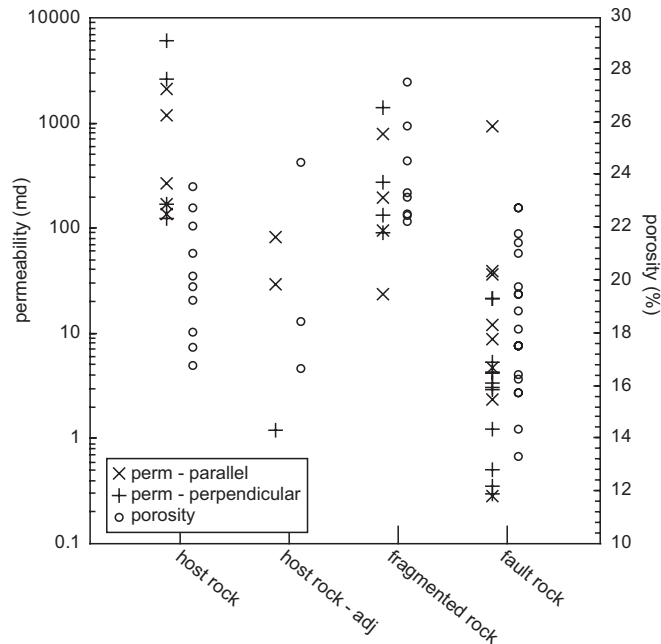
Figure 3.7. Summary plot by sample type for all porosity and air-permeability data.

magnitude have been documented in other aeolian sandstones (Chandler et al., 1989). Reduced permeabilities ranging between 1.2 and 82 md were detected for the three host rock samples collected immediately adjacent to the fault core. Fragmented rock samples show permeabilities that range between 93.7 and 1406 md. Permeability data for the fault rock samples range over two orders of magnitude with lower and upper limits of 0.28 and 38.6 md, respectively. The single outlier fault rock sample that yielded a permeability of 921 md is excluded from this range (see discussion). No significant permeability anisotropy was detected in any of the sample suites based on the examination of differently oriented sample plugs (Figure 3.7).

Porosity and permeability versus confining pressure

In order to investigate the impact of burial depth on porosity and permeability of host and fault rock, we selected a subset of six samples from station 3 for porosity and permeability analysis at stepwise increasing hydrostatic confining pressure (Figure 3.8). The data were collected from 6 MPa up to a maximum confining pressure of 60 MPa, which corresponds to approximately 3 km burial depth. Absolute porosity reductions between initial and final confining pressures range between 1.7 and 3.2%, with the majority of porosity reduction occurring over the first 20 MPa of pressure increase. Ratios between initial and final porosity values range from 0.83 to 0.9. Flodin et al. (in press) found similar porosity reductions

over the same pressure range in a more regional study of Aztec sandstone host rock proper-ties. In addition, that study found negligible hysteresis of porosity when the samples were returned to atmospheric confining conditions. This suggests that porosity reduction was an elastic process for these samples over the range of applied confining pressures. Similar to the porosity data, permeability values show their most significant reduction over the first 20 MPa of applied confining pressure. Ratios between initial and final permeability values range from 0.2 to 0.76, and have a median of 0.67.

Grain size analysis

Grain size distributions were obtained by laser particle size analysis (LPSA) for a subset of samples from each station. The analyses were made using a Coulter™ LS230 Series ana-lyzer, which has lower and upper detection limits of 0.04 and 2000 μm, respectively. The reader is referred to Crawford (1998) for a thorough description of LPSA techniques. Sammis et al. (1987) warn of introducing a small grain size fraction that is not present in the original sample due to grain comminution during the sometimes-forceful disaggregation process. However, because the samples in this study are nearly uncemented, we were able to disag-gregate them with little effort.
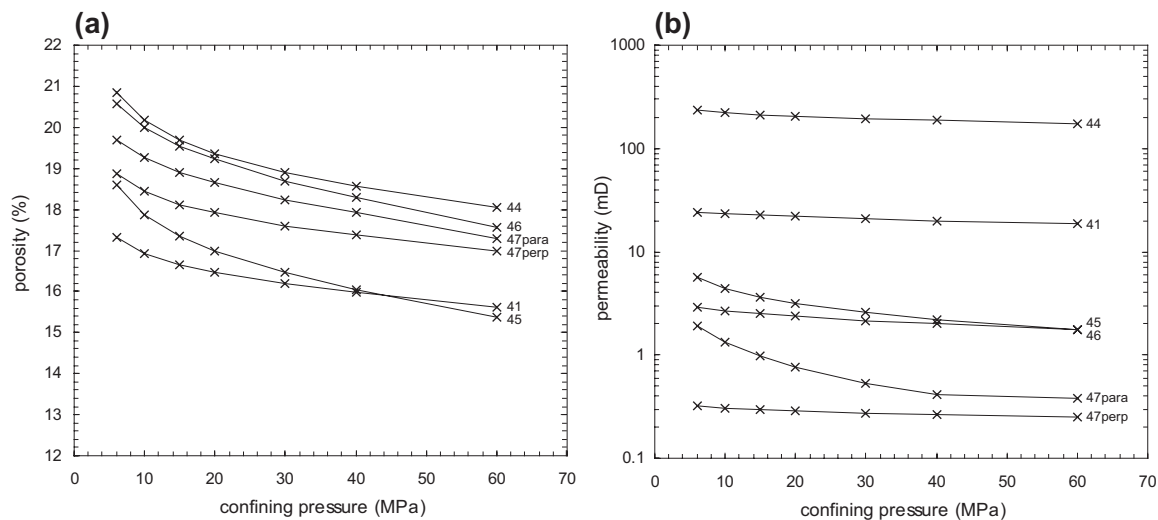
Figure 3.8. (a) Porosity and **(b)** air-permeability versus hydrostatic confining pressure up to a maximum confining pressure of 60 MPa.

Plots, organized by station number, of frequency versus measured grain diameter are shown in Figure 3.9. The raw data used in these plots are also listed in Table 3.2. Most host rock samples have bimodal distributions and all are strongly fine skewed. Fault rock samples are weakly bimodal and are also skewed toward the fine grain fraction. Measured grain sizes range between 0.06 and 840 μm. At least one example from each of the sample suites possesses this full range of grain sizes (e.g., host, fragmented, and fault rock samples 36, 30, and 24c, respectively). However, in most cases fault rock grain sizes span a much narrower range, between 0.06 and 20 μm, with respect to host rock samples. Calculated sorting statistics (Folk, 1968) for host rocks range between 1.61 and 2.98, which corresponds to poorly sorted and very poorly sorted designations. For fault rocks, sorting ranges between 1.72 and 2.95, with a median value of 1.77. Median grain sizes for host rock samples range between 160 and 332 μm, while fault rock median values range between 3 and 51 μm (Table 3.1). Host rock samples adjacent to the faults possess lower median grain sizes (48-139 μm) than host rock samples collected away from the faults. Three host rock samples (41, 42, 44) from station 3 show a trend for smaller median values and decreased sorting with proximity to the fault core (Table 3.1 and Figure 3.9c). In terms of median grain size and sorting, one of the fragmented rock samples (18) has more affinity with fault rocks, while the other fragmented rock sample (30) is more similar to host rocks.

Capillary pressure

Capillary pressure data were collected by conventional high-pressure mercury-injection porosimetry on plug samples using Micromeritics™ Auto Pore III 9420 instrumentation. Epoxy-sheathed, oriented mercury-injection experiments (Schneider et al., 1997) were not performed, because we had not detected any significant anisotropy in our permeability data. The term entry pressure is used below to identify the pressure at which the mercury accesses the largest pore radius size (Pittman, 1992), and is signified by the first slope break in the mercury-air capillary pressure curve at low capillary pressure. The term breakthrough pressure is used to identify the lowest pressure at which a throughgoing fluid pathway forms through the sample. In this study, the breakthrough pressure is estimated at 7.5 to 10% of the cumulative percent of mercury intruded, and will be used to estimate seal capacity in a later section.
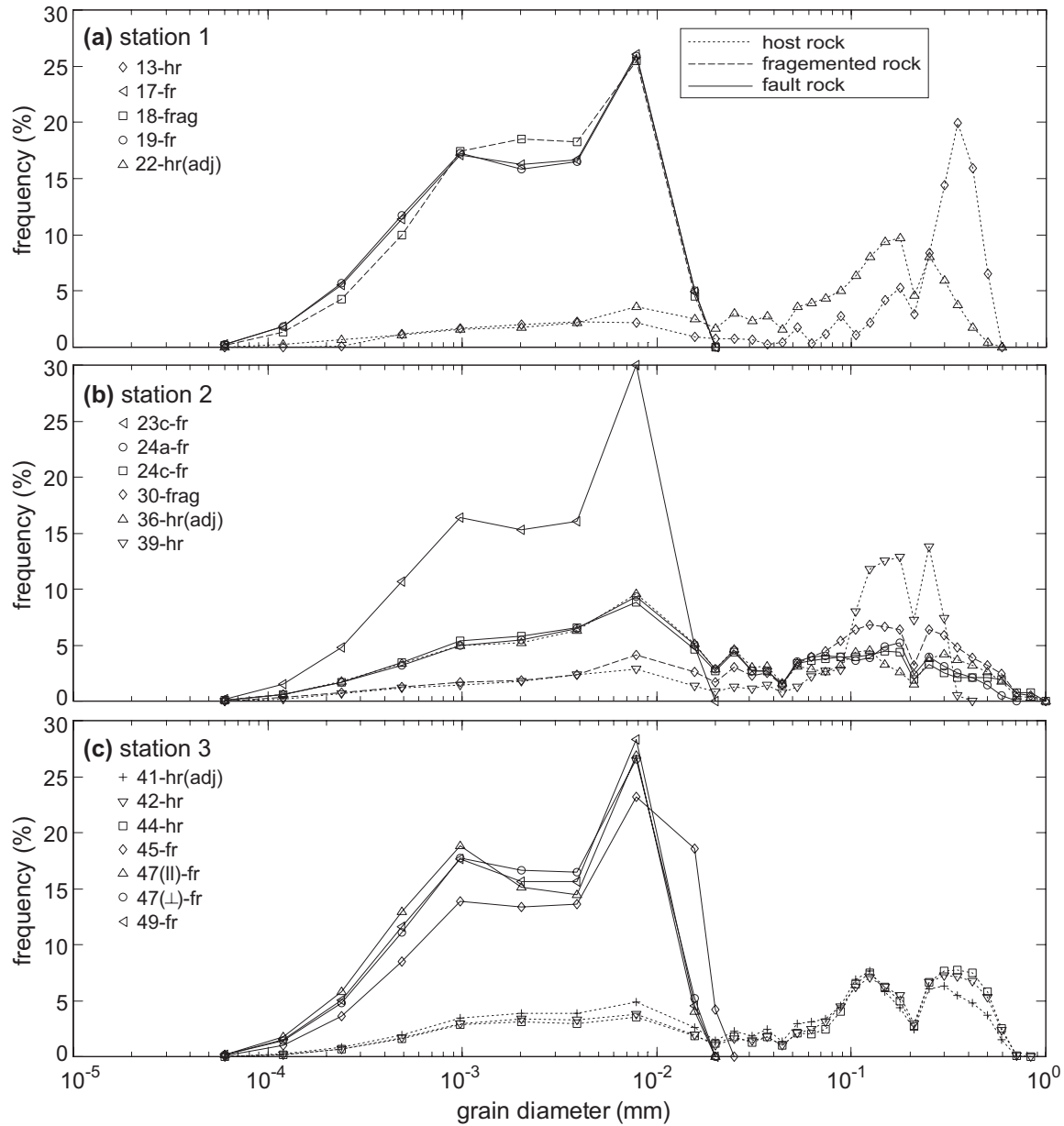
Figure 3.9. Grain size distribution plots for select samples of host rock, fragmented rock, and fault rock, from station 1 **(a)**, station 2 **(b)**, and station 3 **(c)**.

Figure 3.10 shows the mercury-air capillary pressure as a function of cumulative percent intruded mercury up to a maximum applied pressure of 60,000 psi. The curves for the host rock are the most complex, and are different from each other and from the curves representing the deformed samples. Fault rock sample curves possess similar forms and show the highest initial entry pressures. These curves are characterized by a sharp increase in mercury-air capillary pressure followed by a shallow, but steady pressure increase. The

Table 3.2. Grain size distribution data collected using laser particle size analysis (LPSA).

diameter (mm)	weight percent station 1					station 2						station 3						
	13	17	18	19	22	23c	24a	24c	30	36	39	41	42	44	45	47-1	47-2	49
0.84	-	-	-	-	-	-	-	0.77	0.47	0.30	-	-	-	-	-	-	-	-
0.71	-	-	-	-	-	-	-	0.79	0.68	0.41	-	-	0.11	0.09	-	-	-	-
0.59	-	-	-	-	-	-	0.49	1.91	2.41	1.73	-	1.48	2.35	2.51	-	-	-	-
0.50	6.52	-	-	-	0.40	-	1.42	2.08	3.18	2.63	-	3.69	5.27	5.82	-	-	-	-
0.42	15.95	-	-	-	1.75	-	2.10	2.13	3.86	3.16	-	4.80	6.74	7.44	-	-	-	-
0.35	19.92	-	-	-	3.74	-	2.51	2.14	4.81	3.71	0.53	5.48	7.17	7.77	-	-	-	-
0.30	14.40	-	-	-	5.97	-	3.07	2.55	5.87	4.16	7.39	6.30	7.26	7.64	-	-	-	-
0.25	8.37	-	-	-	8.08	-	3.94	3.24	6.38	3.76	13.79	6.01	6.65	6.62	-	-	-	-
0.21	2.91	-	-	-	4.61	-	2.38	1.95	3.19	1.50	7.23	2.46	2.92	2.73	-	-	-	-
0.18	5.28	-	-	-	9.68	-	5.22	4.41	6.36	2.57	12.84	4.39	5.47	5.00	-	-	-	-
0.15	4.17	-	-	-	9.38	-	4.85	4.49	6.61	3.30	12.48	5.78	6.20	6.19	-	-	-	-
0.13	2.22	-	-	-	8.07	-	3.84	4.10	6.80	4.57	11.75	7.64	7.04	7.50	-	-	-	-
0.11	1.13	-	-	-	6.37	-	3.58	3.94	6.35	4.41	8.02	6.86	6.25	6.43	-	-	-	-
0.088	2.75	-	-	-	5.04	-	3.93	3.92	5.35	3.19	2.76	4.57	4.43	4.00	-	-	-	-
0.074	1.17	-	-	-	4.33	-	4.04	3.74	4.48	2.62	2.69	3.37	3.08	2.41	-	-	-	-
0.063	0.37	-	-	-	3.96	-	3.94	3.59	3.92	2.87	2.21	3.12	2.40	2.01	-	-	-	-
0.053	1.79	-	-	-	3.59	-	3.55	3.33	3.34	3.09	1.27	2.96	2.07	2.11	-	-	-	-
0.044	0.44	-	-	-	1.60	-	1.52	1.48	1.45	1.56	0.79	1.38	0.97	1.05	-	-	-	-
0.037	0.22	-	-	-	2.78	-	2.67	2.71	2.55	3.08	1.40	2.42	1.76	1.76	-	-	-	-
0.031	0.66	-	-	-	2.36	-	2.73	2.73	2.29	3.05	1.12	1.89	1.39	1.28	-	-	-	-
0.025	0.76	-	-	-	3.03	-	4.54	4.35	3.04	4.59	1.22	2.25	1.60	1.75	-	-	-	-
0.020	0.75	-	-	-	1.65	-	2.89	2.69	1.64	2.87	0.83	1.39	1.00	1.16	4.16	-	-	-
0.016	0.90	4.91	4.56	4.99	2.52	4.86	5.01	4.61	2.60	5.11	1.31	2.59	1.92	1.82	18.60	4.04	5.17	4.50
0.0078	2.21	26.05	25.49	25.92	3.61	30.27	9.34	8.86	4.13	9.56	2.85	4.91	3.78	3.49	23.23	26.91	26.53	28.30
0.0039	2.26	16.67	18.26	16.49	2.14	16.02	6.46	6.55	2.37	6.30	2.35	3.87	3.28	2.98	13.58	14.48	16.44	15.60
0.0020	1.99	16.27	18.53	15.81	1.74	15.27	5.46	5.79	1.82	5.21	1.76	3.86	3.34	3.12	13.32	15.12	16.61	15.59
0.00098	1.65	17.10	17.47	17.25	1.58	16.40	4.98	5.35	1.68	4.92	1.44	3.47	2.96	2.83	13.84	18.82	17.75	17.67
0.00049	1.16	11.36	9.96	11.77	1.11	10.67	3.22	3.42	1.26	3.33	1.17	1.95	1.65	1.59	8.50	12.93	11.11	11.56
0.00024	0.05	5.53	4.25	5.67	0.63	4.83	1.65	1.71	0.76	1.74	0.66	0.82	0.70	0.67	3.60	5.77	4.79	5.08
0.00012	0.00	1.88	1.32	1.87	0.25	1.51	0.59	0.59	0.31	0.62	0.14	0.26	0.21	0.21	1.05	1.74	1.44	1.53
0.00006	0.00	0.23	0.16	0.23	0.03	0.17	0.08	0.08	0.04	0.08	0.00	0.03	0.03	0.02	0.12	0.19	0.16	0.17

fragmented rock sample shows a somewhat lower entry pressure followed by two slope changes around 10 and 30% intruded mercury. Host rock samples display the lowest entry pressures. Following the initial slope break, fault-adjacent host rock sample 41 shows an additional slope break around 20% intruded mercury, and a gradual steepening of the slope after that point. Curves for the two undamaged host rocks have shallow slopes for the first 60% intruded mercury. Beyond this point, the curves record sharply increasing pressures and two slope breaks for each sample between 65 and 90% intruded mercury.

Discussion

Porosity and Permeability

In order to assess relative changes in porosity and permeability between host and deformed rock, we normalize fault-adjacent host, fragmented, and fault rock porosity and permeability data using expanded median host rock data [ϕ_{median} = 22.4; k_{median} = 626 md (calculated using porosity and permeability data from an additional 20 host rock samples from Flodin et al., in press)] (Figure 3.11). The single outlier fault rock sample (20), with a measured
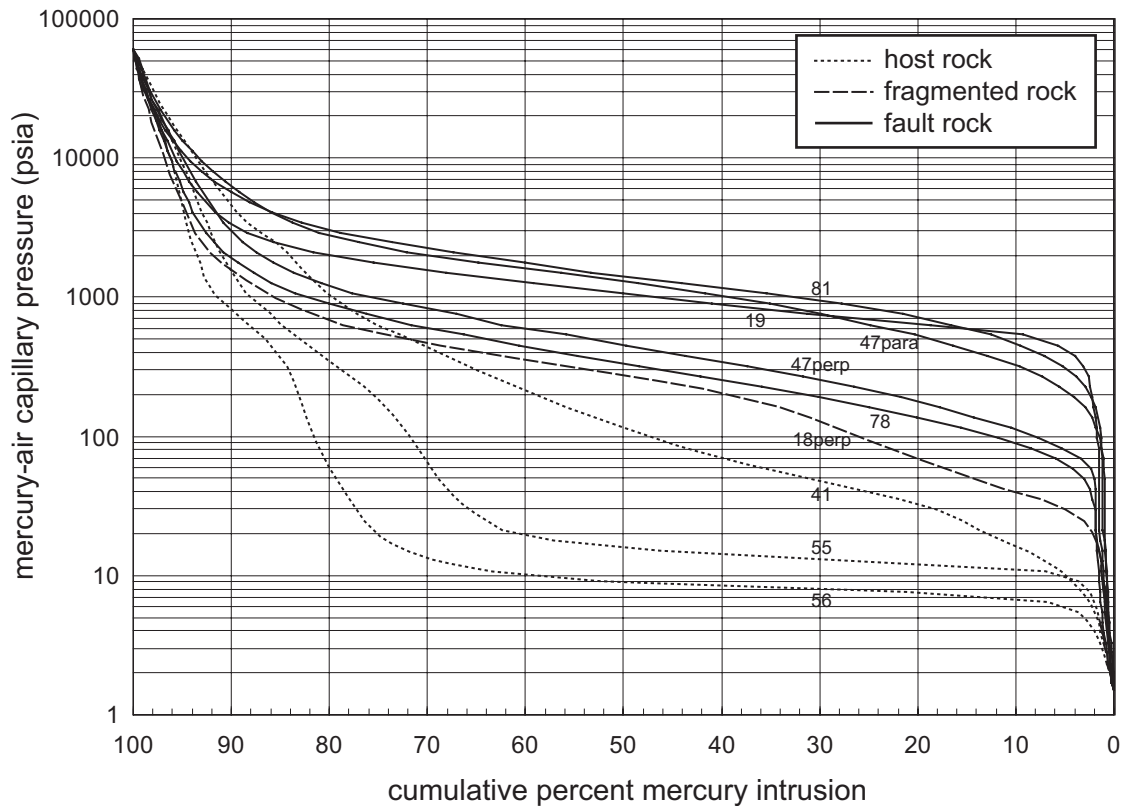
Figure 3.10. Capillary pressure versus cumulative percent intrusion for select samples of host rock (dotted line), fragmented rock (dashed line), and fault rock (solid line). Sample numbers are also shown.

permeability of 921 md, is not included in Figure 3.11. This sample contains a through-going slip surface that is parallel to the plug axis. The very high measured permeability might reflect flow through the fracture-like slip surface and thus might not represent the permeability of the fault rock itself. Slip surfaces were identified in three other petrographi-cally similar samples (samples 19, 48, and 49). However, the slip surfaces in these samples were not throughgoing with respect to the long-axis of the permeability test direction and thus likely did not contribute to flow through the plug.

Permeability reductions range from one to over three orders of magnitude. Given the great variability in host rock permeability, absolute permeability reductions between some host and fault rock could be as small as a factor of five and as large as four orders of magnitude. These orders of magnitude permeability reductions are comparable to reduc-tions found for cataclastic deformation bands formed in high-porosity, low clay-content sandstones. Using localized (1 cc) minipermeameter measurements, Antonellini and

Aydin (1994) found permeability reductions ranging from one to four orders of magnitude (average of three orders of magnitude) between deformation bands and adjacent host rock. Gibson (1998) reported similar ranges of reduction for deformation bands involving only cataclasis using permeability data collected from 1.9-2.5 cm core plugs. Antonellini and Aydin (1994) also found up to seven orders of magnitude permeability reduction for wall rocks adjacent to slip planes. With the exception of sample 20, the slip surfaces contained within the fault rock samples of this study appeared not to have a significant effect on the plug permeability. Fault rock samples 19, 48, and 49 have slip surfaces that crossed the sample plug transverse to the permeability measurement direction. Measured permeabilities for these samples (0.35-4.2 md) fall within the range of permeabilities for fault rocks that do not have slip surfaces.

One surprising result of this study is the relative lack of porosity reduction found in the fault rock samples. The largest absolute porosity reduction between fault rock and median host rock is 9.1%, which equates to a 1.7 factor of change. However, most fault rock porosities display changes much less than this factor. The lowest measured fault rock porosity is 13.3%. In contrast, Myers (1999) estimated fault rock porosities as low as 0.5% using image analysis techniques. Similarly, absolute porosity reductions obtained by image analysis
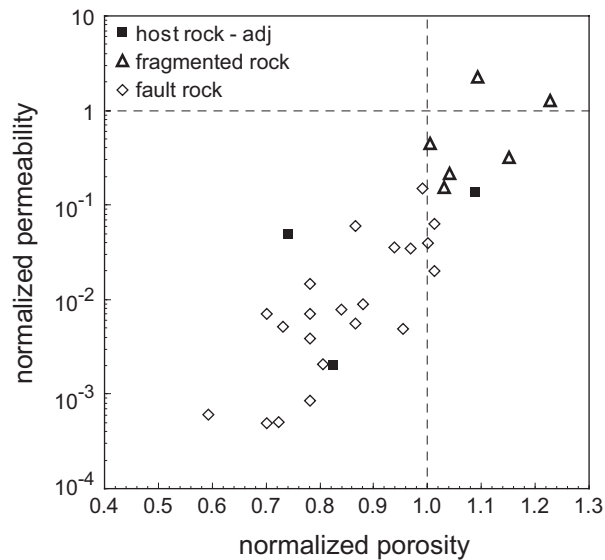
Figure 3.11. Plot showing relative change (increase or decrease) in permeability and porosity for fault rock and host rock collected adjacent to the fault core. See text for values used to normalize the permeability and porosity data.

for deformation band style faults have been reported to be as much as 20%, with relative changes approaching an order of magnitude (Antonellini and Aydin, 1994; Ogilvie and Glover, 2001). These discrepancies are likely due to optical resolution limitations inherent with image analysis techniques. Myers reported a lower optical detection limit of 20 μm. However, our particle size data show median fault rock grain sizes as small as 3 μm, indicating that the pore spaces between these grains are even smaller. Figure 3.12 is a high magnification (1600×) secondary electron image of a freshly broken surface of fault rock. Grains in this image are very angular and range between sub-micron and tens of microns in size, while the pore spaces between the grains range in size from sub-micron to microns.

Despite the relatively high fault rock porosities, permeabilities for these samples are considerably lower than host rock values. Based on a study of laboratory-deformed sandstone, Crawford (1998) concluded that the microporosity between the smallest grain sizes in deformed sandstones increased the tortuosity of the flow path and thus decreased the overall sample permeability. Myers (1999) similarly justifies the exclusion of microporosity and instead measured only the macroporosity (or "effective" porosity), because it is the parameter that most influences flow (Mavko and Nur, 1997).

Some samples appear to show an increase in porosity with respect to median host rock (Figure 3.11). A porosity increase might indicate that the sample in its original, undeformed state had a somewhat higher porosity than median host rock, and with the reduction during deformation, the measured porosity is still greater than the calculated median value. Alternatively, the samples might have dilated relative to their original undeformed state. Thin-section analysis of these samples shows local regions containing a high density of intragranular microfractures. A high fracture density is particularly characteristic of fragmented rock samples 30 (Figure 3.4a) and 33, which show increased permeability with respect to median host rock. In most cases, however, these samples also contain localized zones of damage in the form of sheared joints and deformation bands. The presence of localized damage within otherwise dilatant sample plugs appears to cause a net decrease in permeability (e.g., samples 22, 32, and 34).

A relationship between average shear strain and permeability was investigated by examining the distribution statistics of permeability data for each sample station (Figure 3.13).
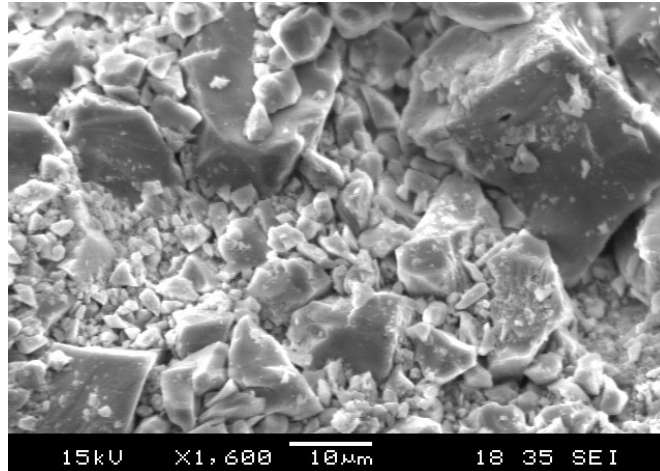
Figure 3.12. Secondary electron image (SEI) of freshly broken fault rock. Note the angular and somewhat equant nature of the fragmented quartz grains and the presence of microporosity.

A relationship between shear strain and permeability is of interest because it could be used for predictive models of fault zone properties for subsurface applications, where only fault slip data are available. However, for this transform to be effective, the slip data would need to be used in conjunction with a fault rock thickness transform (Evans, 1990) in order to estimate the shear strain of subsurface faults. Samples from the three stations show an over-all decrease in permeability with increasing shear strain. Median permeabilities are very similar between stations 1 and 3 (shear strains, γ = 63 and 80, respectively). However, station 3 samples are skewed toward lower values.

Grain size reduction

Grain size distribution data show a consistent trend for grain size reduction from host rock to fragmented rock to fault rock. There appears to be a lower limit of grain size reduction for fault rock samples that is irrespective of average shear strain. Figure 3.14 shows a plot of cumulative weight percent versus grain diameter for all data collected in this study. Seven of the ten analyzed fault rock samples occupy nearly the same area on the left side of this plot. At least one fault rock sample from each station locality plots within this region. These data indicate that the fault rocks reach a level of grain size maturity beyond which no new grains are fractured. Similar observations have been made of grain size reductions for other faulting mechanisms. In a field study of deformation band style faults, Shipton and
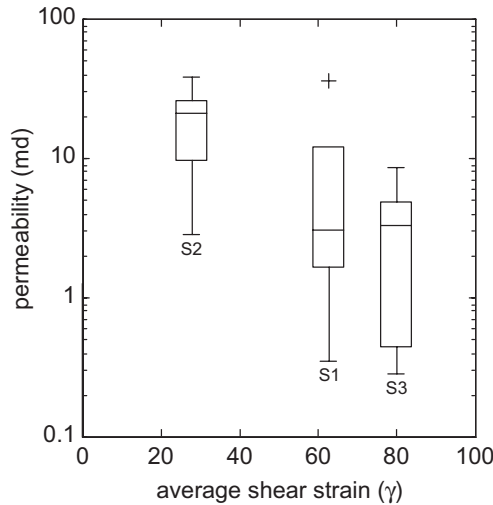
Figure 3.13. Boxplot statistics of fault rock permeability versus average shear strain. Each sample locality is indicated (e.g., S1 = station 1). The line at the center of the box is the sample median; box bottom and top are respectively the first and third quartiles; vertical lines span 1.5 times the interquartile range; a cross explicitly indicates outliers.

Cowie (2001) conclude that there is a maximum limit to grain crushing in the vicinity of a slip surfaces. Mair et al. (2000) similarly find lower limits to grain size reduction for deformation bands formed under controlled laboratory conditions. In a study of deformed crystalline rocks collected from faults related to the San Andreas system of southern California, Blenkinsop (1991) provides a conceptual model for grain size reduction processes that predicts a lower limit of grain size reduction.

It is likely that the lower limit of grain size reduction could be different for these faults had they formed under different confining conditions. Both Engelder (1974) and Marone and Scholz (1989) report a decrease in median grain size with increasing confining stress in deformation experiments of sandstone and unlithified quartz sand, respectively. Similarly, Crawford (1998) suggests that the varying grain size distributions between the deformed sandstones were caused by the different normal stresses under which the experiments were performed. However, the study concludes that the grain size variability could also be due to the fact that the samples had different total strains. Relationships between increasing confining pressure and decreasing lower grain size limits have also been reported in studies of naturally deformed crystalline rock (Sammis et al., 1986; Blenkinsop, 1991).
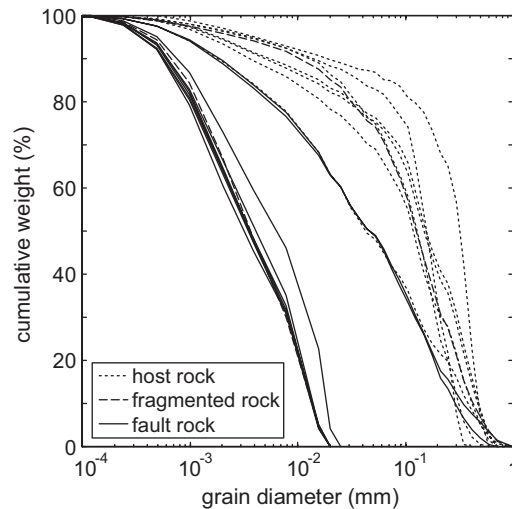
Figure 3.14. Conceptualization of all grain size distribution data shown in Figure 3.9.

Sorting

In general, sorting trends between the sample suites show a decrease in sorting from un-damaged host rock to damaged host and fragmented rock, and an increase in sorting from fragmented rock to fault rock (Table 3.1). Host rock samples 13 and 39 were among the best-sorted rocks examined in this study. However, based on petrographic analysis, these samples had weakly distributed intergranular microfractures. Disaggregation of the frac-tured grains in these samples appears to have increased the fine grain fraction, which led to the poor sorting characteristics. Thus, we envision that the grain size distributions for truly undamaged host rock would indicate even better sorting than the data presented in this study. Good sorting is a typical textural characteristic of aeolian sands (Pettijohn et al., 1972). Among the least sorted in this study are samples that show intense grain fragmenta-tion and only moderate reduction in median grain size. Samples that fall into this category include host rock (samples 22, 36, 41, 42, and 44), fragmented rock (sample 30), and fault rock (samples 24a and 24c). In contrast, samples that show significant median grain size reduction also possess better sorting characteristics relative to damaged host and fragmented rock. Most of the samples in this category are fault rocks that fall within a small range of sorting numbers (1.77 ±0.03). One of the samples in this category (18perp) is classified as fragmented rock. In hand sample, this sample has preserved sedimentary features and as such, is classified as fragmented rock. However, in thin-section, damage in this sample most resembled that of the fault rocks.

Sorting characteristics can be also be qualitatively inferred from the shape of the mercury injection curves. Vavra et al. (1992) argue that better sorting leads to samples with similar pore throat sizes. Uniform pore throat sizes in turn create broad, flat plateaus on the mercury-injection curves that indicate a large volume of mercury intrusion occurs over a very narrow pressure window. With decreased sorting, the plateaus become more steeply sloped (see sample 41 in Figure 3.10). In all samples, the volume of mercury intruded decreases as smaller pore throats are invaded with increasing pressure, resulting in the highest slopes as 100% cumulative mercury intrusion volume is approached. If there are two distinct plateaus on the mercury-injection curve, a bimodal distribution is implied. Grain size distributions inferred from the mercury-injection data (Figure 3.10) support our generalizations concerning grain sorting and sample genesis. Host rock samples 55 and 56 possess the shallowest initial curves, indicating a high degree of sorting. However, beyond 60% intruded mercury there is a rapid and unsteady increase in capillary pressure, which we interpret to be caused by invasion of the mercury into the small pore throats of the intergranular microfractures. Host rock sample 41, which was collected adjacent to the fault core, is characterized by a fairly steep and unsteady increase in capillary pressure. Based on grain size data (Table 3.1), this sample is the least sorted of all samples examined by mercury-injection. Note that, in addition to be being fragmented, sample 41 also has anomalously high clay-content (~7%), which is present as a pore filling cement. The fault rock samples are characterized by shallow, but steady capillary pressure curves that are slightly steeper than the host rock slopes. Likewise, these samples are in general more poorly sorted than host rock samples (Table 3.1).

Sealing capacity

Mercury-injection data is used to estimate the resistance of a rock to invasion by a non-wetting fluid such as gas and most oils. The capillary strength of a rock is described in terms of its breakthrough pressure, which is the pressure at which the non-wetting fluid can form a throughgoing flow path through the rock (Schneider et al., 1997). This measure of fault seal is also elsewhere called displacement pressure (Schowalter, 1979) and threshold pressure (Katz and Thompson, 1987). Breakthrough pressure is measured indirectly from

90

mercury-injection curves using one of several estimation methods. In this study, a range of breakthrough pressures for each sample was determined by picking the mercury-air capillary pressure that corresponds to 7.5% (Schneider et al., 1997) and 10% (Schowalter, 1979) cumulative intruded mercury. Estimated breakthrough pressures for host rock samples range between 7 and 17 psi mercury-air, between 36 and 41 psi mercury-air for a fragmented rock sample, and between 77 and 544 psi mercury-air for fault rock samples (Table 3.1).

Based on the breakthrough pressures, we compute sealing capacity for five fault rocks, one fragmented rock, and three host rocks using representative fluid properties for both oil and gas and the following equations (Sneider et al., 1997):

$$P_{C,h/w} = \frac{\left(\sigma_{h/w} \cos\theta_{h/w}\right)}{\left(\sigma_{Hg/air} \cos\theta_{Hg/air}\right)} P_{C,Hg/air} \text{ ,} \tag{1}$$

and

$$h = \frac{P_{C,h/w}}{\Delta\rho \cdot 0.433} \text{ ,} \tag{2}$$

where P_C is the capillary breakthrough pressure, h is the maximum hydrocarbon height, σ is the interfacial tension between hydrocarbon and brine, θ is the contact angle, and $\Delta\rho$ is the difference in density between the hydrocarbon and brine. Input parameters used to compute maximum sealable hydrocarbon column heights are given in Table 3.3, while the calculated column heights are presented in Table 3.4. Based on the input parameters, fault rock samples show considerable range for hydrocarbon seal potential from 10 to 69 m of gas, or from 17 to 120 m of oil. Three out of five fault rock samples (19perp, 47perp, and 81) fall in the category of a class C seal (30-150 m oil), according to the Sneider Seal Classification

Table 3.3. Input parameters used to calculated hydrocarbon sealing potential (from Sneider et al., 1997).

input parameters	Hg-air	gas-brine	oil-brine
wetting angle (θ)	140	0	0
interfacial tension (σ) (dynes/cm)	480	70	30
brine density (g/cc)		1.11	1.11
hydrocarbon density (g/cc)		0.05	0.8498

Table 3.4. Calculated maximum sealable hydrocarbon column heights using fluid properties given in Table 3.2. Low and high estimates are presented based on mercury-air capillary pressures at 7.5 and 10% cumulative intrusion, respectively.

Sample	Type	gas 7.5%	gas 10%	oil 7.5%	oil 10%
56	hr	1	1	1	1
55	hr	1	1	2	2
41para	hr-adj	2	2	3	4
18perp	frag	5	5	8	9
78	fr	10	11	17	20
47para	fr	12	14	21	25
47perp	fr	35	41	60	72
81	fr	49	59	86	102
19perp	fr	63	69	109	120

system (Sneider et al., 1997), while the other two fault rock samples (47para and 78) correspond to a class D seal (15-30 m oil). Not surprisingly, fragmented rock (18) and fault-adjacent host rock (41para) samples show no potential for sealing an economic accumulation of hydrocarbon. The fragmented rock sample is considered a class E seal (<15 m), while the fault-adjacent host rock sample is considered a class F seal, or waste zone rock, due to both its non-sealing and low permeability nature. The two pristine host rock samples (55 and 56) are reservoir quality rocks (based on porosity and permeability data) with insufficient capacity for seal (<2 m oil column).

Our data indicate that sand-on-sand sheared-joint faults in low clay-content sandstones are capable of sealing small to moderate hydrocarbons columns given that a seam of high breakthrough pressure fault rock is laterally persistent. For sheared-joint faults in the Valley of Fire, continuous fault rock seams were found along faults with as little as 6 m of slip (Myers, 1999). Whether or not the samples with high breakthrough pressures represent a laterally continuous zone of fault rock remains to be answered. The column heights calculated in this study fall within the range of column heights calculated by Gibson (1998) for small offset (centimeters to meters of slip) purely cataclastic deformation bands in clean sandstones. We note, however, that had conditions been favorable in the Aztec sandstone for the post-deformational deposition of cements, the sealing potential of the fault rocks would be significantly higher (Fisher and Knipe, 1998; Gibson, 1998).

92

Equivalent cross-fault permeability

The fault core includes domains of deformed rocks with differing petrophysical properties. Even what is mapped or designated as fault rock is highly heterogeneous and displays a broad range of porosities, permeabilities, and capillary breakthrough pressures. Therefore, an upscaling procedure is adopted to generalize our discretely sampled permeability data. Following the methodology of Jourde et al. (2002), we use a finite-difference solution of the single-phase pressure equation subject to pressure/no-flow boundary conditions to calculate equivalent cross-fault permeability for the mapped areas shown in Figure 3.5. As an example, the model geometry used for the station 1 calculation is presented in Figure 3.15. Fault-parallel equivalent permeability is not considered as the fault maps are of insufficient detail (cf., Myers, 1999) to provide accurate results for the fine-scale calculations. Because slip surfaces are oriented parallel to the flow direction (Figure 3.5), we choose not to include them in our upscaling models. High permeability slip surfaces have been found to bear negligible influence on upscaled cross-fault permeability in cases where the slip surfaces do not cross the fault core (Jourde et al., 2002). In assigning fragmented and fault rock permeabilities to the flow model, we assume that the measured plug permeability values are laterally continuous with respect to the slip direction and thus assign those values over the
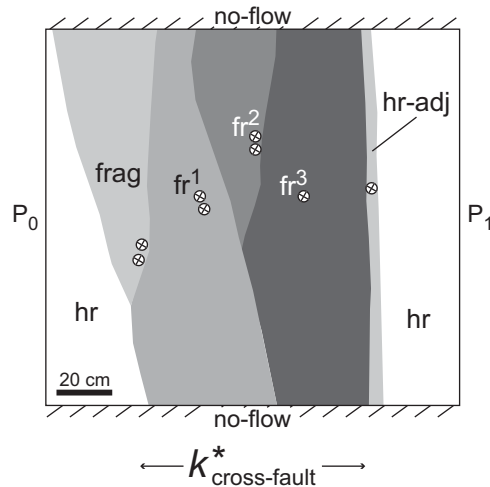
Figure 3.15. Input map used to calculate equivalent cross-fault permeability at station 1. No-flow boundary conditions are imposed along borders perpendicular to the fault zone, while fixed pressure boundary conditions are imposed across the fault zone. fr = fault rock; frag = fragmented rock; hr = host rock; hr-adj = fault-adjacent host rock. Crossed circles are sample localities.

length of the model domain. Only fault-perpendicular plug permeability data were used in this analysis (Table 3.1). A median value of 626 md is assigned to the host rock, except where measured host rock permeability values dictate otherwise, as is the case for the host rock samples collected adjacent to the fault core.

Calculated equivalent cross-fault permeabilities as a function of average shear strain are plotted in Figure 3.16. As a reference point, median host rock permeability is plotted at $\gamma = 0$. The data show a decreasing trend for equivalent cross-fault permeability with increasing shear strain. For each upscaling model, the calculated permeability was most influenced by the least permeable, and most continuous body of fault rock. Because the fault map areas are relatively simply in geometry and structural stratification (Figure 3.5), the upscaled permeabilities closely approach theoretical lower limit harmonic average values (Deutsch, 1989). However, for more complicated fault geometries, computed cross-fault permeabilities have been found to be greater than the harmonic average (Myers, 1999; Flodin et al., 2001). For reservoir confining conditions, upscaled cross-fault fault permeabilities could be expected to scale with the reductions indicated by the confining pressure analyses (Figure 3.8), that is, around a factor of three. We note that the calculated equivalent permeability values would be even lower if the relative permeability curves resulting from multi-phase flow were considered (Manzocchi et al., 2002). Given the high breakthrough pressures for some of the fault rock, and therefore small average pore throat radii, the relative permeability of oil could be reduced significantly relative to the rock's intrinsic permeability.
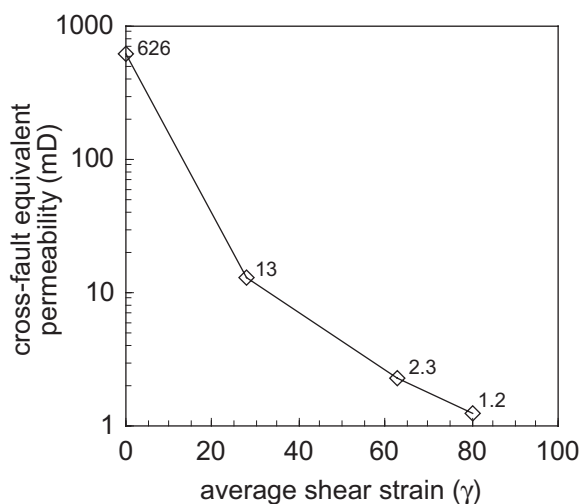
Figure 3.16. Calculated equivalent cross-fault permeability as a function of average shear strain. Median host rock is plotted as a reference starting point. Numbers next to symbols are the calculated upscaled permeability values.

The upscaled cross-fault permeability results show that sand-on-sand faults formed by shearing along joint zones in nearly pure quartz sandstones will act as baffles to subsurface fluid flow production time-scales (tens of years). These data would be useful for estimating the flow properties of sand-prone faults in reservoir models where the faults are explicitly included in the model (e.g., Flodin et al., 2001). Typical fault transmissibility models that use only shale gouge ratio (SGR), in conjunction with permeability transforms, to predict fault baffles during production (e.g., Walsh et al., 1998; Manzocchi et al., 1999) will not be able to predict the impact of purely cataclastic fault rock in high-sand systems.

Conclusions

The following conclusions can be drawn from this study of host, fragmented, and fault rock associated with variously strained sheared-joint based faults in aeolian Aztec sandstone:

1. No significant change in bulk mineralogy between host and fault rock was detected. This indicates that fault rock formation in the study area was primarily a physical process and did not involve significant mass transfer or diagenesis. Two regions of the fault zone do however show anomalously higher pore filling cement concentrations. Clay cements occur in greater abundance in host rock immediately adjacent to the fault core, while both clay and iron-oxides cements are localized around slip surfaces within the fault rock. Silica overgrowth cements occur in negligible quantities.

2. The greatest absolute porosity reduction of fault rock with respect to median host rock is 9.1% (down from 22% for median host), which equates to a factor 1.7 change. However, many fault rock samples show little to no change with respect to median host rock. All fragmented rock samples and two fault rock samples are dilated with respect to median host rock. Porosities range between 13.3 and 22.7% for fault rock, 22.5 and 27.5% for fragmented rock, and 16.7 and 23.5% for host rock.

3. Fault rock permeabilities are one to three orders of magnitude less than median host rock permeabilities. Permeabilities range from 0.28 to 39 md for fault rock, 23 to 1400 md for fragmented rock, and 123 to 6000 md for host rock.

4. There is a trend for a reduction in median grain size from host rock to fragmented rock to fault rock. There also appears to be a trend for decreased sorting from host to fragmented rock, and a trend for increased sorting from fragmented to fault rock.

5. High-pressure mercury-injection analyses on fault rocks derived from nearly pure quartz sandstone show that these rocks are capable of sealing small to moderate hydrocarbon columns if high breakthrough pressure fault rock is present as a continuous interface across the fault surface. For typical fluid properties, calculated hydrocarbon column heights for fault rocks range between 10 and 69 m of gas, and 17 and 120 m of oil.

6. Based on single-phase permeability upscaling calculations, faults formed by shearing along joint zones in nearly pure quartz sandstones will act as baffles to subsurface fluid flow. Upscaled cross-fault permeabilities range between 1.2 and 13 md, from low to high shear strain. These values equate to a one to two orders of magnitude reduction between fault core and median host rock permeability (626 md).

7. There is a relationship between average shear strain and changes in petrophysical properties. Higher shear strain leads to lower permeability, lower median grain size, and in general, higher capillary breakthrough pressure. Correlation of these petrophysical properties with fault throw alone is not a good proxy. Fault throw and fault zone thickness together are required for accurate prediction of fault zone flow properties.

Chapter 4

Computing permeability of fault zones in aeolian sandstone from outcrop measurements

Abstract

The large scale equivalent permeabilities of strike slip faults in porous sandstone are computed from detailed field measurements. The faults, which occur in the Valley of Fire State Park, Nevada, were previously characterized and the flow properties of their individual features were estimated. The faults formed from the shearing of joint zones and are composed of a core of fine grain fault rock (gouge) and deformation bands and a peripheral damage zone of joints and sheared joints. High resolution fault zone maps and permeability data, estimated using image analysis calibrated to actual measurements, are incorporated into detailed finite difference numerical calculations to determine the permeability of regions of the fault zone.

Faults with slips of magnitude 6 m, 14 m and 150 m are considered. The computed fault zone permeabilities are strongly anisotropic in all cases. Permeability enhancement of nearly an order of magnitude (relative to the host rock) is observed for the fault-parallel component in some regions. Fault-normal permeability, by contrast, may be two orders of magnitude less than the host rock permeability. The fault-normal permeability is a minimum for the fault with the highest slip. For a representative fault region, the fault-parallel component of permeability is highly sensitive to the fracture aperture, though the fault-normal permeability is insensitive. The procedures developed and applied in this study can be used for any type of fault for which detailed structural and permeability data are available or can be estimated.

Introduction

Because faults can have a dominant impact on flow in the subsurface, knowledge of their flow properties is essential for the efficient management of groundwater or petroleum resources. The flow properties of faults are in general quite complex because they can act as

conduits or barriers to fluid flow. In most cases a fault displays both aspects of this complex signature in time and space (Smith et al., 1990; Caine et al., 1996; Matthäi et al., 1998; Caine and Forster, 1999; Aydin, 2000). Thus, the accurate description of permeability in the fault zone is an important aspect of the overall characterization of the reservoir or aquifer. Detailed field measurements are capable of providing fine scale descriptions of the fault zone. These descriptions are, however, much too detailed to be used directly in standard finite difference flow simulators. Some type of averaging or upscaling procedure is required before these fine scale fault zone characterizations can be used for reservoir scale flow modeling.

In recent years, many researchers have addressed the upscaling of the permeability properties of heterogeneous porous media in order to incorporate, to the degree possible, fine scale permeability information into large scale flow models. In general, upscaling is required whenever permeability data measured at one scale are to be utilized in analyses conducted over much larger scales. Techniques for the determination of upscaled or equivalent permeability can be classified as either analytical (approximate) or numerical procedures. The computational cost associated with the numerical methods is generally warranted when the resulting upscaled permeabilities are used for reservoir flow simulation. A number of both analytical and numerical techniques are discussed in the reviews by Wen and Gomez-Hernandez (1996) and Renard and de Marsily (1997). The numerical procedures generally entail the solution of the single phase flow equation over the region to be upscaled. The specific techniques differ mainly through the boundary conditions imposed on this local problem, the particular numerical method applied and the size of the local domain considered. In this work, we apply a finite difference numerical procedure with pressure-no flow boundary conditions for the calculation of the large scale permeability of the fault zone.

A number of previous investigators have studied the effects of small scale geologic features on large scale permeability. Durlofsky (1992) showed that small scale permeability variations (cross bedding) in eolian sandstones can reduce the bulk permeability by one order of magnitude and can create a permeability anisotropy of $k_{max}/k_{min} > 5$ (where k_{max} and k_{min} are the maximum and minimum principal values of permeability). Similarly, it has been

98

shown that the presence of joints can increase effective permeability by two orders of magnitude (Taylor et al., 1999; Matthäi et al., 1998) whereas the presence of deformation bands can decrease effective permeability by one to three orders of magnitude (Antonellini and Aydin, 1994; Matthäi et al., 1998; Taylor and Pollard, 2000). Very fine scale features (cross beds, joints and deformation bands) may thus introduce significant permeability anisotropy. Furthermore, these small scale structural heterogeneities must be accurately represented since a misrepresentation of their geometry can lead to order of magnitude error in the estimation of effective permeabilities (Taylor et al., 1999). Thus it is imperative to account for these fine scale features in the calculation of the upscaled permeability.

The faults studied in this paper have been characterized in detail in a previous outcrop study (Myers, 1999). From a hydrologic perspective the faults can be described as being composed of high permeability components (joints, splay fractures and slip surfaces) and low permeability components (fault rock, deformation bands, and sheared joints) embedded in a matrix with intermediate permeability. We study the evolution of the permeability properties of such faults as a function of slip magnitude by calculating the equivalent permeability of large regions of the fault zone. A schematic of our general workflow is shown in Figure 4.1. The bases of our work are sub-centimeter scale resolution field maps that distinguish the various elements of the fault zone (Figure 4.1a). The permeability values of each fine scale fault zone element (joints, sheared joints, fault related deformation bands, slip surfaces, fault rock and the matrix rock) are either measured or estimated (Figure 4.1b) and then input into the detailed description (Figure 4.1c). Numerical simulation of the fine scale input map yields the larger scale permeability of the fault zone of interest (Figure 4.1d). In this study, we follow this workflow to determine the values of fault zone permeability for a range of fault slip magnitudes (6 m to 150 m).

The approach taken here differs from that taken in several earlier studies (e.g., Walsh et al., 1998; Manzocchi et al., 1999) that established correlations for fault thickness and permeability in terms of a few relevant parameters. These correlations were used to derive approximate input to flow simulators. In the present study, the fault descriptions are extremely detailed and the effective flow properties of the fault are computed using numerical solutions. In practice, however, the detailed fault zone information we input into our
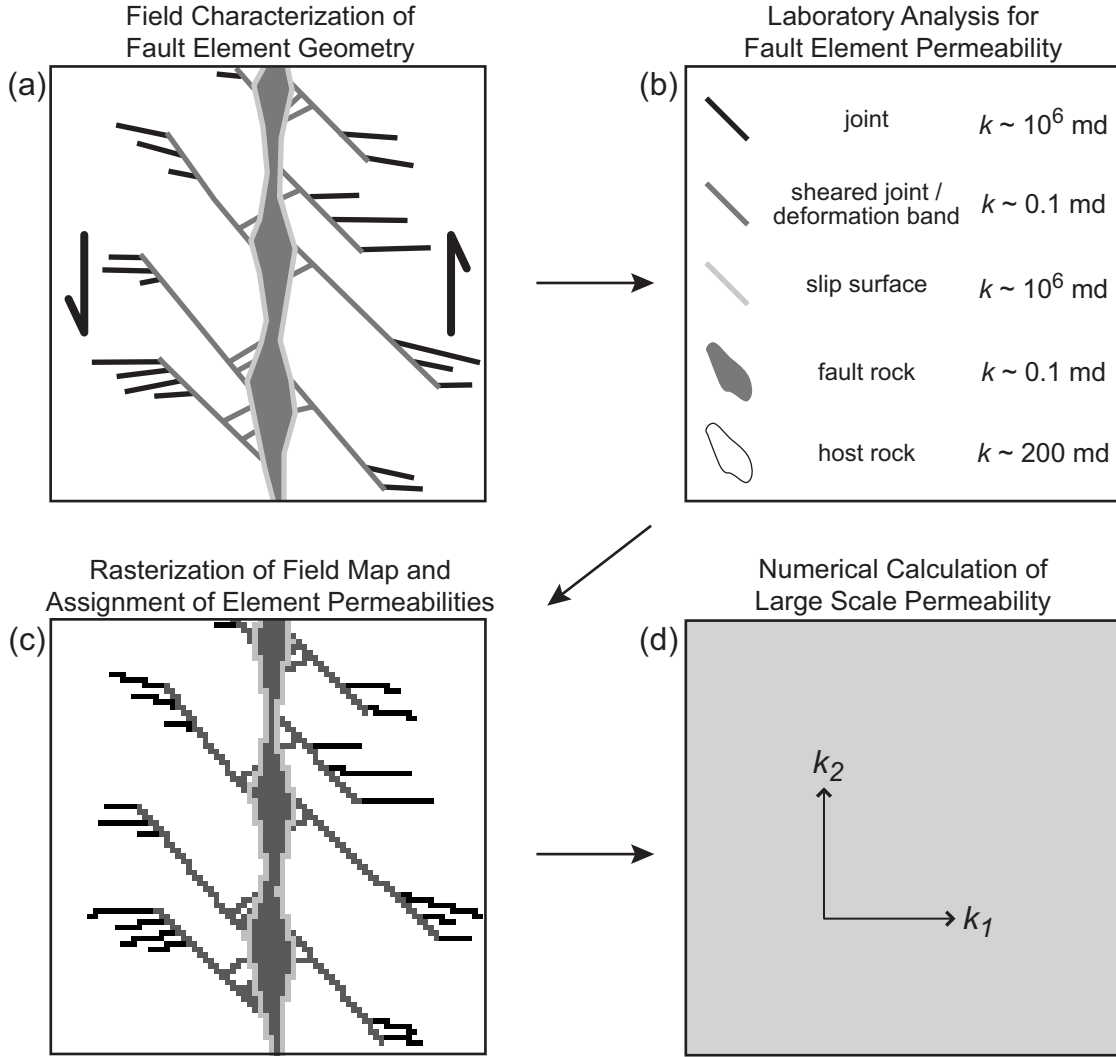
Figure 4.1. Workflow used in this study to determine the large scale permeability of fine scale field characterizations of fault zones.

calculations will not be available for faults in the subsurface or may have different values in different settings. Our calculations are therefore most useful in providing insight into the flow properties of faults and as a means to determine the dominant controls on flow in the fault zone. Once these are clearly established for a particular type of fault, appropriate correlations for fault zone permeability in terms of a few measurable parameters (e.g., fault slip) can be established. We note that the procedure described in this paper for determining fault zone properties can be applied to faults of any type, assuming a detailed geological characterization is available.

An alternate procedure for modeling fluid flow through a fault zone is to use a discrete fracture model. Such models are widely used for simulating pollutant transport in naturally fractured groundwater systems or waste disposal characterizations. Discrete fracture modeling is not generally used in practical reservoir simulation, although there has been some research reported recently on the use of these models within the context of reservoir flows (e.g., Kim and Deo, 1999; Dershowitz et al., 2000; Karimi-Fard and Firoozabadi, 2001). Discrete fracture models have been more geared to fractured systems, which may display more regular distributions, than to highly complex faulted systems. For large scale reservoir flow problems, it would be impractical to represent every element discretely in a fault zone because the fine scale data for the faults in the subsurface are not available and because the computational cost would be very high. In case the flow response of a fault zone is dominated by a single element, then the dominating element can be represented discretely. Hybrid procedures, such as that recently described by Lee et al. (2001), allow for the representation of most of the fractured system in terms of an equivalent permeability but include discretely some number of dominant large scale fractures. This type of approach could potentially be combined with the fault zone permeabilities computed in this paper to more accurately model flow and transport in faulted rock. See Chapter 5 for elaboration on this topic.

Rather than represent fractures explicitly, standard reservoir simulators apply finite difference techniques, which require input in the form of permeability for each simulation grid block. In introducing the effects of the fault zone into standard reservoir flow simulators, it is therefore necessary to represent the fault in terms of a permeability tensor. This treatment offers reasonable accuracy for flow normal to the fault, though it may not be as accurate for flow parallel to the fault, particularly for transport calculations with single very thin but extensive features (e.g., slip surfaces) that can significantly impact flow.

We note that, although both the fault-normal and fault-parallel components of permeability are important, for many flow problems capturing fault-normal permeability is more critical. This is because the fault-normal component of permeability largely determines the degree to which there is pressure communication between adjacent fault blocks. Quantifying the cross-fault communication is often an important issue for the efficient management of a reservoir.

This paper proceeds as follows. We first describe the geological setting and the general characteristics of the faults studied. This is followed by a description of our approach used to calculate fault zone permeability. Next, the permeabilities of the individual fault zone elements are discussed. We then present results for large scale fault zone permeability for faults of slip magnitudes of approximately 6 m, 14 m and 150 m. These results, taken in total, illustrate both the large scale trends as well as the local variability that exist in fault zone permeability.

General description of the faults

The faults studied in this paper occur in Valley of Fire State Park (Figure 4.2), located in the North Muddy Mountains of southern Nevada, USA. We consider faults produced by shearing along well-developed joint zones in the Aztec Sandstone, a high porosity, poorly to moderately cemented eolian sandstone. The Jurassic Aztec Sandstone was deposited in a stable cratonic setting along the western margin of North America (Marzolf, 1983). Myers (1999) described the development of the faults from pre-existing arrays of en echelon joints to various stages of complex fault evolution (Figure 4.3). The angular relationship between joint zone trend and orientation of the principal stresses after the stress or material rotation (Figure 4.3) determines whether the fault system consists of contractional steps (contractional faults) or dilational steps (dilational faults). A photograph of a fault zone in the Valley of Fire, with the various elements labeled, is shown in Figure 4.4.
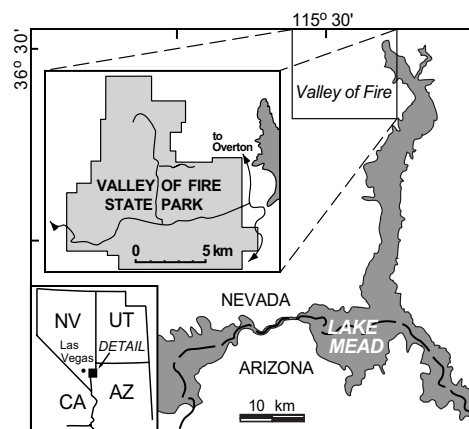
Figure 4.2. Location map of the study area, Valley of Fire State Park, southern Nevada, USA.

Although the methodology described here can be applied to either case, the examples in this paper are selected from contractional en echelon fault systems consisting of steeply dipping faults. In this case, en echelon joint arrays were sheared in such a way that steps between neighboring joints experience contractional deformation resulting in deformation band formation as well as new joints. The fault zones formed by this mechanism are composed of principal structural elements consisting of sheared joints, shear induced joints or splay fractures, and fragmentation zones at large (breccias) and small (gouge/cataclasite/ fault rock) scale. The splay fractures form as an opening mode structure (mode-I) (Brace and Bombolakis, 1963; Cotterell and Rice, 1980), occur along principal planes and are later subjected to progressive shearing. Second and third order splay fractures form through a

Fault Zone Type   **Formation Stage**
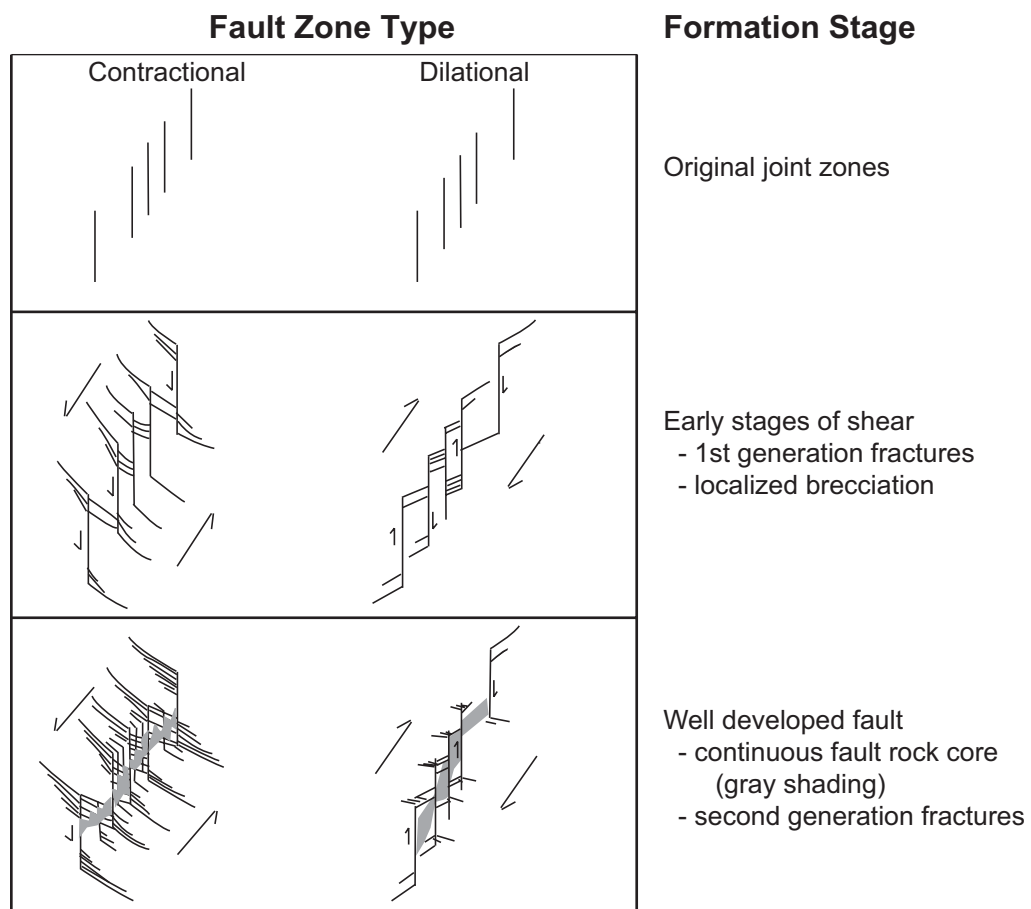
Figure 4.3. Schematic depiction of the fault types that result from shearing of en echelon joint zones and their evolutionary stages as a function of slip magnitude (from Myers, 1999).
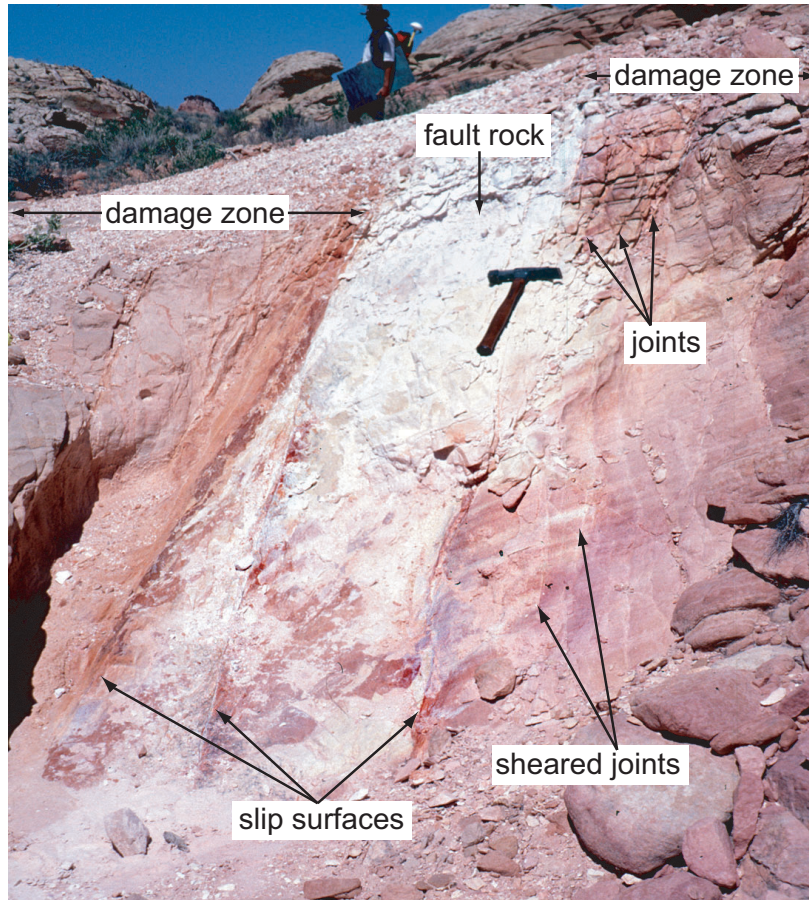
Figure 4.4. Photograph of a fault from the Valley of Fire State Park showing characteristic structural features of the fault core (fault rock and slip surfaces) and the surrounding damage zone (joints and sheared joints). Geologist in background is Stephan Bergbauer.

hierarchical process where opening mode fractures formed at earlier stages are sheared, producing new generations of sheared joints and joints. This iterative process may continue for many stages of fracturing. Deformation bands – thin, tabular zones of strain localization – can reduce the porosity of the sandstone within the bands by one to three orders of magnitude (Antonellini and Aydin, 1994). The deformation bands accommodate slip up to a few centimeters, are restricted to the core of the fault zone, and are generally localized within contractional steps of the sheared joint zones.

Contractional faults show a gradual widening of fault rock/gouge and a peripheral fracture network zone. The final fault zone architecture is a central fine-grained fault core which is bounded on one or two sides by slip surfaces and is surrounded by an elliptical damage zone. We note that, as a consequence of the formation mechanism, most of the fault zone

elements (splay fractures, sheared joints, and slip surfaces) are sub-vertical (Myers, 1999). Therefore, the two dimensional modeling approach employed in this paper is a reasonable approximation.

Modeling approach for the calculation of fault zone permeability

We use a finite difference (or more properly a finite volume) procedure to calculate the equivalent permeability of the fault zone. The overall approach requires the solution of the fine scale single-phase pressure equation subject to appropriate boundary conditions. Single phase, steady state incompressible flow through a heterogeneous porous medium is described by Darcy's Law and the continuity equation:

$$\mathbf{u} = -\frac{1}{\mu}\mathbf{k} \cdot \nabla p \ ,$$

(1)

$$\nabla \cdot \mathbf{u} = 0 \ ,$$

(2)

where $\mathbf{u}$ is the fluid velocity vector, p is pressure, μ is the fluid viscosity, and $\mathbf{k}$ is the permeability tensor.

To calculate the equivalent permeability tensor for a region of the fault zone, we solve the fine scale equations (1) and (2) subject to constant pressure – no flow boundary conditions. Two such solutions are required. In the first solution, flow is driven by a pressure gradient in the x-direction, while in the second solution the pressure gradient is in the y-direction. Following these two numerical solutions, total flow rates through the domain are computed. The equivalent or upscaled permeability, referred to here as $\mathbf{k}^*$, is then calculated by equating the flow rates from the fine scale solutions with those that would result from the imposition of the same boundary conditions on a homogeneous region of permeability $\mathbf{k}^*$.

For a rectangular region of physical dimensions L_x and L_y, with a pressure difference Δp imposed in the x-direction, the x–x component of $\mathbf{k}^*$ (k_{xx}^*) is given by:

$$k_{xx}^* = \frac{Q_x \mu L_x}{L_y \Delta p} \ ,$$

(3)

where Q_x is the total flow rate through the system. An analogous expression gives k_{yy}^*,

105

which is computed following the solution of a flow problem with a pressure difference imposed in the *y*-direction. In general the upscaled permeability tensor also contains a cross term k_{xy}^*. This term, which is non-zero when the principal directions of permeability are not aligned with the coordinate system, can be computed by relating the average Darcy velocity (<**u**>) to the inner product of the upscaled permeability and the average pressure gradient (**k*** · <∇p>). For the fault systems considered here, the principal directions of permeability were found to be in close alignment (within a few degrees) with the general fault orientation in nearly all cases. Thus the cross terms of permeability are small and can be neglected for the cases considered in this paper. Further, because the cross terms of **k*** are small, $k_1 \approx k_{xx}^*$ and $k_2 \approx k_{yy}^*$, where k_1 is the fault-normal permeability and k_2 the fault-parallel permeability. If the fault is not oriented with the coordinate system, k_{xy}^* will in general be significant.

Alternate boundary specifications may be more appropriate in some cases. Periodicity (see e.g., Durlofsky, 1991) may be preferable in cases where high flow features (e.g., slip surfaces) are not continuous over very large distances. This is because periodic boundary conditions tend to "interrupt" the connectivity of features that span the system but are not exactly aligned with the system orientation. This will generally result in lower computed values for fault-parallel permeability than would be obtained using the constant pressure – no flow specifications applied here. Refer to Chapter 5 for further study concerning optimal boundary specification for faulted systems.

The solution of Eqs. (1) and (2) over highly detailed fine scale descriptions of the fault zone, which in our case contain over 10^6 cells (e.g., 2000×2000 pixels), is demanding computationally. The problem is further complicated because the permeability field is highly discontinuous and can vary by over six orders of magnitude over very short distances. A suitable linear solver is therefore required for this problem. In this work we apply an iterative multigrid solver (Ruge and Stuben, 1987) for the fine grid solution. Multigrid solution techniques are particularly adept at the efficient solution of large problems with strongly discontinuous coefficients.

In the results presented in this paper, we compute a single equivalent permeability tensor for a large portion of the fault zone. This quantity is the equivalent or large scale fault zone permeability. Using the procedures applied here, it is also possible to upscale these

fine scale descriptions to coarser scale models containing a specified number of grid blocks. For example, in some applications it might be useful to generate a 10×10 or a 100×100 grid block description of the fault zone in order to retain a higher degree of resolution. In such cases, rather than compute a single $\mathbf{k}^*$ for the entire region, the procedure presented here could be used to compute equivalent permeability tensors for each of the coarse scale grid blocks.

Determination of fault zone permeability

We now consider the fine scale permeabilities of the fault zone elements. We use an isotropic matrix permeability of 200 md, corresponding to a mean value of host rock permeability in this locality (Myers, 1999). It is reasonable to use an isotropic value of permeability for the host rock because the exposures we are modeling are sub-parallel to bedding planes. Within the bedding plane, anisotropy is generally not that significant. Sheared joints, deformation bands, fault rock/gouge, and variably deformed host rock were assigned permeabilities based on previously reported permeability data for these structural elements in the Aztec sandstone. Freeman (1990) used a gas permeameter on small plugs of the Aztec sandstone, and reported that deformation bands cause a two order of magnitude permeability reduction relative to the host rock. Antonellini and Aydin (1994) used a gas injection minipermeameter to measure the permeability of deformation bands, finding them to be two to four orders of magnitude less permeable than the host rock, with an average permeability reduction of three orders of magnitude. Taylor and Pollard (2000) used field measurement of relic fluid gradients in the Aztec sandstone to infer that the permeability of the deformation bands is reduced by 1.3 to 2.3 orders of magnitude relative to the host rock. As will be described next, Myers (1999) estimated the permeability of deformation bands in the Aztec sandstone to be one to four orders of magnitude less than the permeability of the host rock.

Myers (1999) used petrographic image analysis techniques to determine two dimensional porosity from epoxy impregnated thin sections and calculated the permeability of each component of the fault zone by using the Kozeny-Carman relationship. He concluded that, due to a nearly identical degree of grain size reduction, deformation bands and sheared joints have similar permeability values. Thus, in our calculations, a permeability of 0.1 md,

approximately corresponding to a permeability three orders of magnitude smaller than that of the host rock, was assigned to both populations of sheared joints and deformation bands. This value represents the middle range of absolute permeability values reported by the researchers cited above.

Myers (1999) also determined the permeability of the fault rock/gouge material by direct laboratory measurements and image analysis techniques and found the same magnitude of permeability reduction as for deformation bands and sheared joints. This appears to be a reasonable average value although fault rock next to a well developed slip surface usually has a much lower permeability value (Antonellini and Aydin, 1994). In the simulation all sheared materials have been assigned an isotropic permeability value that corresponds to the fault-normal permeability, even though it has been shown by Antonellini and Aydin (1994) that deformation bands or wall rock of slip surfaces may in some cases have anisotropic permeability. Specifically, these investigators reported that permeability normal to the band can be one order of magnitude less than permeability parallel to the band, especially when the grains in the band are oblate. Thin features of low permeability have a relatively small effect, however, on large scale flow parallel to the feature. For such features, assigning an isotropic permeability that is one order of magnitude too small in the direction parallel to the feature generally has little effect on flow results. Thus, in all cases, fault rock/gouge materials were assigned an isotropic permeability of 0.1 md.

Permeability of both joints and slip surfaces (when well-developed) was calculated using a parallel plate model in conjunction with an equivalent porous media representation (Matthäi et al., 1998; Taylor et al., 1999). The permeability for a pixel of width L containing a fracture of aperture b is then given by:

$$k = \frac{b^3}{12L},$$ (4)

We used joint apertures of 0.25 mm inferred from field observations. As this aperture may vary in the subsurface as a function of fluid pressure and regional stress state, we performed simulations for one of the faults using different aperture values in order to test the impact of aperture variation on fault zone permeability. These results are reported below.

Fault zone permeability calculations

We now present simulation results for three faults with different slip magnitudes (6 m, 14 m and 150 m). The input for each case was a large scale map containing several million pixels of permeability data. The calculation of fault zone permeability was accomplished for target regions of typical size of about 2000×2000 pixels. For each value of slip, we consider two or more regions of the fault and present upscaled permeability results for each region.

The input maps for these calculations were compiled at a resolution of 3 mm. The width of the system varies from 6 m wide for the faults with slips of 6 m and 14 m to 4.75 m wide for the fault of slip 150 m. The fault features are color-coded and the appropriate permeability is assigned to each finite difference grid block by projecting the mapped permeability onto the pixels. All features are represented by a minimum of three pixels of resolution (i.e., a minimum of three fine grid blocks per feature). For the joint and slip surface features that are physically smaller than their pixel representation, Eq. (4) is used to provide the input permeability. The results for upscaled permeability were not found to be overly sensitive to the number of pixels used to represent these fine features over a reasonable range of values. This representation may, however, introduce some inaccuracy when it is applied to high permeability features that are oriented skew to the finite difference grid.

Results will be presented in terms of the two principal values of upscaled permeability, k_1 and k_2, for each fault zone. The permeability component k_1 is essentially the fault-normal permeability (also referred to as the fault-perpendicular or cross-fault permeability) and k_2 the fault-parallel permeability.

Fault with 6 meters of slip

The 6 m slip fault is composed of a less dispersed set of joints, sheared joints and deformation band orientations with respect to the two larger slip faults we consider later in this paper (Figure 4.5). This fault represents the incipient stages of fault rock development.

The fault zone permeabilities for the various regions shown in Figure 4.5 illustrate the potential variability of the flow properties of faults. The first region of the fault (upper region in Figure 4.5) shows a fault-perpendicular permeability ($k_1 = 26$) that is considerably higher than that of the other regions ($1.5 \leq k_1 \leq 4.4$). All portions of the fault display high

fault-parallel permeabilities ($1087 \leq k_2 \leq 1587$), with the highest permeability about a factor of eight greater than the host rock permeability. The higher fault-perpendicular permeability in the first region (top region in Figure 4.5) is as a result of the slip surfaces connected across the fault core. These features create a discontinuity in the fine-grained fault rock and provide for a flow pathway across the fault, which in turn results in a higher computed value for k_1. This type of cross-fault connection does not occur in the other four regions. All five regions display high fault-parallel permeabilities because the slip surfaces are through-going in the fault-parallel direction. Note that large scale joints also contribute to this component of permeability in some regions.

The fault-normal components of permeability are impacted not only by the low permeability continuous fault core and deformation bands therein, but also by the extensive sheared joints (blue features in Figure 4.5) outside of the fault core. These features create additional barriers to flow and act to reduce the fault-normal component of permeability (relative to the host rock) even in the case where slip surfaces introduce cross-fault connections (discussed above).

As indicated above, the apertures of fractures in the subsurface are difficult to determine and may in addition depend on the local stress state. In order to assess the sensitivity of the fault zone permeability to the fracture aperture b, we computed k_1 and k_2 as a function of fracture aperture for the enlarged input map shown in Figure 4.5 (by fracture aperture we mean here the apertures of fractures as well as slip surfaces). The results for k_1 and k_2 over the range $0.05 \leq b \leq 0.5$ are shown in Figure 4.6. The computed fault-normal permeabilities (k_1) are insensitive to the fracture aperture and increase by only about 5% over the range considered. The results for fault-parallel permeabilities (k_2), by contrast, are very sensitive to fracture aperture and increase by a factor of 30 from b=0.05 to b=0.5. This is as would be expected when the system contains through-going fractures and slip surfaces. At the larger values of b, we find that $k_2 \sim b^n$, with $n \approx 2.2$. When through-going fractures are evident, we would expect n to be closer to 3 (cf. Eq. (4)). This discrepancy may be due to inaccuracies in our representation of high permeability fractures that are oriented skew to the grid. In any event, the results of Figure 4.6 demonstrate that, given uncertainty in the fracture aperture, estimates for k_2 will be uncertain, while those for k_1 can be made with much higher confidence.

$k_1 = 26.3$
$k_2 = 1140$

$k_1 = 3.0$
$k_2 = 1080$

$k_1 = 2.4$
$k_2 = 1120$

$k_1 = 1.5$
$k_2 = 1370$

$k_1 = 4.4$
$k_2 = 1590$

Legend for Figures 4.5, 4.7, and 4.9

matrix

fault rock

joint

sheared joint or deformation band

slip surface

2 meters

1 meter

k_2 direction

k_1 direction

Figure 4.5. A strike-slip fault with 6 m of slip (from Myers, 1999) and five fault zone regions for which k_1 and k_2 are computed. Note the consistently high (with respect to host rock permeability) fault-parallel permeability (k_2) and the noticeably higher (with respect to the other calculated regions) cross-fault permeability (k_1) for the top region.

The results for this particular fault are of interest because they illustrate the potentially large impact of sub-seismic faults (faults with less than ca. 10 m offset) on fluid flow. Our calculations indicate that permeability in the fault strike direction is enhanced significantly, while permeability across the fault decreases in most regions by nearly two orders of magnitude. In the subsurface, small faults of this type may therefore contribute significantly to large scale flow in the reservoir or aquifer.

111

Fault with 14 meters of slip

A higher slip magnitude ordinarily results in a wider damage zone with a greater number of peripheral fractures. For the fault with 14 meters of slip (Figure 4.7), these trends are not clearly observed, as there appears to be about the same fracture density and a fault rock/ gouge zone of about the same width as for the 6 meter fault considered above. Permeability values for the two fault regions (both modeled with 2000×2000 pixels) are indicated in the figure.

The fault-parallel permeability is comparable to that of the earlier fault example with 6 m slip, while the fault-perpendicular permeability is generally higher for the 14 m fault. Again, the fault-parallel permeability is strongly impacted by the through-going slip surfaces for the lower region. Fault-normal permeabilities are increased in this region as a result of the cross connections between the slip surfaces in the fault core (cf. Figure 4.7), as was also the case for the first region of the fault with 6 m of slip. Fault-normal permeability for the upper region would be even higher except for the large scale, low permeability sheared joints outside of the fault core. The upper region shows a somewhat higher permeability (8.3 md) than the values calculated for most regions of the 6 m case (an average of
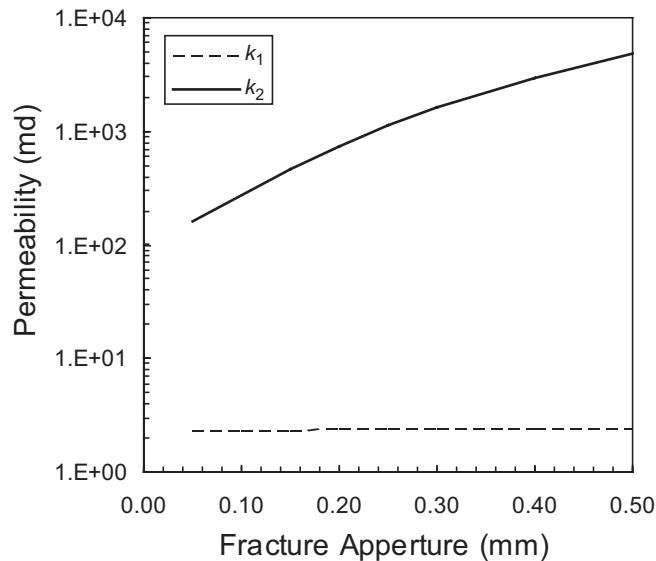

Figure 4.6. Variation of fault zone permeability with fracture aperture computed for the expanded region of Figure 4.5. The fault-normal component of permeability is insensitive to the fracture aperture; the fault-parallel component is highly sensitive.

112

2.8 md for the lower four regions). This is the effect of the narrower regions of fault rock found in the 14 m case with respect to the 6 m case (cf. Figures 4.5 and 4.7).

Fault-normal streamline maps for the upper and lower regions of the 14 m slip fault are shown in Figure 4.8. The different fault-perpendicular permeabilities between the two regions are to some extent reflected in the differing flow geometries. For both maps, the high flow regions in the fault peripheries correspond to high permeability joints. For the upper map (Figure 4.8a) there are no high permeability pathways through the fault rock. Thus, the flow is more evenly spread across the low permeability fault rock. This is in contrast to the lower map (Figure 4.8b) where the flow crosses the fault rock mostly in the two regions (lower and central regions of Figure 4.8b) where slip surfaces cross the fine-grained fault rock. The focused flow through the higher permeability slip surfaces leads to an overall higher large scale permeability.

Fault with 150 meters of slip

This fault (Figure 4.9), the largest slip magnitude fault considered in this paper, corresponds to a seismically observable fault (offset greater than 10 m, which is the lower limit of seismic resolution). At this stage of development the contacts between the highly deformed fault rock and the damage zone in the fault margin are sharp. A fracture hierarchy formed by successive slip on splay fractures is well developed in the fault periphery and extends for several meters into the host rock. The slip surface is well developed and defines an open path between two smooth surfaces. The fracture density and fault rock/gouge thickness are greater in this case than for the faults with 6 m and 14 m of slip. The fault zone model in this case is 4.75 m wide (in contrast to the 6 m wide models considered for the previous two cases) and is represented by 1568×1568 pixels.

For this fault, the upscaled permeabilities for the two regions are very close. For both regions, the fault-perpendicular component of permeability ($k_\perp$) is reduced by over two orders of magnitude relative to the host rock. This large reduction is clearly due to the wide fault rock/gouge zone and to the fact that there are no slip surfaces traversing this zone in the perpendicular direction, as there were in some regions of the faults discussed above. The dense regions of deformation bands at stepovers and sheared joints emanating out from

Figure 4.7. A strike-slip fault with 14 m of slip (from Myers, 1999) and two fault zone regions for which k_1 and k_2 are computed.

the gouge also contribute to the low fault-normal permeabilities. The continuous slip surfaces in the direction along the fault lead to enhanced permeability in the fault-parallel direction. This permeability enhancement, still about a factor of five over that of the host rock, is slightly less than for the previous faults, possibly because of the more extensive regions of sheared joints and deformation bands.
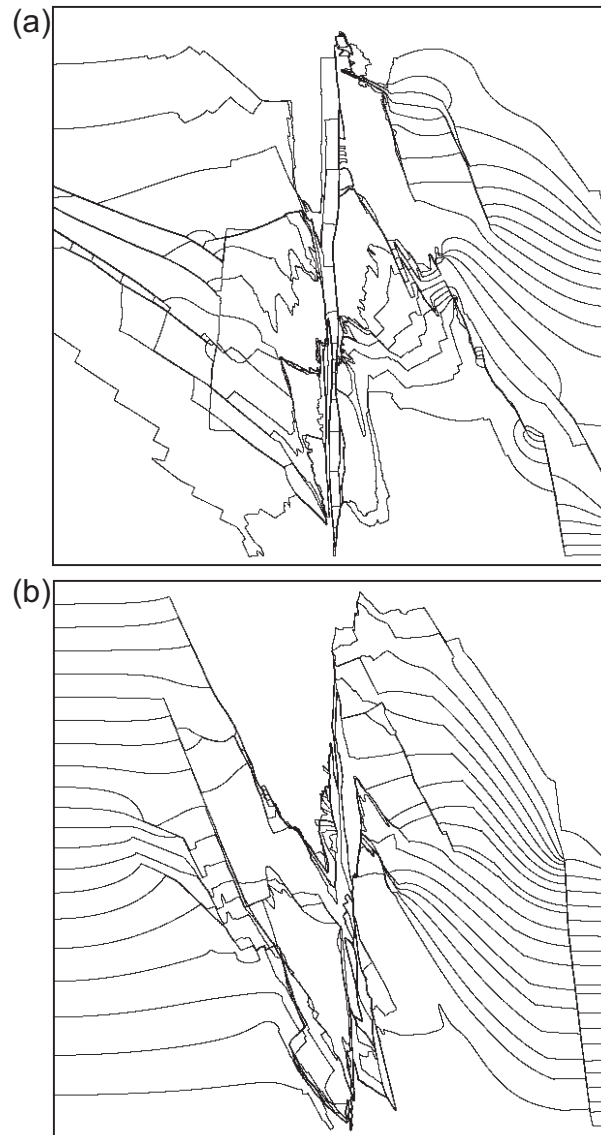
Figure 4.8. Streamline maps of cross-fault flow for the **(a)** upper and **(b)** lower input maps shown in Figure 4.7. In both cases, the flow fields are depicted with 20 streamlines.

Discussion

In this paper, we computed large scale fault zone permeabilities for faults formed by shearing across joint zones in sandstone and characterized by macro-scale fragmentation. Our results demonstrate quantitatively that the hydraulic behavior of a fault cannot always be generalized into two end members; e.g., a fault does not act exclusively as a simple barrier or conduit. The strong impact of low permeability features on the fault-normal

115

permeability, as well as the large effect of extensive slip surfaces on fault-parallel perme-ability, illustrate the importance of a precise determination of the detailed fault zone archi-tecture and the corresponding petrophysical properties. In a modeling study such as this, in which outcrop data is used, these properties can be determined from a combination of *in situ* and core permeability measurements. The estimation of these properties for faults in the subsurface will of course pose a greater challenge.

Although we have considered only a relatively small number of fault regions, it is none-theless useful to comment on the variation of the fault zone permeability (k_1 and k_2) as a function of slip magnitude. The ranges of the fault-parallel permeabilities for the faults with 6 m and 14 m of slip overlap ($1087 \leq k_2 \leq 1587$), so it is difficult to identify any clear trend between these values of slip. These permeabilities are, however, in all cases higher than the fault-parallel permeabilities for the fault with 150 m of slip. Though these differences in the fault-parallel permeabilities are not very large, the results do suggest the presence of a maxi-mum in fault-parallel permeability at some value of slip (~ 10 m), recalling that the perme-ability with zero slip is that of the host rock, 200 md.

A trend can also be observed for the fault-normal component of permeability, though again the number of regions considered is small. Specifically, at the lower values of slip (6 m and 14 m), fault-normal permeabilities are on average higher and show more variation than they do for the fault with 150 m of slip. We cannot conclude from our data whether there is or is not a local maximum in the fault-normal permeabilities, though it is clear that the fault-normal permeability decreases significantly at high slip, when the fault core is wide and continuous.

According to field observation as well as theory, slip magnitude varies along a single fault. Thus, as indicated by the results presented here, the fault zone permeability along the fault will also vary. Therefore, a single fault may show both a trend as well as considerable small scale variation in fault zone permeability (cf. Figure 4.5). Both of these effects can lead to complex flow behavior in the vicinity of the fault.

Because the large scale flow properties of faults are dependent on the fine scale geom-etry and distribution of the fault zone components, more detailed studies such as this will be required to develop a more complete understanding of the impact of faults on flow in the
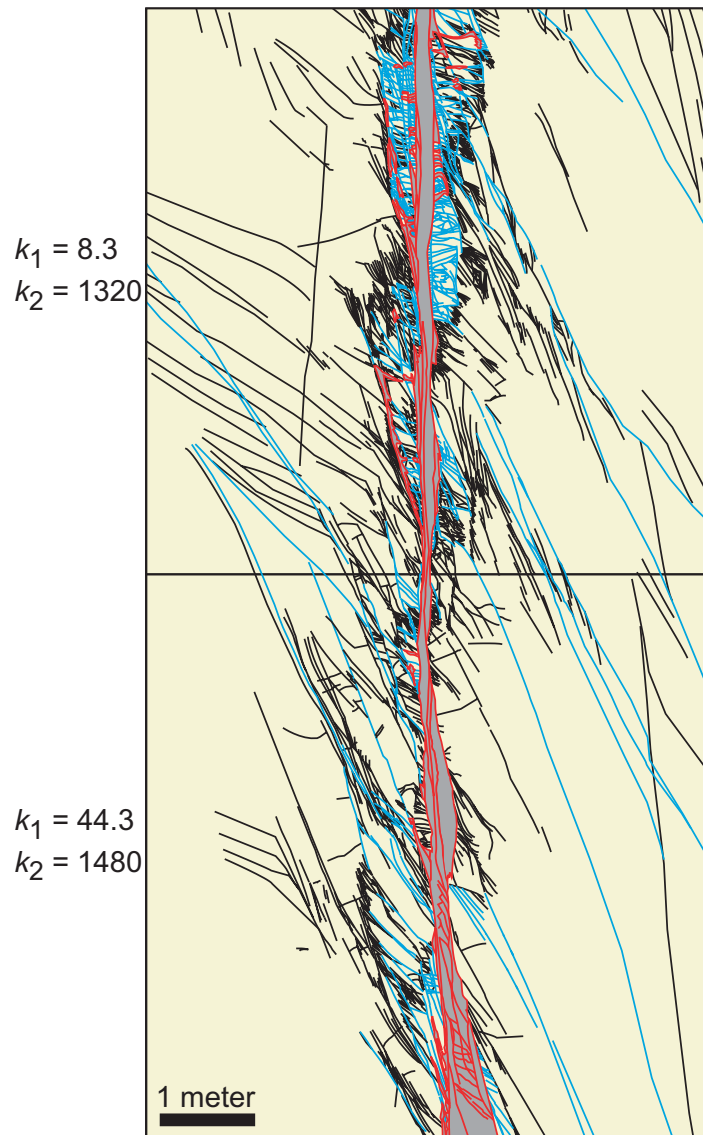
116
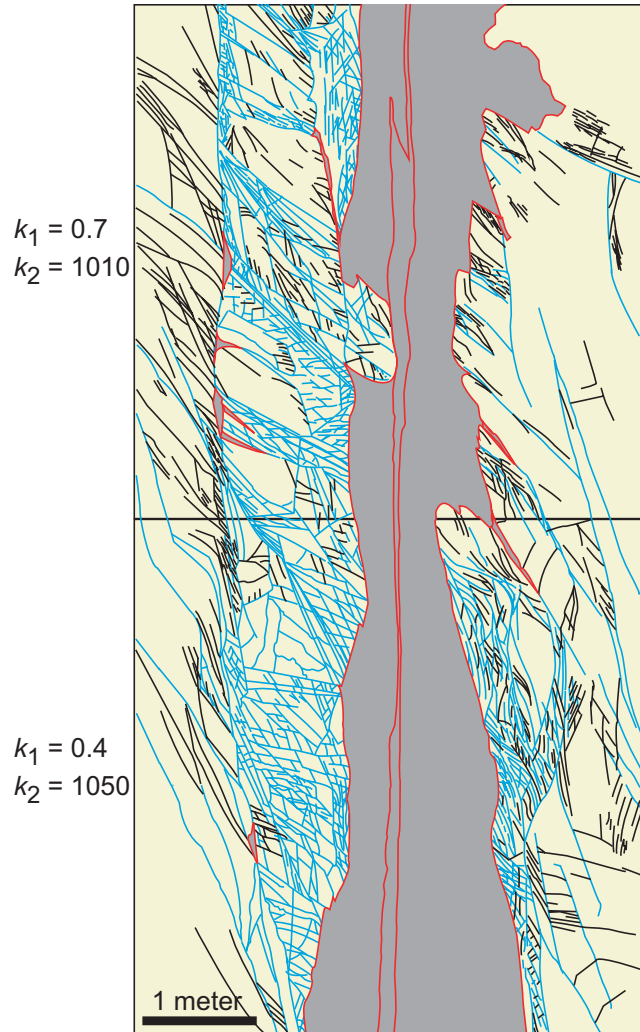
Figure 4.9. A strike-slip fault with 150 m of slip (from Myers, 1999) and two fault zone regions for which k_1 and k_2 are computed. The values of both k_1 and k_2 are lower here than for the other two faults.

subsurface. This type of analysis should be conducted for different types of faults, including faults with clay smears. Once this more comprehensive understanding is achieved, simpler correlations, relating fault zone permeability to appropriate fault zone statistics, can be developed and applied in practice. An initial application of this overall methodology was recently presented by Flodin et al. (2001) (see Appendix B), who introduced fault zone permeabilities as computed here into a reservoir simulation model. The significant impact of the fault zone, as well as the effect of the variation in fault zone properties on large scale reservoir flow and transport, was illustrated for a number of different flow scenarios.

Conclusions

The following main conclusions can be drawn from this work:

(1) A methodology for the determination of fault zone permeabilities for use in large scale reservoir simulation was presented and applied. The method combines fine scale outcrop characterizations, estimates of the properties of fault zone elements, and detailed numerical calculations to arrive at large scale fault zone permeability tensors.

(2) The results illustrate interesting trends in fault zone permeability as a function of shear strain. The fault-parallel component of permeability displays a maximum, while the fault-normal component of permeability is lowest and shows the least variation at the highest value of slip considered (150 m). Results for fault-normal permeability are not sensitive to the fracture aperture, while those for fault-parallel permeability are highly sensitive.

(3) The methods described here can be applied to other types of faults and can be used to develop accurate correlations for fault zone permeability as a function of fault slip and other relevant fault zone petrophysical parameters.

118

Chapter 5

Flow and transport modeling of sheared-joint faults in sandstone: boundary condition effects and explicit fracture modeling

Abstract

Equivalent permeabilities of sheared joint faults in sandstone are shown to be highly sensitive to the local boundary conditions used in the upscaling calculations. When large-scale, through-going features are present, pressure – no-flow and mirror-periodic boundary conditions provide upscaled permeabilities that capture the global flow characteristics of upscaled fault regions. Periodic boundary conditions tend to break the connectivity between both high and low permeability features, which can result in erroneous upscaled permeabilities in regions with through-going features. This sensitivity to boundary conditions calls into question the robustness of the upscaled permeability and suggests that dominant through-going features are best modeled explicitly. In addition, due to the small dimensions and high permeability of some through-going structural features (e.g., slip surfaces), globally upscaled models are inadequate for the modeling of transport. To address these issues, we introduce a step-wise method of removing the through-going high-permeability features from the fine model, upscaling to a coarse grid, and then reintroducing the high-permeability features back into the coarsened model. This procedure is shown to provide coarse models that give accurate predictions for both flow and transport.

Introduction

Reservoir simulation models typically use cell sizes that have dimensions of 50-100 m, while geocellular models of reservoirs have cell dimensions that are smaller (e.g., 1-10 m). Recent efforts describing the flow characteristics of fault zones have utilized outcrop-based models with cell sizes as small as 3 mm (see Chapter 4). To bridge the gap between computationally efficient models that are appropriate for reservoir simulation, and the finer-scale geological models, an upscaling methodology is necessary. The goal of upscaling is to replace the fine-scale model with a coarsened model, while preserving the flow and

119

transport properties of the fine model. A variety of methodologies to upscale flow behavior exist, including both numerical flow simulation (e.g. Durlofsky, 1991) and power averaging techniques (e.g., Deutsch, 1989). Thorough reviews of various upscaling methodologies can be found in Wen and Gomez-Hernandez (1996) and Renard and de Marsily (1997). In this paper, a finite different solution to the single-phase flow equation subject to a variety of boundary conditions is used to calculate upscaled quantities.

This paper builds on Chapter 4 and further explores the effects of boundary conditions on upscaled fault permeabilities. We consider pressure – no-flow, periodic, and mirror-periodic boundary conditions. Additionally, we attempt to improve the accuracy of coarse-scale models by explicitly retaining the most important flow features of the fault zone.

We proceed as follows. The various boundary conditions under investigation are first introduced by examining a simple, idealized permeability field. The different boundary conditions are then applied to more complicated permeability fields that occur in the vicinity of a fault. Based on these results, it is found that some features within the fault zone cannot be accurately upscaled using conventional techniques. This leads to the second focus of the paper, in which the important through-going flow features of the fault zone are explicitly represented, while the remaining features are upscaled. The efficacy of this procedure is demonstrated by comparing global flux and transport calculations between the original fine-scale model, coarsened versions of the original fine-scale model using standard techniques, and coarsened versions of the original fine-scale model where the important through-going features are explicitly represented.

Flow equations and boundary conditions

Single-phase, steady-state incompressible flow through a heterogeneous porous medium is described by Darcy's law and the continuity equation:

$$\mathbf{u} = -\frac{1}{\mu}\mathbf{k} \cdot \nabla p, \tag{1}$$

and,

120

$$\nabla \cdot \mathbf{u} = 0, \tag{2}$$

where u is the fluid velocity vector, p is pressure, μ is the fluid viscosity, and **k** is the permeability tensor. We use a two dimensional finite difference approximation of these combined equations, subject to a variety of boundary conditions, to calculate flow on the fine-scale. The upscaled permeability tensor is subsequently computed from these simulations. In the following subsections, we describe the three different boundary conditions which were applied to the above flow problem, as well as the various techniques used to compute upscaled permeability values.

Pressure – no-flow boundary conditions

The most straightforward boundary condition we apply is that of pressure – no-flow (Figure 5.1a). The flow problem is solved in both the x- and y-directions. In the case of the x-flow solution, we prescribe $p = 1$ on the left-edge and $p = 0$ on the right edge, while no-flow conditions are applied to the other two boundaries. The opposite scenario is used to solve for flow in the y-direction. The equivalent permeability, denoted $\mathbf{k}^*$, is calculated from these two solutions. Assuming that the principal permeabilities are aligned with the x- and y-axes (neglecting the cross terms, k^*_{yx} and k^*_{yx}) the k^*_{xx} component can be computed using the following relationship:

$$k^*_{xx} = \frac{Q_x \mu L_x}{L_y \Delta p}, \tag{3}$$

where Q_x is the total flow rate through the system, L_x and L_y are the system dimensions, and Δp is the pressure difference in the x-direction. A solution for the k^*_{yy} component is obtained using Eq. 3 and the total flow and pressure difference for the y-direction. Note that this method applies outlet averaging to compute $\mathbf{k}^*$ from the fine-scale solution. We note that this was the method used to calculate $\mathbf{k}^*$ for the fault zones in Chapter 4.

(a) Pressure - no-flow

(b) Periodic

target domain

modeled domain

(c) Mirror-periodic

target domain

0.1 md
10 md
100 md
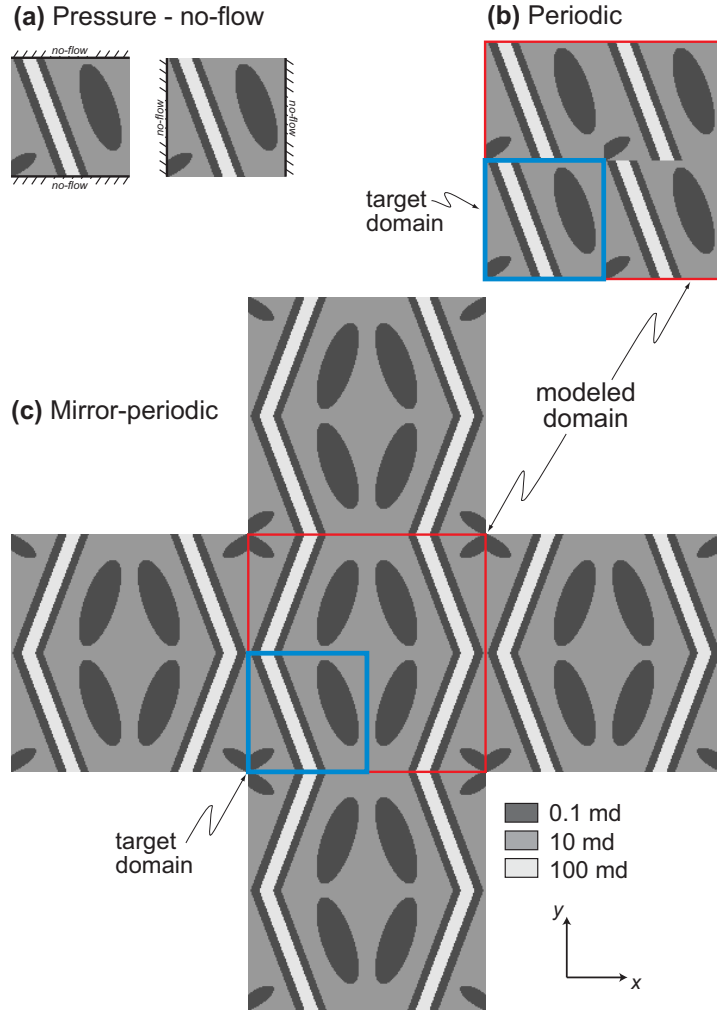
Figure 5.1. Boundary condition examples. **(a)** Pressure – no-flow boundary condition. **(b)** Periodic boundary conditions. **(c)** Mirror-periodic boundary conditions.

When the orientations of the principal permeabilities are unknown, a more general solution for $\mathbf{k}^*$ is desired. In this case the full tensor solution for $\mathbf{k}^*$ is obtained using the following relationship (Wen et al., in review):

$$\langle \mathbf{u} \rangle = -\frac{1}{\mu} \mathbf{k}^* \cdot \langle \nabla p \rangle, \tag{4}$$

where $\langle \mathbf{u} \rangle$ and $\langle \nabla p \rangle$ are the area (in two dimensions) or volume (in three dimensions) averaged Darcy velocity and pressure gradient, respectively. Symmetry for $\mathbf{k}^*$ can be enforced in several different ways. The simplest approach is to set the cross terms equal to the average of the two computed values $[(k^*_{xy} + k^*_{yx})/2]$.

Periodic boundary conditions

Periodic boundary conditions assume that the region of interest is infinitely repeated over the modeling domain. A 4× periodic repetition of the permeability field referred to above is illustrated in Figure 5.1b. From a computational standpoint, flow through the global domain need not be explicitly modeled. Rather, periodic boundary conditions are prescribed by equating flow on one side of the domain to be equal to that on the other side of the domain. That is, for the *x*-direction, $u_x(x = 0, y) = u_x(x = L_x, y)$, and for the *y*-direction, $u_y(x, y = 0) = u_y(x, y = L_y)$. The upscaled permeability tensor $\mathbf{k}^*$ is computed by solving the flow problem with pressure gradients in the *x*- and *y*-directions (pressure is prescribed to be periodic with a jump in the appropriate direction) and then applying Eq. 4. We note that, due to the properties of periodic boundary conditions, the identical $\mathbf{k}^*$ can be computed using the outlet average information (Durlofsky, 1991; 1992).

Mirror-periodic boundary conditions

Mirror-periodic boundary conditions are applied by first reflecting the modeling domain in the *y*-direction, and then reflecting the doubled domain again in the *x*-direction (Figure 5.1c). Standard periodic boundary conditions are then applied to the 4× mirrored domain. Because of symmetry, the mirrored domain (red box, Figure 5.1c) can be repeated in a truly periodic manner. A 5× periodic repetition of this mirrored domain is shown in Figure 5.1c. The motivation for reflecting the domain is to ensure connectivity across the domain borders. This method was applied by Martys et al. (1999) in flow simulations of three dimensional pore space models. Their application of mirror-periodic boundary conditions enforced pore connectivity across the domain boundaries. The upscaled permeability tensor $\mathbf{k}^*$ is computed in a similar manner as in the case of standard periodic boundary conditions. Again, from the computational standpoint, flow need not be modeled across the infinitely periodic domain.

Comparison of boundary conditions

For $\mathbf{k}^*$ to be considered a truly *effective* quantity, the computed $\mathbf{k}^*$ for a given permeability field should be the same regardless of the chosen boundary conditions. In practice, however, $\mathbf{k}^*$ computed for heterogeneous permeability fields are rarely found to be boundary condition independent. As an example of the variation in $\mathbf{k}^*$ computed with different boundary conditions, we examine the permeability field shown in Figure 5.1. This model permeability field is characterized by a through-going, high-permeability layer (100 md) imbedded within a low-permeability layer (0.1 md), both of which are oriented 20° from vertical and imbedded within an intermediate-permeability matrix (10 md). Two non-through-going, low permeability features (0.1 md) also occur within the matrix.

Permeability tensors calculated for this field using the various boundary conditions and upscaling techniques are shown in Figure 5.2. The upscaled permeability tensors for the domains shown in Figures 5.1a and 5.1c (red box) calculated using Eq. 3 and pressure – no-flow boundary conditions are both represented by the axis-aligned tensor shown in Figure 5.2a.
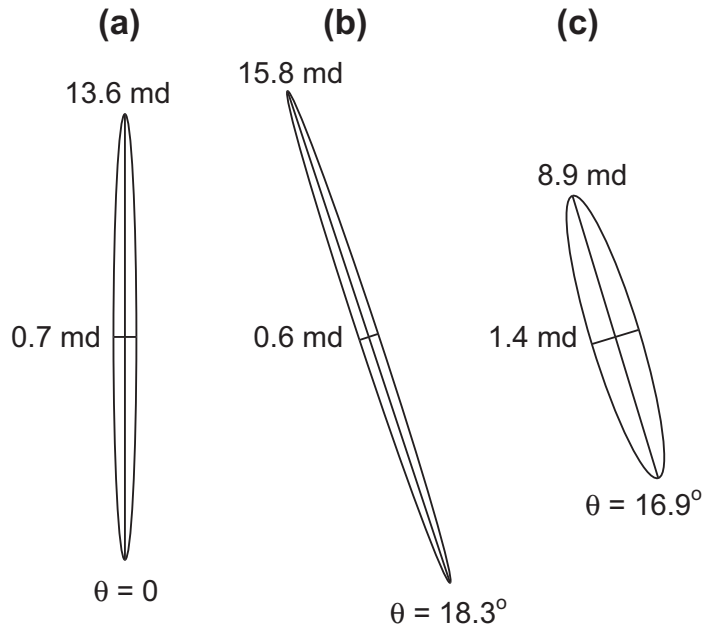

Figure 5.2. Permeability tensors for the permeability field shown in Figure 5.1 calculated using the various boundary conditions. **(a)** Outlet averaged pressure – no-flow, and area averaged mirror-periodic boundary condition results. **(b)** Area averaged pressure – no-flow and target domain mirror-periodic boundary condition results. **(c)** Periodic boundary condition results.

Using Eq. 4 and mirror-periodic boundary conditions to model flow over the entire mirrored domain shown in Figure 5.1c (red box) similarly leads to the tensor shown in Figure 5.2a. The symmetry of the mirror-periodic model results in a no-flow condition on the mirror boundaries, which in turn yields the exact same flow solution as that found for the standard pressure – no-flow simulation. Furthermore, both the pressure no-flow model, and the mirror-periodic model computed over the target domain (Figure 5.1c, blue box) yield the same tensor when calculated using Eq. 4 (Figure 5.2b). Because these two boundary conditions will always yield the exact same results, we only focus attention on pressure – no-flow conditions in subsequent discussions.
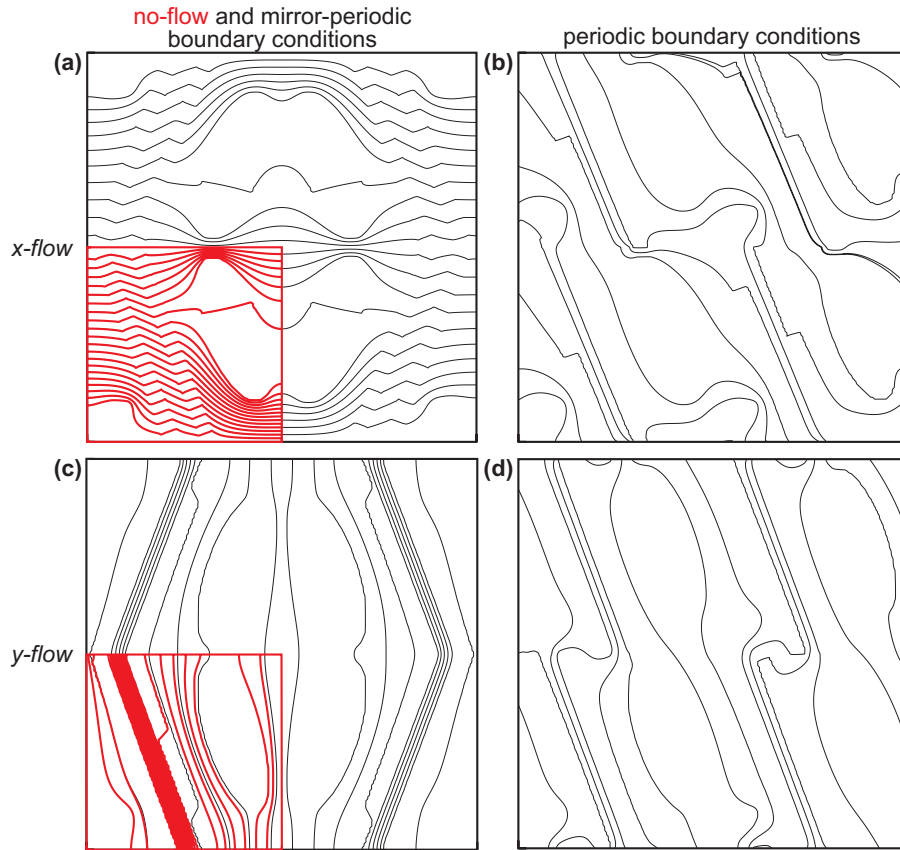

Figure 5.3. Streamline maps for the permeability fields shown in Figure 5.1. Streamlines for no-flow (red) and mirror-periodic boundary condition simulations for the **(a)** *x-* and **(c)** *y*-directions. Streamlines for periodic boundary condition simulations for the **(b)** *x-* and **(d)** *y*-directions.

In contrast to the no-flow conditions, $\mathbf{k}^*$ calculated using Eq. 4 and periodic boundary conditions yields a tensor with less contrast between the principal values than those calculated with the pressure – no-flow results (Figure 5.2c). This is due to the fact that the highest and lowest permeability features are disrupted across the periodically reproduced domains (see Figure 5.1b), which results in the loss of connectivity. In the resulting calculation of $\mathbf{k}^*$ for this system, matrix flow dominates. These similarities and dissimilarities between boundary conditions are also reflected in the streamline maps shown in Figure 5.3.

In light of the results discussed above, it is useful to consider scenarios where one boundary condition would be more appropriate than the other. Two fracture geometries are shown in Figure 5.4, a left-stepping en echelon fracture set (left), and a single, through-going fracture (right). The fractures have high permeability (k_h) relative to the matrix (k_l). We consider upscaling these models to 3×3 grids and focus on predicting global flow in the y-direction, Q_y. In the case of pressure – no-flow boundary condition simulations, k_{yy} for the three central blocks reflect the high permeability of the fractures, because each of the cells contains a locally through-going fracture (Figure 5.4b). In the case of periodic boundary condition simulations, k_{yy} for the three central blocks reflect the low permeability of the matrix (Figure 5.4c), because periodic repetition of the domain cells locally disconnects the fractures. Now considering the global flow, Q_y for the en echelon fracture geometry should reflect the low permeability matrix due to the disconnected nature of the fractures and lack of communication between them. By contrast, Q_y for the through-going fracture model should reflect the permeability of the fracture itself. Periodic boundary conditions are therefore more appropriate for naturally disconnected fracture geometries, while the pressure – no-flow boundary conditions are more appropriate for through-going fracture geometries (Figure 5.4d). This demonstrates that the appropriate local boundary conditions might depend on the larger-scale connectivity of the dominant fault zone features. In the next section, the effects of boundary conditions on upscaled quantities are further explored by examining permeability fields that occur in the vicinity of a fault zone.

(a) Original fracture geometry

(b) 3x3 k_{yy} pressure - no-flow bc result

(c) 3x3 k_{yy} periodic bc result

(d) Global Q_y

k_l k_h $k_l <<< k_h$
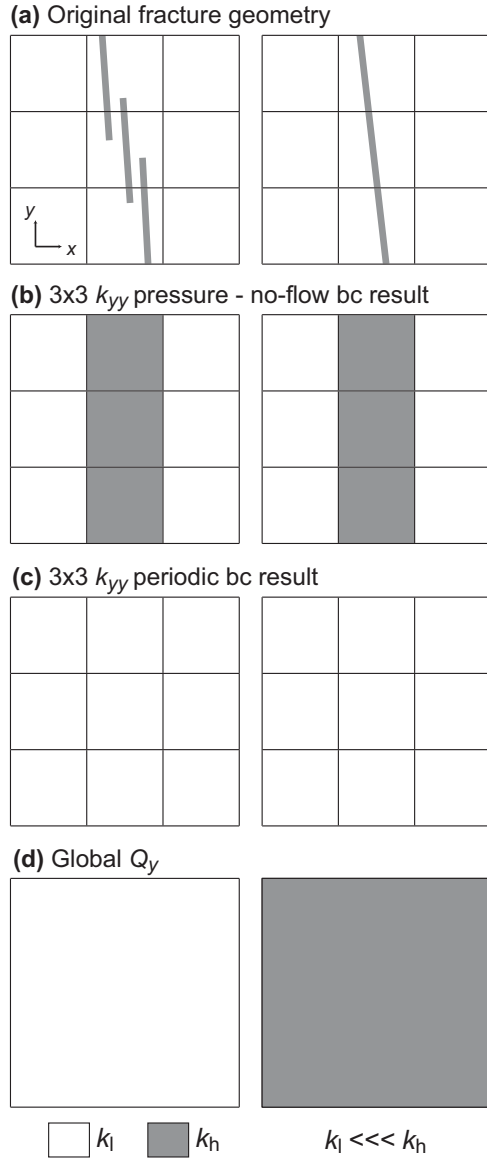
Figure 5.4. Schematic example illustrating the effects of boundary conditions used to compute **k**ˣ. **(a)** En echelon stepping fractures (left), and a single, through-going fracture (right). **(b)** 3×3 vertical upscaling using pressure – no-flow boundary conditions. **(c)** 3×3 vertical upscaling using periodic boundary conditions. **(d)** Global Q_y for both domains.

Application to fault zone permeability upscaling

The faults we study formed by shearing along preexisting joint zones in sandstone, and occur within the Aztec sandstone located in the Valley of Fire State Park of southern Nevada (Figures 1.1 and 1.3). The details of the formation mechanism of this style of faulting are discussed by Myers (1999) and elsewhere in this thesis (see Chapter 1 and Appendix A). Because this paper focuses on the effects of boundary conditions on the upscaled fault regions and not on absolute fault permeability (see Chapter 4), we chose to focus our attention on a single outcrop map of a fault (Figure 5.5).

(a) Fault with 14 m left-lateral slip
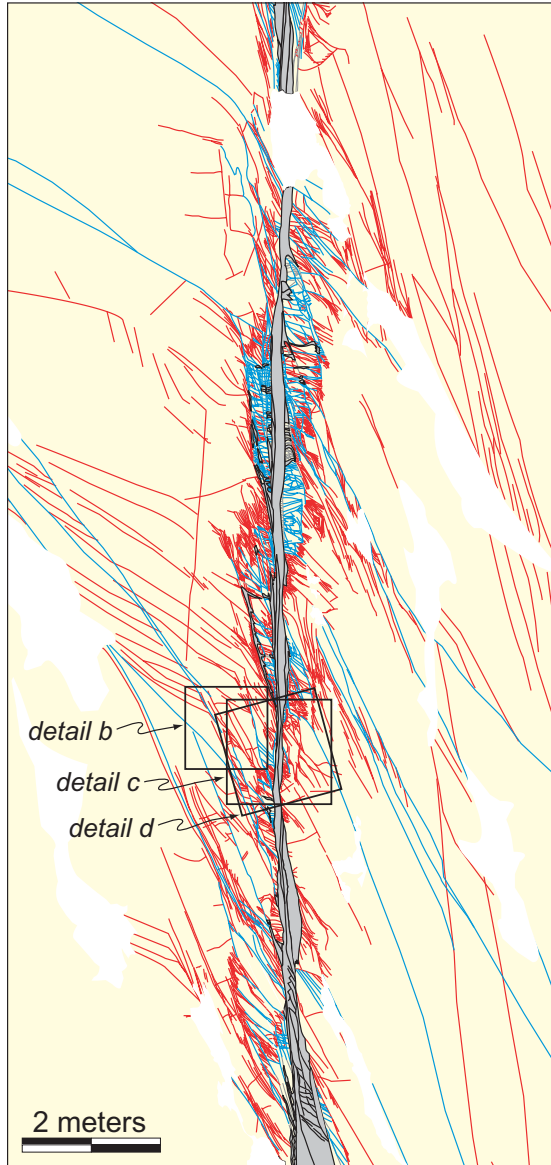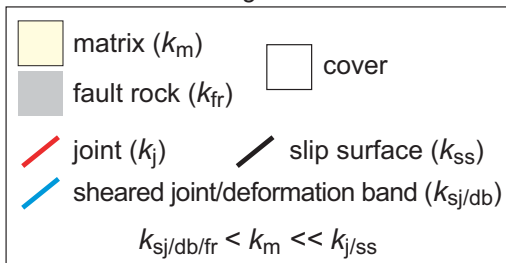
(b) Fault damage zone
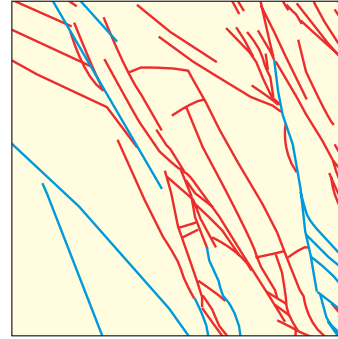
(c) Fault core

(d) Fault core - 15° CCW

detail b

detail c

detail d

2 meters

Legend

matrix (k_m)

fault rock (k_{fr})

cover

joint (k_j)

slip surface (k_{ss})

sheared joint/deformation band ($k_{sj/db}$)

$k_{sj/db/fr} < k_m << k_{j/ss}$
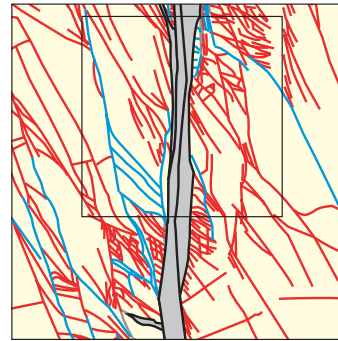
Figure 5.5. (a) Map of a sheared joint fault with 14 m left-lateral offset (after Myers, 1999). **(b)** Sub-region chosen from the fault damage zone. Model dimensions are 400×400. **(c)** Sub-region chosen from the fault core. Inset black box is the region shown in Figure 5.6a. Model dimensions are 500×500. **(d)** 15° counterclockwise-rotated version of the sub-region shown in *part (c)*. Model dimensions are 500×500.

128

The fault shown in Figure 5.5 consists of 5 structural elements, each of which exhibits a particular permeability characteristic. The elements are joints, sheared joints, deformation bands, fault rock, and slip surfaces, all of which are embedded within relatively undeformed host rock. Assignment of permeability to each of the elements is discussed in detail in Chapter 4 and by Myers (1999). We chose not to include the inherent variability in fault rock permeability values reported in Chapter 3, and instead apply a single, representative value of 0.1 md, in accord with the value used in Chapter 4. Similarly, sheared joints and deformation bands are assigned a permeability of 0.1 md. Permeability for joints and slip surfaces are calculated using a parallel-plate model with an aperture of 0.25 mm. Finally, host rock is assigned a permeability of 200 md.

Upscaling results

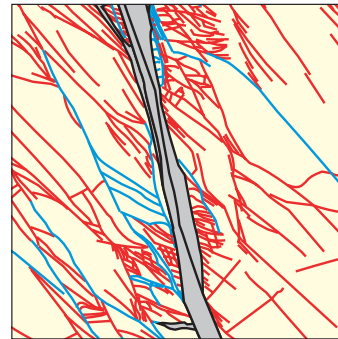We choose three regions from the fault zone shown in Figure 5.5a to investigate. For each of the three regions, three upscaling methods are evaluated: (1) pressure – no-flow with $\mathbf{k}^*$ computed from the outlet average (no-flow-outlet); (2) pressure – no-flow with $\mathbf{k}^*$ computed from the area average (no-flow-area); and, (3) periodic boundary conditions. The first region is extracted from the fault damage zone (Figure 5.5b). This region of the fault is characterized by the occurrence of variably oriented structural elements (joints and sheared joints) that do not form a connected network at the larger-scale. Results for the simulations of this permeability field using the three different boundary conditions are presented in Table 5.1. Principal permeabilities calculated using no-flow-area and periodic boundary conditions are in qualitative agreement. The no-flow-outlet result deviates slightly from the

Table 5.1. Upscaling results for the maps shown in Figures 5.5b-5.5c.

input map	boundary condition	principal permeability		
		k_1	k_2	θ
Fault damage zone	no-flow outlet	1026.4	210.5	-
(Figure 5.5b)	no-flow area	1708.8	154.0	26.8
	pbc	1250.6	184.1	30.0
Fault core	no-flow outlet	4274.8	4.9	-
(Figure 5.5c)	no-flow area	4267.7	4.9	-0.29
	pbc	1740.1	4.9	0.22
Fault core - 15° CCW	no-flow outlet	3552.1	5.5	-
(Figure 5.5d)	no-flow area	4298.9	4.5	14.7
	pbc	2309.7	229.6	32.9

other two results due to the fact that the cross-terms are implicitly assumed to be zero. As such, this result does not reflect the 26-30° orientation of $\mathbf{k}^*$. The periodic and no-flow-area results are in fair agreement because the permeability field lacks through-going features with high-contrast permeability.

The second region is of an area selected from the fault core (Figure 5.5c). This area of the fault zone is characterized by a through-going low-permeability fault rock seam with associated through-going high permeability slip surfaces. In the immediate periphery of the fault rock zone is a dense network of joints, sheared joints, and deformation bands. No-flow-area and no-flow-outlet calculations of k_1 yield nearly identical results, while the periodic boundary condition result is over a factor of two less (Table 5.1). In all three cases, nearly all of the flow in the k_1 direction is focused along the through-going slip surfaces. For the k_2 direction, all methods yield the same results because of the presence of the through-going low permeability fault rock. Because the two dominant low and high permeability features are aligned with the y-axis, the cross-terms are negligible and the principal permeabilities are not rotated (Table 5.1). Hence, the close agreement between the no-flow-outlet and no-flow-area results. For this case, the calculation with periodic boundary conditions gives lower values for k_1 because the large-scale connectivity is not maintained.

The third region is a 15° counterclockwise-rotated version of approximately the same fault core region used in the second example (Figure 5.5d). This example shows the greatest difference in results between the no-flow and periodic boundary condition simulations. The principal permeabilities for both no-flow methods are in relatively good agreement, though the no-flow-outlet result does not recover the 15° counterclockwise rotation of the model domain (Table 5.1). Compared to the no-flow results, k_1 for the periodic boundary condition result is nearly a factor of two less, while k_2 is more than an order of magnitude greater. This is due to the fact that, in the periodic domain, the low permeability fault rock no longer forms a lateral barrier and flow is allowed to bypass the fault core to some extent. This leads to the anomalously high k_2 value and the greater rotation of the principal permeabilities.

Discrete fracture modeling

The results of the previous section illustrate that the upscaled permeabilities of fault zones can be highly dependent on the boundary conditions used for the $\mathbf{k}^*$ calculation. These ambiguities result when we try to "effectivize" dominant through-going features. This sensitivity to boundary conditions is perhaps not surprising since homogenization theory requires that the relevant heterogeneities be small relative to the size of the upscaled region. This requirement is clearly violated in our calculations. For this reason, we now explore the notion of explicitly representing the dominant through-going high permeability features in otherwise upscaled fault permeability models. The procedure is as follows. First, we remove the high permeability, through-going features from the fine-scale fault permeability field. We then upscale this model to a coarse grid. Finally, we reintroduce the high permeability features back into the coarsened model.

Lee at el. (2001) take a similar approach to modeling flow in fractured reservoirs. In their three-step methodology, they first derive an analytical solution to account for the permeability influence of the shortest fractures. They then apply a numerical boundary element method to upscale the medium length fractures embedded within the permeability field obtained from the analytical result. Finally, they explicitly model the longest fractures within the permeability field obtained in the previous two steps. Our methodology differs in that we explicitly model the slip surfaces as local grid refinements to our coarsened model (similar to the approach of Durlofsky et al, 1997), whereas Lee et al. (2001) represent the large fractures as producing wells. In the next section we apply our methodology to an example fault zone and test the accuracy by comparing global flow rates and oil cut (fraction of oil in a produced well) between a fine-scale model and the upscaled models. The reader is referred to Durlofsky et al. (1997) for a discussion on calculating oil cut in a unit mobility ratio displacement simulation.

Application to a fault zone example

We apply our upscaling methodology to a 300×300 sub-region selected from the fault map shown in Figure 5.5c (Figure 5.6a). In the first step, we remove the through-going slip surfaces from the fine-scale fault map (Figure 5.6b), and then upscale to a coarse grid. For
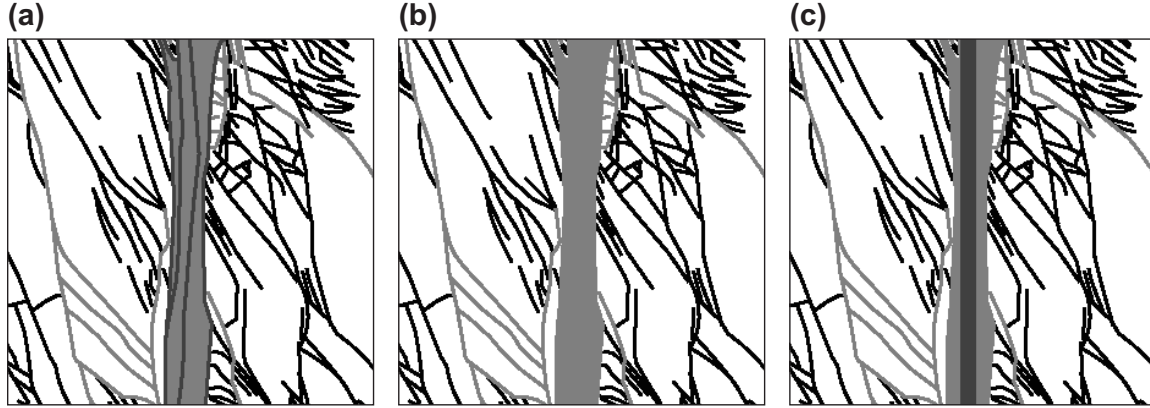
Figure 5.6. (a) Sub-region of the fault core shown in Figure 5.5c. **(b)** The same region shown in *part (a)* without the through-going slip surfaces. **(c)** The same region shown in *part (b)* with a uniform 13-pixel wide slip surface added. All regions have model dimensions 300×300.

the local upscaling problem we use no-flow boundary conditions and compute $\mathbf{k}^*$ using the outlet average. To test the robustness of the upscaling, four different grid coarsenings were chosen: 50×50, 30×30, 10×10, and 3×3 (Figures 5.7a-5.7d). Finally, we reintroduce a single, uniform slip surface to the central portion of the upscaled models. The properties and dimensions of the uniform slip surface were calibrated to the original fine-scale model. This was done by matching global flow rates between the original fine-scale model and a modified version of the fine-scale model with the single uniform slip surface (Figure 5.6c) (Table 5.2). Replacing the original slip surfaces with the uniform slip surface in the fine-scale model was done simply for numerical convenience. Specifically, the finite difference code applied in this study uses Cartesian grids, so slip surfaces not aligned with the *y*-axis could not be accurately modeled on coarse grids. The uniform slip surface we apply to the fine model is, however, aligned to the *y*-axis.

Comparisons of global flow results between the variously upscaled models with the reintroduced uniform slip surface model are shown in Table 5.2. Flow rates in the *y*-direction are in fair agreement (all within 18% of the fine-grid result) between all of the tested models (Table 5.2). However, for flow in the *x*-direction, the upscaled models differ from the fine model by as much as 50%. In the 50×50 case, the *x*-flow was overestimated, while in the other cases it was underestimated (Table 5.2). These discrepancies are likely due to
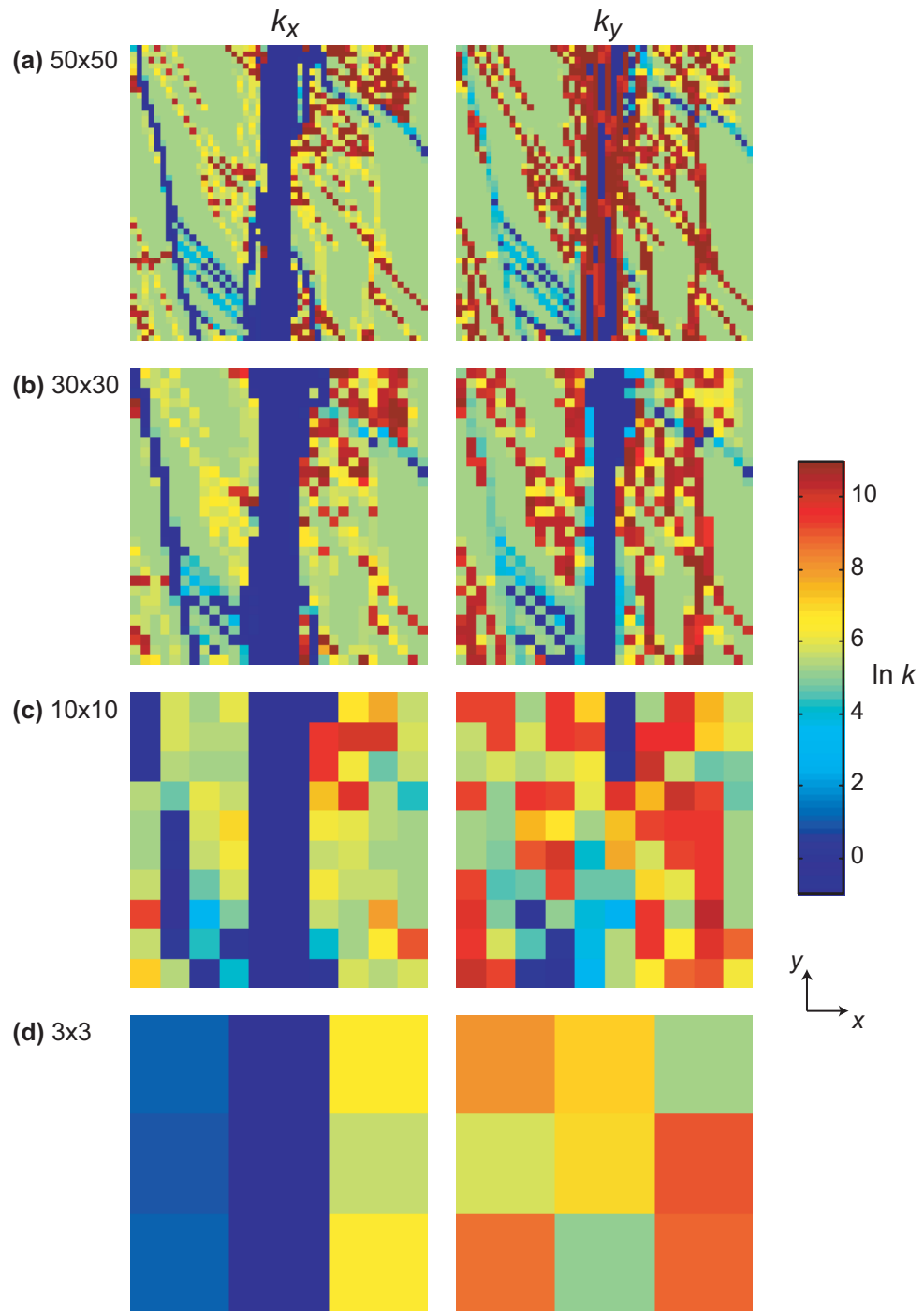
Figure 5.7. Upscaling results using local pressure – no-flow boundary conditions and the input map shown in Figure 5.6b.

Table 5.2. Global flow characteristics for the permeability field shown in Figures 5.6a, 5.6c, and 5.7a-5.7d. uniSS = uniform slip surface.

input model	dimension	global	
		Q_x	Q_y
original with uniSS (Figure 5.6c)	300×300	1.16	6574.9
coarsened model (Figure 5.7a) with added uniSS	50×50	1.74	7025.7
coarsened model (Figure 5.7b) with added uniSS	30×30	0.90	6777.1
coarsened model (Figure 5.7c) with added uniSS	10×10	0.85	7766.1
coarsened model (Figure 5.7d) with added uniSS	3×3	0.76	7016.2

permeability changes in the fault periphery of the upscaled models. High flow features that were locally continuous in the fine model were rendered discontinuous in the coarsened model.

To test the transport properties of the upscaled models, we simulate the outlet oil cut (F_o) in an oil-water system, as a function of pore volume injected (pvi = Qt/V_p, where t = time and V_p = pore volume). To simplify the results, we assume that oil and water have the same properties (unit mobility ratio displacements). For the fractional flow simulations in the x-direction (fault-perpendicular flow), the finer upscaled models better match the flow behavior of the original models (Figure 5.8a). This is likely due to the increasing loss of connection of high permeability features in the fault periphery with increasing coarsening, which was similarly noted in the previously discussed global flow calculations. All of the upscaled models adequately reproduced the initial breakthrough behavior of the fine-scale models for flow in the y-direction (fault-parallel flow) (Figure 5.8b). Note that this break-through occurs at very early time (0.05 pvi). Also shown on the fractional flow curves is the result for a 1×1 globally upscaled region, which is the approach taken in Chapter 4. In this case, the permeability is homogeneous and breakthrough occurs at 1 pvi. This indicates that, although the flux can be adequately matched using a single global value for $\mathbf{k}^*$, the transport behavior cannot. However, as indicated by the above results, the transport proper-ties can be greatly improved through the reintroduction of the slip surfaces, even when the model is otherwise very coarse.
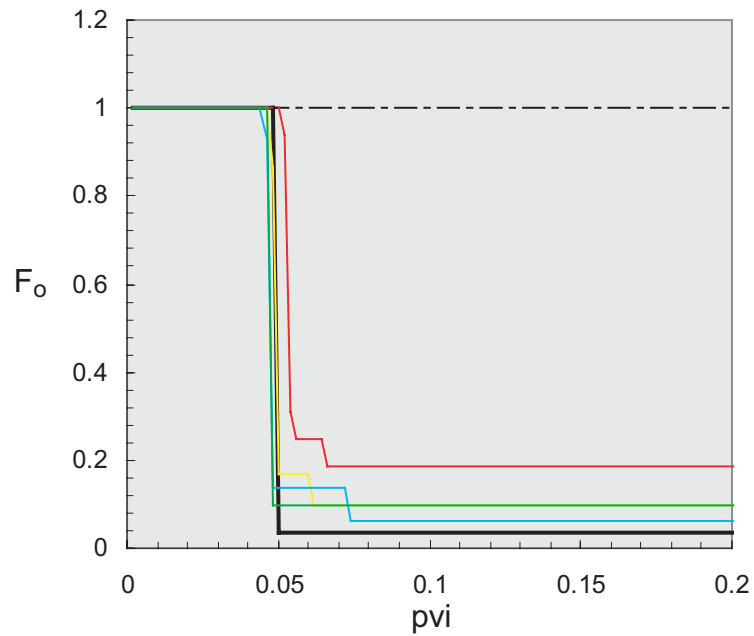
(a) *x-flow*
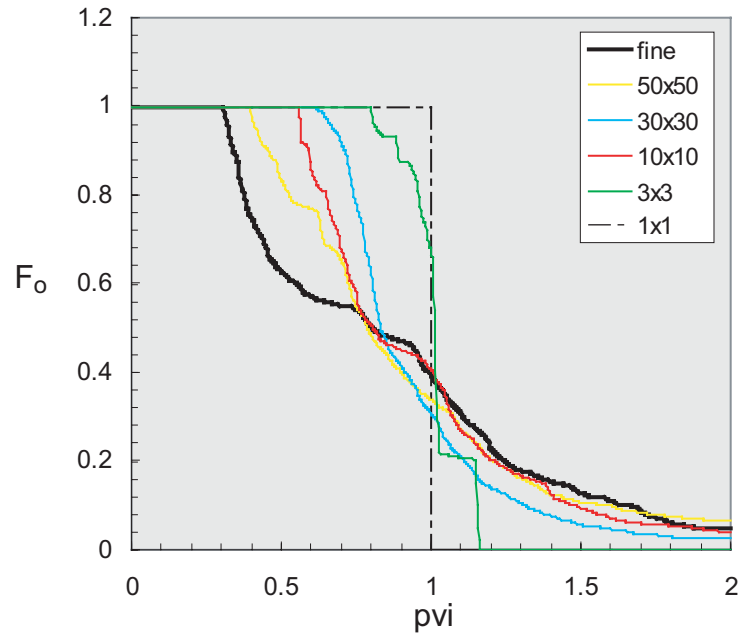
(b) *y-flow*

Figure 5.8. Fractional flow of oil (F_o) versus pore volume injected (pvi) at the outlet edges for **(a)** *x-* and **(b)** *y*-flow.

135

Conclusions

The choices of pressure – no-flow, periodic, and mirror-periodic boundary conditions applied to fault permeability upscaling problems are shown to influence calculated results in many cases. Considering fault parallel flow, the greatest effect is due to the difficulty of capturing the effects of through-going, high permeability features. In the case of the faults that we study, the features that most impact the calculated permeability are the slip surfaces. High permeability joints in the fault damage zone have less effect because they tend to be less continuous, due to both their small dimensions and the fact that they are interrupted by low permeability sheared joints and deformation bands. Pressure – no-flow boundary conditions are found to better represent upscaled quantities than do periodic boundary conditions for the large-scale features considered here. This is due to periodic boundary conditions breaking connectivity of through-going low and high permeability features across the modeling domain. However, we find that rather than attempting to upscale the through-going features, a better course of action is to model them explicitly and to upscale the background of less connected features. In doing so, we find significant quantitative improvements in representing the flow behavior of fault zones using highly coarsened models.

136

Appendix A

Faults with asymmetric damage zones in sandstone, Valley of Fire State Park, southern Nevada

Abstract

Models for the evolution of faults formed by shearing along joints zones in Aztec sandstone, Valley of Fire, Nevada predict damage zones either localized within the fault core or symmetrically distributed about the core or a slip surface therein. We expand these models by presenting two examples of faults with asymmetric damage from the same field locality. We attribute asymmetric damage to the inherited geometry of a parent joint with a peripheral joint breakdown fringe. One example is of a fault formed along a parent joint with continuous breakdown fringe. The other example is of a fault formed in part along a parent joint with abrupt breakdown fringe. When compared to the symmetric examples the damage in the asymmetric case is minimized due to the presence of an already through-going surface.

Introduction

Numerous examples of faults which form along preexisting weaknesses (e.g., joints, veins, bedding surfaces) in rock have been described in granites (e.g., Segall and Pollard, 1983), carbonates (e.g., Willemse et al., 1997), shales (e.g., Engelder et al., 2001), sandstones (e.g., Myers and Aydin, *in review*), and layered clastic sequences (e.g., Kim et al., 2001). In this paper, we focus on faults formed along joint zones in sandstone with particular attention on the formation of asymmetric damage zones.

Myers and Aydin (*in review*) propose that initial joint zone configuration bears strong influence on the final outcome of damage distribution on faults with small to moderate offsets in sandstone. We present a companion model to that of Myers and Aydin to explain new observations of asymmetric damage with respect to the fault core and associated slip surfaces along small offset faults. In this paper, we briefly introduce the geological setting

of the study area and the concepts of fault evolution reported by Myers and Aydin. We then present examples of asymmetric joint breakdown fringe and fault architectures with asymmetric damage zones. Finally, we offer our conceptual model that relates faults with asymmetric damage zones to preexisting joint breakdown geometry.

Geologic setting

We focus on faults in the Jurassic Aztec sandstone exposed within the Valley of Fire State Park of southern Nevada (Figure A.1), the same field locality of Myers and Aydin (*in review*). The Aztec sandstone is of aeolian origin and is correlative with the Navajo sandstone of the Colorado Plateau (Blakey, 1989). It is poorly to moderately well-cemented and is composed mostly of rounded to well-rounded quartz sand and has less than 5 percent detrital feldspar and lesser amounts of clay and opaque minerals.

Within the vicinity of the Valley of Fire, the Aztec sandstone has been subjected to at least two distinct deformation events. (1) Shortening related to the Cretaceous and early-Tertiary(?) Sevier orogeny (Bohannon, 1983). During this period, the Aztec sandstone was deformed by deformation band based faults and slip along dune boundary interfaces (Hill, 1989; Myers, 1999; Taylor, 1999). (2) Strike-slip and normal faulting apparently related to
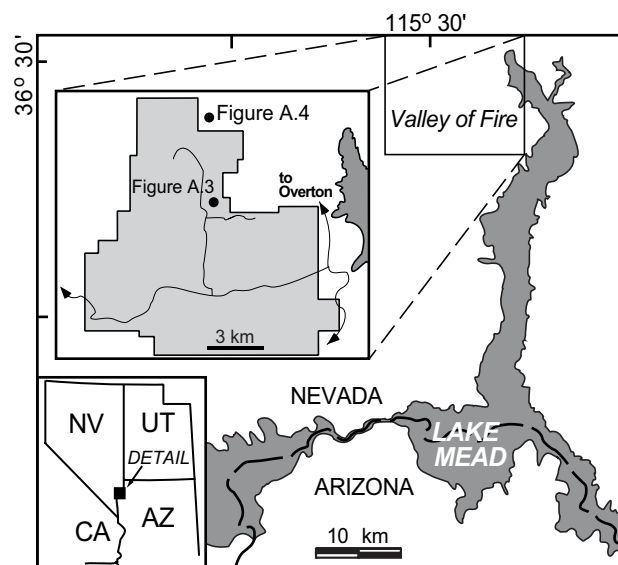

Figure A.1. Map of the study area, Valley of Fire State Park, southern Nevada, USA (after Myers, 1999). Note the approximated locations for Figures A.3 and A.4.

138

Miocene Basin and Range extension. During this period, the Aztec sandstone within the Valley of Fire deformed by sheared joint based strike-slip faulting with a lesser normal slip component (Myers and Aydin, *in review*). Jointing of the Aztec sandstone is considered to have occurred sometime after the formation of the deformation bands and before the formation of the strike-slip faults (Myers, 1999; Taylor, 1999).

Sheared-joint faults in sandstone

Myers and Aydin (*in review*) describe a hierarchical process of fault evolution that begins with shearing along preexisting joint zones, this in turn creating fragmentation zones at joint intersections and newly formed joints near the ends of preexisting joints and in areas of preexisting joint stepovers. This process is repeated as localized shear strain continues to accumulate; fragmentation zones are further crushed to form isolated pockets of fault rock. Eventually, a through going slip surface develops and the discontinuous fault rock pockets coalesce to form a continuous fault rock seam. Myers and Aydin present a conceptual model based on three end-member preexisting joint configurations: (1) en echelon joint zones that have the same step- and shear-sense (e.g., right-stepping joints and right-lateral shear); (2) en echelon joint zones that have opposite step- and shear-sense (e.g., right-stepping joints and left-lateral shear); and, (3) subparallel joint zones characterized by a large joint length to joint spacing ratio. In each case, fault related damage is more or less symmetrically distributed with respect to a centrally located fault core and associated slip surface (i.e., damage occurs on both sides).

Field observations

The architecture of faults that form along preexisting joint zones is influenced by the spatially arrangement of the preexisting joints. In order to understand fault zone architectures with asymmetric damage zones, we first examine the breakdown fringe patterns of unsheared joint zones.

Joints with asymmetric breakdown fringe

Previous studies have described the formation of a breakdown fringe along the perimeter of opening mode (mode I) fractures (Hodgson, 1961; Pollard and Aydin, 1988; Younes and Engelder, 1999). Breakdown fringes are caused by either spatially or temporally varying stress about a mode I fracture (Pollard et al., 1982). Continuous breakdown where the fringe joints share a surface with the parent joint is generally attributed to spatial variations in stress. Abrupt breakdown where the parent and fringe joints do not share a common surface is generally attributed to temporal variations in stress (Pollard and Aydin, 1988; Younes and Engelder, 1999).

We present two different examples of joint breakdown pattern that are asymmetrically distributed with respect to a through-going parent joint (Figure A.2). In both cases, the parent joint surfaces have preserved features diagnostic of opening mode displacement discontinuity (e.g., rib marks and hackle) and lack noticeable shear displacement discontinuity. The first (Figures A.2a and A.2b) is an example of continuous breakdown. Each joint in the breakdown zone forms a continuous surface with the parent joint below. In map view, these fringe joints show a slightly curving geometry in a direction concave away from the parent joint. Measured away from the parent joint, the fringe joints form angles between 8°-13° with respect to the parent joint. The second example (Figures A.2c and A.2d) is that of abrupt breakdown: no continuous surface exists between the parent joint and the fringe joints. In this example, angles between the fringe joints and the parent joint range from 33°-37°. Most of the fringe joints are confined to one side of the parent joint. However, some of the fringe joints locally extend to the other side of the parent joint tipline (arrow, Figures A.2c and A.2d). In outcrop, the abrupt breakdown joints generally have a straight trace (Figure A.2c).

Faults with asymmetric damage zones

We present two field examples of faults with asymmetric damage zones. The first example shows a slip surface with secondary fractures that have a smooth, continuous connection to the through-going slip surface (Figure A.3). The second example is a slip surface with a set of secondary fractures that have a sharp, discontinuous connection to the through-going slip surface (Figure A.4).
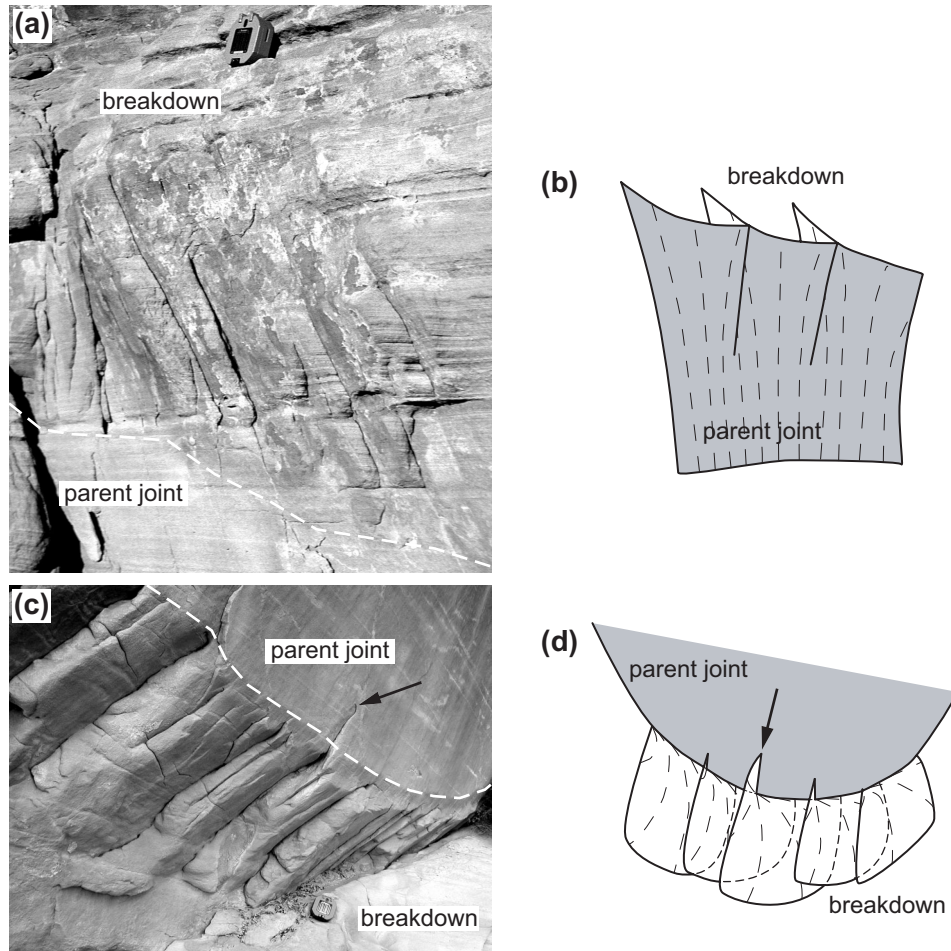
140

Figure A.2. Asymmetric joint breakdown fringe in sandstone. **(a)** Field example of continuous joint breakdown fringe. **(b)** Schematic drawing of continuous joint breakdown. **(c)** Field example of abrupt joint breakdown fringe. **(d)** Schematic drawing of abrupt joint breakdown. In parts **a** and **c**, the white dashed line demarcates the approximate boundary between the parent joint and the breakdown zone. A Brunton compass is shown in both pictures for scale.

Slip surface with curved peripheral fractures

The fault shown in Figure A.3 shows a maximum left-lateral offset of approximately 1 cm. Two general observations are made about this fault. First, damage is localized along one side of the fault. Second, compared to faults formed along en echelon joint zones with similar offset magnitude (Myers and Aydin, *in review*), damage is greatly minimized. Slip along this fault is localized along a slightly undulating and through-going slip surface. At first glance, all of the joints emanating from the through-going slip surface might be interpreted as splay fractures formed in response to shearing across a planar discontinuity
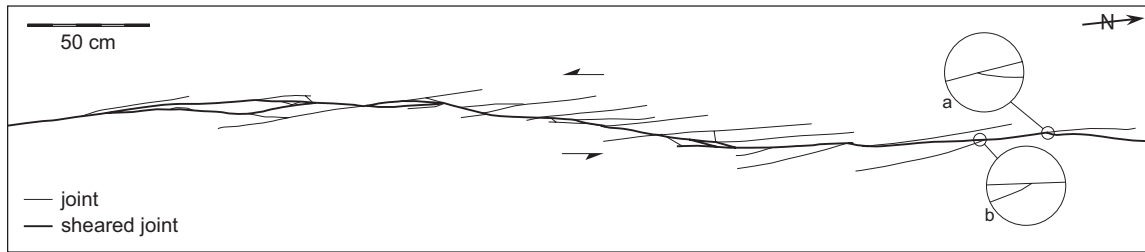
Figure A.3. Strike-slip fault with 1 cm maximum left-lateral offset that is characterized by curved secondary fractures localized primarily on one side of a through-going slip surface. **(a)** Detail of the intersection between a peripheral fracture and the through-going slip surface. **(b)** Detail of the intersection between a peripheral fracture and the through-going slip surface.

(e.g., Segall and Pollard, 1983). However upon closer examination of the fracture intersections, many of the abutting relationships are atypical of those normally found between splay fractures and parent sheared joints (e.g., *inset a*, Figure A.3) (e.g., Martel and Boger, 1997). Splay fractures are generally found to truncate against the parent sheared surface (e.g., *inset b*, Figure A.3), whereas here most of the peripheral fractures are continuous with the through-going fractures. Away from the through-going slip surface, the peripheral joints follow a curved trace. Close to the slip surface, the average angle between the parent sheared joint and peripheral joints is 9º (±3º), while the angle between the last increment of the peripheral joint tip and that of the parent joint is 21º (±7º).

Slip surface with primarily straight peripheral fractures

The fault shown in Figure A.4 has a maximum apparent left-lateral offset (with a minor normal-slip component) of 85 cm that occurs near the center of the fault and decreases approximately linearly toward both ends. When viewed along its entire length, this fault shows considerable variability with respect to peripheral damage. The northern half of the fault (north of the midsection of *inset b*, Figure A.4a) is characterized by approximately symmetrically distributed peripheral fractures about a complicated network of subparallel and branching slip surfaces. The peripheral joints in this section of the fault form acute angles with slip surfaces that face in a direction opposite to the slip sense. These peripheral joints might also be viewed as right-stepping. These observations contrast with observations of the southern portion of the fault where the peripheral joints are localized along the
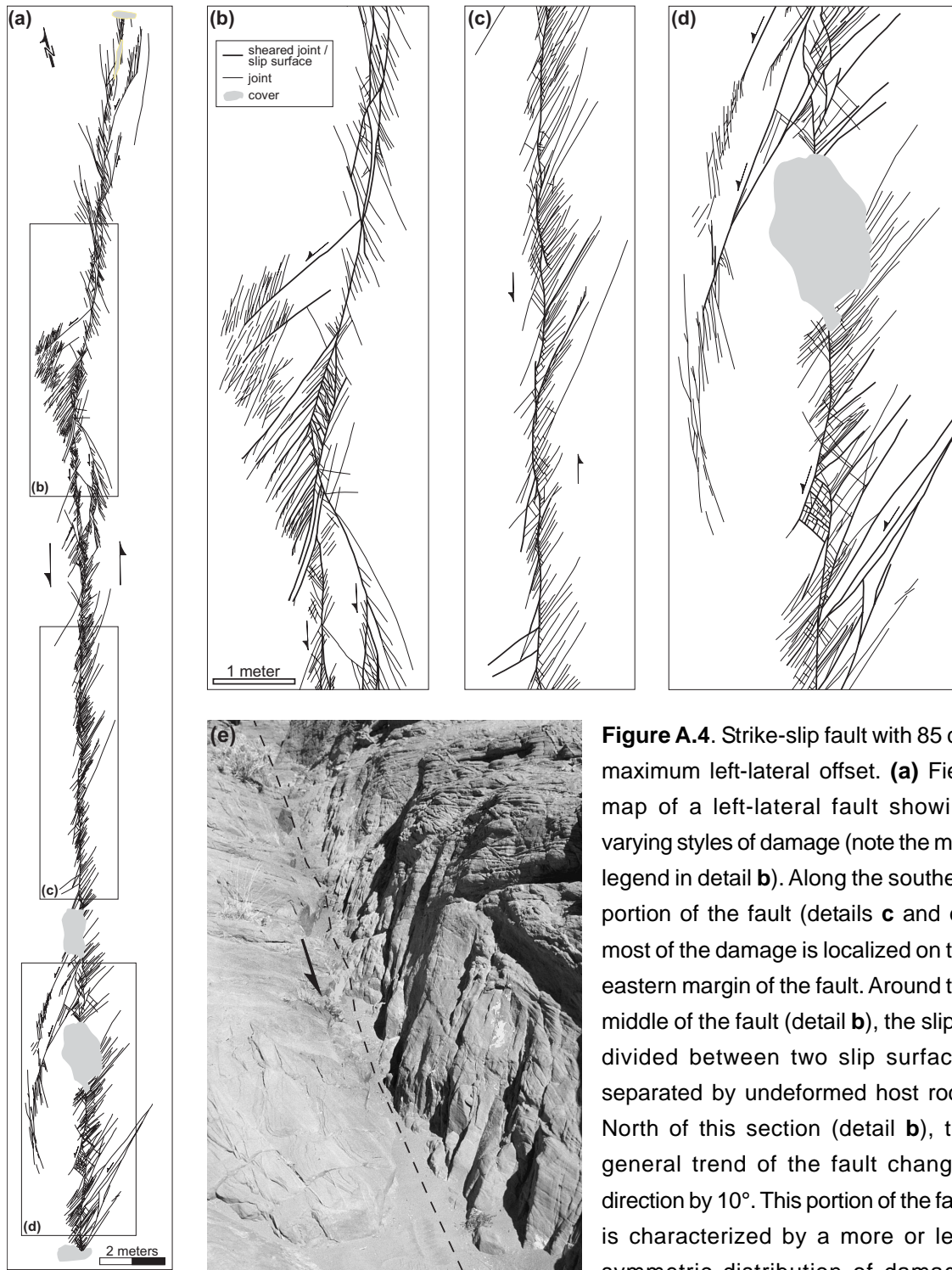
Figure A.4. Strike-slip fault with 85 cm maximum left-lateral offset. **(a)** Field map of a left-lateral fault showing varying styles of damage (note the map legend in detail **b**). Along the southern portion of the fault (details **c** and **d**), most of the damage is localized on the eastern margin of the fault. Around the middle of the fault (detail **b**), the slip is divided between two slip surfaces separated by undeformed host rock. North of this section (detail **b**), the general trend of the fault changes direction by 10°. This portion of the fault is characterized by a more or less symmetric distribution of damage. **(e)** Field photo of the area mapped in part *c* of this figure (view north). Note the greater abundance of structures on the right side of the main fault trace. Most of the shear offset has been accommodated along a primary slip surface on the left side of the fault (shown schematically as a dashed line). However, some of the fractures in the fault periphery have been reactivated in shear.

143

Figure A.5. Equal-area lower hemisphere stereonet plot of a representative number of fractures from the map shown in Figure A.4. Three separate groups of joints are identified. *Set 1*: A preexisting joint 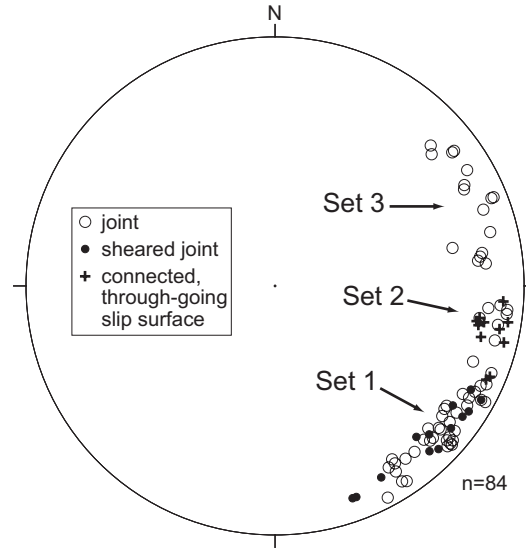breakdown set that has a left-stepping configuration. *Set 2*: Fault related joints localized near the fault core and between closely spaced primary joints. *Set 3*: Fault related splay fractures in the fault periphery associated with left-lateral slip that have a right-stepping configuration. Sheared fracture orientations (sheared joints and slip surfaces) coincide only with Set 1 and 2 orientations.

eastern periphery of the fault with respect to the through-going slip surface (Figures A.4c, A.4d, and A.4e). The peripheral joints in the southern section form an acute angle with the through-going slip surface, which faces in the same direction as the slip sense. These peripheral joints are also viewed as left-stepping. The angle of intersection between the left-stepping joints and the through-going slip surface is 33º (±9º), while for the right-stepping joints the angle is 25º (±7º).

Three fracture sets are identified in the mapped area shown in Figure A.4 (Figure A.5). The dip of all measured fractures (joints, sheared joints, and slip surfaces) is 78º (±5º). Most Set 1 fractures are joints that, based on crosscutting relationships, appear to be some of the oldest features of the fault. Some Set 1 joints are sheared (filled circles, Figure A.5) as evidenced by the recognition of both offset markers and attendant splay fractures. Set 2 fractures include joints, sheared joints, and through-going slip surfaces. Joints and sheared joints in Set 2 orientations are generally confined to the fault core. Set 3 fractures consist

144

entirely of joints and appear to be some of the youngest features of the fault zone based on crosscutting relationships.

Conceptual model

We present a conceptual model (Figure A.6) that is complementary to models presented by Myers and Aydin (*in review*) for fault zone development along preexisting joints. In our model, the breakdown geometry of the original joint plays an important role in architectural evolution of the fault. In contrast to Myers and Aydin's models, damage is preferentially localized to one side of the through-going slip surface where off-fault [damage zone] strain is accommodated along preexisting weaknesses in the joint breakdown fringe zone.

We propose that the fault shown in Figure A.3 formed along a joint zone with dominantly asymmetric continuous breakdown fringe. The overall configuration and angular relationships between the through-going and peripheral fractures are nearly identical between the unsheared and sheared examples (Figures A.2a and A.3, respectively). However, the terminal orientations of the peripheral fractures in the sheared example are at a higher angle of intersection compared to the unsheared case (~21° compared to ~10°, respectively).

The fault shown in Figure A.4 is proposed to have formed at least in part (Figures A.4c and A.4d) along a joint zone with abrupt breakdown fringe. Peripheral fractures along the fault shown in Figure A.4 have two general orientations with respect to the through-going slip surface. We attribute the formation of the right-stepping peripheral joints along this fault to be splay fractures related to left-lateral shear strain accommodation where the apex of the acute angle between the splay fractures and the parent sliding fracture points in the direction of slip (e.g., Cruikshank et al., 1991; Engelder, 1987). However, the left-stepping joints along this fault do not have the typical angular relationship found between splay fractures and sheared parent fractures with a left-lateral sense. Thus, we interpret the left-stepping joints in the southern region of the fault (Figures A.4c and A.4d) to have formed prior to the faulting and attribute their origin to joint breakdown fringe.

original joint
geometry
(no slip)

asymmetric
breakdown fringe

through-going
parent joint

early stage
of shearing
(cm's slip)

damage localized
along preexisting
fringe joints

sheared
parent joint

mature stage
of shearing
(m's slip)

minimal damage
and fault rock
development

primary slip surface

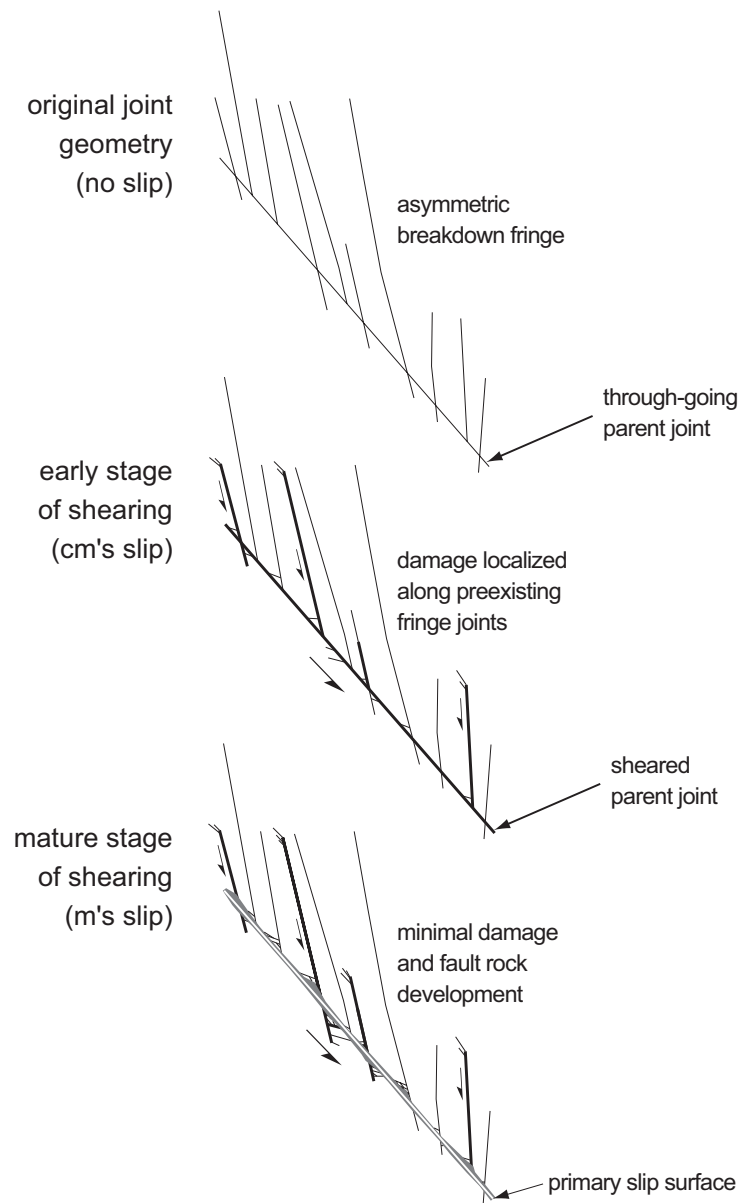**Figure A.6**. Conceptual model for the development of an asymmetric damage zone about a fault formed along preexisting joints with breakdown fringe (format after Myers and Aydin, *in review*). The conceptual model we show is of a left-stepping asymmetric abrupt breakdown fringe subjected to left-lateral shear, but a right-stepping breakdown fringe subjected to left-lateral shear is also possible.

146

Discussion

The strike-slip faults we describe are part of the same family of faults described by Myers and Aydin (*in review*). In many cases, different fault architectures implying different evolutionary paths occur along the same fault. For example, the architecture of the northern part of the fault shown in Figure A.3 implies an initial joint configuration similar to dilational-stepping (en echelon) joint zones described by Myers and Aydin, whereas the southern portion implies an initial configuration similar to an abrupt joint breakdown fringe. In this case, we suggest that the differing fault architectures along the same fault are related either to the current depth of outcrop exposure or to the slip tendency of the parent joint and the fringe joints. The latter factor is controlled by the orientation of the principle stresses with respect to the parent and fringe joints, whereas the former is just a matter of chance. The northern exposure of this fault is more than a meter higher in elevation. The geometries we describe where both parent joint and breakdown joints are exposed at the same outcrop level must be of limited extent given that the initiation points for the breakdown joints are localized along the parent joint tipline and that the extent of their overlap is generally small (cf. Figure A.2). Thus, the dilational-stepping joints along the northern portion of the fault are likely the upward extension of the breakdown fringe joints along the southern portion.

Conclusions

We present an intriguing fault architecture in which damage is localized along one side of a slip surface and interpret this pattern in terms of the initial joint breakdown fringe geometry. This provides a complementary model to that of Myers and Aydin (*in review*) for damage zone geometry around faults formed by shearing across preexisting joints. In contrast to previously developed models, fault damage is minimized due to the nearby presence of an already through-going parent fracture surface. Fragmentation and fault rock along the through-going slip surface is minimized, as the primary slip surface develops along the already through-going parent joint surface without breaking the bridges of intact rock between en echelon segments.

Acknowledgements

Appendix B

Representation of fault zone permeability in reservoir flow models

Abstract

Faults can act as fluid flow barriers, conduits, or barrier/conduit systems in reservoirs. Their accurate representation in reservoir flow simulations is essential if realistic predictions are to be attained. In this work we compute the effective flow characteristics of faults using fine-scale field-based data. The faults we focus on are in porous aeolian sandstone and were formed by shearing along preexisting joint zones. To find the bulk flow characteristics of the fault zones, we develop a computationally efficient upscaling methodology that combines numerical flow modeling and power averaging. By analyzing faults with different slip magnitudes, we are able to produce a relationship between fault permeability and fault slip. Slip magnitude is one of the few fault parameters that can be measured remotely in the subsurface and we show how it can be used to estimate the variation in permeability along a fault. We present three different flow simulation scenarios using variable fault properties derived using our new procedure. For each scenario, we present a second "tuned" case where we replace our variable fault-zone permeability by a fault with a constant permeability and width. In one case, we find no significant difference in flow response between the variable and constant permeability faults. The other two cases display differences, mostly with regard to breakthrough time and liquid production rates. Because the reservoir flows considered here are relatively simple, we postulate that the differences between the variable and constant permeability fault descriptions will become greater for more complex systems.

Introduction

Faults are common features in oil and gas reservoirs. They can act to impede or enhance fluid flow dramatically (Caine et al., 1996), thereby playing an important role in reservoir performance (Aydin, 2000). However, despite their strong impact on flow, typical reservoir simulation models represent faults in a highly simplified manner. Faults in these models are often used as adjustable parameters, with their gross impact on flow behavior "tuned" so the

149

global model predictions agree with observed production data. The use of these models as predictive tools is therefore quite limited in many cases.

The purpose of this paper is to develop and apply a new procedure for assigning permeability values to grid blocks representing the fault zone in flow simulation models. We consider the case of faults in sandstone reservoirs. The grid block permeability values are determined using the results from detailed analog outcrop studies (Myers, 1999) and from previously developed numerical solutions using a power averaging technique (Deutsch, 1989; Myers, 1999) and a full numerical solution (Durlofsky, 1991; Jourde et al., 2002) for computing fault zone permeabilities. These results provide an estimate of fault zone permeability, on the scale of 1-20 meters, as a function of the local fault slip magnitude. Through the application of this procedure, we demonstrate the impact of detailed fault zone descriptions on large-scale reservoir flows. Comparisons with large-scale flow results using a simple fault treatment, as commonly employed in current practice, are also presented. These comparisons demonstrate the qualitative improvements obtained using our procedure and the inaccuracies inherent in the simpler approaches.

Our methodology takes a markedly different approach than that taken by previous workers (Walsh et al., 1998; Manzocchi et al., 1999). In the previous work, the fault zone flow properties were approximated with reference to global trends of fault zone thickness and permeability. In the current work, we focus on faults formed by a particular mechanism and derive fault zone flow properties from detailed, millimeter-scale inputs maps.

We note that the methodology used in this study differs from that used in Chapters 4 and 5. The methods used in this appendix preceded those used in the earlier chapters, and can be considered an earlier version of our upscaling methodology. At the time this work was completed, our finite difference upscaling code was capable of handling only a 300×300 region. Subsequent improvements to the code allowed us to handle regions as large as 2000×2000, enabling us to skip the indirect power averaging step and to instead directly simulate flow across the entire region of interest (see Chapter 4).

This paper proceeds as follows. We first describe the fault systems considered, both in a geologic and hydraulic context. We then describe our methodology for upscaling fine scale fault maps to determine equivalent grid block permeability in both the fault parallel

150

and fault perpendicular directions. Following, we apply our upscaled fault permeabilities to two-dimensional reservoir-scale simulations. This allows us to assess the differences between using variable or constant property faults in reservoir flow modeling. We conclude with a brief summary and some suggestions for future work.

Geologic description of faults

We consider a hierarchical faulting process in sandstone that involves shearing along pre-existing joint zones, which results in the subsequent formation of secondary joints and fault rock (Myers, 1999). This process contrasts with deformation banding, another faulting process identified to operate in porous sandstone (Aydin and Johnson, 1978). It suffices to note that the products of these two processes are quite different from each other.

To provide some background, a few definitions are first provided. A joint (or mode I fracture) is a stress-induced discontinuity that exhibits only opening displacement; two once-adjacent surfaces are displaced in a direction predominantly perpendicular to the surfaces. A sheared joint is a fracture that originated as a joint and was later subjected to a shear displacement due to a change in the local loading state. Features related to the shearing of joints are new opening mode (I) splay fractures. These features form in response to tensile stress concentrations at the ends of (and sometimes along) sheared joints. Fault rock is a very fine grain (clay size particles) product of the frictional wear of host rock due to normal and shear stresses across the fault. Breccias zones (or fragmentation zones) are comprised of angular host rock fragments defined by closely spaced fractures within the matrix. Fault rock zones are generally bound on either side by slip surfaces, which are planar features that accommodate large amounts of shear displacement (decimeters to kilometers). The fault core encompasses only the most deformed features (fault rock, fault breccia, slip surfaces) of a fault zone. The fault damage zone bounds the fault core and contains attendant structures related to the growth of the fault.

The sheared-joint faults considered in this study occur in the Jurassic Aztec sandstone of southern Nevada, a high porosity sandstone (18-25%) of aeolian origin that is time-correlated to the more widespread Navajo sandstone of the Colorado Plateau (Blakey, 1989). A conceptual model for the evolution of these faults is described in great detail by

Myers (1999). In summary, these faults form by a hierarchical process of fault evolution that begins with shearing along preexisting joint zones. This in turn creates fragmentation zones at joint intersections as well as newly formed splay fractures near the ends of preexisting joints. This process is repeated as localized shear strain continues to accumulate; fragmentation zones are further crushed to form isolated pockets of fault rock. Eventually, a through going slip surface develops and the once-discontinuous fault rock pockets coalesce to form a continuous fault rock seam.

A field example of a reservoir-scale fault formed by this mechanism is shown in Figure B.1. Figure B.1a is a field photograph of a 2 kilometer long strike-slip fault. Figure B.1b shows a detailed image of a small section of the same fault. Two map examples of faults are shown in Figure B.2. The faults have primarily strike-slip offsets of 6.2 m (Figure B.1a) and 150 m (Figure B.1b). As seen in Figure B.2a, the fault with lower slip magnitude, the fault rock is not continuous. This is not the case for the larger slip fault shown in Figure B.2b where the fault rock seam is wide and continuous. Note that in these maps, gray-shaded line
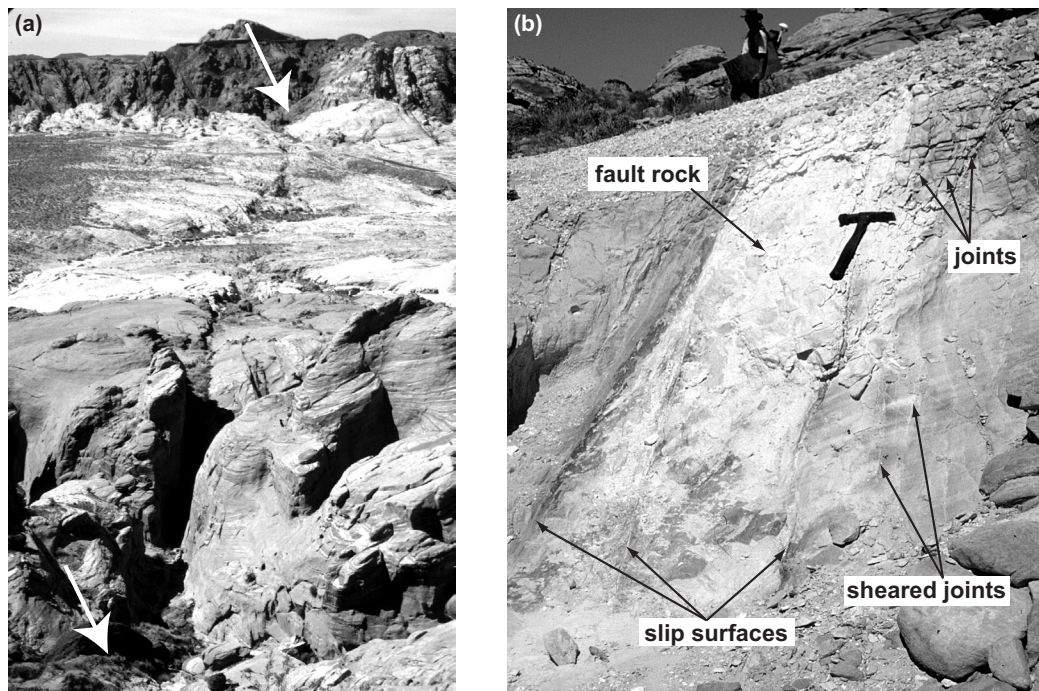

Figure B.1. Field photographs of (joint-based) faults focused on in this study. **(a)** Reservoir-scale, left lateral strike-slip fault with a maximum slip magnitude of 83 m. Distance between the white arrows is approximately 2 kilometers. **(b)** Detail image of a portion the fault shown in *part a*. Hammer for scale.
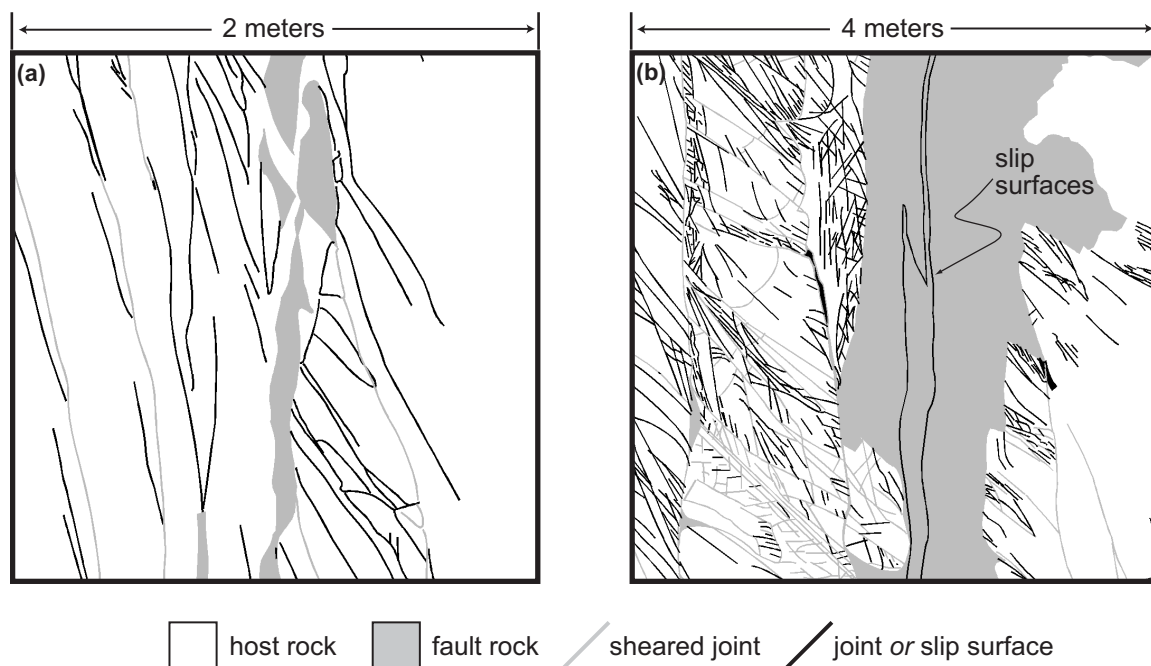
152

Figure B.2. Pixel-based maps of two faults formed by shearing along joint zones in sandstone. **(a)** Fault with 6.2 meters left-lateral slip, **(b)** Fault with 150 meters left-lateral/ oblique-normal slip. Fault maps from Myers (1999).

features represent sheared joints, while gray-shaded area features represent rock fault. Joints and slip surfaces are not distinguished from each other and are represented by black line features.

Permeability of structural elements

In this paper, we consider the fault zones to be a three-system mixture of host rock matrix, joints/slip surfaces, and sheared joints/fault rock. We assign the host rock matrix a permeability of 200 md, an average reported permeability for the Aztec sandstone in the study area (Myers, 1999). We recognize the wide range of permeability variation inherent to aeolian sand systems (e.g., Goggin et al, 1988) but do not include this in our current model as we wish to isolate the flow effects of the fault.

From a reservoir flow point-of-view, sheared joints are considered to behave in a similar manner to fault rock (Myers, 1999). Sheared joints generally contain narrow seams of fault rock at their core produced by frictional wear during shear displacement. Fault rock

permeabilities determined in the laboratory have been reported to be as low as 0.001 md (Antonellini and Aydin, 1994; Faulkner and Rutter, 1998). In our models, we assign a permeability of 0.1 md for the fault rock. This is lowest reported fault rock permeability estimate by Myers (1999) who obtained this number using a methodology that combines petrographic digital image analysis and the Kozeny-Carman relationship.

We similarly postulate that joints and slip surfaces exert the same influence on flow because both are generally planar, smooth surfaces with measurable aperture. In our models of fault permeability, we represent these discontinuous features by an equivalent porous media (Taylor et al., 1999). We calculate the permeability of the joints and slip surfaces using a simple parallel plate model:

$$k_j = \frac{b^3}{12L},\tag{1}$$

where k_j is the computed joint permeability, b is the fracture aperture, and L is the pixel dimension times the number of pixels used to represent the width of the feature in the input map. It is necessary to use Eq. (1) to account for oversampling effects due to input map resolution constraints (Matthäi et al., 1998). We use a joint aperture width of 0.25 mm; a value used in other fracture flow-modeling studies in sandstone (Matthäi et al., 1998).

Fault permeability upscaling

The fault zones modeled in this study are characterized by highly detailed two-dimensional maps (see Figure B.2). These maps typically contain about 2×10^6 pixels of data, covering an area of 1-20 square meters. A high degree of upscaling is therefore required before these characterizations can be used in flow models. The basic parameters we wish to compute from the fault models are the overall x (fault perpendicular) and y (fault parallel) compo-nents of permeability. We designate these quantities as   and k_y^*, where the * superscript indicates that these permeabilities are "upscaled" or "equivalent" fault zone properties.

The components of the upscaled permeability tensor could best be computed by solving the single-phase flow equation over the entire 2×10^6 pixel region for each fault character-ization. Then, by solving for flow in both the x- and y-directions, the components of $\mathbf{k}^*$ could be readily determined. However, this is a computationally expensive (and difficult)

154

approach, particularly since the fault zone components display a seven order of magnitude variation in permeability. An alternate, more computationally efficient procedure is to use two or more successive steps to obtain a single upscaled permeability. However, a preliminary analysis showed that such a procedure could yield some inaccuracy for the fault models considered here. Specifically, we found that the multi-step procedure may lose important large-scale connectivity effects, which can significantly impact the resulting equivalent permeability results.

The approach taken in this work entails a combination of numerical flow simulation (Durlofsky, 1991; Jourde, et al., 2002) and power averaging (Deutsch, 1989; Myers, 1999). This procedure is approximate, though it can be expected to provide reasonable values for $\mathbf{k}^*$ and to capture correct trends for the variation of $\mathbf{k}^*$ along the fault. In this approach we solve the single-phase flow equation over a representative sub-region of the fault zone and subsequently compute k_x^* and k_y^* for this region. Then, we determine power-averaging exponents that give the same values of k_x^* and k_y^*. These exponents are then applied to the full fault zone model. We now describe this procedure in more detail.

We consider four fault regions (two of these regions are shown in Figure B.2), each with a different amount of slip. For each fault region, we extract a representative sub-region of the fault zone and then solve for flow in both the *x*- and *y*-directions. These solutions apply fixed pressure boundary conditions on opposite sides of the region and no-flow conditions on the other two boundaries. Previous numerical calculations on the same systems showed that the principal directions of the full permeability tensor tend to be parallel and perpendicular to the fault orientation (Jourde et al., 2002). Therefore, the pressure-no flow boundary conditions specified here can be expected to provide reasonable accuracy in the models. The sub-regions are of dimension 300×300 pixels, in contrast to the overall maps of each zone that contain up to 1500×1500 pixels.

Following the 300×300 flow solutions, we compute k_x^* and k_y^* for the sub-region using standard procedures (Durlofsky, 1991). Next, we apply power averaging to the 300×300 maps and determine the power averaging exponents (designated ω_i, where $i=x$ or y) required to provide the same k_x^* and k_y^* as were computed numerically. Power averaging techniques

(Deutsch, 1989; Myers, 1999) are computationally efficient and compute upscaled permeabilities based simply on the relative abundance of the various components. Specifically, for a three-component mixture consisting of host rock, fault rock and joints, Myers (1999) applied the following power-averaging procedure (Deutsch, 1989):

$$k_i^* = \left(V_j\, k_j^{\omega_i} + V_g\, k_g^{\omega_i} + V_h\, k_h^{\omega_i} \right)^{1/\omega_i}, \tag{2}$$

where k_i^* is the upscaled permeability in the x- or y-direction, V_j is the volume fraction of joints, k_j is joint permeability, V_g is the volume fraction of fault rock, k_g is fault rock permeability, V_h is the volume fraction of host rock, k_h is host rock permeability, and ω_i is the averaging exponent. For fault-parallel flow (k_y^*), the flow is dominated by the high permeability joint zones in the periphery of the fault zone that are oriented sub-parallel to the main fault core. In this case, positive values of ω result ($\omega_y > 0$), reflecting the dominating influence the joints have on flow in the fault parallel direction. Conversely, for fault perpendicular flow (k_x^*), the flow is dominated by the presence of the fault rock and $\omega_x < 0$ is obtained.

Figure B.3 shows the fine scale input maps for the four 300×300 fault sub-regions. The numerically computed upscaled permeabilities are listed (k_x^* and k_y^*) as well as the corresponding averaging exponents ω_x and ω_y that yield these upscaled permeabilities. For k_y^*, ω_y ranges between 0.53 and 0.76 and does not show any particular trend with respect to fault slip (note that fault slip is the only distinguishing parameter between the various fault regions). Because of the relatively narrow range of variation in ω_y and the lack of a clear trend with fault slip, we use an average value of ω_y of 0.57 in the calculations below. For k_x^*, there is a general trend of decreasing ω_x with increasing slip. We therefore model ω_x as a function of fault slip as follows:

$$\omega_x = -0.0034\xi - 0.29, \tag{3}$$

where ξ is the slip magnitude (in meters) for the fault region under consideration. This equation is valid for $0.08 \leq \xi \leq 208$ m. The minimum slip in our models is 0.08 m ($\omega_x = -0.29$), while the maximum slip is 150 m ($\omega_x = -0.8$). We note that, due to the large effect of fault

156

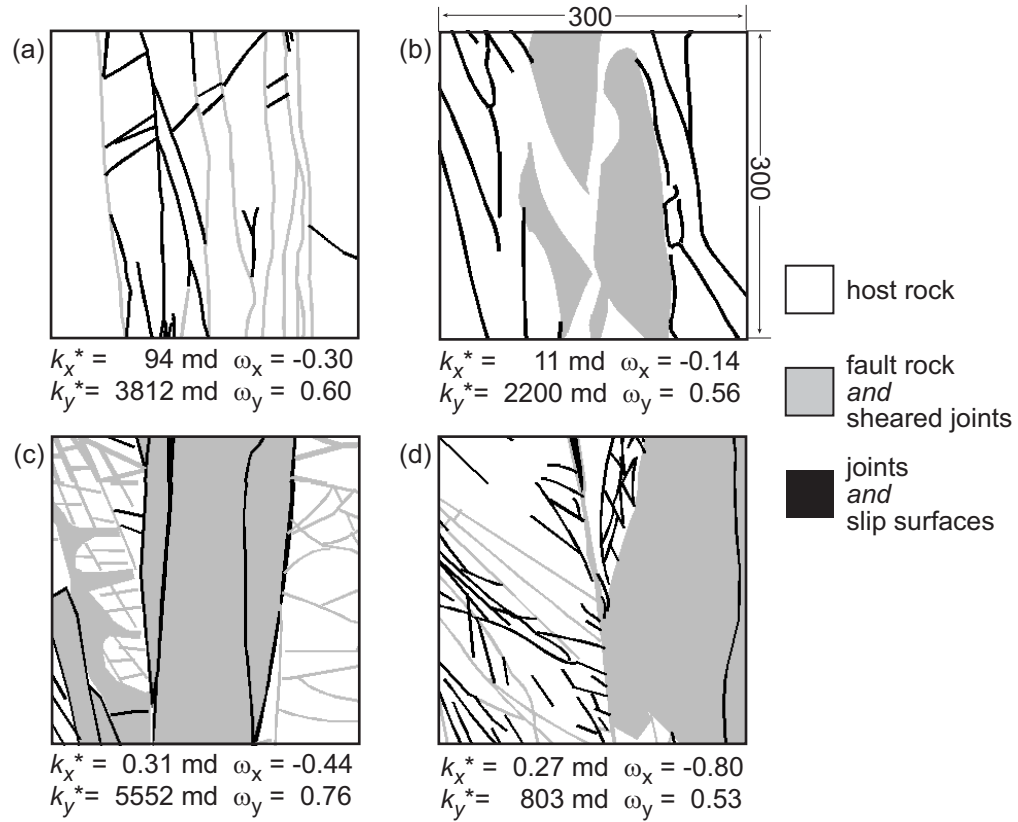Figure B.3. 300x300 pixel fault maps used in numerical flow simulation to calibrate w for power averaging. Numerically computed effective permeabilities are shown with a corresponding w for each fault map. (a) 8 cm slip, (b) 6.2 m slip, (c) 14 m slip, (d) 150 m slip. All maps extracted from data of Myers (1999).
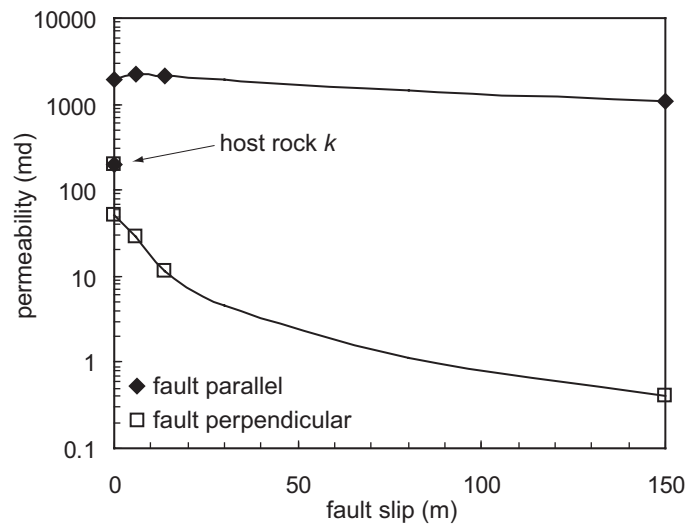

Figure B.4. Fault permeability versus slip transforms used for flow simulation input.

157

rock on cross-fault flow, a variable value of ω_x is justified because there is an increasing volume fraction of fault rock as slip magnitude increases. In addition, the fault rock is more continuous at greater slip magnitude (compare Figure B.1a with B.1b) (Myers, 1999).

The final step in our procedure entails the calculation of $\mathbf{k}^*$ for the overall fault regions characterized by 1500×1500 pixels. We accomplish this by applying the ω_x and ω_y determined in the calibration step above to the entire 1500×1500 pixel region. The computed $\mathbf{k}^*$ for this final step are presented in Figure B.4. For the fault-parallel flow direction, the presence of the joints dominates and k_y^* quickly jumps to an order of magnitude above host rock permeability (200 md) for the 8 cm slip case (1955 md). The joints exert maximum influence on fault parallel permeability in the 6.2 m slip case (=2200 md) and then decreases for the 14 m and 150 m slip cases (=1070 md for the 150 m slip case). This steady decrease in permeability is likely due to the increasing abundance of fault rock in the fault periphery at the greater slip magnitudes, which divides and disconnects the fault periphery into smaller domains of fractured rock (Jourde et al., 2002). For the fault perpendicular direction, k_x^* rapidly decreases with the onset of fault slip (=50 md for the 8 cm case) to a final low permeability of 0.4 md for the 150 m slip case.

Before presenting large-scale simulation results, we now briefly indicate ways in which our models of the fault zone can be improved. More accurate upscaled block permeabilities could be obtained via a full solution of the single-phase flow equation over the entire 1500×1500 pixel regions (see Chapter 4). This would eliminate the need for power averaging in the overall methodology. However, it may still be useful to generate power averaging exponents using a calibration approach similar to that introduced here, since fault maps in the future may contain even higher levels of resolution (e.g., 10^7-10^8 pixels) which flow simulators might not be able to handle. More accurate upscaled fault zone permeabilities will also need to account for the geostatistical variation of permeability for given structural elements, as well as for variability in joint aperture. This will give rise to non-deterministic upscaled fault zone permeabilities, which could then be applied to reservoir simulators using some type of sampling approach.
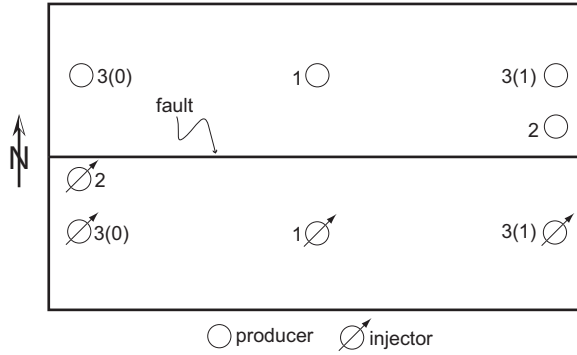
Figure B.5. Schematic drawing of simulation domain showing approximate well locations for all three test cases (numbered).

Flow simulation

In this section we apply the upscaled block permeabilities to a simple two-dimensional flow model containing a single reservoir-scale fault. We begin by describing how we introduce the variable fault properties into our flow model. We then explain how the properties of the constant permeability fault are determined. Finally, we present results for three different model scenarios.

Variable fault property assignment

A single, horizontally oriented fault occupies the middle of the model and extends to both sides of the simulation domain (Figure B.5). For symmetry reasons, we consider only half of the fault. Because slip is the controlling parameter that dictates fault permeability, we begin building our variable fault property case by assigning slip values along the length of the fault. We consider the fault slip magnitude to be maximum at the center of the fault (the east end or right hand side of the domain), and apply a simple linear slip profile that
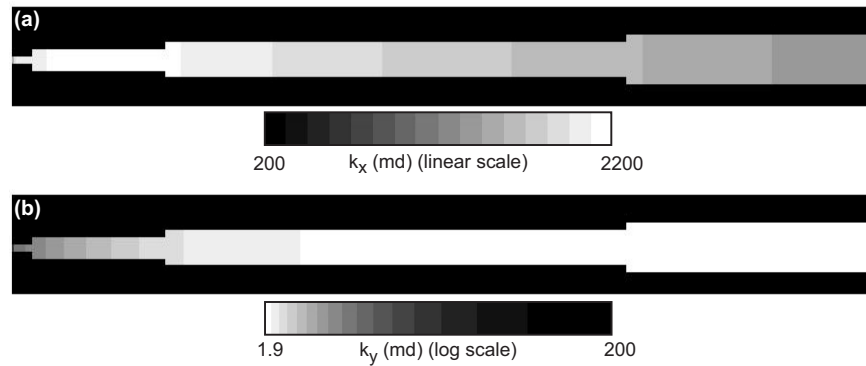

Figure B.6. Permeability maps for the faults used in the variable fault property cases. **(a)** *x*-direction. **(b)** *y*-direction. Both maps have a 15× vertical exaggeration. Note that the gray-shaded scale bars are reversed between *parts a* and *b*.
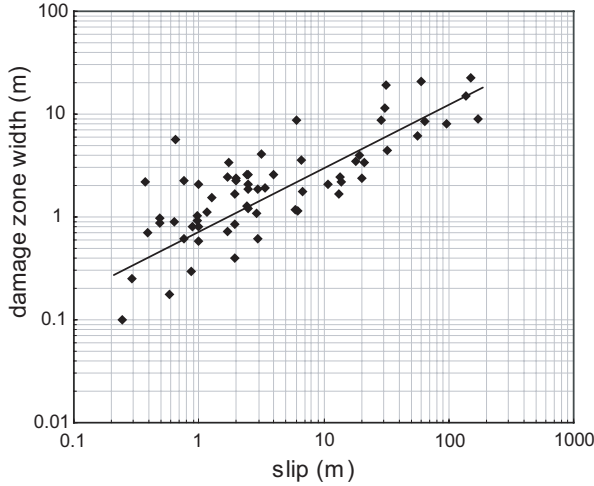
Figure B.7. Fault damage zone width versus fault slip. From Myers (1999).

decreases to zero at the fault tip in the west end of the domain. An empirically derived relationship between fault length and maximum slip magnitude is used to calculate the slip maximum at the east of the model fault. Specifically, we use a value of 0.03 times the total fault length obtained from analysis of a global fault data set (Cowie and Scholz, 1992). In our model, the fault half-length is 1400 meters, which equates to a maximum fault slip of 84 meters (0.03×2800 meters).

Block equivalent permeabilities are assigned to respective grid blocks based on the local slip magnitude at that location (Figure B.6). We decrease the grid spacing toward the west end of the fault as the fault properties change most rapidly in the low slip region of the fault (see Figure B.4). The width (the north-south dimension of the model fault) over which we assign the fault block permeabilities is determined according to the set of empirical data presented in Figure B.7. This plot presents data for fault slip versus fault damage zone width collected within the study area (Myers, 1999). In general, we assign the upscaled fault properties over wider areas as slip increases (cf. Figure B.6).

Constant fault property assignment

In our subsequent flow simulations, we will compare modeled flow responses between variable and constant fault property cases. In the constant permeability case, we assign a single fault permeability value over a three-meter wide (north-south dimension) area for the entire fault. In practice, a fault transmissibility multiplier would be applied between the cells on either side of the fault. This is analogous to the procedure we apply here. To

160

Table B.1. Reservoir and fluid properties.

thickness	10	ft
porosity, ϕ	25	%
total compressibility, c	3×10^{-5}	psi^{-1}
density, ρ		
oil	49	lbm/ft^3
water	63	lbm/ft^3
formation volume factor, B		
oil	1.05	rbbl/STB
water	1.03	rbbl/STB
viscosity, μ		
oil	4.0	cp
water	0.38	cp
relative permeabilities		
oil	1.0	@ $S_{wc} = 0.25$
water	0.4	@ $S_{or} = 0.35$

determine the constant fault permeability, we first run the variable fault permeability model. Then we force a match of the global liquid production rates at 200 days by adjusting the constant permeability value assigned to the fixed fault. We note that, in actual practice, this constant fault permeability is not determined from a detailed fault characterization as is done here. Rather, it is determined as a history matching parameter.

Reservoir flow simulations

For the flow simulations we consider a two-dimensional, two-phase (oil - water) simulation model. The model is of dimensions 291×31 blocks, which equates to an area of approximately 1400×800 m^2. No-flow conditions are assigned on the domain boundaries. The grid
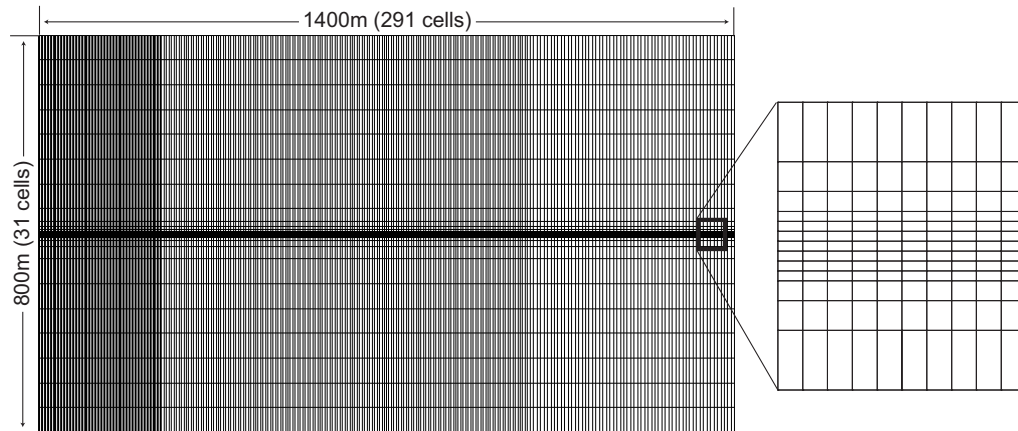
Figure B.8. Simulation grid geometry.

dimensions are not uniform and are gradually refined toward the fault, as can be seen from Figure B.8. The compressibility of the model is dominated by rock compressibility. Initial reservoir pressure is 3200 psi. The producer and injector have fixed bottomhole pressures of 2000 and 4200 psi, respectively. Other pertinent reservoir parameters are listed in Table 1.

We investigate three different cases to study the effects of faults on reservoir-scale flow. See Figure B.5 for a schematic representation of the model domain with the locations of injector-producer well pairs for each case. In each case we perform two flow simulations, the first with the detailed fault properties, the second with a single valued fault permeability that is tuned to the variable fault property case as described above. In the first case we are able to match all production history by replacing the variable fault model with the fixed model. The subsequent two test cases, however, illustrate a progressive departure of agreement between the variable and constant fault property models.
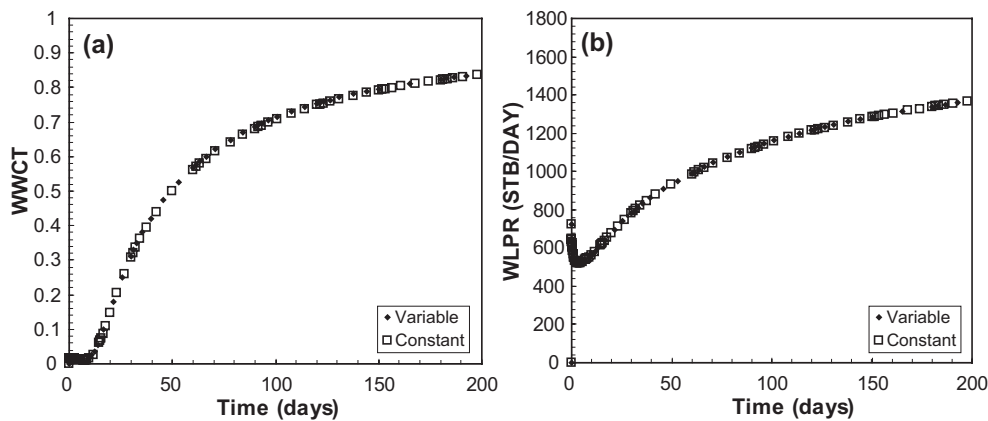

Figure B.9. Centered wells (Case 1). **(a)** Water-cut (WWCT) and **(b)** liquid production rate (WLPR).
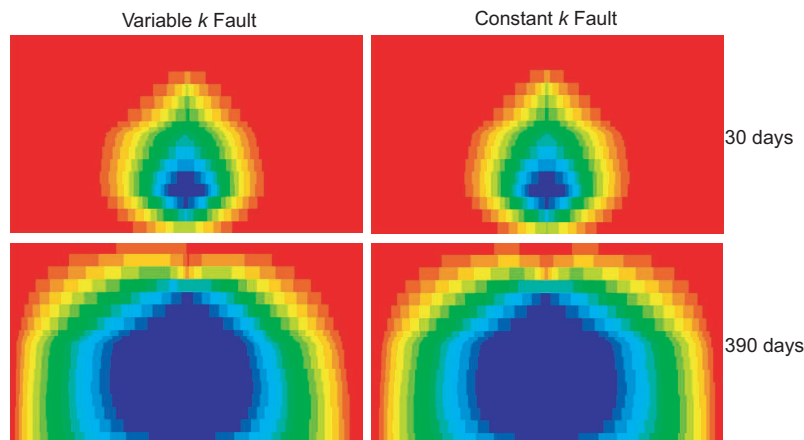

Figure B.10. Oil saturation profiles for the centered wells (case 1).

162

Case 1: Centered wells

The first test case has a simple model arrangement with an injector – producer pair placed on either side of the fault in the middle of the model domain. For the fixed fault permeability case, a single permeability value of 2.55 md provided a very close match between flow rates at the time of 200 days (and at all times throughout the simulation). Producer water cuts and liquid production rates are shown in Figures B.9a and B.9b, respectively. A very close match was obtained for the entire production run. Oil saturation profiles are shown for the variable and fixed fault property cases in Figure B.10. Breakthrough occurred rapidly, within the first month of production, with both models showing similar profiles. At 390 days a very slight asymmetry in the oil saturation profile can be seen in the variable fault model due to the higher fault zone permeability in the tip region of the variable fault case (west end).
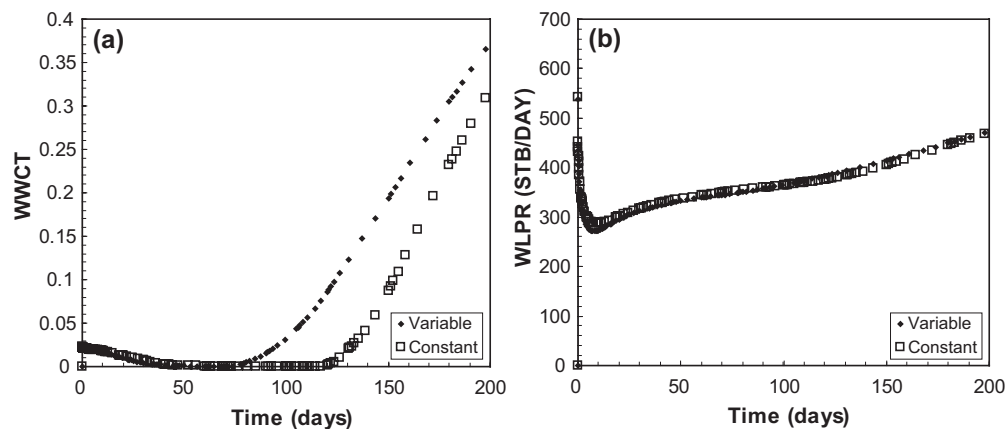

Figure B.11. Peripheral wells (Case 2). **(a)** Water-cut (WWCT) and **(b)** liquid production rate (WLPR).
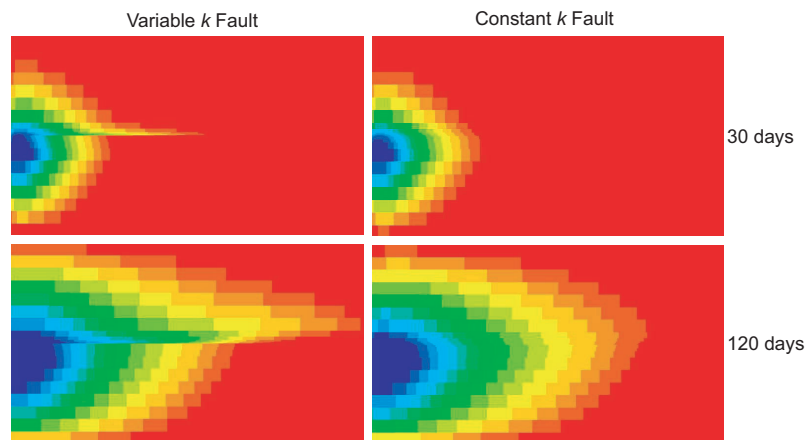

Figure B.12. Oil saturation profiles for the peripheral wells (case 2).

163

Case 2: Peripheral wells

The injector – producer pair for another test case is placed on either side of the fault and on opposite ends of the model domain (see Figure B.5). For the fixed fault permeability case, a single permeability value of 3 md was found to provide a match for global liquid production rates. Producer water cuts and liquid production rates for this case are shown in Figures B.11a and B.11b, respectively. Even though global production rates were well matched between the two cases for the entire production history, breakthrough times between the two cases were found to differ by 43 days. The difference in flow behavior between these two models is most evident in the oil saturation profiles shown in Figure B.12. In the variable fault property case, the injector is very close to the low slip region of the fault (west end) with higher cross-fault and fault-parallel permeabilities. In this case, injected water rapidly crosses the fault. The fault parallel permeability influence is also quite evident in the variable fault property case. Here we see the water front quickly propagate along the fault periphery, aiding in the more rapid breakthrough for the variable fault case. None of these effects are evident in the constant fault property case where we see a nearly symmetric advance of the waterflood eastward through the model domain.

The oil saturation maps also provide qualitative insight into the waterflood efficiency between the variable and fixed scenarios. In the variable case, locating the injector well in the high permeability region of the fault tip directs most of the water flood across the fault to the producer side, leaving a large unswept region in the southeastern corner of the model domain. The opposite occurs in the fixed fault property case where most of the water is directed down the injector side. In the variable fault property case, it would have been more efficient to switch the locations of the injector-producer pair.

Case 3: Two injector-producer pairs

This test case was performed in two stages. In the first stage we calibrate the fixed fault permeability to a single injector-producer pair located in the west end of the domain. In this first stage we were able to match global liquid production rates at 200 days with a constant permeability of 14.3 md. This constant fault permeability is an order of magnitude larger
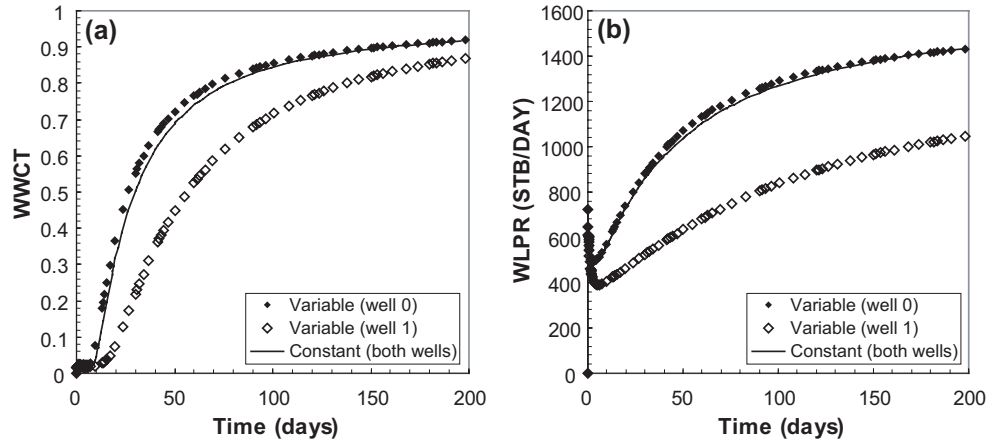
Figure B.13. Two injector - producer pairs (Case 3). **(a)** Water-cut (WWCT) and **(b)** liquid production rate (WLPR).
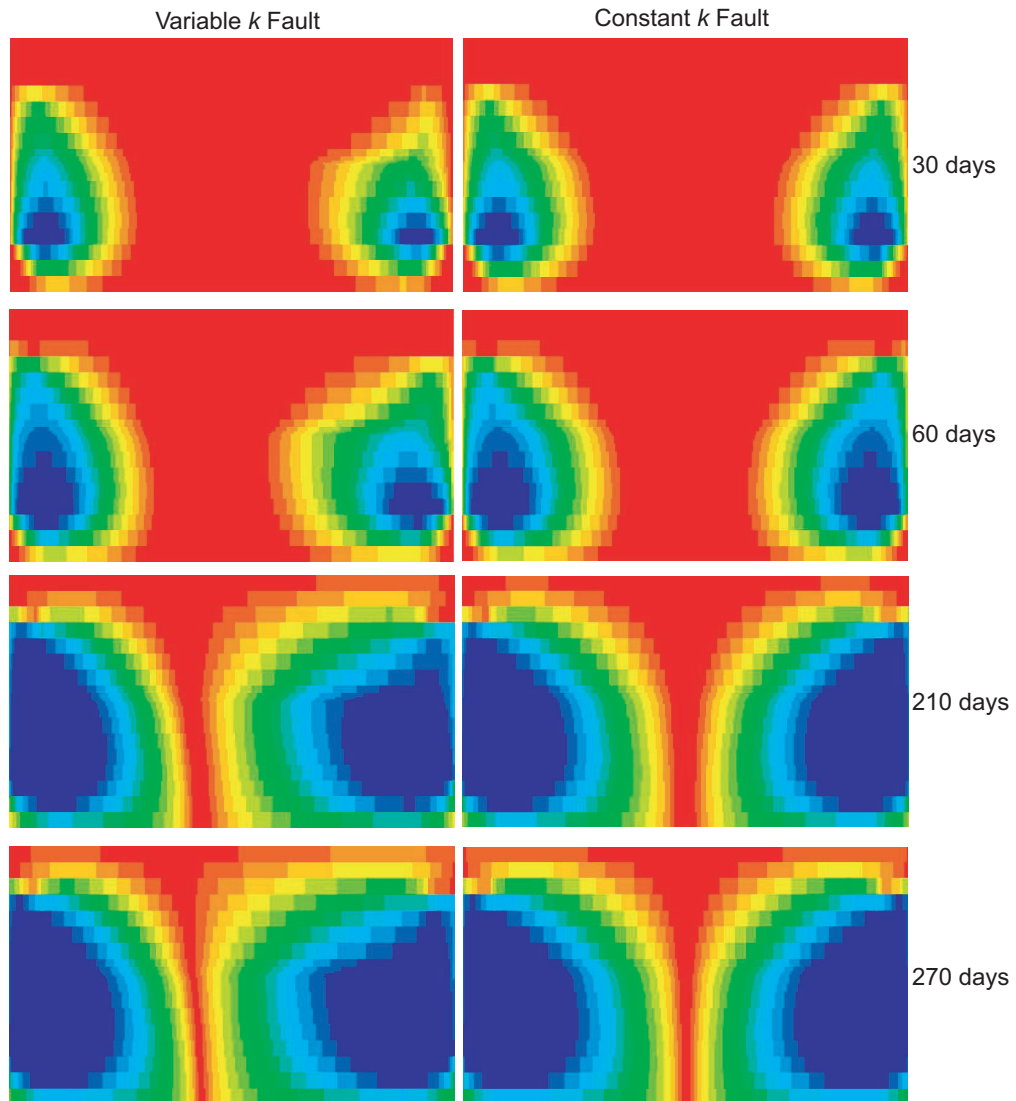

Figure B.14. Oil saturation profiles for the two injector - producer pairs (case 3).

than the fixed permeabilities obtained in the first two model runs. This is due to the fact that the injector-producer pair is very near the western fault tip, which has higher permeability.

In the second stage, we add an additional injector-producer pair to the east end of the domain, keeping the calibrated fault permeability from the first stage fixed. Producer well water cut and liquid production rates for this second stage run are presented in Figures B.13a and B.13b, respectively. Note that, in these plots the results for both wells in the constant permeability case are represented by a single line (the well responses are identical due to symmetry). Both plots show significant differences between the variable and constant property cases. Results for the constant permeability case tend to remain closer to those for the well pair located in the higher permeability western end of the domain. Oil saturation profiles for this case are presented in Figure B.14. The saturation profiles show a pronounced asymmetry in the variable fault model. In the variable permeability model, the eastern well pair shows a more widespread water sweep than the western well pair. This is due to the presence of the lower permeability eastern fault end. At 270 days, the water saturation front due to interaction between the eastern well pair has reached the north side of the model domain.

This example clearly demonstrates that although the use of constant property faults may be adequate for some reservoir simulation calculations, in other cases it is important to model the fault variability along the length of the fault.

Summary

We present a geologically based methodology for the representation of faults in reservoir-scale flow simulations. We begin by upscaling fine scale permeability data of fault zones determined in the field and characterized in the laboratory. Because the fine scale data maps are very large (1500×1500), we apply a computationally efficient upscaling scheme that combines power averaging and numerical modeling. Based on our upscaling analysis, we derive a relationship between fault slip and equivalent fault permeability. This relationship is then applied to the representation of a fault in reservoir-scale flow simulations.

We found that, in some cases, a constant permeability fault can accurately portray the flow behavior of a more complex fault. However, we also presented cases for which this

approach is inaccurate and more realistic variable fault property models are required. In the future, we plan to further refine our methodology by including geostatistical information on the fault components and by computing upscaled permeability directly over the entire fine scale fault maps. We expect that this will provide a more predictive overall methodology.

References

Anderson, E.M., 1951, The dynamics of faulting and dyke formation with applications to Britain: Edinburgh, Oliver and Boyd, 266 p.

Anderson, R.E., 1973, Large-magnitude late Tertiary strike-slip faulting north of Lake Mead, Nevada: U.S. Geological Survey Professional Paper 794, 18 p.

Anderson, R.E., and Barnhard, T.P., 1993, Heterogeneous Neogene strain and its bearing on horizontal extension and horizontal and vertical contraction at the margin of the extensional orogen, Mormon Mountains area, Nevada and Utah: U.S. Geological Survey Bulletin, B2011, 5 sheets, 113 p.

Anderson, R.E., and Barnhard, T.P., 1993a, Heterogeneous Neogene strain and its bearing on horizontal extension and horizontal and vertical contraction at the margin of the extensional orogen, Mormon Mountains area, Nevada and Utah: U.S. Geological Survey Bulletin, B2011, 113 p.

Anderson, R.E., and Barnhard, T.P., 1993b, Aspects of three-dimensional strain at the margin of the extension orogen, Virgin River depression area, Nevada, Utah, and Arizona: Geological Society of America Bulletin, v. 105, p. 1019-1052.

Anderson, R.E., Barnhard, T.P., and Snee, L.W., 1994, Roles of plutonism, midcrustal flow, tectonic rafting, and horizontal collapse in shaping the Miocene strain field of the Lake Mead region area, Nevada and Arizona, Tectonics, v. 13, p. 1381-1410.

Antonellini, M., and Aydin, A., 1994, Effect of faulting on fluid flow in porous sandstones: petrophysical properties: AAPG Bulletin, v. 78, p. 355-377.

Antonellini, M., and Aydin, A., 1995, Effect of faulting on fluid flow in porous sandstones: geometry and spatial distribution: AAPG Bulletin, v. 79, p. 642-671.

Antonellini, M., Aydin, A., and Pollard, D.D., 1994, Microstructure of deformation bands in porous sandstones at Arches National Park, Utah, Journal of Structural Geology, v. 16, p. 941-959.

Armstrong, R.L., 1968, Sevier orogenic belt in Nevada and Utah: Geological Society of America Bulletin, v. 79, p. 429-458.

Axen, G.J., 1993, Ramp-flat detachment faulting and low-angle normal reactivation of the Tule Springs thrust, southern Nevada: Geological Society of America Bulletin, v. 105, p. 1076-1090.

Aydin, A., 1978, Small faults formed as deformation bands in sandstone: Pure and Applied Geophysics, v. 116, p. 913-942.

Aydin, A., 2000, Fractures, faults, and hydrocarbon entrapment, migration, and flow: Marine and Petroleum Geology, v. 17, p. 797-814.

Aydin, A., and Johnson, A.M., 1978, Development of faults as zones of deformation bands and as slip surfaces in sandstone: Pure and Applied Geophysics, v. 116, p. 931-942.

Barton, C.C., 1983, Systematic jointing in the Cardium sandstone along the Bow River, Alberta, Canada [Ph.D. Thesis]: Yale University, 1 sheet, 302 p.

Bear, J., 1972, Dynamics of fluids in porous media: Elsevier press, New York, 764 p.

Beard, L.S., 1996, Paleogeography of the Horse Spring Formation in relation to the Lake Mead fault system, Virgin Mountains, Nevada and Arizona, *in* Beratan, K.K., ed., Reconstructing the history of Basin and Range extension using sedimentology and stratigraphy: Geological Society of America Special Paper, v. 303, p. 27-60.

Bernabé, Y., Fryer, D.T., and Hayes, J.A., 1992, The effect of cement on the strength of granular rocks, Geophysical Research Letters, v. 19, p. 1511-1514.

Billingsley, G.H., and Bohannon, R.C., 1995, Geologic map of the Elbow Canyon quadrangle, northern Mohave County, Arizona: U.S. Geological Survey Open-File Report 95-560, scale 1:24,000, 1 sheet, 16 p.

Blakey, R.C., 1989, Triassic and Jurassic geology of the southern Colorado Plateau, *in* Jenny, J.P., and Reynolds, S.J., eds., Geologic evolution of Arizona: Arizona Geological Society Digest, v. 17, p. 369-396.

Blenkinsop, T.G., 1991, Cataclasis and processes of particle size reduction: Pure and Applied Geophysics, v. 136, p. 59-86.

Bohannon, R.G., 1979, Strike-slip faults of the Lake Mead region of southern Nevada: SEPM Pacific Coast Paleogeography Symposium, v. 3, p. 129-139.

Bohannon, R.G., 1983a, Mesozoic and Cenozoic tectonic development of the Muddy, North Muddy, and northern Black Mountains, Clark County, Nevada: Geological Society of America Memoir, v. 157, p. 125-148.

Bohannon, R.G., 1983b, Geologic map, tectonic map and structure sections of the Muddy and Northern Muddy Mountains, Clark County, Nevada: U.S. Geological Survey Miscellaneous Investigations Series, Map I-1406, 2 sheets.

Bohannon, R.G., 1984, Non-marine sedimentary rocks of Tertiary age in the Lake Mead region, southeastern Nevada and northwestern Arizona: U.S. Geological Survey Professional Paper, 122, 72 p.

Bohannon, R.G., 1992, Geologic map of the Weiser Ridge quadrangle, Clark County, Nevada: U.S. Geological Survey Report GQ-1714, 1 sheet.

Bohannon, R.G., Grow, J.A., Miller, J.J., and Blank, R.H. Jr., 1993, Seismic Stratigraphy and tectonic development of Virgin River depression and associated basins, southeastern Nevada and northwestern Arizona: Geological Society of America Bulletin, v. 105, p. 501-520.

Brace, W.F., 1964, Brittle fracture of rocks, *in* Judd, W.R., ed., State of stress in the Earth's crust: New York, Elsevier, p. 111-174.

Brace, W.F., and Bombolakis, E.G., 1963, A note on brittle crack growth in compression: Journal of Geophysical Research, v. 68, p. 3709-3713.

169

Brock, W.G., and Engelder, T., 1979, Deformation associated with the movement of the Muddy Mountain overthrust in the Buffington window, southeastern Nevada: Geological Society of America Bulletin, v. 88, p. 1667-1677.

Caine, J.S. and Forster, C.B., 1999, Fault zone architecture and fluid flow: Insights from field data and numerical modeling, *in* Haneberg, W.C., Mozley, P.S., Moore, J.C., and Goodwin, L.B., eds., Faults and subsurface fluid flow in the shallow crust: American Geophysical Union, Geophysical Monograph, v. 113, p. 101-127.

Caine, J.S., Evans, J.P., and Forster, C.B., 1996, Fault zone architecture and permeability structure: Geology, v. 24, p. 1025-1028.

Çakir, M., Aydin, A., and Campagna, D.J., 1998, Deformation pattern around the conjoining strike-slip fault systems in the Basin and Range, southeast Nevada: the role of strike-slip faulting in basin formation and inversion: Tectonics, v. 17, p. 344-359.

Campagna, D.J., and Aydin, A., 1994, Basin genesis associated with strike-slip faulting in the Basin and Range, southeastern Nevada: Tectonics, v. 13, p. 327-341.

Carpenter, D.G., 1989, Geology of the North Muddy Mountains, Clark County Nevada, and regional structural synthesis: fold-thrust and Basin and Range structure in southern Nevada, southwest Utah, and northwest Arizona: [M.S. Thesis] Oregon State University, 145 p.

Carpenter, D.G., and Carpenter, J.A., 1994, Fold-thrust structure, synorogenic rocks, and structural analysis of the North Muddy and Muddy Mountains, Clark County, Nevada, *in* Dobbs, S.W., and Taylor, W.J., eds., Structural and stratigraphic investigations and petroleum potential of Nevada, with special emphasis south of the railroad valley producing trend: Nevada Petroleum Society Conference II, p. 65-94.

Chandler, M.A., Kocurek, G., Goggin, D.J., and Lake, L.W., 1989, Effects of stratigraphic heterogeneity in eolian sandstone sequence, Page sandstone, northern Arizona: AAPG Bulletin, v. 73, p. 658-668.

Childs, C., Sylta, Ø., Moriya, S., Walsh, J.J., and Manzocchi, T., 2002, A method for including the capillary properties of faults in hydrocarbon migration models, *in* Koestler, A.G., and Hunsdale, R., eds., Hydrocarbon seal quantification: Norwegian Petroleum Society (NPF), Special Publication, v. 11, p. 187-201.

Christensen, N.I., and Wang, H.F., 1985, The influence of pore pressure and confining pressure on dynamic elastic properties of Berea sandstone, Geophysics, v. 50, p. 207-213.

Cooke, M.L., 1997, Fracture localization along faults with spatially varying friction: Journal of Geophysical Research, v. 102, p. 22,425-22,434.

Cotterell, B., and Rice, J.R., 1980, Slightly curved or kinked cracks: International Journal of Fracture, v. 16, p. 155-169.

Cowie, P.A., and Scholz, C.H., 1992, Displacement-length scaling relationships for faults: data synthesis and discussion: Journal of Structural Geology, v. 14, p. 1149-1156.

Crawford, B.R., 1998, Experimental fault sealing: shear band permeability dependency on cataclastic fault gouge characteristics, *in* Coward, M.P., Daltaban, T.S., and Johnson, H., eds., Structural geology in reservoir characterization: Geological Society of London, Special Publications, v. 127, p. 27-47.

Cruikshank, K.M., and Aydin, A., 1995, Unweaving the joints in the Entrada Sandstone, Arches National Park, Utah, U.S.A.: Journal of Structural Geology, v. 17, p. 409-421.

Cruikshank, K.M., Zhao, G., and Johnson, A.M., 1991, Analysis of minor fractures associated with joints and faulted joints, Journal of Structural Geology, v. 13, p. 865-886.

Curewitz, D., and Karson, J.A., 1997, Structural settings of hydrothermal outflow: fracture permeability maintained by fault propagation and interaction: Journal of Volcanology and Geothermal Research, v. 79. p. 149-168.

Davatzes, N.C., and Aydin, A., in press, Overprinting faulting mechanisms during the development of multiple fault sets, Chimney Rock fault array, Utah, USA: Tectonophysics.

Davis, G.H., Bump, A.P., Garcia, P.E., Ahlgren, S.G., 2000, Conjugate Riedel deformation band shear zones: Journal of Structural Geology, v. 22, p. 169-190.

Dershowitz, B., LaPointe, P., Eiben, T., and Wei, L.L., 2000, Integration of discrete feature net-work methods with conventional simulator approaches: SPE Reservoir Evaluation & Engineering, v. 3, p. 165-170.

Deutsch, C., 1989, Calculating effective absolute permeability in sandstone/shale sequences: SPE Formation Evaluation, v. 4, p. 343-348.

Dholakia, S.K., Aydin, A., Pollard, D.D., and Zoback, M.D., 1998, Fault-controlled hydrocarbon pathways in the Monterey Formation, California: AAPG Bulletin, v. 82, p. 1551-1574.

Dinwiddie, C.L., Molz, F.J, Murdoch, L.C., and Castle, J.W., 1999, A new mini-permeameter probe and associated analytical techniques for measuring the in-situ spatial distribution of permeability: EOS, Transactions, American Geophysical Union Fall Meeting, v. 80, p. F349.

Duebendorfer, E.M., and Black, R.A., 1992, Kinematic role of transverse structures in continental extension: an example from the Las Vegas Valley shear zone, Nevada: Geology, v. 20, p. 1107-1110.

Duebendorfer, E.M., Beard, L.S., and Smith, E.I., 1998, Restoration of Tertiary deformation in the Lake Mead region, southern Nevada: the role of strike-slip transfer faults, *in* Faulds, J.E., and Stewart, J.H., eds., Accommodation zones and transfer zones: regional segmentation of the Basin and Range province: Geological Society of America Special Paper, v. 323, p. 127-148.

Dunn, D.E., LaFountain, L.J., and Jackson, R.E., 1973, Porosity dependence and mechanism of brittle fracture in sandstone: Journal of Geophysical Research, v. 78, p. 2403-2417.

Durlofsky, L.J., 1991, Numerical calculation of equivalent grid block permeability tensors for heterogeneous porous media: Water Resources Research, v. 27, p. 699-708.

Durlofsky, L.J., 1992, Modeling fluid flow through complex reservoir beds: SPE Formation Evaluation, v. 7, p. 315-322.

Durlofsky, L.J., Jones, R.C., and Milliken, W.J., 1997, A nonuniform coarsening approach for the scale-up of displacement processes in heterogeneous media: Advances in Water Resources, v. 20, p. 335-347.

Dvorkin, J., and Brevik, I., 1999, Diagnosing high-porosity sandstones: strength and permeability from porosity and velocity: Geophysics, v. 64, p. 795-799.

Dvorkin, J., and Nur, A., 1996, Elasticity of high-porosity sandstones: theory for two North Sea data sets: Geophysics, v. 61, p. 1363-1370.

Dyer, J.R., 1983, Jointing in sandstones, Arches National Park, Utah [Ph.D. Thesis]: Stanford University, 2 sheets, 202 p.

Ehrlich, R., Kennedy, S.K., Crabtree, S.J., and Cannon, R.L., 1984, Petrographic image analysis I: analyses of reservoir pore complexes: Journal of Sedimentary Petrology, v. 54, p. 1365-1376.

Engelder, J.T., 1974, Cataclasis and the generation of fault gouge: Geological Society of America Bulletin, v. 85, p. 1515-1522.

Engelder, T., 1987, Joints and shear fractures in rock, *in* Atkinson, B.K., ed., Fracture mechanics of rock: London, Academic Press, p. 27-69.

Engelder, T., 1989, Analysis of pinnate joints in the Mount Desert Island granite: implications for post-intrusion kinematics in the coastal volcanic belt, Maine: Geology, v. 17, p. 564-567.

Engelder, T., Haith, B.F., and Younes, A., 2001, Horizontal slip along Alleghanian joints of the Appalachian plateau: evidence showing that mild penetrative strain does little to change the pristine appearance of early joints: Tectonophysics, v. 336, p. 31-41.

Evans, J.P., 1990, Thickness-displacement relationships for fault zones: Journal of Structural Geology, v. 12, p. 1061-1065.

Faulkner, D.R., and Rutter, E.H., 1998, The gas permeability of clay-bearing fault gouge at 20 degrees C, *in* Jones, G., Fisher, Q.J., and Knipe, R.J., eds., Faulting, fault sealing, and fluid flow in hydrocarbon reservoirs: Geological Society of London, Special Publications, v. 147, p. 147-156.

Fisher, Q.J., and R.J. Knipe, 1998, Fault sealing processes in siliciclastic sediments, *in* Jones, G., Fisher, Q.J., and Knipe, R.J., eds., Faulting, fault sealing, and fluid flow in hydrocarbon reservoirs: Geological Society of London, Special Publications, v. 147, p. 117-134.

Fleck, R.J., 1970, Tectonic style, magnitude, and age of deformation in the Sevier orogenic belt in southern Nevada and eastern California: Geological Society of America Bulletin, v. 81, p. 1705-1720.

Fletcher, R.C., and Pollard, D.D., 1981, Anti-crack model for pressure solution surfaces: Geology, v. 9, p. 419-424.

Flodin, E.A., and Aydin, A., in review-a, Evolution of a strike-slip fault network, Valley of Fire, southern Nevada: Geological Society of America Bulletin.

Flodin, E.A., and Aydin, A., in review-b, Faults with asymmetric damage zones in sandstone, Valley of Fire State Park, southern Nevada: Journal of Structural Geology.

Flodin, E.A., Aydin, A., Durlofsky, L.J., and Yeten, B., 2001, Representation of fault zone permeability in reservoir flow models: SPE paper 71671, presented at the SPE Annual Technical Conference and Exhibition, New Orleans, 10 p.

Flodin, E.A., Prasad, M., and Aydin, A., in press, Petrophysical constraints on deformation styles in Aztec Sandstone: Pure and Applied Geophysics.

Folk, R.L., 1968, Petrology of sedimentary rocks: University of Texas, Austin Publication, 170 p.

Fowles, J., and Burley, S., 1994, Textural and permeability characteristics of faulted, high porosity sandstones: Marine and Petroleum Geology, v. 11, p. 608-623.

Freeman, D.H., 1990, Permeability effects of deformation bands in porous sandstones: [M.S. Thesis], University of Oklahoma, 90 p.

Freund, R., 1974, Kinematics of transform and transcurrent faults: Tectonophysics, v. 21, p. 93-134.

Gal, D., Dvorkin, J., and Nur, A., 1999, Elastic-wave velocities in sandstones with non-load bearing clay: Geophysical Research Letters, v. 26, p. 939-942.

Gibson, R.G., 1994, Fault-zone seals in siliciclastic strata of the Columbus Basin, offshore Trinidad: AAPG Bulletin, v. 78, p. 1372-1385.

Gibson, R.G., 1998, Physical character and fluid-flow properties of sandstone-derived fault zones, *in* Coward, M.P., Daltaban, T.S., and Johnson, H., eds., Structural geology in reservoir characterization: Geological Society of London, Special Publications, v. 127, p. 83-97.

Goggin, D.J., Chandler, M.A., Kocurek, G., and Lake, L.W., 1988, Patterns of permeability in eolian deposits: Page sandstone (Jurassic), northeastern Arizona: SPE Formation Evaluation, v. 3, p. 297-306.

Goggin, D.J., Thrasher, R.L., and Lake, L.W., 1988, A theoretical and experimental analysis of minipermeameter response including gas slippage and high velocity flow effects: In Situ, v. 12, p. 79-116.

Graham, B., Antonellini, M., and Aydin, A., in press, Formation and growth of normal faults in carbonates within a compressive environment: Geology.

Granier, T., 1985, Origin, damping, and pattern of development of faults in granite: Tectonics, v. 4, p. 721-737.

Hill, R.E., 1989, Analysis of deformation bands in the Aztec sandstone, Valley of Fire State Park, Nevada: [M.S. Thesis], University of Nevada Las Vegas, 68 p.

Hodgson, R.A., 1961, Classification of structures on joint surfaces, American Journal of Science, v. 259, p. 493-502.

Jaeger, J.C., and Hoskins, E.R., 1966, Rock failure under the confined Brazilian test: Journal of Geophysical Research, v. 71, 2651-2659.

Jamison, W.R., and Stearns, D.W., 1982, Tectonic deformation of Wingate sandstone, Colorado National Monument: AAPG Bulletin, v. 66, p. 2584-2608.

Jourde, H., Flodin, E.A., Aydin, A., Durlofsky, L.J., and Wen, X.-H., 2002, Computing permeability of fault zones in aeolian sandstone from outcrop measurements: AAPG Bulletin, v. 86, p. 1187-1200.

Karimi-Fard, M., and Firoozabadi, A., 2001, Numerical simulation of water injection in 2D fractured media using discrete-fracture model: SPE paper 71615, presented at the SPE Annual Technical Conference and Exhibition, New Orleans, Sept. 30 - Oct. 3.

Kattenhorn, S.A., Aydin, A., and Pollard, D.D., 2000, Joints at high angles to normal fault strike: an explanation using 3-D numerical models of fault-perturbed stress fields: Journal of Structural Geology, v. 22, p. 1-23.

Katz, A.J., and Thompson, A.H., 1987, Prediction of rock electrical conductivity from mercury injection measurements: Journal of Geophysical Research, v. 92, p. 599-607.

Kelly, P.G., Sanderson, D.J., and Peacock, D.C.P., 1998, Linkage and evolution of conjugate strike-slip fault zones in limestones of Somerset Northumbria: Journal of Structural Geology, v. 20, p. 1477-1493.

Kim, J.G. and Deo, M.D., 1999, Comparison of the performance of a discrete fracture multi-phase model with those using conventional methods: SPE paper 51928, presented at the SPE Reservoir Simulation Symposium, Houston, Feb. 14-17.

Kim, Y.-S., Andrews, J.R., and Sanderson, D.J., 2001, Reactivated strike-slip faults: examples from the north Cornwall, U.K.: Tectonophysics, v. 340, p. 173-194.

Knipe, R.J., Fisher, Q.J., Jones, G., Clennell, M.B., Farmer, A.B., Kidd, B., McAllister, E., Porter, J.R., and White, E.A., 1997, Fault Seal prediction methodologies, applications and successes, *in* Møller-Pedersen, P., and Koestler, A.G., eds., Hydrocarbon seals - importance for exploration and production: Norwegian Petroleum Society (NPF), Special Publication, v. 7, p. 5-40.

Knipe, R.J., Jones, G., and Fisher, O.J., 1998, Introduction, *in* Knipe, R.J., Jones, G., and Fisher, O.J., eds., Faulting, fault sealing and fluid flow in hydrocarbon reservoirs: Geological Society of London, Special Publications, v. 147, p. VII-XXI.

Langenheim, V.E., Glen, J.M., Jachens, R.C., Dixon, G.L., Katzer, T.C., and Morin, R.L., 2000, Geophysical constraints on the Virgin River depression, Nevada, Utah, and Arizona: U.S. Geological Survey Open-File-Report 00-407, 26 p.

Langenheim, V.E., Grow, J.A., Jachens, R.C., Dixon, G.L., and Miller J.J., 2001, Geophysical constraints on the location and geometry of the Las Vegas Valley shear zone, Nevada: Tectonics, v. 20, p. 189-209.

Lee, S.H., Lough, M.F., and Jensen, C.L., 2001, Hierarchical modeling of flow in naturally fractured formations with multiple length scales: Water Resources Research, v. 37, p. 443-455.

Lin, P., and Logan, J.M., 1991, The interaction of two closely spaced cracks: a rock model study: Journal of Geophysical Research, v. 96, p. 21,667-21,675.

Lo, T.W., Coyner, K.B., and Toksöz, M.N., 1986, Experimental determination of elastic anisotropy of Berea sandstone, Chicopee shale, and Chelmsford granite: Geophysics, v. 51, p. 164-171.

Logan, J.M., Friedman, M., Higgs, N., Dengo, C., and Shimamoto, T., 1979, Experimental studies of simulated fault gouge and their application to studies of natural fault zones: U.S. Geological Survey Open-File-Report 79-1239, p. 305-343.

Longwell, C.R., 1949, Structure of the northern Muddy Mountain area, Nevada: Geological Society of America Bulletin, v. 60, p. 923-967.

Longwell, C.R., 1960, Possible explanation of diverse structural patterns in southern Nevada: American Journal of Science, v. 258-A, p. 192-203.

Main, I.G., Kwon, O.K., Ngwenya, B.T., and Elphick, S.C., 2000, Fault sealing during deformation band growth experiments in porous sandstone: Geology, v. 28, p. 1131-1134.

Mair, K., Main, I.G., and Elphick, S.C., 2000, Sequential growth of deformation bands in the laboratory: Journal of Structural Geology, v. 22, p. 183-186.

Manzocchi, T., Heath, A.E., Walsh, J.J., and Child, C., 2002, The representation of two phase fault-rock properties in flow simulation models: Petroleum Geoscience, v. 8, p. 119-132.

Manzocchi, T., Walsh, J.J., Nell, P., and Yielding, G., 1999, Fault transmissibility multipliers for flow simulation models: Petroleum Geoscience, v. 5, p. 53-63.

Marone, C., and Scholz, C.H., 1989, Particle-size distribution and microstructures within simulated fault gouge: Journal of Structural Geology, v. 11, p. 799-814.

Marshak, S., and Mitra, G., 1988, Basic methods of structural geology: New Jersey, Prentice Hall, 446 p.

Martel, S.J., 1990, Formation of compound strike-slip fault zones, Mount Abbot quadrangle, California: Journal of Structural Geology, v. 12, p. 869-882.

Martel, S.J., and Boger, W.A., 1998, Geometry and mechanics of secondary fracturing around small three-dimensional faults in granitic rock: Journal of Geophysical Research v. 103, p. 21,299-21,314.

Martel, S.J., Pollard, D.D., and Segall, P., 1988, Development of simple strike-slip fault zones in granitic rock, Mount Abbot quadrangle, Sierra Nevada, California: Geological Society of America Bulletin, v. 100, p. 1451-1465.

Martys, N.S, Hagedorn, J.G., Goujon, D., and Devaney, J.E., 1999, Large-scale simulations of single and multi-component flow in porous media: The International Society for Optical Engineering (SPIE), v. 3772, p. 205-213.

Marzolf, J., 1983, Changing wind and hydraulic regimes during deposition of the Navajo and Aztec sandstones, Jurassic (?) southwestern United States, *in* M.E. Brookfield, and Ahlbrandt, T.S., eds., Eolian sediments and processes: Amsterdam, Elsevier, p. 635-660.

Marzolf, J.E., 1990, Reconstruction of extensionally dismembered early Mesozoic sedimentary basins; Southwestern Colorado Plateau to the eastern Mojave Desert, *in* Wernicke, B.P., ed., Basin and range extensional tectonics near the latitude of Las Vegas, Nevada: Geological Society of America Memoir, v. 176, p. 477-500.

Matthäi, S.K., Aydin, A., Pollard, D.D., and Roberts, S., 1998, Numerical simulation of deviations from radial drawdown in a faulted sandstone reservoir with joints and zones of deformation bands, *in* Knipe, R.J., Jones, G., and Fisher, O.J., eds., Faulting, fault sealing and fluid flow in hydrocarbon reservoirs: Geological Society of London, Special Publications, v. 147, p. 157-191.

Mavko, G., and Nur, A., 1997, The effect of percolation threshold in the Kozeny-Carmen relation: Geophysics, v. 62, p. 1480-1482.

Mavko, G., Mukerji, T., and Dvorkin, J., 1998, The rock physics handbook, tools for seismic analysis in porous media: Cambridge, Cambridge University Press, 329 p.

McGarr, A., Pollard, D.D., Gay, N.C., and Ortlepp, W.D., 1979, Observations and analysis of structures in exhumed mine-induced faults: U.S. Geological Survey Open-File-Report 79-1239, p. 101-120.

Mollema, P.M., and Antonellini, M., 1999, Development of strike-slip faults in the dolomites of the Sella Group, northern Italy: Journal of Structural Geology, v. 21, p. 273-292.

Myers, R.D., 1999, Structure and hydraulics of brittle faults in sandstone [Ph.D. Thesis]: Stanford University, 176 p.

Myers, R.D., and Aydin, A., in review, The evolution of fault zones from joint zones in porous sandstone: Journal of Structural Geology.

Nelson, R.A., and Handin, J., 1977, An experimental study of fracture permeability in porous rock: AAPG Bulletin, v. 61, p. 227-236.

Nemat-Nasser, S., and Horii, H., 1982, Compression-induced nonplanar crack extension with application to splitting, exfoliation and rockburst: Journal of Geophysical Research, v. 87, p. 6805-6821.

Nicholson, C., Seeber, L., Williams, P., and Sykes, L.R., 1986, Seismic evidence for conjugate slip and block rotation within the San Andreas fault system, southern California: Tectonics, v. 5, p. 629-648.

Nur, A. and Simmons, G., 1969, Stress-induced velocity anisotropy in rock - an experimental study: Journal of Geophysical Research, v. 74, p. 6667-6674.

Nur, A., Ron, H., and Beroza, G.C., 1993, The nature of the Landers-Mojave earthquake line: Science, v. 261, p. 201-203.

Nur, A., Ron, H., and Scotti, O., 1986, Fault mechanics and the kinematics of block rotations: Geology, v. 14, p. 746-749.

Ogilvie, S.R., and Glover, P.W.J., 2001a, The petrophysical properties of deformation bands in relation to their microstructure: Earth and Planetary Science Letters, v. 193, p. 129-142.

Ogilvie, S.R., and Glover, P.W.J., 2001b, The influence of deformation bands upon fluid flow using profile permeametry and positron emission tomography: Geophysical Research Letters, v. 28, p. 61-64.

Ohlmacher, G.C., and Aydin, A., 1997, Mechanics of vein, fault and solution surface formation in the Appalachian Valley and Ridge, Tennessee, U.S.A.: implications for fault friction, state of stress and fluid pressure: Journal of Structural Geology, v. 19, p. 927-944.

Pachell, M.A., and Evans, J.P., 2002, Growth, linkage, and termination processes of a 10-km-long strike-slip fault in jointed granite: the Gemini fault zone, Sierra Nevada, California: Journal of Structural Geology, v. 24, p. 1903-1924.

Peacock, D.C.P., 2001, The temporal relationship between joints and faults: Journal of Structural Geology, v. 23, p. 329-341.

Pettijohn, F.J., Potter, P.E., and Siever, R., 1972, Sand and sandstone: Berlin, Springer-Verlag, 618 p.

Pipiringos, G.N., and O'Sullivan, R.B., 1978, Principal unconformities in Triassic and Jurassic rocks, western interior United States - a preliminary report: U.S. Geological Survey Professional Paper, 1035-A, 29 p.

Pittman, E.D., 1981, Effect of fault-related granulation on porosity and permeability of quartz sandstones, Simpson Group (Ordovician), Oklahoma: AAPG Bulletin, v. 65, p. 2381-2387.

Pittman, E.D., 1992, Relationship of porosity and permeability to various parameter derived from mercury injection-capillary pressure curves for sandstone: AAPG Bulletin, v. 76, p. 191-198.

Pollard, D.D., and Aydin, A., 1988, Progress in understanding jointing over the past century: Geological Society of America Bulletin, v. 100, p. 1181-1204.

Pollard, D.D., Segall, P., and Delaney, P.T., 1982, Formation and interpretation of dilatant echelon cracks: Geological Society of America Bulletin, v. 93, p. 1291-1303.

Poole, F.G., 1964, Paleowinds in the western United States, *in* Nairn, A.E.M., Problems in paleoclimatology: London, John Wiley, p. 394-406.

Prasad, M., 2001, Mapping impedance microstructure in rocks with acoustic microscopy: The Leading Edge, v. 20, p. 172-179.

Prasad, M., and Manghnani, M.H., 1997, Effects of pore and differential pressure on compressional wave velocity and quality factor in Berea and Michigan sandstone: Geophysics, v. 62, p. 1163-1176.

Prasad, M., Manghnani, M. H., and Siegesmund, S., 1994, Velocity and attenuation characteristics of selected KTB core samples: Scientific Drilling, v. 4, p. 221-231.

Prasad, M., Palafox, G., Nur, A., 1999, Velocity and Attenuation Characteristics of Daqing sandstones: Effects of permeability on velocity and attenuation anisotropy: AGU 1999 Fall Meeting, EOS, 80.

Renard, Ph., and de Marsily, G., 1997, Calculating equivalent permeability: A review: Advances in Water Resources, v. 20, p. 253-278.

Riedel, W., 1929, Zur mechanik geologischer brucherscheinungen: Centralblatt für Mineralogie, Geologie, und Paleontologie B, p. 354-568.

Rogers, A.M., and Lee, W.H.K., 1976, Seismic study of earthquakes in the Lake Mead, Nevada-Arizona region: Bulletin of the Seismological Society of America, v. 66, p. 1631-1657.

Ron, H., Aydin, A., and Nur, A., 1986, Strike-slip faulting and block rotation in the Lake Mead fault system: Geology, v. 14, p. 1020-1023.

Ron, H., Nur, A., and Aydin, A., 1986, Strike-slip faulting and block rotation in the Lake Mead fault system: Geology, v. 14, p. 1020-1023.

Ruge, J.W., and Stueben, K., 1987, Algebraic multigrid (AMG), *in* McCormick, S.F., ed., Multigrid Methods, SIAM Frontiers in Mathematics, v. 5, p. 73-130.

Sammis, C., King, G., and Biegel, R., 1987, The kinematics of gouge deformation: Pure and Applied Geophysics, v. 125, p. 777-812.

Sammis, C., Osborne, R.H., Anderson, J.L., Badert, M., and White, P., 1986, Self-similar cataclasis and the formation of fault gouge: Pure and Applied Geophysics, v. 124, p. 53-78.

Schowalter, T.T., 1979, Mechanics of secondary hydrocarbon migration and entrapment: AAPG Bulletin, v. 63, p. 723-760.

Scott, T.E., and Nielson, K.C., 1991, The effects of porosity on the brittle-ductile transition in sandstones: Journal of Geophysical Research, v. 96, p. 405-414.

Segall, P., and Pollard, D.D., 1980, Mechanics of discontinuous faults: Journal of Geophysical Research, v. 85, p. 4337-4350.

Segall, P., and Pollard, D.D., 1983, Nucleation and growth of strike-slip faults in granite: Journal of Geophysical Research, v. 88, p. 555-568.

Shipton, Z.K., and Cowie, P.A., 2001, Damage zone and slip-surface evolution over ˜m to km scales in high-porosity Navajo Sandstone, Utah: Journal of Structural Geology, v. 23, p. 1825-1844.

Shipton, Z.K., Evans, J.P., Robeson, K.R., Forster, C.B., and Snelgrove, S., 2002, Structural heterogeneity and permeability in faulted aeolian sandstone: implications for subsurface modeling of faults: AAPG Bulletin, v. 86, p. 863-883.

Sibson, R.H, 1987, Earthquake rupturing as a mineralizing agent in hydrothermal systems: Geology, v. 15, p. 701-704.

Smith, D.A., 1966, Theoretical considerations of sealing and non-sealing faults: AAPG Bulletin, v. 50, p. 363-374.

Smith, D.A., 1980, Sealing and nonsealing faults in Louisiana Gulf Coast salt basin: AAPG Bulletin, v. 64, p. 145-172.

Smith, L., Forster, C., and Evans, J., 1990, Interaction of fault zones, fluid flow, and heat transfer at the basin scale, *in* Newman, S., and Neretnieks, I., eds., Hydrogeology, Selected Papers, Hydrogeology of low permeability environments: Hanover, Verlag Heinz Heise, v. 2, p. 41-67.

Sneider, R.M., Sneider, J.S., Bolger, G.W., and Neasham, J.W., 1997, Comparison of seal capacity determinations: conventional cores vs. cuttings, *in* Surdam, R.C., ed., Seals, traps, and the petroleum system: AAPG Memoir 67, p. 1-12.

Sternlof, K., and Pollard, D.D., 2001, Deformation bands as linear elastic fractures: progress in theory and observation: AGU Transactions, Fall Meeting.

Stewart, J.H., 1980, Geology of Nevada: Nevada Bureau of Mines and Geology Special Publication, v. 4, 136 p.

Stewart, J.H., and Carlson, J.E., 1978, Geologic map of Nevada, 1:500,000 scale: U.S. Geological Survey Map MF-930, 2 sheets.

Stewart, J.H., Poole, F.G., and Wilson, R.F., 1972a, Stratigraphy and origin of the Chinle Formation and related Upper Triassic strata in the Colorado Plateau region: U.S. Geological Survey Professional Paper, v. 690, 336 p.

Stewart, J.H., Poole, F.G., and Wilson, R.F., 1972b, Stratigraphy and origin of the Triassic Moenkopi Formation and related strata in the Colorado Plateau region: U.S. Geological Survey Professional Paper, v. 691, 195 p.

Swanson, M.T., 1988, Pseudotachylyte-bearing strike-slip duplex structures in the Fort Foster brittle zone, south Maine: Journal of Structural Geology, v. 10, p. 813-828.

Taylor, W.L., 1999, Fluid flow and chemical alteration in fractured sandstones: [Ph.D. Thesis] Stanford University, 411 p.

Taylor, W.L., and Pollard, D.D., 2000, Estimation of in situ permeability of deformation bands in porous sandstone, Valley of Fire, Nevada: Water Resources Research, v. 36, p. 2595-2606.

Taylor, W.L., Pollard, D.D., and Aydin, A., 1999, Fluid flow in discrete joint sets: field observations and numerical simulations: Journal of Geophysical Research, v. 104, p. 28,983 - 29,006.

Tchalenko, J.S., 1970, Similarities between shear zones of different magnitudes: Geological Society of America Bulletin, v. 81, p. 1625-1640.

Tchalenko, J.S., and Ambraseys, N.N., 1970, Structural analysis of the Dasht-e-Bayaz (Iran) earthquake fractures: Geological Society of America Bulletin, v. 81, p. 41-60.

Vavra, C.L., Kaldi, J.G., and Schneider, R.M., 1992, Geological applications of capillary pressure: a review: AAPG Bulletin, v. 76, p. 840-850.

Walsh, J.J., Watterson, J., Heath, A.E., and Childs, C., 1998, Representation and scaling of faults in fluid flow models: Petroleum Geoscience, v. 4, p. 241-251.

Watts, N.L., 1987, Theoretical aspects of cap-rock and fault seals for single- and two-phase hydrocarbon columns: Marine and Petroleum Geology, v. 4, p. 274-307.

Wen, X.-H., and Gomez-Hernandez, J.J., 1996, Upscaling hydraulic conductivities in heterogeneous media: an overview: Journal of Hydrology, v. 183, p. ix-xxxii.

Wen, X.-H., Durlofsky, L.J., and Edwards, M.G., in review, Improved upscaling of complex geologic models on Cartesian grids: Mathematical Geology.

Wepfer, W.W., and Christensen, N.I., 1990, Compressional wave attenuation in oceanic basalts: Journal of Geophysical Research, v. 95, p. 17,431-17,439.

Wernicke, B., Axen, G.J., and Snow, J.K., 1988, Basin and Range extensional tectonics at the latitude of Las Vegas, Nevada: Geological Society of America Bulletin, v. 100, p. 1738-1757.

Wilkins, S.J., Gross, M.R., Wacker, M., Eyal, Y., and Engelder, T., 2001, Faulted joints: kinematics, displacement-length scaling relationships and criteria for their identification: Journal of Structural Geology, v. 23, p. 315-327.

Willemse, E.M.J., and Pollard, D.D., 1998, On the orientation and patterns of wing cracks and solution surfaces at the tips of a sliding flaw or fault: Journal of Geophysical Research, v. 103, p. 2427-2438.

Willemse, E.M.J., Peacock, D.C.P., and Aydin, A., 1997, Nucleation and growth of strike-slip faults in limestones from Somerset, U.K.: Journal of Structural Geology, v. 19, p. 1461-1477.

Wilson, J.T., 1965, A new class of faults and their bearing on continental drift: Nature, v. 207, p. 343-347.

Wilson, R.F., and Stewart, J.H., 1967, Correlation of Upper Triassic(?) formations between southwestern Utah and southern Nevada: U.S. Geological Survey Bulletin, 1244-D, 20 p.

Wong, T.F., David, C., and Zhu, W., 1997, The transition from brittle faulting to cataclastic flow in porous sandstones; mechanical deformation: Journal of Geophysical Research, v. 102, p. 3009-3025.

Yin, H., and Dvorkin, J., 1994, Strength of cemented grains: Geophysical Research Letters, v. 21, p. 903-906.

Younes, A.I., and Engelder, T., 1999, Fringe cracks: key structures for the interpretation of the progressive Alleghanian deformation of the Appalachian plateau: Geological Society of America Bulletin, v. 111, p. 219-239.

Zhao, G., and Johnson, A.M., 1992, Sequence of deformations recorded in joints and faults, Arches National Park, Utah: Journal of Structural Geology, v. 14, p. 225-236.

Zoback, M.L., Anderson, R.E., and Thompson, G.H., 1981, Cainozoic evolution of the state of stress and style of tectonism of the Basin and Range province of the western united States: Philosophical Transactions of the Royal Society of London, v. A-300, p. 407-434.